1988-08

Cryocoolers 5 International Cryocooler Conference Proceedings

Cryocoolers Conference

Proceedings of the 5th International Cryocoolers Conference (1988, August 18 - 19, 1988, Naval Postgraduate School, Monterey, California)
http://hdl.handle.net/10945/66475

INTERNATIONAL CRYOCOOLER

PROCEEDINGS

CONFERENCE

CRYOCOOLERS 5

August 18 - 19, 1988

Naval Postgraduate School • Monterey, California

CHAIRMAN'S MESSAGE

I am pleased to enclose your copy of the proceedings of the Fifth International Conference on Cryocoolers. I was honored and happy to have been chairman of this event for 1988. We had a very interesting and rewarding group of sessions covering many familiar projects as well as new emerging technologies. Papers on pulse tubes, magnetic refrigeration and long life space components were presented to the attendees.

Our setting at the Naval Postgraduate School in Monterey, California turned out to be an excellent choice. We had cool but beautiful weather with a location by the sea. Our social highlight was our banquet at the Monterey Bay Aquarium. Our Naval hosts provided all that we needed as far as on-site support.

The world of cryogenics is a growing technology with a rapidly expanding future in applications. Along with our previous research projects in sensors, we had a paper on medical applications and we look forward to being an integral partner in applications of superconductivity.

I wish to thank all the people who helped make the conference the success that it was. The authors submitted more papers than in any previous conference. Special thanks go to my co-chairman Dr. Alfred Johnson, the program committee chaired by Ron White, my secretary Carol Clark, the moral support of my co-workers, the administrative support of personnel of the Universal Technology Corporation especially Faye Geidner and Jill Jennewine, and Howard Wolf of the Air Force acoustic fatigue group for his support in publishing these proceedings. Without the help of these and many others, we would not have achieved the success that we did.

On a personal note, I was transfered on 28 Aug 1988 to a new assignment in the acoustic fatigue group of the Aeronautical Systems Division. I regret no longer being in cryogenics and will miss the conference and particularly the outstanding individuals that are the attendees. I will follow your progress in cryogenics and hope that your next conference in 1990, chaired by Dr. Peter Kerney of CTI Corp, will present more breakthroughs and applications than ever before.

Paul Lindquist
Chairman, Cryocoolers-5

GENERAL INFORMATION

Conference Committee

CHAIRMEN

Paul Lindquist
AFWAL/FDSG
Wright-Patterson AFB, OH 45433-6553
513/255-5229

Alfred Johnson
M4/929
Aerospace Corp.
P.O. Box 92957
Los Angeles CA 90009

PROGRAM COMMITTEE

Ronald White, Chairman, AFWAL/FIEED

Peter Kerney, CTI-Cryogenics

Otto C. Ledford, Advanced Technology

W. George Patton, D.T. Naval Ship R&D Center

Ray Radebaugh, National Bureau of Standards

George Robinson, Massachusetts Institute of Technology

CONFERENCE COORDINATORS

Faye Geidner
Jill Jennewine
Universal Technology Corporation
4031 Colonel Glenn Highway
Dayton OH 45431-1600
513/426-8530

ADVISORY BOARD

John Barclay, Astronautics

Stephen Castles, NASA/Goddard

Gordon Davey, University of Oxford, U.K.

Andre DeVilliers, Riverside Research

Yoshihiro Ishizaki, Japan, Consultant

Ralph Longsworth, APD-Cryogenics

Martin Nisenoff, Naval Research Laboratory

Samuel Russo, Hughes Aircraft Co.

Joseph Smith, MIT

Michael Superczynski, D.T. Naval Ship R&D Center

Walter Swift, Creare R&D Inc.

Klaus Timmerhaus, University of Colorado

Graham Walker, General Pneumatics Corp.

CONTENTS

CONTENTS (CONT.)

CONTENTS (CONT.)

SESSION I

J-T COOLING

CHAIRPERSON: E. EDELSACK
VICE CHAIRPERSON: P. KERNEY

RECENT DEVELOPMENTS IN JOULE-THOMSON COOLING: GASES, COOLERS AND COMPRESSORS

W. A. Little

Physics Department
Stanford University
Stanford, CA 94305

ABSTRACT

During the past several years some striking advances have been made in the performance of miniature Joule-Thomson refrigerators. They can now be fabricated in a wide range of shapes and sizes and can be made with several gas circuits and multiple stages of expansion. These features allow the refrigerators to operate at low temperatures with good efficiency. A major breakthrough has occurred in cooling technology through the development of certain hydrocarbon-nitrogen gas mixtures for JT cooling, with cooling capacities as much as ten times that of pure nitrogen, yet have a boiling point close to that of nitrogen itself. The gases are safe to use and are non-flammable. This makes possible low pressure operation of compressors in closed cycle systems and greatly extends the operational utility of Joule-Thomson refrigerators. These and other developments in JT refrigerator technology are reviewed.

Introduction

It was just over ten years ago, at an earlier meetings of this group[1] that the possibility of developing microminiature, Joule-Thomson (JT) refrigerators of sufficiently small size to be useful for cooling superconducting devices in a miniature, ambient temperature package, was suggested. This and a great deal more has been accomplished since that time[2]. It is the purpose of this paper to discuss these developments and, in particular, to discuss those developments which have occurred in the past few years since this subject[3] was last reviewed.

Cooling is achieved in a JT refrigerator by passing high pressure gas through a counter-current heat exchanger, expanding it to lower pressure thereby causing it to cool by the Joule-Thomson effect, and then passing the cold gas back through the heat exchanger to pre-cool the incoming gas, before exiting the refrigerator. The system needs, in addition to the heat exchanger and expansion valve, which are usually referred to as the "refrigerator", some means for recompressing the gas, and of cleaning and drying it so as to prevent condensation of impurities in the refrigerator. In discussing the system we will focus first on the refrigerators, then on the gases used as the working fluids, then on the cleaning process and finally on the compressors needed to provide a continuous source of high pressure gas.

Microminiature Refrigerators

Microminiature refrigerators are fabricated using a photolithographic process somewhat analogous to that used in the fabrication of integrated circuits in the semiconductor

industry. In this process, the gas channels of the heat exchanger, expansion capillary and boiler of the refrigerator are abrasively etched in thin, planar glass substrates. These substrates are then fused together to yield a laminated glass plate containing the pattern of channels of the complete refrigerator. Typical dimensions of the channels are 200μ wide by 30μ deep and the size of an 80 K, N_2 refrigerator with a capacity of 250 mW is 7.5 cm x 1.4 cm x 0.2 cm. In manufacturing, the depths of the channels have to be controlled to about ± 2μ to obtain an acceptable yield, and the final asssembly must provide a bond between the substrates capable of withstanding internal pressures in excess of 180 atm. This technology, which originated at Stanford University and was developed extensively at MMR Technologies, Inc. in Mountain View, has now matured and microminiature refrigerators operating from ambient to 80K are in use in university and industrial R&D laboratories worldwide and are found in instrumentation which is used principally in the semiconductor industry.

A typical device used in a low temperature microprobe is shown in Figure 1. The alumina substrate at the cold end contains a heater and a miniature Si-diode thermometer allowing temperature control over the entire operating range of the refrigerator. The photolithographic fabrication process allows great flexibility in the design of the refrigerators. In particular, more complex cycles than the simple, single expansion Hampson cycle can be used with a minor change in the fabrication process and negligible increase in cost. The Linde cycle has been utilised in all the refrigerators which are now in commercial use. In this, the gas is expanded in two stages, allowing higher efficiency and operation at lower temperatures than with a simple, single expansion. Multi-gas refrigerators have been fabricated for operation to 20K, using argon and hydrogen and a three stage unit 1.5" in diameter and 0.10" thick is under development for operation at helium temperatures. These require finer channels and almost an order of magnitude tighter control of the channel dimensions because of the low viscosity of the hydrogen. This has posed a serious challenge to the technology and difficulties encountered here have delayed the commercial availability of such coolers. Progress has been made recently with the use of sputtering techniques for better control of the thickness of the bonding layer and work is proceeding with magnetron-enhanced-reactive-ion plasma etching to obtain more precisely controlled channel dimensions. A 7 layer refrigerator of exactly the same outside dimensions as that shown in Figure 1, but which will operate to 27 K with neon or 20 K with hydrogen is expected to be available in the next few months [4].

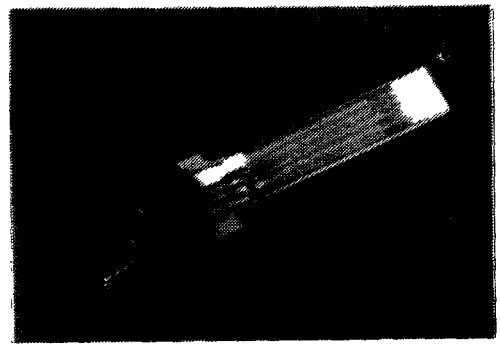

Figure 1. Microminiature refrigerator
for 80 K operation.
(Courtesy MMR Technologies, Inc.)

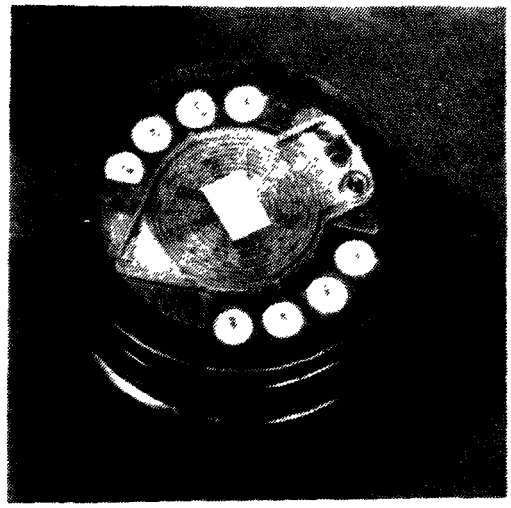

Figure 2. Fast Cooldown Microminiature refrigerator.
Cooldown time < 2 secs to 90 K.
Dimensions 1" x 0.8" x 0.05".
(Courtesy MMR Technologies, Inc.)

The refrigerators can be made in a wide range of sizes and capacities. In Figure 2 is shown a fast cooldown version, less than 1" in diameter, which can cool to 90 K in under 2 seconds using argon. These refrigerators are extremely rugged. Several of these have been subjected to acceleration tests in excess of 30,000 g's without any failures. In Figure 3 is shown the argon and hydrogen stage of a three stage refrigerator designed for helium temperature operation. Perhaps the most distinctive feature of these refrigerators is their low noise operation. Although the gas flow through some of the channels approaches sonic velocities, no measurable noise is observed on the cold stage, presumably due to the rigid construction of the refrigerator. This has made it possible to use the refrigerators for

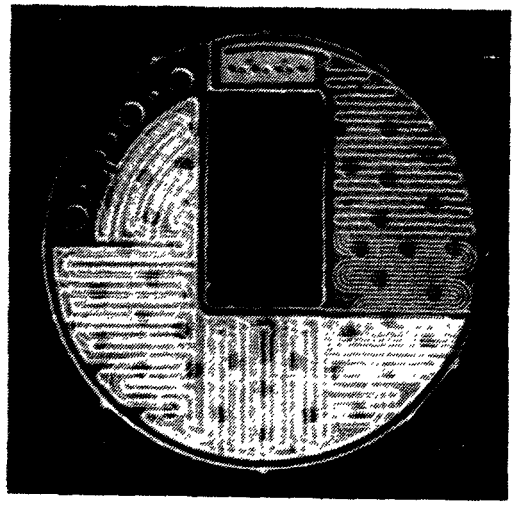

Figure 3. Argon-hydrogen stages of a 3-stage 10 K refrigerator.
(Courtesy MMR Technologies, Inc.)

sensitive electrical measurements in Deep Level Transient Spectrometry (DLTS), Van der Pauw measurements of semi-insulating, semiconductor materials and in FTIR instruments. It is expected to be of importance for use with superconducting devices.

Use with Gas Mixtures

Until a few years ago the only gases which were used in JT systems in the US and NATO countries were the pure elemental gases, argon, nitrogen and hydrogen. Hydrogen must be cooled to below its inversion point, near 200 K before JT cooling can occur and argon and nitrogen, when operated from ambient temperature have a low thermodynamic efficiency for cooling. However, it was claimed in a patent application filed in the UK in 1971, by Alfeev et al.[5] from the Soviet Union, that substantially higher thermodynamic cooling efficiencies could be attained in JT refrigerators by the use of nitrogen-hydrocarbon mixtures. Several mixtures were described with different efficiencies and different boiling points. One, in particular, consisting of a mixture of 30% by volume nitrogen, 30% methane, 20% ethane and 20% propane afforded a 10- to 12-fold increase in efficiency in their cooling unit, compared to the efficiency obtained using nitrogen alone, and had a boiling point of 80 K at ambient pressure. We learned of this work in 1982 and verified the essence of their claims in a series of measurements using our microminiature refrigerators. An example of the use of one such mixture in a MMR refrigerator is shown in the cooldown curves in Figure 4. A spectacular increase in capacity is obtained - a 250 mW, N_2 refrigerator develops a capacity of 2.5 Watts at 120 K when used with this gas mixture at 120 atm. input pressure.

In spite of this enormously enhanced cooling efficiency, virtually no interest developed in

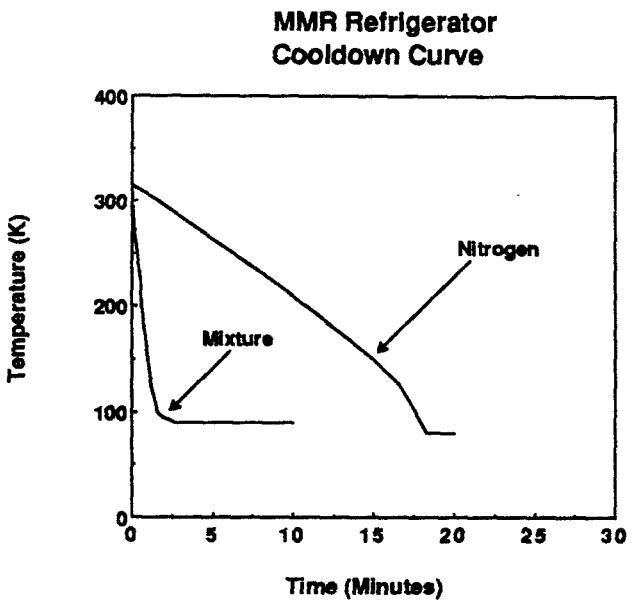

Figure 4. Comparison of cooldown time for an MMR refrigerator using nitrogen and with the nitrogen-hydrocarbon gas mixture. Both at 100 atm.

this capability in the US, either in military circles or in commercial applications, because of the flammablity or possible explosive potential of the mixture when mixed with air. In 1985 we discovered[6] that the addition of the fire retardant compound Freon 13B1, CF_3Br known as "Halon", at a concentration of a few percent by volume, rendered the mixture essentially non-flammable. However, more importantly, Halon, which freezes at 105 K, is soluble at these concentrations in the hydrocarbon components of the mixture and allows use of the non-flammable mixtures in a JT refrigerator to temperatures below 77 K. This now has opened the door to the use of these mixtures in high efficiency JT refrigeration systems. The mixtures, however, are not without their problems. We noted early on that at certain pressures and in certain refrigerators, some mixtures gave unstable operation, exhibiting large dynamic fluctuations in the boiler temperature. In addition, for different mixtures, the minimum temperature attained was a rapidly varying function of the composition of the mixture, and also, commercially supplied mixtures often gave widely different results. The temperature fluctuations appear to arise from the presence of two or more liquid components in the boiler, each with a different bubble point. The second problem arises from the dependence of the bubble point on the solubility of the hydrocarbon components in nitrogen at the lowest temperatures and is intrinsic to such mixtures. The variations in the behavior of nominally similar mixtures, from different suppliers, appears to be due to the order followed in mixing, the temperature at which it is done and possibly, stratification of the gas in the cylinder for some mixtures. In order to understand these problems better we have developed a two-pronged attack. First, we have begun a program aimed at deriving the phase diagram of a series of gas mixtures using an empirically determined equation of state which can be generalised for arbitrary mixtures. Second, we have built our own mixing station, which allows us to prepare mixtures under more controlled conditions.

Calculation of Phase Diagrams of Gas Mixtures

Over the past forty years a number of methods have been developed for the calculation of the entropy, enthalpy, pressure and fugacity of gases as a function of density and temperature. These are based on one of several theoretically derived equations of state, which can be described by a small set of numerical parameters. These can be programmed on a personal computer to give reasonably accurate phase diagrams which encompass the critical region and allow the calculation of the properties of both the liquid and gaseous phases. One such program, DDMIX (1988) which calculates many of the properties of most of the common gases uses in these mixtures is available from the National Bureau of Standards[7]. We had developed previously[8], our own program to allow a more detailed study of the several liquid components present. The calculation of the isenthalps and isobars in a TS diagram is shown in Figure 5 for the nitrogen-hydrocarbon mixture indicated. The boiling point involves a special calculation so the two phase region is not shown in this figure. As can be seen from the isenthalps, cooling from 300 K to about 120 K occurs for a single expansion of the gas from 60 atm. to 1 atm. Calculations of the thermodynamic efficiency for the cooling process for this and other mixtures gives values which range from 40% to 70% of that of Carnot in the temperature range from 80 K to 140 K. These figures, taken in conjuction with the small residual heat losses for a JT refrigerator and the simplicity of the device, makes the JT refrigerator now, an extremely attractive mode of refrigeration for this temperature range.

The properties of the mixtures can be varied over a wide range of values by varying the concentration of the lower boiling point components to obtain operation at lower temperatures, and the concentration of higher boiling point components to obtain higher efficiency at lower pressures. We have used one composition (50% nitrogen, 28.4%

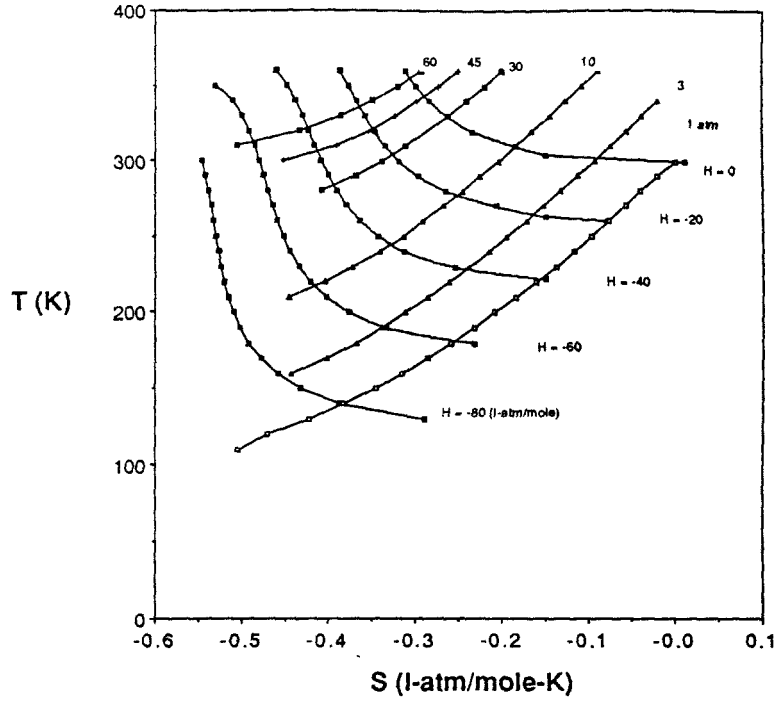

Figure 5. Calculated isenthalps and isobars in the
TS–Diagram for the hydrocarbon gas mixture :
27% methane, 50% ethane, 13% propane and 10% n-butane.

methane, 14.2% ethane, 7.1% propane) for refrigeration at 81.3 K at an input pressure of 55 atm., and another with (34.6% methane, 53.4% ethane, 7.3% propane, 4.7% halon) for refrigeration at 136 K with an input pressure of 30 atm. These mixtures offer the possibility of using compressors at a pressure an order of magnitude lower than those which have been used hitherto for JT systems.

Of special interest for the cooling of superconducting devices is the possibility of attaining temperatures below 80 K with a single gas in a JT refrigerator. Alfeev. et al. claim that by the partial substitution of nitrogen with neon in such mixtures, temperatures down to 63 K are attainable. We have done some work in this area and have obtained a temperature of 68 K at ambient pressure with a mixture having the composition 25% nitrogen, 25% methane, 20% neon, 15% ethane and 15% propane. At reduced pressure the temperature was lowered to 65 K. Further work needs to be done here to obtain the optimum mixture composition for minimum temperature operation and reasonable efficiency. This is being pursued both theoretically at Stanford and experimentally at MMR Technologies, Inc.

Gas Dryers

Joule-Thomson refrigerators require a gas supply which is relatively free of condensible impurities. The smaller versions of the microminiature refrigerators are particular sensitive to such impurities, which condense in the fine gas channels, reducing the flow

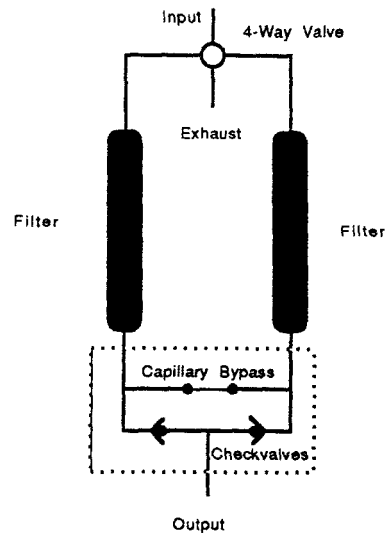

Figure 6. Schematic of reversible zeolite dryer.

and eventually causing a blockage. Upon warming up the exchanger, the frozen impurities melt, clear and leave no permanent impairment in the performance of the cooler. Water vapor is by far the most common contaminant. Dryers using molecular sieves in the form of a long column, can reduce the moisture content to the parts-per-million level, which is then sufficient to allow continuous operation for many hours. However, where a refrigerator is to run continuously for thousands of hours without clogging, the impurity content must be reduced to the parts-per-billion level. A simple zeolite dryer cannot maintain this level of purity. While the moisture is readily absorbed in the first few centimeters of the column, the continuous passage of the dry gas through the column, gradually transports the band of moisture along the column until it reaches the far end and then sweeps it out and in to the refrigerator. This can be prevented by the use of a gettering type of dryer, which reacts irreversibly with the impurity . These are available as point-of-use dryers[9], but normally must be operated hot - at 450° C. They are suitable for use with the inert gases, such as He, Ne or Ar but not with the hydrocarbons and most other gases, which react with the getter. In particular, they are unsuitable for use with the gas mixtures discussed earlier.

We have had considerable success with a reversible dryer illustrated in Figure 6. In this, two zeolite drying columns are used alternately, with a fraction of the dry gas at high pressure from one column used after expansion to ambient pressure, to sweep the impurities from the other column. With this arrangement the water content can be reduced to the parts-per-billion level, allowing essentially clog-free operation. The performance of the dryer is generally limited not by the drying ability of the zeolite but by the failure of valves or valve seats in the extremely dry environment in which they must operate.

Compressors

Until recently, the use of JT coolers with compressors in closed cycle operation have been largely unsuccessful. The compressors needed have to have a compression ratio of 150:1 to 300:1, which is much higher than that for other cooling cycles. This normally requires,

three or four stages of compression and the final stages must operate in a dry, clean atmosphere at extremely high pressures i.e. 150 - 300 atm. The last two factors severely limit the life of the sealing rings . At these extremely high pressures and normal operating speeds, the pv-rating of most dry, bearing materials is exceeded. In addition, the lubricity of many sealing materials goes to zero in such a dry environment, resulting in catastrophic failure of the rings in a few hours of operation. Oil lubricated compressors on the other hand avoid some of these problems, but the presence of oil vapor within the compressor causes other problems such as fouling of the valves and contamination of the filters.

In the past five years we have participated in a development program with Showa Seiki, Showa Precision Machinery Co., Ltd. in Amagasaki, Japan on the development of a small, dry, oil-free compressor for use with our JT systems. This program has solved all the problems originally encountered for this system. The key to this successful development has been in the design of the sliding seals, the choice of seal material, the surface finish of the cylinders and the piston supports. The development has been spurred on by the availability now of gas mixtures, which allow operation of the compressors with JT refrigerators at much reduced pressures. Testing of these compressors has been underway for the past three years. One such compressor has been in continuous operation at 1 atm. input pressure, 75 atm. output pressure, with a flow of 1.5 l/m, with no maintenance, for 8,000 hours with no measureable degradation in performance over this period. A second unit designed for operation at 140 atm. and a flow of 2 l/m has been operating for 3,000 hrs at this point, also without maintenance for this period. This unit, which is designed for laboratory use, is shown in Figure 7. Testing is now proceeding on the operation of the complete closed cycle system with compressor, dryer and JT refrigerator.

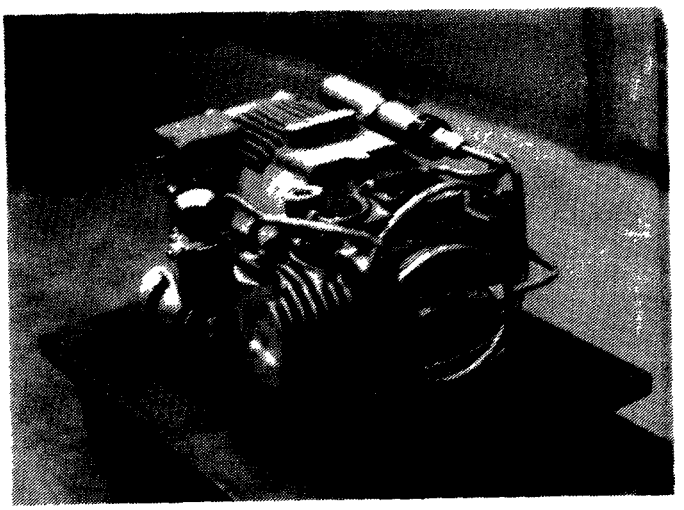

Figure 7. Three stage compressor for operation at 140 atm., and flow of 2.0 l/m. Outer case removed.
(Courtesy MMR Technologies, Inc.)

Discussion

We believe that it is now possible to build compressors suitable for use with JT refrigerators, capable of running continuously without maintenance for periods of the order of a year with excellent reliability. The use of the mixed gas as the working fluid appears now to make possible light-weight, closed cycle systems with an efficiency equal

to or better than that of current Stirling cycle coolers. Single gas, JT coolers working at ambient pressures appear capable of operating at temperatures near 65 K. These look particularly attractive for use with high-T_c superconducting devices in view of the relatively high efficiency of refrigeration, small heat losses and low noise operation of these JT microminiature refrigerators. The fabrication process, developed for micro-miniature refrigerators, is not limited to small scale cooler fabrication but is also adaptable to the fabrication of much larger coolers, suitable for cooling such devices as CMOS microprocessors, DRAM memory units and large array detectors. These larger coolers are presently under development.

Acknowledgements

The work reported here was done at MMR Technologies, Inc. with the help of Mark Dubois, Bill Shubin, Dave Connell, Frank Tochez and Herb Edman, to whom I am indebted. Part of this work was supported by the Office of Naval Research under Contract N00014-86-C-0301.

References

1. W. A.Little, "Scaling of Miniature Cryocoolers to Microminiature Size", in Proceedings of the NBS Cryocooler Conference, ed. J. Zimmerman and T. M. Flynn, NBS Spec. Publ. No. 508, p.75 (1978).

2. W. A. Little,"Integrated Cryogenic Chip Carrier for High Speed CMOS and Superconducting Devices", Proc. Symp. Low Temperature Electronics and High Temperature Superconductors, **88-9**, The Electrochemical Society, Inc., Pennington, New Jersey (1988), 251-259.

3. W. A. Little, "Microminiature Refrigeration", Rev. Sci. Instrum. **55**, 661 (1984).

4. MMR Technologies, Inc. private communication.

5. V. N. Alfeev, et al., Great Britain Patent No. 1,336,892 (1973).

6. W. A. Little, U.S. Patent application, Serial No. 919,699 (1985), Patent Pending.

7. NBS Standard Reference Database 14 DDMIX (1988), available from Joan Sauerwein, Standard Reference Data, National Bureau of Standards, Bldg. 221/A323, Gaithersburg, MD 20899, (301) 975-2208.

8. Calculations were done, based on the BWR equations, (M. Benedict, G. B. Webb and L. C. Rubin, J. Chem. Phys.**8**, 334 (1940) and J. Chem Phys. **10**, 747 (1942)). This work, done in collaboration with Al Nash, will be published elesewhere.

9. Available from SAES Getters/ U. S. A., Inc., 1122 E. Cheyenne Mtn. Blvd., Colorado Springs, CO 80906, Tel. (303) 576-3200.

DEVELOPMENT AND TESTING OF AN 80 K OXIDE SORPTION CRYOCOOLER

Steven Bard
Jack A. Jones

Jet Propulsion Laboratory
California Institute of Technology
Pasadena, California 91109

Abstract

The design, development and testing of a multiple stage 80 K sorption cooler is described. The 80 K stage consists of two praseodymium cerium oxide (PCO) chemisorption compressors which compress oxygen from 0.03 MPa (4.4 psia) to 2.8 MPa (404 psia) by thermally cycling between 370°C and 650°C. The high pressure gas produced by the compressors flows through a Joule-Thomson (J-T) expansion cycle. A carbon/krypton sorption cooler, simulated here by an open-cycle J-T refrigerator flowing a gas mixture of methane/Freon-14, provides an upper stage precooler temperature of 140 K. Thermoelectric coolers provide two additional upper stage precooler temperatures of 200 K and 225 K. Experimental temperature, pressure, and flow rate profiles are presented.

Based on these experiments, an improved high-efficiency flight design has been developed, which requires approximately 100 Watts of energy per Watt of cooling at 80 K. This reasonably low power requirement, combined with high anticipated reliability, an expected lifetime of 5-10 years, and the absence of vibration and electromagnetic interference, has made sorption coolers a prime candidate for a number of spaceborne cooling applications.

1. Introduction

Sorption refrigeration represents a technology which can naturally meet the cooling demands of many future spaceborne instruments which require extremely low vibration environments, high operational reliability, and long life (5-10 years). Historically, the major disadvantage of 80 K sorption coolers has been low efficiency relative to mechanical coolers [1,2]. The recent discovery of improved sorbent/gas combinations [3,4], and the development of an innovative compressor design [4], has led to efficiency levels which are now competitive.

The design and testing of an 80 K laboratory breadboard sorption cooler, which uses some of these newly discovered materials, is described here. The 80 K cascaded Joule-Thomson (J-T) refrigerator also contains three precooler stages. Separate thermoelectric cooler (TEC) stages provide 225 K and 200 K temperatures, and a carbon/krypton sorption cooler provides 140 K. Details of the development and testing of the upper stage 140 K

carbon/krypton system, and the integrated testing of both sorption stages, are described elsewhere [4,5]. In the experiments described in this paper, the 140 K carbon/krypton sorption cooler stage has been simulated by an open-cycle J-T cooler.

The following section reviews the fundamentals behind the operation and design of sorption coolers, including the choice of sorbent and gas materials, and a description of the overall system design. Next, the experimental hardware is described, including the sorption compressors, J-T valves, and thermoelectric coolers (TEC's). The experimental results and current development status are discussed in the final sections.

2. Sorption Cooler Principle of Operation and System Design

Sorption refrigeration is a logical adaptation of the well known Joule-Thomson (J-T) expansion cycle, wherein a compressed refrigerant gas is expanded through an orifice to obtain a highly cooled and partially liquefied fluid [6]. Evaporation of the liquid by the instrument detector heat load provides the desired cooling effect. With sorption refrigeration, the gas is stored in a sorbent material via chemical or physical adsorption. When the sorbent bed is subsequently heated, the working fluid is pressurized and driven off, serving as the refrigerant gas for the J-T expansion cycle. A closed cycle system is obtained by resorbing the evaporated gas returning from the J-T expander in a cooled sorbent bed. By alternately heating and cooling several sorbent beds, the J-T cycle can be supplied by a steady stream of high and low pressure gas.

Because of the absence of motors and mechanical displacement devices, sorption compressors are environmentally benign, generating no magnetic, electric or vibration fields. The system is completely sealed, with no lubricants, and can be easily vacuum-baked to achieve the necessary system cleanliness. This, combined with the absence of moving parts, enables the system to achieve excellent operational reliability and long life.

JPL has conducted feasibility testing on a number of promising candidate sorbent/working fluid combinations over the past 10 years [1-5,7]. Figure 1 summarizes the cooling temperature ranges of some of the most promising of these materials, and highlights the selection of the optimal combination for a two-stage 80 K/140 K cooler.

A major factor in choosing the appropriate sorbent/gas combination for a given refrigeration temperature is the available heat rejection temperature. Typically, the lower the heat rejection temperature, the greater the adsorption capacity of a given sorbent. Previously, the only known means to obtain sorption refrigeration in the 80 K range was by physically adsorbing nitrogen to activated carbon at temperatures of about 225 K [1,2]. This low heat rejection temperature is feasible for only limited spacecraft applications, and requires extremely large radiators.

The major breakthrough which led to the work described here was the discovery of an oxide compound, praseodymium cerium oxide ($Pr_{1-n}Ce_nO_x$,

given the acronym PCO), used initially by Union Carbide Corp. for oxygen separation from air [8]. The PCO/O_2 sorption/desorption chemical reaction was found to be fully reversible, with no degradation of the oxygen uptake capacity encountered after testing for over 7000 cycles [8], thus making it a suitable candidate material for sorption refrigeration. To achieve reasonable J-T expansion efficiencies, the oxygen generated by the PCO/O_2 compressors must be precooled by a separate upper stage sorption cooler to approximately 140 K, prior to expansion through the J-T.

A carbon/krypton physical adsorption system has been chosen as the 140 K upper stage precooler. Gas adsorption in both the PCO/O_2 and C/Kr systems occurs at temperatures well above 225 K, so there is no need for low heat rejection temperatures. The C/Kr sorption cooler has been built and successfully tested [4,5], but was simulated here by an open-cycle J-T cooler using a gas mixture combination of 25% methane and 75% Freon-14. The gas mixture produces a greater cooling power than the two existing C/Kr compressors can generate, and produces a more stable upper stage temperature. The gas mixture has a saturation temperature of about 139 K at an atmospheric pressure of 0.1 MPa. It was operated at a high pressure

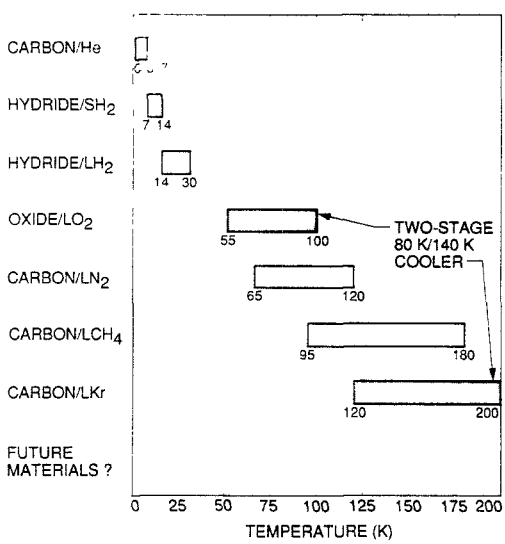

Fig. 1 Temperature ranges of sorption cooler stages.

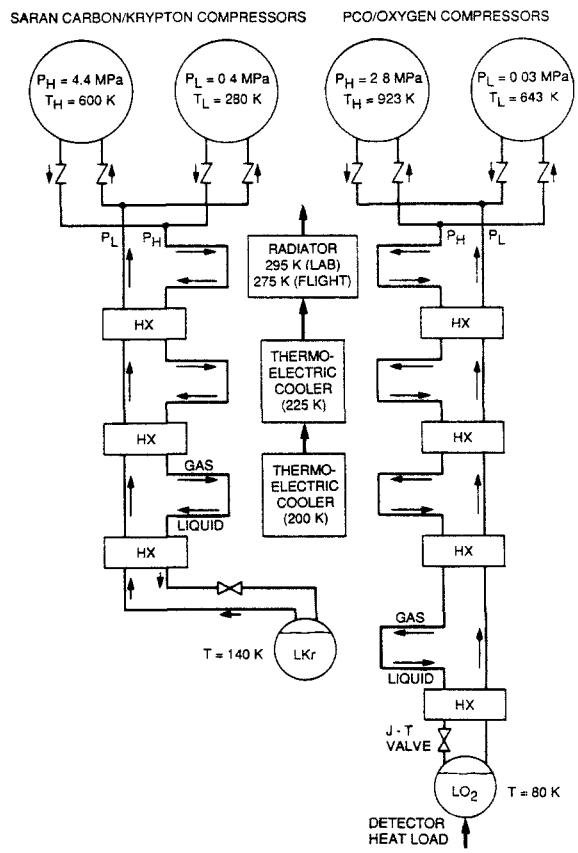

Fig. 2 Schematic of two-stage 80 K/140 K sorption cooler.

of 7.83 MPa (700 psia), and produced a flow rate through its J-T valve of about 160 sccm. Krypton itself was not used as the open cycle J-T fluid because the gas mixture has a higher J-T efficiency and a much lower cost.

A simplified schematic of the two-stage closed-cycle cooler is shown in Fig. 2, together with nominal values of operating temperatures and pressures. Note that the 140 K carbon/krypton stage actually liquefies the high pressure oxygen prior to expansion in the J-T valve to its ultimate low temperature of 80 K. In a similar manner, a 200 K thermoelectric cooler (TEC) is used to liquefy the high pressure krypton (or methane/Freon-14) prior to expansion in its J-T valve to 140 K. Liquefying the high pressure refrigerant fluids prior to J-T expansion removes the latent heat of vaporization, and thus greatly improves the J-T efficiency. Finally, an upper stage of cooling is provided by a 225 K TEC, which is also used as the heat sink for the 200 K TEC.

The low pressure sides for each stage are fixed at the respective oxygen and krypton saturation pressures at 80 K and 140 K. The high side pressures are set by the liquefication pressures of oxygen and krypton at their respective precooler temperatures of 140 K and 200 K. The compressor operating temperatures are based on the adsorption isotherm data for the PCO/O_2 and C/Kr systems [4,5] and the required pressure cycle limits. It is theoretically possible to operate the oxide stage at temperatures down to just above the freezing point of oxygen (54.4 K), but the heat exchanger design must allow for extremely small pressure drops.

3. Experimental Hardware Design

A simplified schematic of a generic sorption compressor design is shown in Fig. 3. A key element of the compressor is the gas-gap heat switch, which allows the sorbent bed to be alternately thermally isolated from, and then thermally connected to, the external heat sink radiators. Heat conduction across the switch is accomplished by filling the 2.29 mm (0.090 inch) gap with a low pressure (approximately 10 torr) gas. Isolation is subsequently achieved by evacuating the gap to about 10^{-3} torr. The heat switch gas for the laboratory breadboard cooler, nitrogen, is supplied from a regulated storage bottle, and the gap is evacuated with a laboratory cryopump. Venting may be eliminated for a flight cooler by using a closed cycle heat switch which utilizes a gas source and getter system. To reduce radiative heat leaks across the gap, five layers of

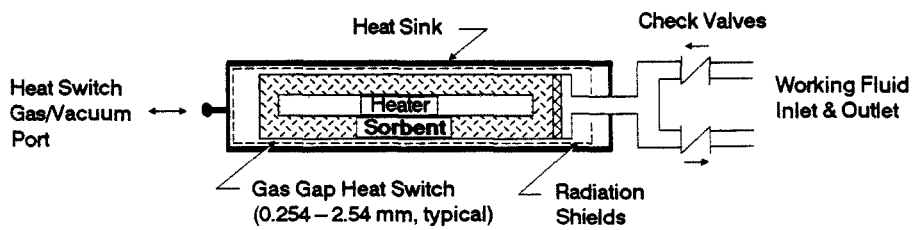

Fig. 3 Sorption compressor concept.

nickel foil, coated with vacuum deposited gold, are placed in the gap as radiation shields.

Referring to Fig. 3, the pressure vessel cylinder, containing about 200 g of PCO, is a 2.54 cm (1.0 inch) OD by 12.7 cm (5 inch) long canister constructed of Inconel 625. The oxygen flows in and out of the canister through a small, 1.59 mm OD (1/16"), Inconel 625 capillary tube. A 1 micron sintered Inconel filter prevents PCO powder from leaking out of the canister.

Although the sorption compressors are perhaps the most unique element of the sorption cryocooler, a second and very important element is the cryostat, which typically interfaces with an instrument focal plane (simulated here by a heater), and contains the J-T expanders, counterflow heat exchangers, and thermoelectric coolers noted in Fig. 2.

The cryostat consists of three concentric shields, surrounded by an external housing which is maintained at room temperature (294 K) by a recirculating water cooler. The housing surrounds a 225 K shield, which is cooled by a series of six 4-stage TEC's. The 225 K shield surrounds, and acts as a heat sink for, a 3-stage TEC which cools the next shield to 200 K. Very high thermally conductive flexible copper straps allow independent thermal expansion of the TEC's relative to their respective thermal shields. All TEC's were purchased from Marlow Industries.

Each of the cryostat radiation shields are constructed of thin, gold-plated copper material, with additional multilayer insulation (MLI) between the 140 K, 200 K, 225 K, and 294 K shields. The shields are suspended in position relative to each other by a series of low thermal conductivity plastic supports.

The J-T valves are commercially manufactured sintered flow restrictor filters from Mott, Inc. These J-T valves have been found to be extremely reliable, repeatable, and non-clogging, due primarily to their relatively large flow area compared to a fixed orifice. As added protection, zeolite filters are located upstream of both J-T valves to remove possible trace contaminants. The liquid Kr (or CH_4/Freon-14) and liquid O_2 are collected downstream of the J-T valves by means of centrifugal swirling inside small cylinders, 1.27 cm (1/2 inch) OD x 1.27 cm (1/2 inch) long. The boiled gas is then withdrawn from the center of the cylindrical dewars as heat is added to the dewar walls. A small heater bonded to the oxygen dewar wall provides a simulated detector heat load.

Figure 4 shows a photograph of the PCO/O_2 sorption cooler with the two-stage J-T cryostat. The cryostat is the cylindrical object on the bench at the left, the bottle of mixed gas is located to the left of the cryostat, and the PCO/O_2 compressors are located behind the panel under the window on the right. The data acquisition/control system can be seen at the far right. The system can be made much more compact for flight, but one of the advantages of sorption coolers, the ability to locate the cryostat remotely from the compressors, is evident.

Fig. 4 80 K sorption cooler laboratory breadboard system.

4. Experimental Results

Figure 5 shows experimental compressor temperature, compressor pressure, and refrigerator high and low pressures as a function of time over several compressor cycles. As the compressors are heated, the oxygen is desorbed and pressurized, until the outlet check valve opens at ~410 psia (2.83 MPa). Further heating produces outflow of oxygen from the compressors, as indicated by the slightly rising refrigeration system high pressure. Next, as the compressors cool, the pressure decreases until the inlet check valve opens at ~3.3 psia (0.023 MPa). Further cooling produces inflow of oxygen from the low pressure side of the J-T cycle, as indicated by the decreasing refrigeration system low pressure. Note that the two compressors were operating approximately in-phase during the 100 minutes shown in Fig. 5. There are slight design differences between both compressors, and thus their cycle times are not identical (28.9 min and 29.5 min for units A and B, respectively).

Figure 6 shows the cold stage temperature, refrigerator low pressure, and flow rate variation with time, over a 5 hour period. The oscillations are due to the inherent intermittent compressor operation, with the peaks caused by compressor intake strokes. Note that the temperature oscillations directly follow the pressure oscillations, as the cold stage temperature is equal to the saturation temperature of oxygen at the corresponding low pressure.

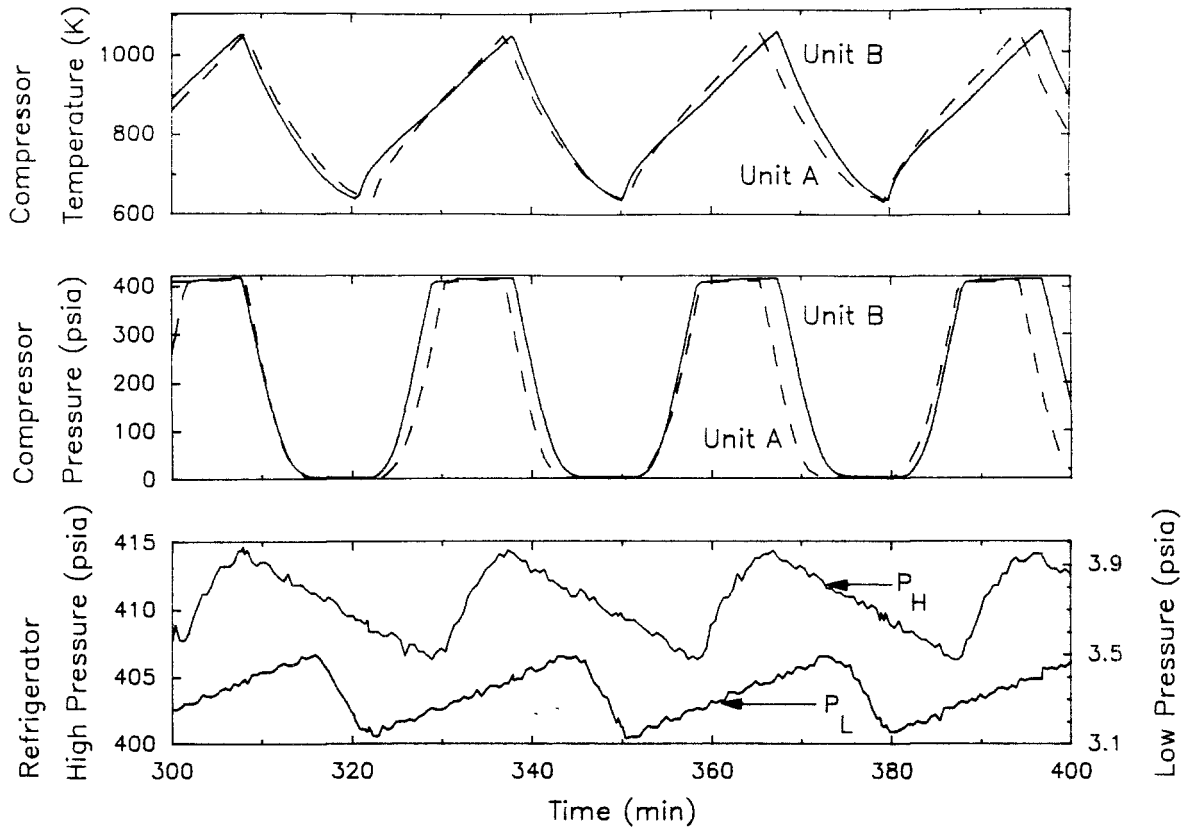

Fig. 5 PCO/O_2 compressor temperature and pressure, and refrigerator high and low pressures, as a function of time.

Although the operating characteristics of the sorption cooler can be seen to be quite dynamic, with complex oscillations of pressures and flow rate, the temperature stability of the 80 K stage was maintained within ± 0.4 K throughout the 7 hour test period. This value could be reduced by approximately 50% by operating the two compressors out-of-phase. The temperature stability can be further improved by operating slightly above the saturation temperature, by applying additional heater power to the cold stage, thus eliminating the temperature oscillation correspondence with the fluctuating low pressure. With closed-loop feedback control on the cold stage heater, the temperature stability could be improved to within ± 0.1 K.

Over the 7 hour test, the two PCO/O_2 compressors produced a time-averaged flow rate of 71 sccm, with a total time-averaged compressor input power of 96 W. This flow rate produces a gross cooling power of 0.274 W at 80 K, assuming a heat exchanger effectiveness of 0.95. The gross cooling power consists of a parasitic heat load of 0.11 ± 0.010 W, and an additional 0.164 W generated by the cold stage heater. The gross cooling power calculation is not very sensitive to the heat exchanger effectiveness,

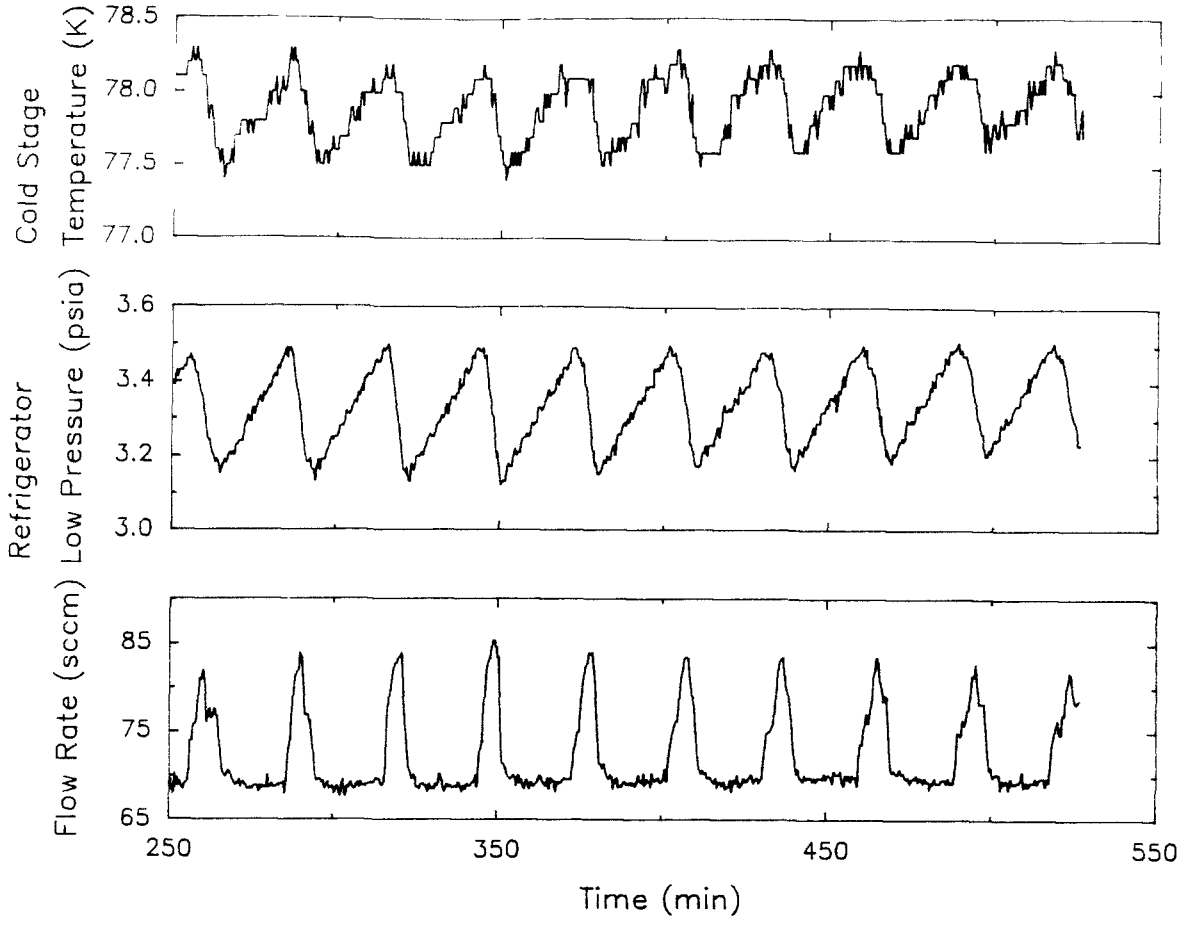

Fig. 6 Cold stage temperature, refrigerator low pressure, and oxygen flow rate as a function of time over a 5 hour test period.

as it ranges from 0.269 W to 0.279 W, for heat exchanger effectiveness values of 0.9 to 1.0, respectively.

5. Development Status

A technology development program is underway at JPL to develop a flight-like, two-stage 80 K/140 K sorption cooler, within the next few years. This program includes component reliability studies, analytical performance modeling, critical component development, and research on advanced sorbent/gas combinations.

The laboratory breadboard cooler described here and in Ref. 4 was the first critical step in the technology development program. It is basically a proof-of-principle model and test bed for the 80 K/140 K sorption cooler, and was not designed for high efficiency. The power requirements can be greatly reduced for a flight cooler, particularly by

miniaturizing the cryostat and by using an innovative high-efficiency compressor design, as described below.

The laboratory cryostat housing is a 35.6 cm (14 inch) diameter, by 35.6 cm (14 inch) long, aluminum cylinder. The large size was chosen for ease of assembly and disassembly, but at the price of large parasitic radiative heat leaks. Thermal analysis indicates that the heat load on the laboratory cryostat 225 K stage can be reduced by over 90% by miniaturizing the cryostat [9]. The preliminary design of a miniaturized flight cryostat, geared towards a specific instrument, has been completed.

A great performance improvement can be obtained by using an innovative compressor design in which the energy released from the PCO/O_2 compressors during their cooling phase is used to heat the C/Kr compressors during their heating phase. Because the PCO/O_2 compressors operate in a much higher temperature regime than the C/Kr compressors, as shown in Fig. 2, the C/Kr compressors can be powered by no additional energy beyond that needed to heat the PCO/O_2 compressors. In addition, the compressor can be designed with much lower heat losses than for the current laboratory PCO/O_2 compressor. A flight design implementing this heat recuperation scheme has been developed, analyzed, and will be fabricated in the near future.

Further efficiency improvements can be achieved by using an optimized PCO formula, $Pr_{0.92}Ce_{0.008}O_x$, which has a usable oxygen loading of 1.5%, compared with the 1.2% oxygen loading for the currently used $Pr_{0.8}Ce_{0.2}O_x$. In addition, we are actively investigating some alternate candidate high efficiency sorbent/gas combinations which have even greater gas loading.

Table 1 summarizes the analytically predicted refrigerator coefficient of performance (COP) of a flight cooler which incorporates the features described above, including all compressor power and TEC power. The refrigerator COP is simply the ratio of the cooling power, Q_c, to the input power, Q_{in}:

$$COP = Q_c/Q_{in}. \tag{1}$$

The efficiency, expressed as fraction of Carnot efficiency, is given by

$$COP/COP_{Carnot} = [Q_c/Q_{in}]/[T_c/(T_o-T_c)]. \tag{2}$$

Substituting a heat rejection temperature of T_o = 275 K, a cooling temperature of T_c = 80 K, an input power of Q_{in} = 113 W, and a cooling load of Q_c = 1 W, results in COP = 1 W/113 W = 0.009, and an efficiency of COP/COP_{Carnot} = 0.022. For comparison, this efficiency is about 32% of that for the Oxford Stirling Cooler being developed by British Aerospace Corp. (COP/COP_{Carnot} ~ 0.07) [10].

Note that a sorption cooler can never achieve the Carnot efficiency given in the denominator on the right hand side of Eq. (2). Because it is actually a refrigerator driven by a heat engine, the maximum COP achievable by a sorption cooler is a product of a heat engine Carnot efficiency and a refrigerator Carnot COP. Although the efficiency is not as high as for some mechanical coolers, the power requirement is quite low for many low cooling load applications. The reasonably low power requirement, combined with high reliability, long-life, and absence of vibration and electromagnetic interference, makes sorption coolers ideal for many applications.

Table 1. Flight cooler performance predictions

Heat Rejection Temperature (K)	1/COP (Watt Heating/Watt Cooling)
275	113
250	107
225	98

6. Conclusions

Development of the 80 K laboratory breadboard cooler and the successful preliminary testing described here have been a major step in demonstrating the feasibility of using sorption coolers for long duration, vibration-free, spaceborne cryogenic cooling applications. A high-efficiency flight cooler, building on the experience of the design presented here, is currently being developed.

This research described in this paper was carried out by the Jet Propulsion Laboratory, California Institute of Technology, under contract with the National Aeronautics and Space Administration. The authors would like to thank Bill Boulter, Dave LaCasse, Tony Agajanian, Peter Bruneau, Lloyd Swanson, and Glenn Bummer for their contributions to the cooler fabrication.

7. References

[1] Bard, S., "Development of an 80-120 K Charcoal-Nitrogen Adsorption Cryocooler," Proc. Fourth Biennial Intern. Cryocoolers Conf., pp. 43-57, (1986).

[2] Bard, S., "Improving Adsorption Cryocoolers by Reducing Void Volume and Multistage Compression," Cryogenics, 22, 450, (August/September 1986).

[3] Jones, J. A., and Blue, G. D., "Oxygen Chemisorption Compressor Study for Cryogenic J-T Refrigeration," AIAA 22nd Thermophysics Conference, Honolulu, HA, (June 8, 1987).

[4] Bard, S., Jones, J. A., and Schember, H. R., "A Two-Stage 80 K/140 K Sorption Cryocooler," 12th International Cryogenic Engineering Conference, Southampton, England, (June 12-15, 1988).

[5] Schember, H. R., "Development of an Adsorption Compressor for Use in Cryogenic Refrigeration," to be presented at the AIAA 27th Aerospace Sci. Meeting, Reno, NV, (Jan. 8-12, 1989).

[6] Barron, R., "Cryogenic Systems," McGraw-Hill, (1966).

[7] Jones, J. A. and Golben, P. M., "Design, Life Testing and Future Designs of Cryogenic Hydride Refrigeration Systems," Cryogenics, 25, (1985).

[8] Mullhaupt, J. T., "Process and Composition for Separation of Oxygen from Air Using Pr-Ce Oxides as the Carrier," U.S. Patent #3,980,763, (Sept. 1, 1976).

[9] Bard, S., Wen, L., and Hughes, R. W., "Performance Analysis of an 80 K/140 K Sorption Cryocooler," in progress, to be submitted to AIAA J. of Thermophys. and Heat Transfer, (1988).

[10] "Mechanical Cryogenic Coolers for Space Applications," British Aerospace Technical Publication, Space and Communications Division, (1988).

A NON-CLOGGING, TEMPERATURE-SENSITIVE, CLOSED-CYCLE LINDE-HAMPSON CRYOCOOLER*

K. Hedegard, G. Walker, S. Zylstra
General Pneumatics Corporation
Western Research Center
7662 E. Gray Road, Suite 107
Scottsdale, AZ 85260

**Presented at the International Cryocooler Conference
August, 1988, Monterey, California**

ABSTRACT

A novel design for a non-clogging, quick cooldown Joule-Thomson (J-T) nozzle was described in a previous paper "Temperature Sensitive Variable Area Flow Regulator for Joule-Thomson Nozzles" presented at the fourth International Cryocooler Conference in 1986. The design utilized differential thermal expansion and a tapered annular orifice with labyrinth flow spoilers to achieve temperature-dependent flow and avoid the problem of orifice blockage by flow contaminants. Prototype miniature cryostats were fabricated and tested with performance exceeding expectations.

Work has now been completed to extend the new nozzle design to higher flow capacities and incorporate it in a prototype cryocooler for delivery to NASA. The system liquefies nitrogen in a closed Linde-Hampson cycle to provide continuous useful refrigeration. The prototype cryocooler combines the new cryostat design with a specially-developed four-stage reciprocating compressor and a refrigeration-load dependent closed loop speed control. The compressor utilizes extensive in-house research and testing on materials and configurations for piston seals and valves optimized for minimum leakage, dead volume, flow restriction, and wear.

INTRODUCTION

Joule-Thomson nozzles (cryostats) typically require high purity gas and thorough filtration to prevent blockage of the expansion orifice with condensed gaseous contaminants and solid particulates. A temperature/load sensitive J-T nozzle has been developed which tolerates high levels of both gaseous and particulate contamination in the supply flow.

* Supported by the National Aeronautics and Space Administration Small Business Innovative Research (SBIR) Phase II Program Contract No. NAS10-11322

This paper details the design and performance of the non-clogging J-T expansion nozzle as it was developed for integration into a closed Linde-Hampson cycle cryocooler for NASA. The cryocooler's oilless high pressure gas compressor and system feedback control loop are also discussed.

CRYOSTAT DESIGN

A cross-section of the J-T cryostat is shown in Figure 1. The temperature/load responsive demand flow capability of the cryostat results from differential contraction of the structural components. During cooldown and steady state operation, the thermally active sheath contracts and expands to a greater extent than the thermally stable core. The core and sheath are essentially fixed at the end opposite the nozzle, which forces all temperature induced component movement to take place at the expansion orifice.

FLOW REGULATION

The cryostat's ability to regulate flow in response to heat load is due primarily to the heat-exchanger-induced temperature gradient running the length of the structural components. The finned tube of the Giauque-Hampson recuperative heat exchanger is wound around the periphery of the thermally active sheath. The recuperative heat exchange process creates an ambient to cryogenic temperature gradient along the length of the sheath and core. The effectiveness of the heat exchange process defines the temperatures along the gradient. Heat exchange effectiveness may be considered in terms of the surface areas available for heat transfer and the velocities of the opposing gas flows. With fixed surface areas, the effectiveness will vary in relationship to the gas velocities.

The boil-off rate of the puddled liquid cryogen corresponds to the applied heat load. When an increase in the applied heat load is experienced, a corresponding increase in the boil-off flow rate is produced. The increased flow velocity decreases the heat exchange effectiveness, which results in a shift in the temperature gradient experienced by the structural components. This shift acts to increase the mean temperature of the structural components. The temperature increase causes the thermally active sheath to expand more than the thermally stable core. This results in an increased flow area, a higher mass flow rate through the expansion orifice and an increase in cooling capacity. This process is reversed to adjust to a decrease in applied heat load.

ANNULAR EXPANSION ORIFICE

The converging annular expansion orifice is formed by the position of the tapered tip within the tapered seat. The resulting flow annulus has a relatively large circumference for a small flow area so that the susceptibility to clogging is much less than for a small circular hole.

Labyrinth flow spoiler grooves in the tapered tip provide turbulence voids which help break up and clear condensed contaminants, while generating turbulence walls which enhance the flow friction of the annulus.

The tapered nozzle geometry determines the variation in mass flow rate resulting from contraction or expansion of the structural components. The nozzle included angle is the principle factor in determining the change in flow area and resultant mass flow rate. A large included angle will produce a greater change in flow area for a given linear movement than will a small included angle.

Flow studies were conducted with nozzles of different angles, aspect ratios (length to diameter), and labyrinth spoiler configurations and spacing. The studies allowed characterization of the flow parameters and J-T effectiveness based on the above parameters. This resulted in a nozzle design with optimum performance for the intended flow regime.

MICROMETER FLOW ADJUSTMENT

The cryostat flow rate (hence cooling capacity) can be manually adjusted prior to, or during, operation with the micrometer flow adjustment. The mechanism permits presetting of the cooldown flow rate and fine or gross adjustment of the steady state flow rate to achieve specific cooling capacities. The adjustment mechanism is also used in fine tuning the closed loop cryocooler for maximum performance.

The flow adjustment design has been modified to increase its accuracy, repeatability and position retention. The modifications included the addition of adjustable linear thrust bearings, hardened bearing surfaces and an adjustment to eliminate screw thread backlash. The micrometer adjustment has a range of .25 cm and a flow adjustment accuracy to within .3 l/min. during operation of the cryostat.

PERFORMANCE

The J-T cryostat was subjected to a series of performance tests to determine its maximum cooling capacity, expansion space backpressure, responsiveness to heat load variations, and cooldown characteristics with different applied heat loads. The performance testing was conducted with the cryostat inserted in a test dewar with a thin wall (.25 mm) 321 stainless steel coldwell insulated by a vacuum of 3×10^{-6} Torr.

The metal coldwell was equipped with a cable-type heating element coiled and soldered to the outer surface at the base of the coldwell in the region where the liquid nitrogen puddled. A platinum RTD temperature sensor was mechanically fastened to the bottom of the coldwell, with a thermal paste used to increase heat transfer. The heater and temperature sensor were both calibrated by immersion in liquid nitrogen prior to testing. All tests were conducted with the cryostat calibrated to provide a nitrogen flow rate of 65 l/min. at 138 bar. The cryostat cold end components have a thermal mass of approximately 92 grams which requires removal of 8000 Joules during cooldown. The cooling capacities reported include the parasitic heat load of the test dewar. A turbine flow meter calibrated at standard temperature and pressure was used to measure the cryostat exhaust flow rate. However, the calibration curve invalidates flow rates below 5 l/min. and above 140 l/min.

HEAT LOAD RESPONSIVENESS

This test series characterized the cryostat's ability to adjust the flow rate in response the variations in the applied heat load. As noted on the graph in Figure 2, the cryostat achieved cooldown to 80 K in approximately two minutes with zero applied heat load. The cryostat reduced and maintained the flow rate below 5 l/min. in approximately 25 minutes. The flow rate did not increase until the applied heat load reached approximately 1 watt. The flow rate then increased in proportion to the applied heat load until the flow regulating capability was overpowered at approximately 30 watts.

The liquified nitrogen temperature remained at 80 K for flows of up to approximately 40 l/min. At this point the increasing back pressure (vapor pressure) acted to increase the nitrogen boiling point above 80 K. The maximum stable temperature of 84 K was noted at the 30 watt heat load setting. Testing was conducted with decreasing heat loads with similar results.

COOLDOWN CHARACTERIZATION

This test series characterized the temperature and flow parameters of the cryostat when subjected to cooldown sequences with differing applied heat loads. The graphs in Figures 3 to 8 plot the results of these tests at heat load settings of zero, 5 watts, 10 watts, 15 watts, 20 watts and 25 watts. The cooldown characteristics at given heat loads are summarized in the following table:

	HEAT LOAD-WATTS					
	0	5	10	15	20	25
MIN. TEMP. ACHIEVED (K):	80	80	80	81	81	83
COOLDOWN TIMESPAN (min):	2	2	3	3	4	7
TIME TO STABILIZE (min):	13	20	6	10	12	16
STABILE FLOW RATE (l/m):	0	15	30	40	45	67
TEMP. FLUCTUATION (K):	<1	<1	1	1	<1.2	<1.4

MAXIMUM COOLING CAPACITY

With an inlet pressure of 138 bar, the cryostat could be manually adjusted to provide a maximum cooling capacity of 37 watts at 85 K with a flow rate of 100 l/min.

EXPANSION SPACE PRESSURE

Testing was conducted to determine the expansion space pressure (cryogen vapor pressure) based on the flow rate. The expansion space pressure is a function of the return flow pressure drop through the Giauque-Hampson heat exchanger. At flow rates up to approximately 40 l/min., the expansion space pressure remained at 1.41 bar. The expansion space pressure then increased linearly to a maximum of 1.96 bar at 100 l/min. flow.

LINDE-HAMPSON CRYOCOOLER SYSTEM DESCRIPTION

The non-clogging cryostat has been integrated into a closed Linde-Hampson cycle cryocooler to provide useful refrigeration on a continuous basis. The cryocooler is currently undergoing performance and environmental testing prior to delivery to NASA.

The system includes an oilless high pressure four-stage gas compressor to feed the cryostat. The compressor utilizes specially developed one-way piston seals constructed of a self lubricating material. The pressure actuated valves were developed specifically to provide minimal leakage and dead volume. The compressor is designed to supply the cryostat

with nitrogen compressed to 172 bar at flow rates up to 100 l/min. The compressor is capable of compressing the gas to 242 bar at flow rates up to 200 l/min. The system is controlled by a feedback control loop which automatically adjusts the compressor mass flow rate to balance the applied heat load.

CONCLUSION

The non-clogging, temperature/load sensitive J-T cryostat developed during this program exhibited the ability to accurately adjust the flow rate in response to the applied heat load. It provided rapid cooldown with varying heat loads and is capable of being adjusted to a variety of flow regimes and cooling capacities. The J-T cryostat has been integrated into a closed Linde-Hampson cycle cryocooler and in currently undergoing system level performance testing.

REFERENCES

[1] Wade,L., an investigation into the mechanics of Joule-Thomson valve plug formation, in Advances in Cryogenic Engineering, Volume 33, pp. 699-706 (Plenum Press, New York, 1987)

[2] Lester, J.M., Benedict, B., Joule-Thomson valves for long term service in space cryocoolers, Proceedings of the Third Cryocooler Conference, Boulder, Colorado, Sept. 17-18, 1984.

[3] Walker, G., Joule-Thomson Apparatus with Temperature Sensitive Annular Expansion Passageway, U.S. Patent #4,631,928, General Pneumatics Corporation, Dec. 30, 1986, 5 pp.

[4] Walker, G., Refrigerant Expansion Device with Means for Capturing Condensed Contaminants to Prevent Blockage, U.S. Patent #4,738,122, General Pneumatics Corporation, Apr. 19, 1988, 5 pp.

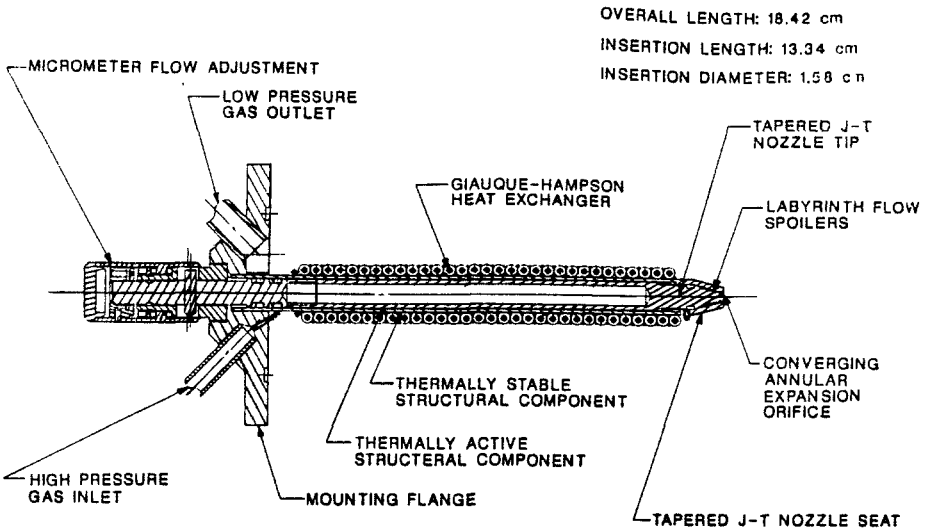

FIGURE 1: CRYOSTAT CROSS-SECTION

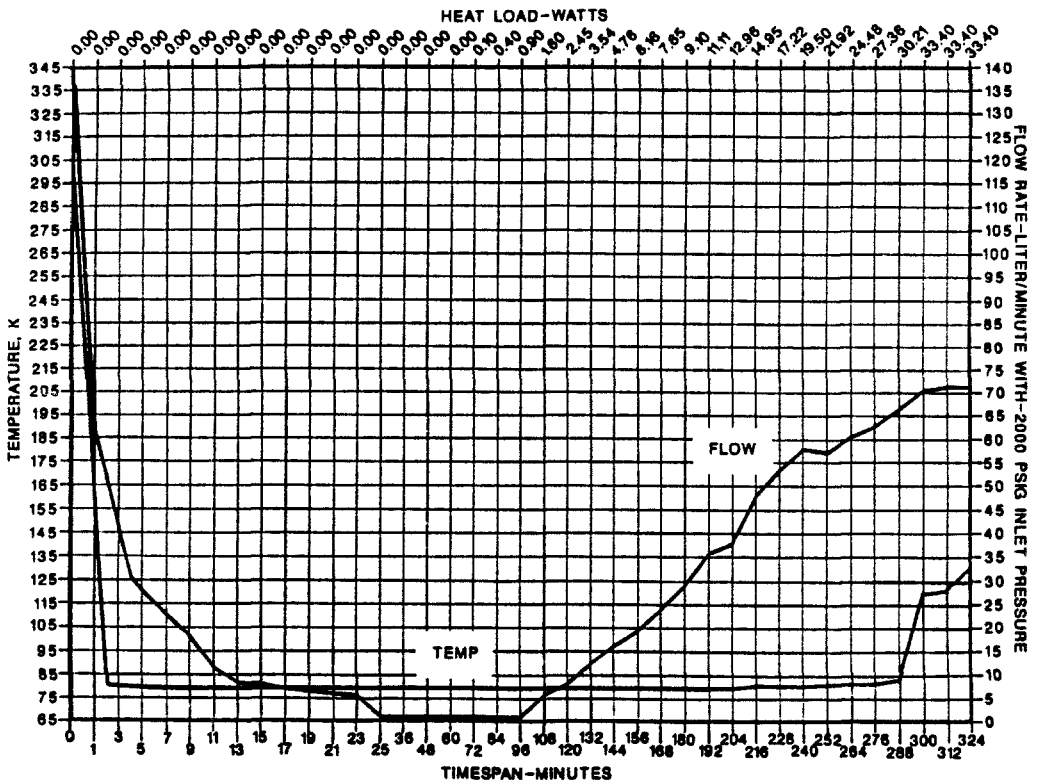

FIGURE 2: FLOW RESPONSITIVITY TO HEAT LOAD DEMAND

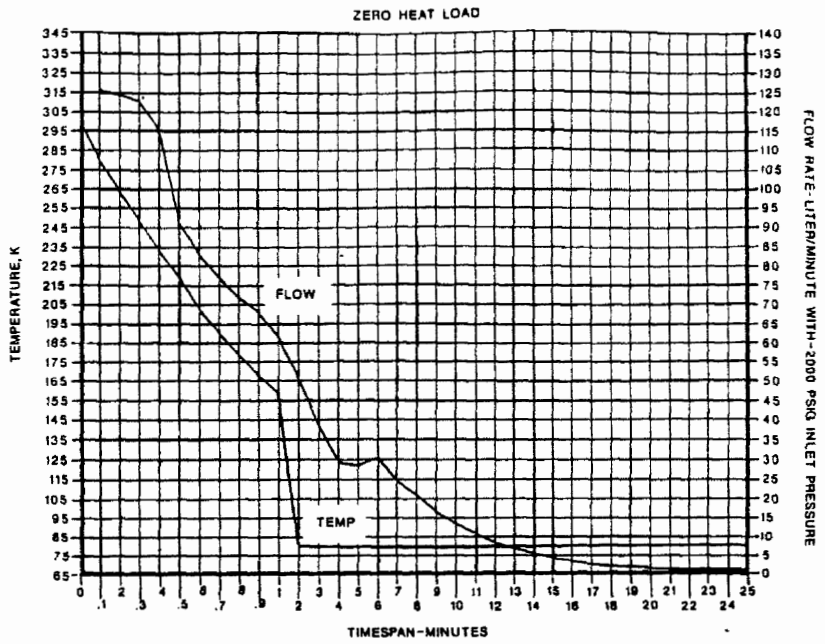

FIGURE 3: ZERO HEAT LOAD COOLDOWN CHARACTERISTICS

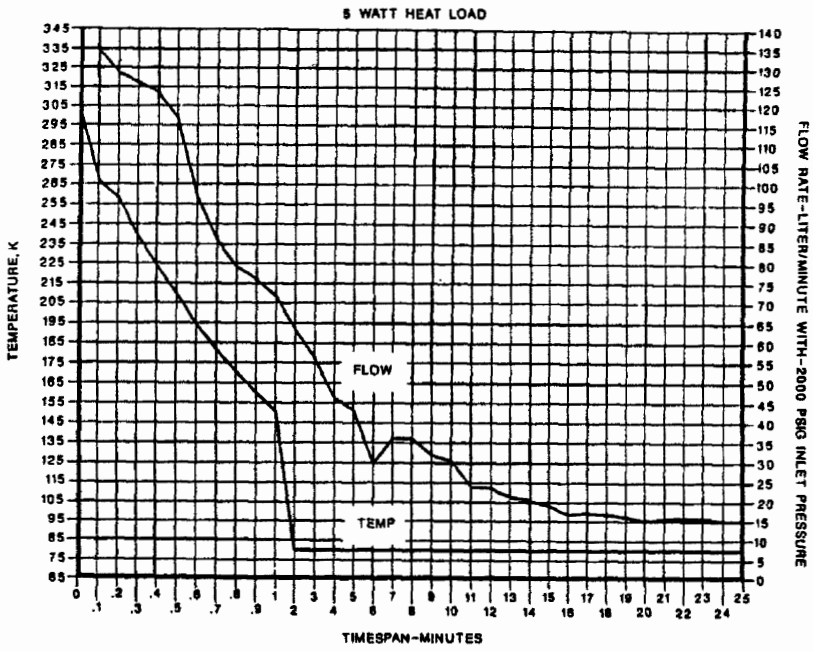

FIGURE 4: 5 WATT HEAT LOAD COOLDOWN CHARACTERISTICS

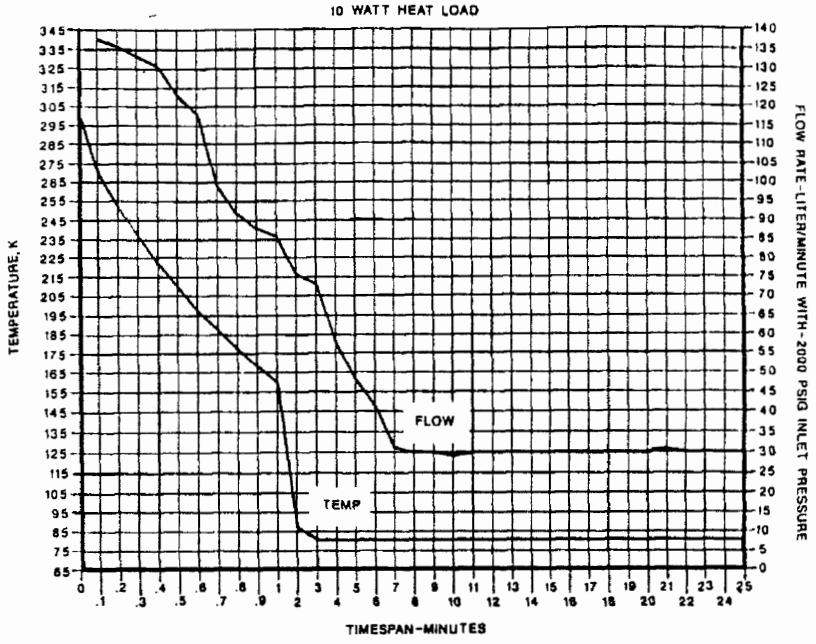

FIGURE 5: 10 WATT HEAT LOAD COOLDOWN CHARACTERISTICS

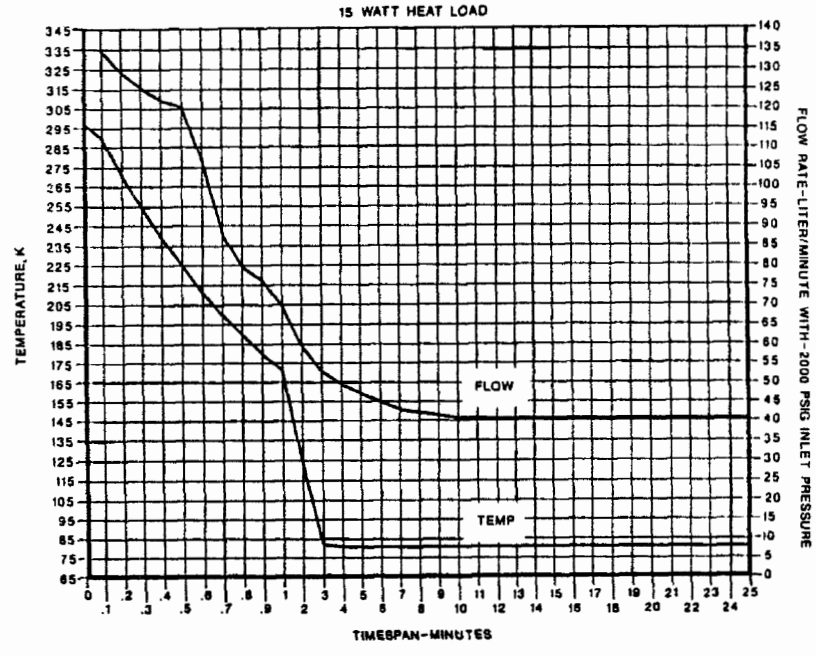

FIGURE 6: 15 WATT HEAT LOAD COOLDOWN CHARACTERISTICS

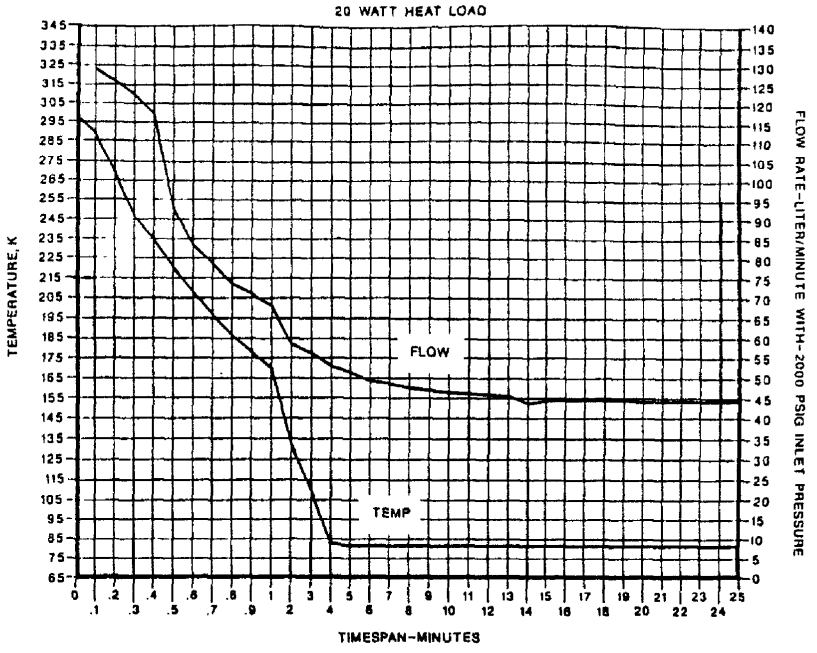

FIGURE 7: 20 WATT HEAT LOAD COOLDOWN CHARACTERISTICS

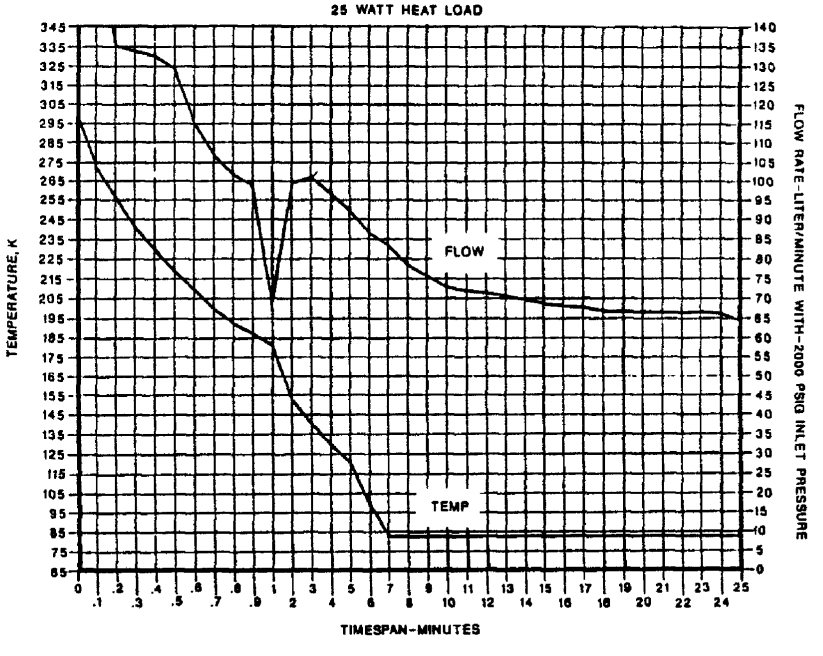

FIGURE 8: 25 WATT HEAT LOAD COOLDOWN CHARACTERISTICS

DEVELOPMENT OF A HYBRID GIFFORD-MCMAHON JOULE-THOMPSON BASED NEUROMAGNETOMETER®: CRYOSQUID™*

D. S. Buchanan and D. N. Paulson
Biomagnetic Technologies inc.
San Diego, CA 92121

G. A. Klemic and S. J. Williamson
Neuromagnetism Laboratory
Department of Physics
New York University
New York, NY 10003

Abstract

A closed-cycle refrigerated, single-channel Neuromagnetometer has been developed which operates at noise levels equivalent to those of dewar based systems. The device uses a commercial Gifford-McMahon cryocooler to which a non-magnetic Joule-Thompson cooler and support stage have been added. The magnetic sensor is a second-order gradiometer connected to a DC SQUID. Residual vibration induced magnetic noise, which at discrete frequencies is approximately 30-50 db above the white noise level, is removed using a PC based digital comb filter resulting in a system noise of approximately 20 fT/$\sqrt{Hz}$. The system will operate at any orientation. Two of these systems, including gantries, have been built and installed at New York University in a magnetically shielded room.

1. Purpose

Current Neuromagnetometers[1] use dewars to maintain the 4 K environment necessary for operating SQUIDS and superconducting pickup coils. The dewar maintains a reservoir of liquid helium (LHe) in which the superconducting elements of the system are immersed. A typical system has a reservoir of 10 liters of LHe which provides for approximately three days of operation between transfers of LHe yielding a consumption of 2-3 liters of LHe per day. There are several problems associated with having large reservoirs of LHe. First, in typical installations in the United States no He recovery system is used so that this non-renewable resource is lost. Second, because of the large reservoir of liquid, typical dewars cannot be tilted beyond 45 degrees, thus restricting the area of the scalp that can be monitored magnetically. In order to measure over opposite hemispheres of the brain simultaneously, special dewars having tipped coil arrays have been built[2]. These dewars in general are not suitable for more general types of measurements. Third, the use of LHe presents a safety problem. In the event of an accidental loss of vacuum in the insulating regions of the dewar, flash boil-off of 10 litres of LHe could explode the dewar and produce about 7700 litres of gas which could displace the oxygen in an enclosed room.

The purpose of this project was to provide a closed-cycle refrigerated, single-channel Neuromagnetometer called CryoSQUID. It was to be reasonably small (11 kg), operate at current LHe based noise levels (20 fT/$\sqrt{Hz}$), run continuously for more than one month between routine maintenance and more

than one year between major maintenance, and operate at orientations from 0 to 135 degrees from vertical allowing measurements to be taken over opposite hemispheres of the brain simultaneously. Where possible, commercially available technology was to be used. Existing 4.5 K platforms were unsuitable because they were either too magnetic, too vibrationally noisy for use with SQUID-based systems, or simply too large.

2. Construction

2.1. Thermal

2.1.1. Gifford-McMahon

The starting point for the construction of the CryoSQUID is a commercial Gifford-McMahon (GM) cryocooler. A multi-stage all Joule-Thompson (JT) cooler was ruled out for a number of reasons, among which were: development and construction of the compressors necessary to handle the different stages was deemed unfeasible in the time frame allowed, the safety hazard associated with the handling of high pressure hydrogen in a hospital environment, and JT devices are more prone to interruption of operation arising from plugging of the JT impedance. The GM unit we chose[3] has two stages and is capable of 2 watts of cooling at 15 K. In constructing CryoSQUID the performance of the unit as measured by cooling power is degraded considerably, by 30-50%[4], by separation of the valve motor (VM) from the expander by 4 meters. This distance eliminates the magnetic and acoustic noise due to the (VM) by placing it outside of the magnetically shielded room (MSR) in which the units are installed. Under the final operating conditions the first stage of the GM unit operates at approximately 60 K while the bottom stage operates at 10-12 K. A side benefit of this separation is the reduction in the vibrational noise caused by the gas surges in the expander. This is because of the increased time constant for flow into the expander caused by the long lines from the VM to the expander.

2.1.2. Joule-Thompson loop

A non-magnetic, low capacity, helium JT loop is added to the GM unit to provide the 4.5 K stage to which the electronics (SQUID and pickup coil) are attached. The JT loop consists of three helically wound counterflow heat exchangers connected through two isotherms, one at 60 K and the other at 12 K. The final exchanger terminates through the JT impedance into a 30 cm^3 collection volume. Each of the isotherms is packed with activated charcoal to act as a cold trap for the supply gas. Gas is supplied to the JT at 2.31 MPa from the same compressor that supplies the GM cooler. The flow rate is 0.025-0.033 standard litres per second (slps) with a return pressure of 0.10-0.11 MPa. Two units are run in parallel from the same compressor. A supplementary compressor is used to boost the return gas to the GM return pressure of 0.59-0.62 MPa. Commercial helium compressors are used[5] with a total power consumption of 4.8 kW. The 30 cm^3 collection volume serves two purposes: the first is to provide a thermal mass to damp out any temperature fluctuations and the second is to provide

a thermal reservoir for an intermittent operating mode which is described below. There is another protection against thermal noise built into the system in the form of a weak thermal coupling between the electronics and the 4.5 K platform. The time constant for this coupling is on the order of 1-2 minutes.

The counterflow heat exchangers are constructed by inserting multiple small tubes, which carry the supply gas, inside a single larger tube which carries the return gas. Separation manifolds are provided at each end of each exchanger to break out the supply and return flows for them to be brought into thermal equilibrium with the GM cooler. The calculated efficiencies for each of these heat exchangers exceeds 95%. Since at no time during the development of CryoSQUID were the efficiencies of the heat exchangers a problem, the efficiencies were never measured. The calculated cooling power of the system is 56 mW given a flow rate of 0.029 slps from 2.31 to 0.11 MPa. The JT impedance is a fixed impedance consisting of a pressed sintered metal plug.

The longest sustained operation of the system has been 4 weeks after which it was shut down to ship to New York University (NYU). Since arriving at NYU the longest the system has run is 3 weeks at which time the GM failed due to leaks in the room temperature plumbing. No evidence of plugging of the impedance has been observed even under conditions where the GM displacer has failed.

2.2. Magnetic

The SQUID sensor consists of a standard Biomagnetic Technologies inc. (BTi) DC SQUID which is attached to a superconducting pick-up coil. This coil is a second-order gradiometer with a 2 cm in diameter and a 5 cm baseline This combination, in the absence of external noise sources such as dewars etc., has an intrinsic equivalent noise level of less than 10 $fT/\sqrt{Hz}$. When combined in the CryoSQUID a noise level of 20-25 $fT/\sqrt{Hz}$ is achieved.

2.3. Mechanical/Shielding

A major problem associated with using any GM type cooler is the amount of vibration present in the system. In magnetic measurements systems such as these, the signals of interest are typically 6-8 orders of magnitude below the ambient local fields. In addition the local field is spatially non-uniform. Vibration of the pickup coil therefore leads to spurious signals. Measurements done on a several cryocooler systems[6] which use a fluidic drive for the displacer exhibited displacements of the cold finger tip along its axis of 0.03 to 0.08 mm depending on the exact implementation of the GM scheme. These displacement measurements were done both when the GM was at room temperature and when is was cold, using an accelerometer[7]. Measurements made on the final system indicated that a displacement of 0.03 mm either inside or outside of a MSR would lead to induced signals about 5000 times the system noise level. Systems employing a motor driven displacer exhibited too much side torque from the motor. Any neuromagnetic sensor attached to such a mount would have an unacceptable level of vibrational noise introduced by the cooler. Mechanically mounting the pickup coil to a separate, large, stable mass with only flexible thermal coupling to the cold finger would

eliminate the direct vibration of the coil. This approach was rejected because the system under development had to be relatively small and highly mobile.

An alternate mounting scheme was suggested by the observation that while the cold finger of the system was moving on the order of 0.03 mm, the warm end of the system, i.e. the top flange, was moving less than 0.003 mm. Calculations showed that this was consistent with the interpretation that most of the motion of the cold finger was due to the stretching of the stainless steel pressure vessel under the oscillating pressure. If the magnetic sensor could be mounted to the top flange while attaching it thermally to the cold finger the noise due to vibration might be manageable.

A prototype constructed to test this showed that the vibrational noise was not eliminated, but it was reduced to a manageable level. It also revealed that the vibrational noise was very stable, and was represented by noise peaks at the fundamental frequency of 2.4 Hz and its harmonics. A real time digital comb filter, based on a personal computer, was assembled which was able to reduce this noise to the white noise level of the system with minimal distortion to the signal. This filter will be described more fully below.

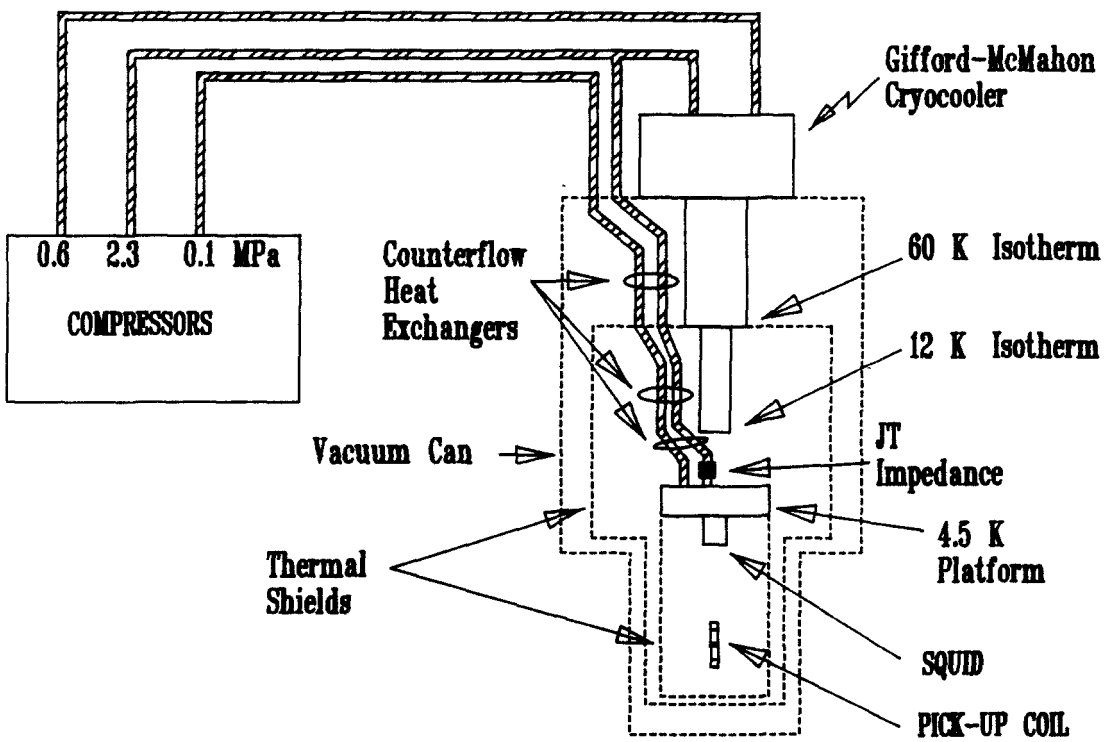

Fig. 1. System Schematic. The final system weight, excluding compressors, was 12.4 Kg. Gas handling system and split VM not shown.

Once the JT loop is mounted and the electronics attached, suitable thermal shielding must be provided. Two thermal shields are used. A '60 K' shield is attached to the first stage of the GM unit (Fig. 1) and a second shield is attached to the 4.5 K stage. No intermediate shield is necessary. Both shields are constructed from fiber reenforced plastics (FRP) which are isothermed along their length. The bottom of the '60 K' shield runs at about

90-100 K while the bottom of the '4 K' shield may run as hot as 10 K. This later temperature was never measured but was derived from heat flow calculations assuming a heat input to the shield of 20 mW. Superinsulation is used around both shields.

The entire assembly is placed in a vacuum-tight can also made from FRP which attaches to a nylon annulus. This annulus serves as a place for mechanical and electrical feed-through and mates the FRP can to the GM cooler.

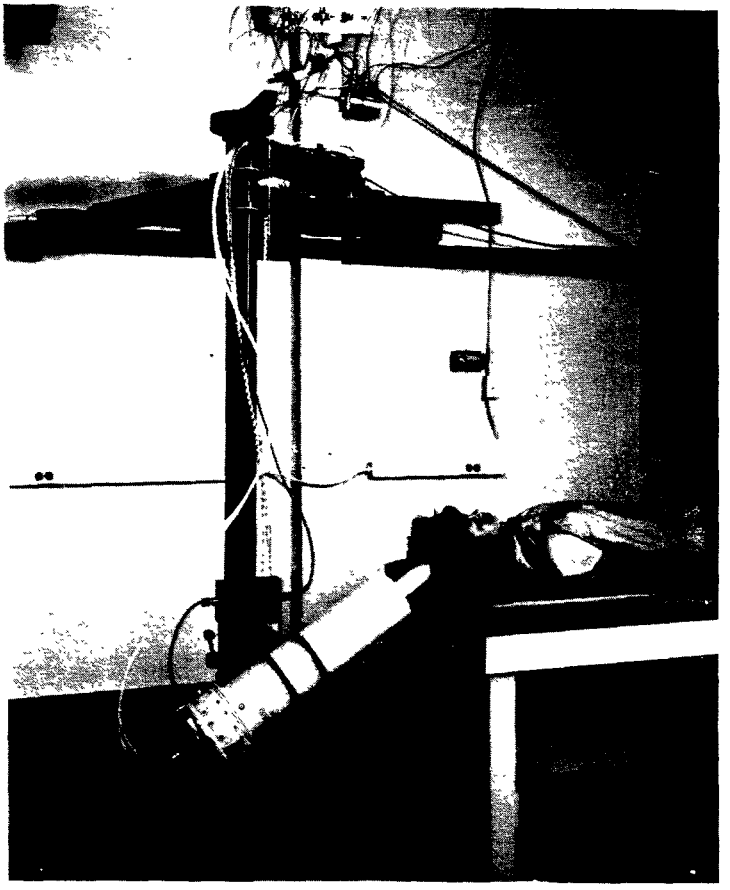

Fig. 2. CryoSQUID plus gantry as assembled at BTi. Note the two arm supports to the wall.

2.4. Gantry

In addition to the device itself a gantry was designed to support and manipulate two CryoSQUIDs inside an MSR, in a way that would permit its use in conjunction with a standard 5 channel Neuromagnetometer. The resulting gantry had to be non magnetic and provide a very rigid platform for the units in order to minimize vibrational noise. The resulting tripod like support system is shown in Fig. 2. By having two arms attached to the wall with pneumatic brakes at each joint, the required stability was achieved. The brakes are designed to be operated by a single switch located on the gantry

for ease of operation. The gantries were constructed by Hercules Manufacturing of Escondido, CA.

3. Performance

3.1.Thermal

3.1.1. General

A typical cool-down from room temperature to a stable operating temperature for the 4.5 K platform takes 20 hours on the installed system. This may be compared with a 12 Hr cool-down when the VM in attached directly to the expander.

Once cool the system provides a stable thermal platform. The measured heat leaks due to external sources (i.e. not the JT flow) are 18 mW for the 4.5 K stage and 1.9 W for the 60 K stage.

The 4.5 K stage heat leak is determined by measuring the boil-off rate of the reservoir with no input flow. The heat leak into the 60 K stage is determined by measuring the temperature difference across the copper thermal lags between the shield and the first stage of the GM unit. That is, it represents the heat being intercepted from room temperature by the shield. The calculated heat leak to the 4.5 K stage from conduction and radiation is 11.6 mW. The calculated heat leak to the 60 K shield from radiation, and conduction down the support structure is 0.39 W. While there is reasonable agreement for the 4.5 K stage the 60 K stage shows a large discrepancy.

3.1.2. Continuous mode

The system can be run in two fundamentally different modes, a continuous mode, which will be described here, and an intermittent mode described below. In the continuous mode all parts of the system, VMs, compressors etc., run continually. There are several problems associated with this mode of operation. First, the movement of the displacer and gas in the expander leads to vibrational noise in the sensor. As mentioned previously this noise can be removed with a filter. Second, and more serious for neuromagnetic work, is the audible noise from the same sources. This has proved impossible to eliminate. It should be pointed out that an all JT device would eliminate this problem entirely. Third, there is a thermal oscillation present when the JT is running at the full flow rate, Fig. 3. At the end of the cool-down period the system is stable for several hours and then starts to oscillate at a rate of once every 10-40 minutes. The rate seems to depend on the heat leak to the 4.5 K stage. The temperature rises to 5-6 K while the JT return flow increases by a factor of 2-3. It was found that the JT supply flow simultaneously increases by a factor of 2-3 also. We were never able to positively identify the cause of the oscillation but we believe that when the helium reservoir fills, the boil-off rate increases slightly lowering the temperature of the gas going to the JT impedance which causes the flow rate through the impedance to go up. This forces some liquid into the heat exchanger where it boils off and drops the liquid level in the reservoir. Then the boil-off rate drops

allowing the temperature of the impedance to increase and the flow through the impedance to decrease. After enough helium re-condenses in the reservoir, the cycle repeats. Fluctuations of order 0.02 MPa in the supply pressure confirmed that some liquid was boiling off and re-condensing. This oscillation can be controlled by adjusting a needle valve in the supply line (V4 Fig.4) at room temperature to lower the flow of helium through the impedance to the point where there is no condensation in the reservoir.

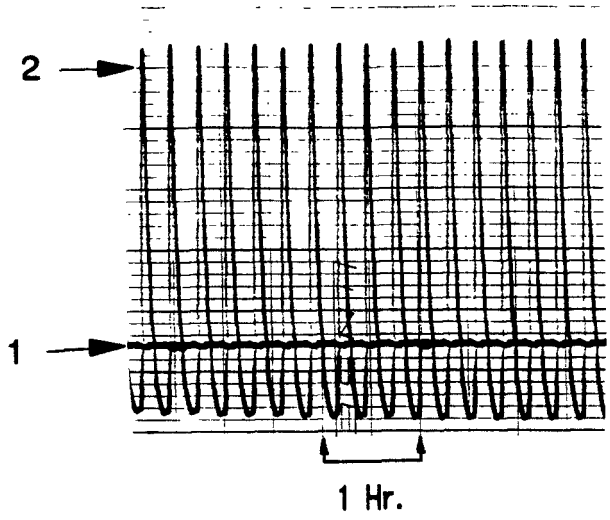

Fig. 3. 1) The temperature oscillations. The amplitude is approximately 1 K. 2) The return flow oscillations. The oscillations represent a factor of 2 change in the flow rate from minimum to maximum.

By looking at the SQUID output during these oscillations one can tell something about the thermal isolation of the SQUID from the cooling platform. When the thermometer showed about a swing of about 1 K during an oscillation the output from the SQUID showed a 0.012 φ_0 swing, where φ_0 in the flux quantum, h/2e. A typical value for the temperature coefficient of a SQUID is 0.1 φ_0/K implying there is a temperature swing at the SQUID of 12 mK or an isolation factor of about 100 at low frequencies.

In this mode the system can actually be operated at any orientation since there is no liquid in the reservoir. Operation has been successfully tried at 180 degrees (upside down).

3.1.3. Intermittent mode

In the intermittent mode the VM is shut down during the measurement time and the JT flow is reduced in order to reduce the heat load on the system. By shutting down the VM all vibration noise, magnetic and auditory, is eliminated from the system. During the time the VM is off cooling is provided by the evaporation of the helium condensed in the reservoir. Measurements showed that this one shot lifetime of the system is about 20 minutes, at the end of 20 minutes the system begins to warm up and, if the VM is restarted at that time, approximately 2 hours would be required to re-stabilize the system. On the other hand if the system is re-started prior

to the 20 minute limit, recovery is much shorter. Tests were run at BTi which showed that using a 33% duty cycle with the VM off up to 10 minutes (that would be 10 minutes with the VM off and 20 minutes with the VM on) that 4-5 hours of operation were possible before requiring a longer (2-3 hour) recovery time. The advantage of this mode is that it fits in with a number of evoked response experiments. In these, data are acquired for a short period (1-7 minutes) and then the measurement conditions are changed, for example the subject or the CryoSQUID is moved. Depending on the number of variables a typical measurement might last 2-3 hours. For a 2 hour measurement the system could be operated at a 50% duty cycle. By the end of that time the subject begins to fatigue even if the measurement is not yet finished. The result is that intermittent operation allows for a large variety of measurements to be performed.

It should be noted that many valves are required to implement these various modes of operation. The system was designed to be as easy to operate as possible so that a gas handling system using solenoid valves was designed to implement these modes. A schematic is shown in Fig. 4.

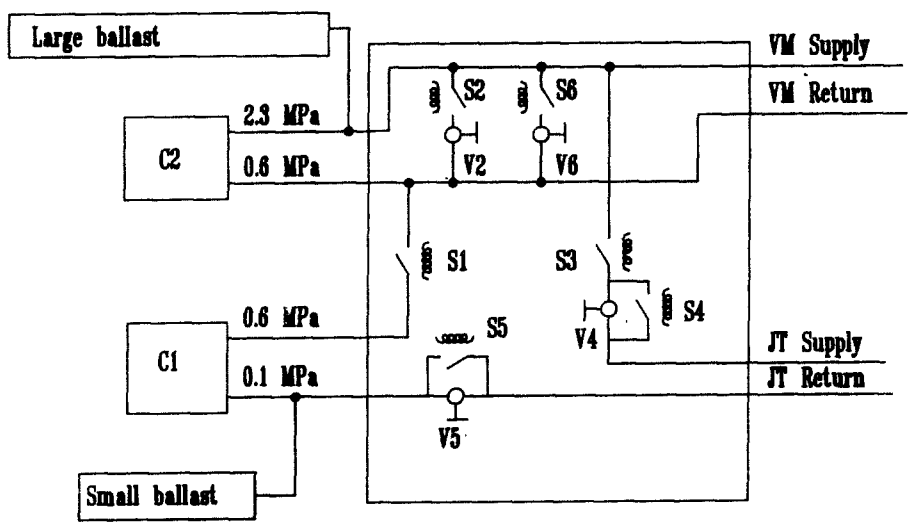

Fig. 4. Automated valve system for control of operation of CryoSQUID. S? are solenoid valves which are controlled by a logic circuit not shown. V? are needle valves for controlling gas flows.

For the intermittent operating mode a TTL level input was provided to allow computer control. The data acquisition software provided by BTi was altered to automatically turn the VM off and on immediately prior to and after data is acquired. With this method no one forgets to turn the system back on when data collection is finished.

3.2. Magnetic

3.2.1. Continuous mode

The noise of the system while operating in the continuous mode is shown in the top trace of Fig. 5. All noise measurements are done inside of the

MSR at New York University's Neuromagnetism Laboratory. Note the 2.4 Hz 'comb' of noise due to the operation of the GM system. Expanded measurements of these peaks show that they have bandwidths of less than 0.01 Hz. Because the VM is synchronized with the power line, the noise peaks are phase locked to the 60 Hz line frequency. It is these two facts that allow the digital filtering of the signal to remove essentially all of the induced noise.

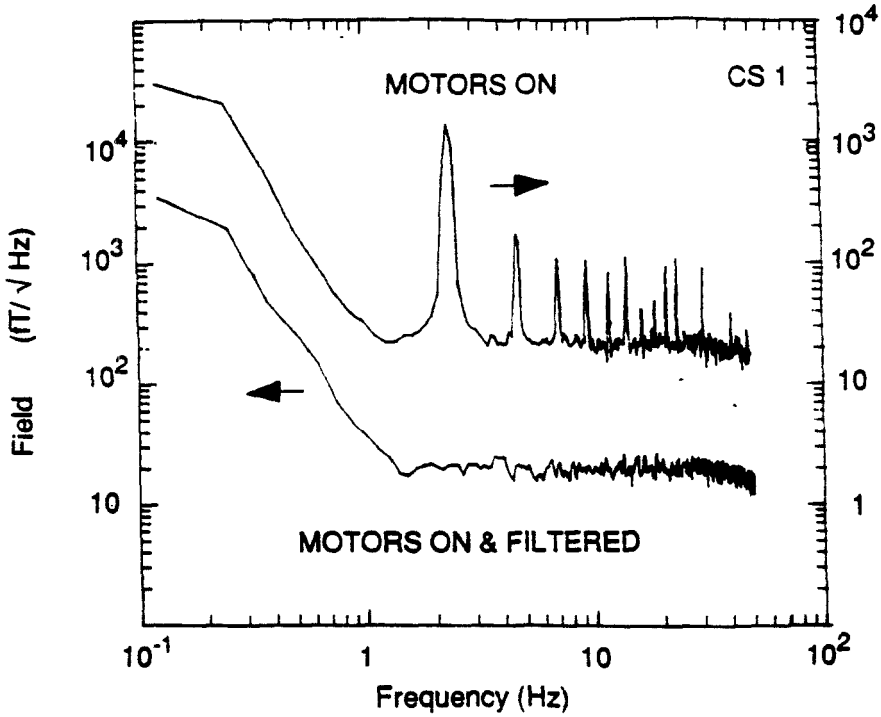

Fig. 5. 0.1-50 Hz spectra of one CryoSQUID operating in a MSR with the VM on, with and without the comb filter. Note the vertical scale offset between the two curves.

A 2.4 Hz analog comb filter would be prohibitive to build because of the size of the capacitors required. On the other hand a digital comb filter is feasible to implement at these frequencies. An IBM PC based filter was constructed. A Labmaster[8] 12 bit A/D board was used in external trigger mode to sample two channels of signal from the two CryoSQUIDS. It is triggered at 4320 Hz giving an sampling rate per channel of 2160 Hz. The external trigger is locked to the local line frequency by a phase locked loop. Each signal is low pass filtered at 750 Hz for anti-aliasing.

The image of the noise for each channel is built up in a buffer and is adaptively updated. This image is subtracted from the signal on a continuous basis and the result output on a pair of DACs. The image is updated by adding to it a fraction of the difference between the signal and the image. Because this process is repeated at exactly 1.2 Hz only signals at 1.2 Hz and its harmonics are accumulated in the buffer. By varying the fraction of the difference used to update the noise image, the effective adaptation time of the filter can be varied and the resulting phase shifts to the signal controlled. This filter can adapt to the noise from the Cryo-

SQUIDS with an effective adaptation time of 1 minute. This leads to no appreciable distortion to the signals of interest from 0.1-500 Hz. The lower trace of Fig. 5 shows the reduction of the vibrational noise in the spectrum when then system operates in the continuous mode with the filter engaged.

3.2.2. Intermittent mode

Fig. 6 shows the noise of the system when the VM is turned off. In this mode the system essentially behaves like a dewar based system while the VM is off except for the fact that it can be operated at angles up to 135 degrees from vertical.

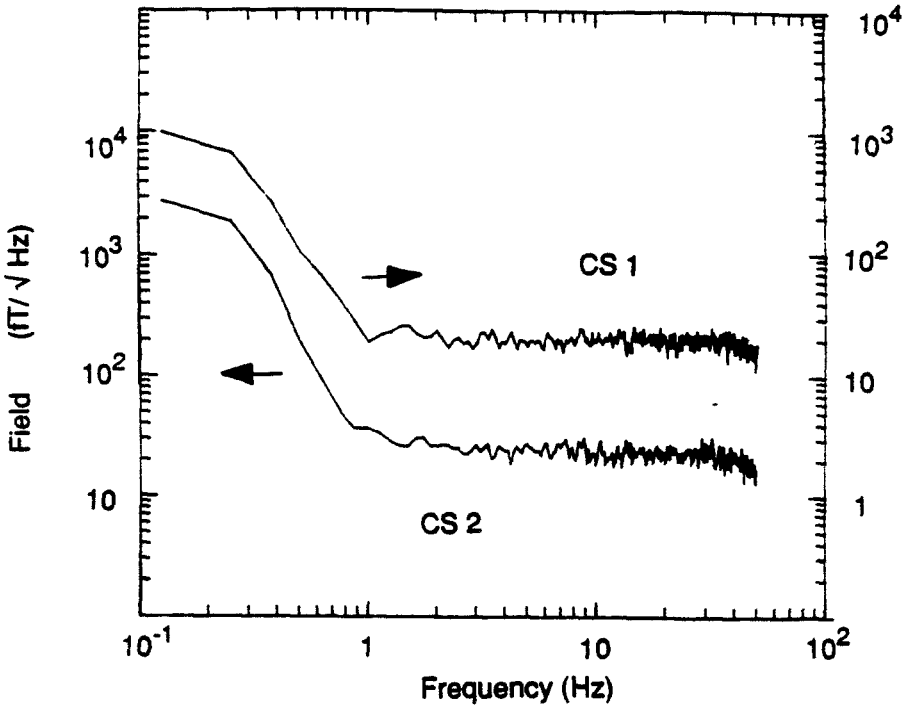

Fig. 6. 0.1-50 Hz spectra of both CryoSQUIDs in the MSR with the VM off. Note the vertical scale offset between the two curves.

4. Application: An Auditory Evoked response

One important application of this device is to monitor simultaneously neural activity at two different locations in the brain. As an illustration we show a result obtained when a subject listens to a briefly presented tone provided by airline style plastic earphones. With binaural presentation it is then possible to compare the activity in the auditory areas of cortex in the left and right hemispheres. The stimuli were tone bursts, each 40 ms in duration and having a tone frequency of 1 kHz. Each burst rose to full amplitude over a period of 5 ms and fell to zero during a comparable period. The intensity was 60 dB above the subject's threshold.

The auditory areas of human cortex are rather confined, and electrical

currents flowing within active neurons, which give rise to extracranial magnetic fields, can be approximated by a short line element of current (known as a 'current dipole'). The surface of the cortex lies perpendicular to the scalp, some 6 cm above the ear canal, thus neuronal currents flowing perpendicular to the cortical surface are themselves tangential to the overlying scalp. Such a source produces a field that loops around the axis of the dipole, producing one area of the scalp where the field emerges and another where it enters[9]. Each CryoSQUID was positioned over a different hemisphere, with the sensor directed to a point on the scalp just above and back of the ear, near one of the field extrema from the source in that hemisphere. Recordings obtained simultaneously within a bandwidth of 1 to 150 Hz showed simultaneous, well-defined peak fields occurring approximately 200 ms following onset of the tone, as illustrated in Fig. 7 for averages of 100 responses. The polarity of the fields indicate that the respective current dipoles are directed downward into the depth of each auditory cortex. These findings demonstrate that the temporal response of cortical activity in the right and left hemispheres can be monitored separately and simultaneously by using the pair of CryoSQUIDs.

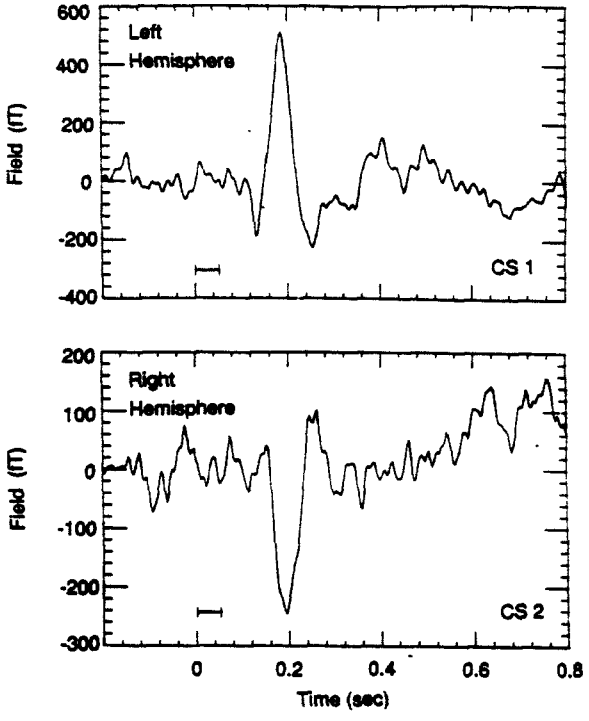

Fig 7. Auditory evoked fields measured simultaneously from both hemispheres of the brain using CryoSQUIDs.

5. Conclusion

We have successfully constructed what we believe is the first mechanically cooled, SQUID based magnetometer to operate at essentially the SQUID noise level. The system is light weight and mobile; being capable of opera-

tion at any angle from vertical. Two units have been successfully integrated with an existing 5 channel Neuromagnetometer inside an MSR and have been shown to be useful in the measurement of neuromagnetic fields.

We would like to thank Ray Sarwinski for all his help in the design of the heat exchangers and other useful discussions throughout this project. We would also like to thank Ralph Longsworth for his timely inputs and Brenda Butensky for assistance with the neuromagnetic measurements.

* Supported in part by Air Force Office of Scientific Research contracts AFOSR-84-0313, F49620-85-K-0004, and F49620-86-C-0131.

1. See for example: S. J. Williamson, M. Pelizzone, Y. Okada, L. Kaufman, D. B. Crum, J. R. Marsden, Magnetoencephalography with an array of SQUID sensors. IN: H. Collar, P. Berglund, M Krusius, adds, Proceedings of the Tenth International Cryogenic Engineering Conference. Butterworth, Buildford: 339-348 (1984).

2. J. Knuutila, S. Ahlfors, A. Ahonen, J. Hallstrom, M. Kajola, O. V. Lounasmaa, V. Vilkman, and C. Tesche, A Large-Area Low-Noise Seven-Channel DC SQUID Magnetometer for Brain Research. Helsinki Univ. of Tech. Low Temp. Laboratory Report TKK-F-A613 (1987).

3. Model 202, APD Cryogenics; 1833 Vultee St.; Allentown, PA 18103.

4. R. Longsworth, private communication.

5. Model #'s RL-02 and HC-4, APD Cryogenics; 1833 Vultee St.; Allentown, PA 18103.

6. Model #'s 201 and 202 APD Cryogenics; 1833 Vultee St.; Allentown, PA 18103. Model #GB220 Cryomech Inc.; 1630 Erie Blvd. East; Syracuse, NY 13210.

7. Model # 3125A made by Dytran; 21592 Marilla Ave.; Chatsworth CA 91311.

8. Labmaster A/D D/A for IBM PC #020009 by Scientific Solutions; 6225 Cochran Rd.; Solon, OH 44139.

9. S. J. Williamson and L. Kaufman, "Analysis of Neuromagnetic Signals", In: "Handbook of Electroencephalography and Clinical Neurophysiology, Volume 1 Revised", A. Gevins and A. Remond, Eds. (Elsevier, Amsterdam, 1987), pp. 405-448.

SESSION II

MAGNETIC REFRIGERATION

CHAIRPERSON: J. LUDWIGSON
VICE CHAIRPERSON: G. PATTON

THE MAGNETOCALORIC EFFECT IN ERBIUM

C.B. Zimm, P.L. Kral, J.A. Barclay

Astronautics Corporation of America; Technology Center, Madison, WI 53716

and

G. F. Green
W. G. Patton

D. W. Taylor Naval Ship R&D Center; Bethesda, MD 21402

ABSTRACT

Magnetic refrigeration above 1 K has been under development at several locations since the mid 1970's because of its potential for high efficiency and reliability. Such refrigerators are based on the magnetocaloric effect in magnetic materials. The proper choice of material is essential for high performance designs. Below about 20 K, paramagnetic materials such as gadolinium gallium garnet are useful magnetic refrigerants. Above 20 K the refrigerant must be an exchange-coupled magnetic material used near its ordering temperature. One of the necessary characteristics of a good refrigerant is a large adiabatic temperature change, ΔT_S, upon application of or removal of a magnetic field. Magnetic elements with large magnetic moments potentially have large ΔT_S, as indicated by previous measurements in Gd, Dy, Tb, and Ho. Another candidate material is Er, which has one antiferromagnetic transition at 84 K, another at 52 K, and a ferromagnetic transition near 19 K. We report on the measurement of the heat capacity and ΔT_S in Er between 10 K and 100 K in several magnetic fields up to 7.5 T. The suitability of Er as a magnetic refrigerant is discussed.

I. INTRODUCTION

Many applications of superconductors require cooling to liquid helium temperature to maintain the superconducting properties of wire in a magnet, motor, generator, or other device.[1] For example, the Navy anticipates the use of helium liquefiers on ships with superconducting drive motors. An efficient, reliable, and cost effective method of providing the refrigeration for liquefaction of the cryogen is a goal of many research and development efforts around the world. Specifically, at the David W. Taylor Naval Ship R&D Center there is a program to investigate magnetic refrigerators as a means to satisfy these cooling requirements with a high-performance, advanced liquefaction unit.[2]

Magnetic refrigerators are based on the temperature and magnetic field dependence of the entropy of certain magnetic materials. The entropy change can be represented by the following equation:

$$dS = \left(\frac{\partial S}{\partial T}\right)_H dT + \left(\frac{\partial S}{\partial H}\right)_T dH \qquad (1)$$

where S is entropy, T is absolute temperature, and H is applied magnetic field strength. By use of a Maxwell relation this equation can be rewritten in terms of directly measurable quantities; i.e.,

$$dS = \left(\frac{C_H}{T}\right) dT + \mu_O V_M \left(\frac{\partial M}{\partial T}\right)_H dH \qquad (2)$$

where C_H is the heat capacity at constant field strength, μ_O is the permeability in vacuum, M is the magnetization, and V_M is the volume of the magnetic material. Eqn. (2) can be solved for the temperature change under adiabatic conditions, i.e. dS = 0, to give

$$dT = \left(\frac{-T\mu_O V_M}{C_H}\right) \left(\frac{\partial M}{\partial T}\right)_H dH \qquad (3)$$

which when integrated over magnetic field changes, yields the resultant adiabatic temperature change ΔT_S. In the design of magnetic refrigerators the entropy-temperature curves which implicitly contain C_H and ΔT_S are absolutely essential. Hence, measurements that produce C_H and ΔT_S such as described in this paper are required for the design data base. The requirements for a good ferromagnetic refrigerant have been previously discussed.[3,4,5]

The Navy magnetic refrigerator design uses a magnetic material that acts as its own regenerator, i.e., an active magnetic regenerator.[2,6] For high efficiency the heat transfer between the heat exchange fluid and the magnetic refrigerant must be excellent. The Navy has developed a unique fabrication method that produces a uniform bed of very small parallel flow channels. The "jelly-roll" assembly procedure has been described earlier.[2] One of the requirements for this fabrication method is a malleable magnetic refrigerant. Many of the ferromagnetic intermetallic compounds that are good refrigerants are brittle[8] in comparison to the metallic rare earth elements. Because of the malleability requirement and the presence of large magnetic moments in the rare earth elements, several of these elements have been investigated as potential magnetic refrigerants. Field dependent adiabatic temperature change measurements have been reported on Gd[8], Dy[9], Ho[10], and Tb[10].

Erbium is another rare earth element that has a large magnetic moment ($\mu \sim 9\ \beta$, where β is the Bohr magneton) and several magnetic transitions which may have a large field-dependent entropy associated with them. Erbium has a hexagonal close-packed crystal structure and exhibits a complex magnetic structure[11,12] due to a competition among several mechanisms such as exchange, crystalline field, magnetoelastic, and electronic Zeeman interactions. At 84 K, there is a transition from the almost random order of the high temperature paramagnetic state to a type of antiferromagnetic order with the magnetic moments pointing along the c-axis of the crystal but slowly changing in magnitude and direction, i.e., sinusoidally modulated. At near 52 K, the basal plane magnetic moment orders in a spiral pattern such that the overall order is still antiferromagnetic. The sinusoidal modulation of the moments along the c-axis also becomes more square-wave in character. Finally, at near 18-20 K, a transition into a spiral ferromagnet occurs with the c-axis moment now fixed but the basal plane moment still rotating through the crystal. This produces a conical magnetic structure.

We report the measurements of the field dependent heat capacity and adiabatic temperature change for Er from about 10 K to about 110 K in fields up to 7.5 T.

II. EXPERIMENTAL METHOD

The erbium sample used in this study was machined from a cast polycrystalline ingot of 99.9% atomic purity with respect to other rare earths. The ingot was produced by Research Chemicals of Phoenix, AZ. It was mounted in a cryostat as described below.

The heat capacity and temperature change of the sample upon change in applied field were measured by an adiabatic method. The sample was brought to internal thermal equilibrium at a temperature T_i, either a known heat pulse for C_B or a known change in external magnetic field for ΔT_S was applied, and then the final temperature T_f was observed. The temperature was taken to be the average of T_i and T_f. Correction for heat lost to the surroundings was done by a simple linear extrapolation to the middle of the heat pulse or field change. This correction was quite small because the time constant for internal thermal equilibrium of the sample was typically several orders of magnitude shorter than the time constant for equilibration with the surroundings. Excellent thermal isolation was ensured by suspending the sample via linen threads, using high resistance leads for the heater and thermometer, winding the heater directly on the sample, and placing the thermometer in a snug hole at the center of the sample. The sample was surrounded by a can maintained at a temperature intermediate between the initial and final temperature of the sample. This can was surrounded in turn by two more isothermal cans sharing a common vacuum as shown in Fig. 1. The temperatures of the sample and the surrounding cans were measured by carbon-glass thermometers.

The corrections for the heat capacity of the thermometer, heater wire, threads and varnish attached to the 0.030 kg sample were typically on the order of 5%. For ΔT_S, the measured values were corrected for addenda by multiplying by the ratio of the total heat capacity of the erbium and addenda to that of the erbium alone. The heat capacity values used for the corrections were the average of the values at the initial and final applied fields. The approximately ellipsoidal sample had a length to diameter ratio of 3.0 and was oriented with its long axis parallel to the field. Demagnetization corrections to the applied field have not been made but in light of the published magnetization data[13], the corrections are small except for the 1T data in the ferromagnetic regime, i.e., below 20 K.

The data were taken automatically, with the magnet power supply, the persistent mode switch heater, the temperature controller for the can surrounding the sample, the heat pulser for the sample, and the voltmeter measuring the temperatures under the control of a HP 9000-300 series computer. Because the time constant for cooling the sample and surrounding cans is extremely long, all the data were taken in a stepwise warming mode, with the temperatures of the cans and the sample stabilized before each heat pulse or field change. Before each run, the sample was cooled from greater than 100 K to 4.2 K in zero applied field. For heat capacity measurements, the length of the heat pulse was about 1/4 of the thermal time constant of the sample and the power of the heat pulse was chosen to warm the sample by 0.5 - 1 K.

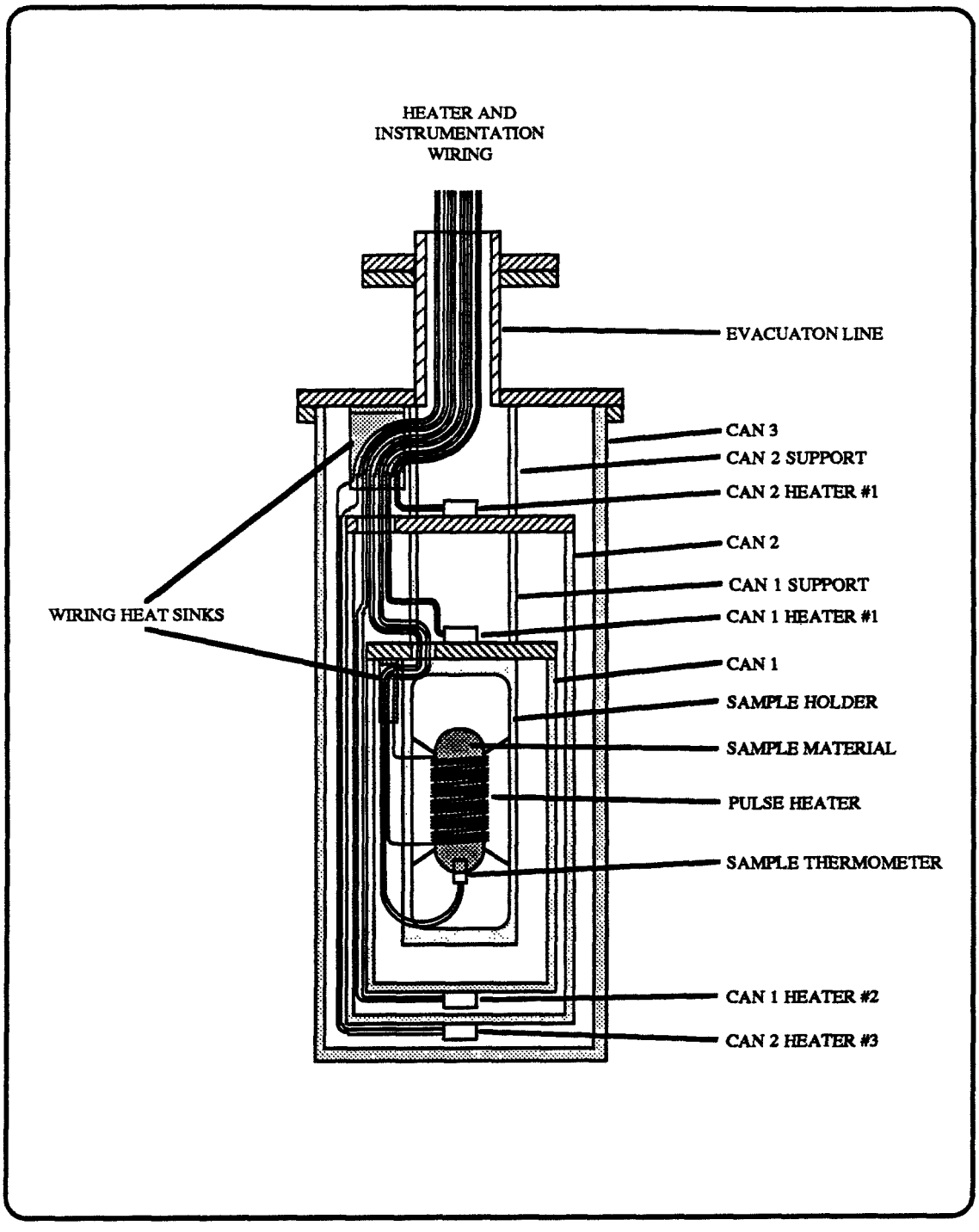

Fig. 1. Heat capacity apparatus, showing the suspended sample surrounded by isothermal shields.

III. RESULTS AND DISCUSSION

Figure 2 shows the measured heat capacity for the polycrystalline sample of erbium at various applied magnetic fields.

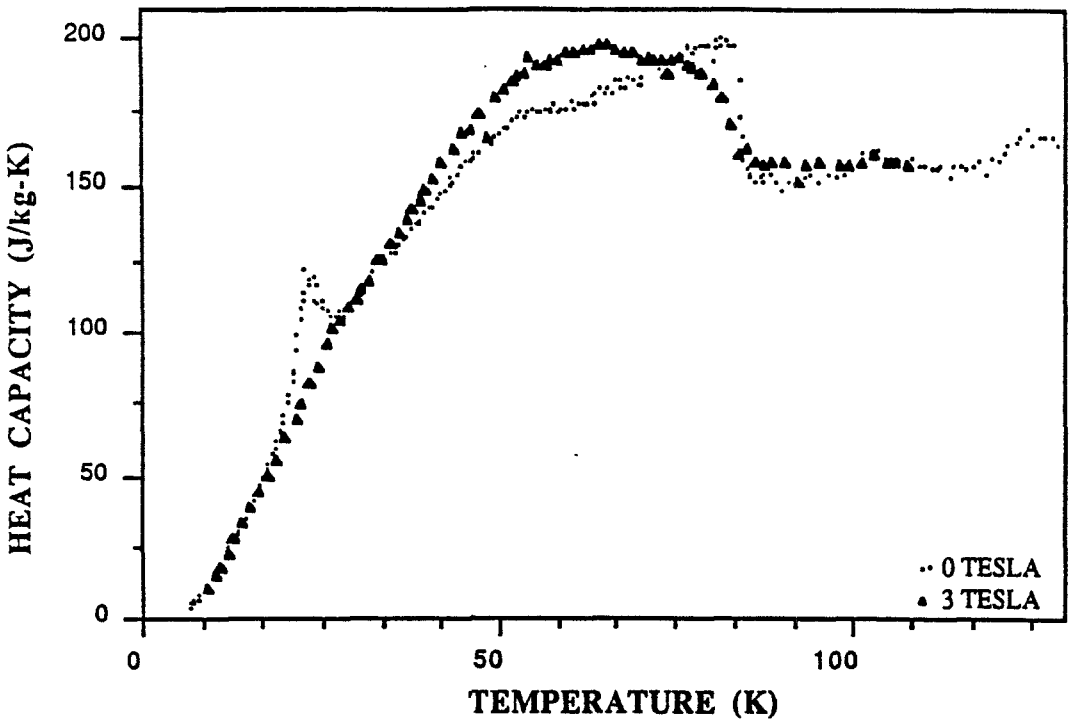

Fig. 2. The measured heat capacity of a polycrystalline sample of erbium in various applied magnetic fields. The data has been corrected for addenda, but not for demagnetization effects.

The zero field curve is consistent with that seen by previous authors.[14] Neutron scattering experiments[11] and theoretical calculations[15] have explained the features of this curve in terms of magnetic structural transitions. The large step at 84 K corresponds to an antiferromagnetic ordering of the c-axis moments, the broad shoulder stretching from 30 K to 80 K corresponds to the ordering of moments in the ab plane. The sharp spike near 20 K is a first order transition to a ferromagnetic cone structure. Application of a 1 Tesla field strongly couples to the ferromagnetic moment and washes out the low temperature peak, but has little effect at higher temperature. Stronger magnetic fields broaden the 84 K transition and also remove the entropy between the 20 K and 84 K transitions at higher temperature.

Figure 3 shows the measured changes in temperature of the thermally isolated sample upon changing the magnetic field.

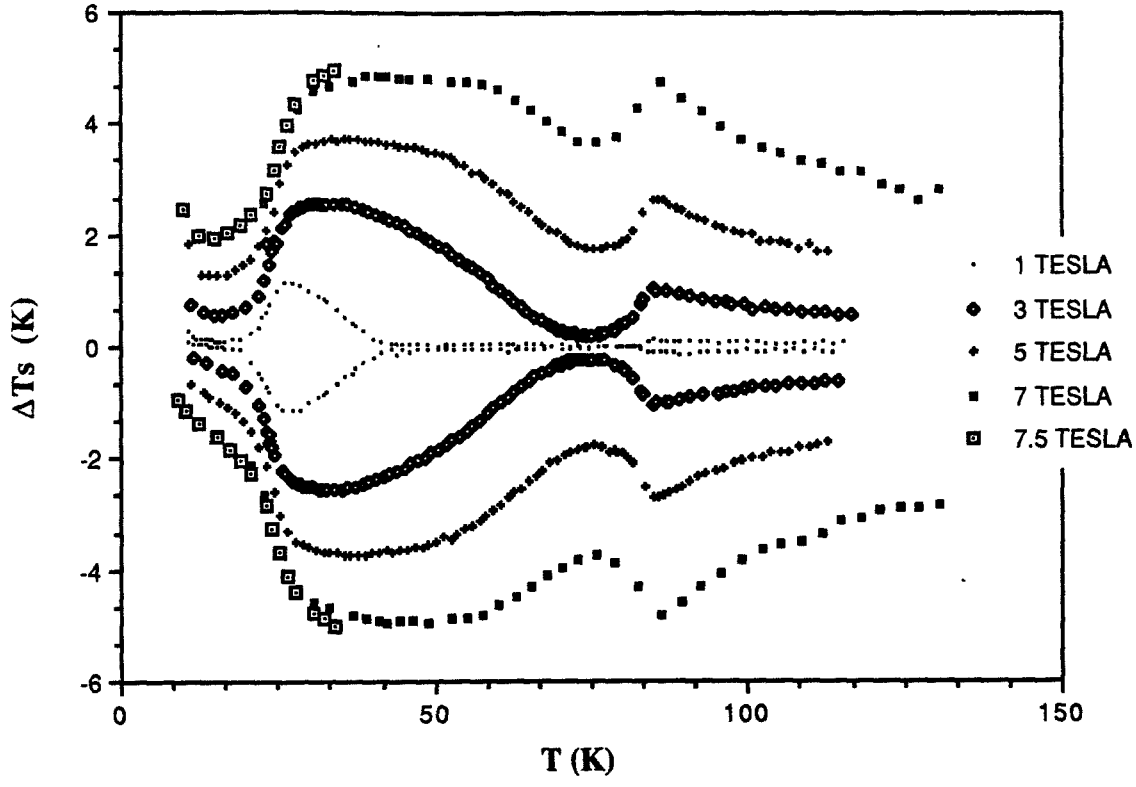

Fig. 3. The measured change in temperature of Erbium upon a change in applied magnetic field, from 0 to the specified value (upper curves) and from the specified value to 0 (lower curves).

The positive changes in temperature plotted in Figure 3 occurred when the field was increased from zero to the specified value, the negative changes occurred when the field was decreased back to zero. Note that curves are symmetrical about zero temperature change above 20 K, indicating that the adiabatic magnetization process above the ferromagnetic transition is reversible. This characteristic is necessary for efficient magnetic refrigeration. Below 20 K, however, a magnetization-demagnetization cycle warms the sample. The eddy current heating for this 10mm diameter sample at 10 K should produce only a few mK temperature rise in the slow (10^2-10^3 sec) field changes used; hence the heating is ascribed to magnetic hysteresis which is also noted below 18-20 K in reported neutron scattering measurements.[11]

Because the heat capacity has field dependence over a wide range of temperature, we would also expect to see changes in temperature produced by a changing applied magnetic field over a correspondingly wide range of temperature. Figure 3 shows that this is indeed the case. The 1 Tesla field only produces temperature changes just above the low temperature ferromagnetic transition. The 3 Tesla field also produces temperature changes at the 84 K transition. Fields of 5 and 7 Tesla produce appreciable temperature change throughout the 25 K to 110 K region.

The results reported here are for a cast polycrystalline sample whose crystallites are presumably unaligned. The effect of magnetic field on the magnetization of single crystal specimens is clearly dependent on the angle the field makes with respect to the c-axis.[13] Directional effects would also be expected on rolled sheet specimens, for which the repeated cold rolling and annealing during fabrication could produce considerable crystallite alignment.[16]

Unfortunately, the adiabatic temperature change at any given temperature and field change for erbium is much less than that obtained at the Curie point of a simple ferromagnet such as GdPd shown in Figure 4.

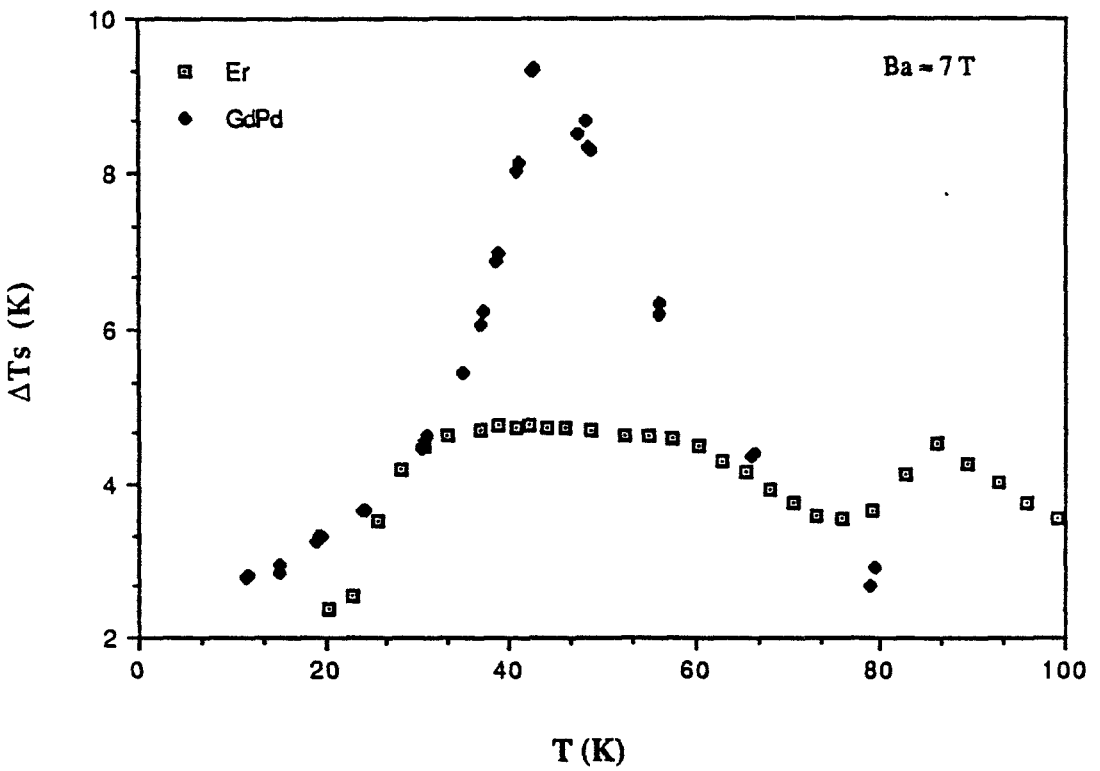

Fig. 4. A comparison of the measured ΔT_S for erbium to that for the simple ferromagnet GdPd for an applied field change from 0 to 7 Tesla.

This reduction of peak ΔT_S is because the considerable crystal field and exchange anisotropy of erbium prevents changing from nearly complete magnetic disorder to magnetic order with a reasonable magnetic field, in contrast to what may be done just above the Curie point for a simple ferromagnet.

If erbium is to be used in a magnetic refrigerator, the relatively small temperature changes produced by magnetization or demagnetization of erbium requires use of regeneration to achieve useful temperature span. The optimal material to use in an active magnetic regenerator refrigerator would have its adiabatic temperature change proportional to temperature.[5] The adiabatic temperature change for erbium is approximately independent of temperature, so it would have to be blended with other materials such as dysprosium or holmium to produce a good magnetic regenerative bed material.

IV. ACKNOWLEDGEMENTS

This work was performed at the Astronautics Technology Center as part of a magnetic refrigerator development program funded by internal R&D funds and customer contracts. The apparatus described here was developed in part with support from the Department of Energy and the Strategic Defense Initiative. These measurements on Er were supported b y the D.W. Taylor Naval Ship R&D Center. Support from these sources is gratefully acknowledged. Technical discussions with several members of the Thermo-Magnetic Device Department and support from H. Harkness, J. Laatsch and C. Chamberlain are especially noted.

V. REFERENCES

1. J.A. Barclay, "Magnetic Refrigeration: A Review of a Developing Technology", Advances in Cryogenic Engineering, 33, 719 (1988).

2. G. Patton, G. Green, J. Stevens, and J. Humphrey, "Reciprocating Magnetic Refrigerator", Proceedings of the Fourth International Cryocooler Conference, p. 65 (1986).

3. T. Hashimoto, T. Numazawa, M. Shino and T. Okada, "Magnetic Refrigeration in the Temperature Range from 10 K to Room Temperature: The Ferromagnetic Refrigerants", Cryogenics, 21, 647 (1981).

4. M.E. Wood and W.H. Potter, "General Analysis of Magnetic Refrigeration and Its Optimization Using a New Concept: Maximization of Refrigerant Capacity", Cryogenics 25, 607 (1985).

5. C.R. Cross, J.A. Barclay, A.J. DeGregoria, S.R. Jaeger and J.W. Johnson, "Optimal Temperature-Entropy Curves for Magnetic Refrigeration", Advances in Cryogenic Engineering, 33, 767 (1988).

6. J.A. Barclay, "The Theory of an Active Magnetic Regenerative Refrigerator", in Refrigeration for Cryogenic Sensors (NASA Conference Publication 2287), M. Gasser, editor, p. 375 (1983).

7. A. Lawley, "Mechanical Properties - Plastic Behavior", in Intermetallic Compounds, J.H. Westbrook, editor, Wiley, New York, p. 464 (1967).

8. S.M. Benford and G.V. Brown, "T-S Diagram for Gadolinium Near the Curie Temperature", J. Appl. Phys., 52 (2110) (1981).

9. S.M. Benford, "The Magnetocaloric Effect in Dysprosium", J. Appl. Phys., 50, 1868 (1979).

10. G. Green, W. Patton and J. Stevens, "The Magnetocaloric Effect of Some Rare Earth Metals, Advances in Cryogenic Engineering, 33, 777 (1988).

11. M. Habenschuss, C. Stassis, S.K. Sinha, et al., "Neutron Diffraction Study of the Magnetic Structure of Erbium", Phys. Rev. B, 10, 1020 (1974).

12. K.A. McEwen, "Magnetic and Transport Properties of the Rare Earths", in Handbook on the Physics and Chemistry of Rare Earths, Vol. 1 (Metals), K.A. Gechneidner, Jr. and L. Eyring, editors, North Holland, p. 427 (1978).

13. J.L. Feron, G. Hug, and R. Pauthenet, "Magnetische Eigenschaften von einigen einkristallinen Seltenen Erden", Z. Angew. Phys., 30, 61 (1970).

14. R.E. Sckochdopole, M. Griffel, and F.H. Spedding, "Heat Capacity of Erbium from 15 to 320 K", J. Chem. Phys., 23, 2258 (1955).

15. R.R. Rao and J.V.S.S. Narayana Murty, "Magnetic Contribution to the Specific Heats of Gadolinium, Dysprosium, and Erbium", J. Low Temperature Phys., 33, 413 (1978).

16. T.E. Scott, "Plastic and Mechanical Properties", in Handbook on the Physics and Chemistry of Rare Earths, Vol. 1 (Metals) K.A. Geschneidner and L. Eyring editors, North Holland, p. 593 (1978).

PERFORMANCE RESULTS OF A LOW-TEMPERATURE MAGNETIC REFRIGERATOR

J.A. Barclay, C.K. Campenni, C.R. Cross, J.A. Hertel,
D.D. Hill, S.R. Jaeger, S.F. Kral, F.C. Prenger,
T.M. Stankey, J.R. Trueblood, C.B. Zimm

Astronautics Corporation of America;Technology Center,Madison, WI 53716

ABSTRACT

Magnetic refrigeration has been used for over 50 years as a technique to achieve temperatures below 1 K. However, in the past ten years, the technology has been developing for refrigeration applications above 1 K up to, and including heat pumps above room temperature. The work has been multinational in scope and has focused on analysis of magnetic thermodynamic systems, investigation of magnetic materials suitable for refrigerants, and development of prototype refrigerators.

Astronautics Corporation of America is developing efficient, continuous magnetic refrigerator stages that operate from 1.5 K to 4.5 K and 4 K to 15 K. The lower temperature stage will produce superfluid helium while using a liquid helium bath (4.2 K) as the heat sink. The higher temperature stage is intended as an alternative to the Joule-Thomson (J-T) loop in a standard Gifford-McMahon, J-T hybrid refrigerator operating from 4 K to 3.5 K. The 1.5 K to 4.5 K magnetic prototype has been designed, built and is under test. The refrigerator is described and its predicted performance along with several subassembly test results are presented.

I. INTRODUCTION

Magnetic refrigeration has been identified as a technology that offers increased efficiency and higher reliability compared to existing low-temperature gas-cycle stages. The underlying principle for magnetic refrigeration is the magnetocaloric effect (MCE), i.e., when certain magnetic materials are placed in a magnetic field, the materials heat up; when the materials are removed from the field they cool. The larger the change in magnetic field, the larger the effect for a given material. In order to use the MCE, magnetic refrigerators must exploit the temperature and magnetic field dependence of the magnetic entropy of a solid material in a cycle to extract heat from a low temperature source and transfer it to a higher-temperature sink. The increased efficiency is due primarily to the reversible temperature change of the magnetic material upon insertion into and removal from a region of high magnetic field. When this process is coupled with highly effective heat transfer to the thermal load and heat sink, the thermodynamic efficiency remains high. The high efficiency is obtained most easily in the very low-temperature regions where it is most difficult for gas-cycle refrigerators to operate effectively. Therefore, a gas-magnetic or cryogen-magnetic hybrid refrigerator naturally promises better performance than an all-gas or all cryogen refrigerator for applications where substantial cooling powers at very low

temperatures are required. For example, the cooling of NbTi superconductors from 4.2 K to 1.8 K improves their performance dramatically because of the large improvement in heat transfer with superfluid helium II and the 25-50% increase in current density. Superconductor applications presently under development such as superconducting magnetic energy storage (SMES) systems and the continuous electron beam accelerator (CEBAF) plan to use 1.8 K refrigeration.

Several experimental magnetic refrigerators (MR's) have been built to operate in the 1.8 K to 4.5 K temperature range.[1-11] The basic Carnot cycle used in several of these MR's is shown in Fig. 1.

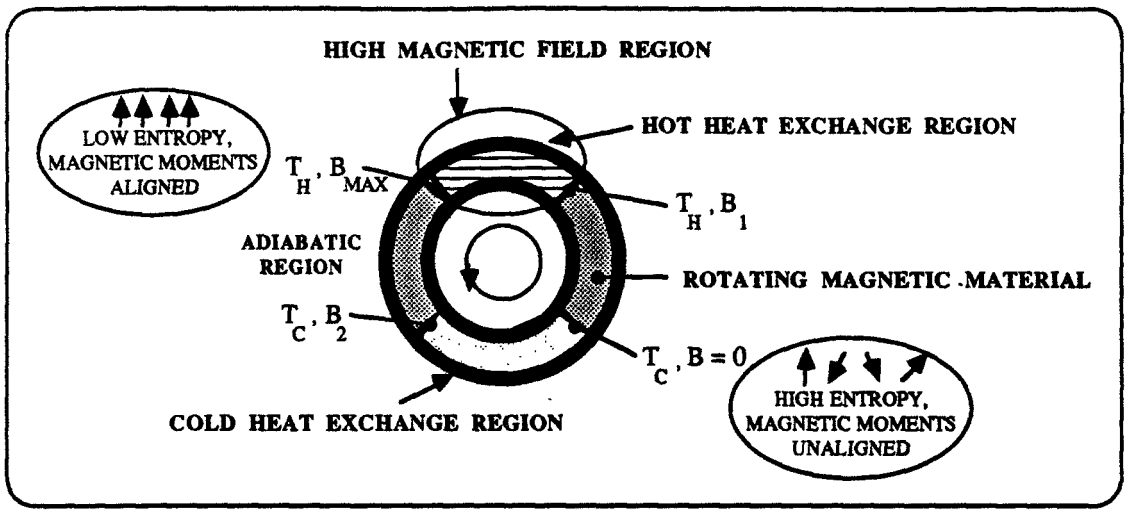

Fig. 1. Schematic of a magnetic refrigerator that executes the Carnot cycle. The magnetic material is rotated clockwise.

In this schematic, a rotating wheel of magnetic material moves in and out of a region of high magnetic field. Reciprocating and charge/discharge units have also been built. Each method of magnetization and demagnetization has its merits. Specifically, the characteristics of rotary motion include:

- continuous cooling and heat rejection;
- force compensation (as much as possible) by continuous material passage in and out of magnetic field;
- time independent magnetic flux is possible;
- balanced bearing loads can be achieved in some designs;
- other field geometries besides solenoidal are possible; but
- seals and flow control of the heat transfer fluid may be difficult.

Because of the continuous refrigeration, the possibility of balanced bearing loads, and the existence of a constant magnetic flux, the rotary design has the highest suitability for many applications.

This paper describes an advanced rotary MR prototype developed in our laboratories.

II. DESCRIPTION OF A 1.5 K TO 4.5 K PROTOTYPE

The Astronautics magnetic refrigerator for 1.5 K to 4.5 K operation is a Carnot-cycle rotary device based on an earlier prototype built at Los Alamos National Laboratory (LANL).[12] Liquid helium at near 4.2 K is its heat sink and superfluid helium near 1.8 K is the thermal load. Significant design enhancements have been added to the LANL unit to increase simplicity, reliability, user friendliness and thermal performance. The device has also been thoroughly analyzed during the design process. Each of the key components will be briefly described.

Several magnetic materials can be used as the refrigerant in this temperature range, but gadolinium gallium garnet (GGG) was chosen as the baseline material because of the extensive data base available. The heat transfer from the thermal load to the GGG and from the GGG to the heat sink is accomplished by OFHC copper bars connected to fins in close proximity to the GGG. The GGG in the form of fins is mounted on a wheel hub to increase the contact area for heat transfer. Helium gas in a sealed housing surrounding the Cu and GGG fins completes the thermal path. The wheel hub is supported on a MoS_2 dry lubricated precision ball bearing. The wheel is driven by a rim gear operated from room temperature by the drive motor. The drive shaft is a stainless steel, thin-walled tube and sealed at room temperature using a ferrofluid seal. The drive motor is a synchronous permanent magnet motor with a conventional speed controller. The magnets are of conventional design using readily available NbTi superconducting wire. A Helmholtz configuration of solenoids was used to simplify magnet construction. The magnet support shell is the primary structural element of the prototype. The top and bottom of the shell have high permeability material to reduce any stray magnetic flux. Instrumentation is attached at every key location in the prototype (a total of about 90 transducers are used). A data acquisition system is used to record the performance data during experiments. The specifications of the magnetic refrigerator are summarized in Table I.

During operation, the magnetic refrigerator is inserted into a cold box, evacuated, and precooled with a two-stage Gifford McMahon cycle gas refrigerator. Liquid helium is then circulated through the heat exchanger and the vapor cooled leads for the superconducting magnets before operation proceeds. Several components of this apparatus have been tested as subassemblies to validate the model calculations that have been done. A schematic diagram of the apparatus is shown in Figure 2.

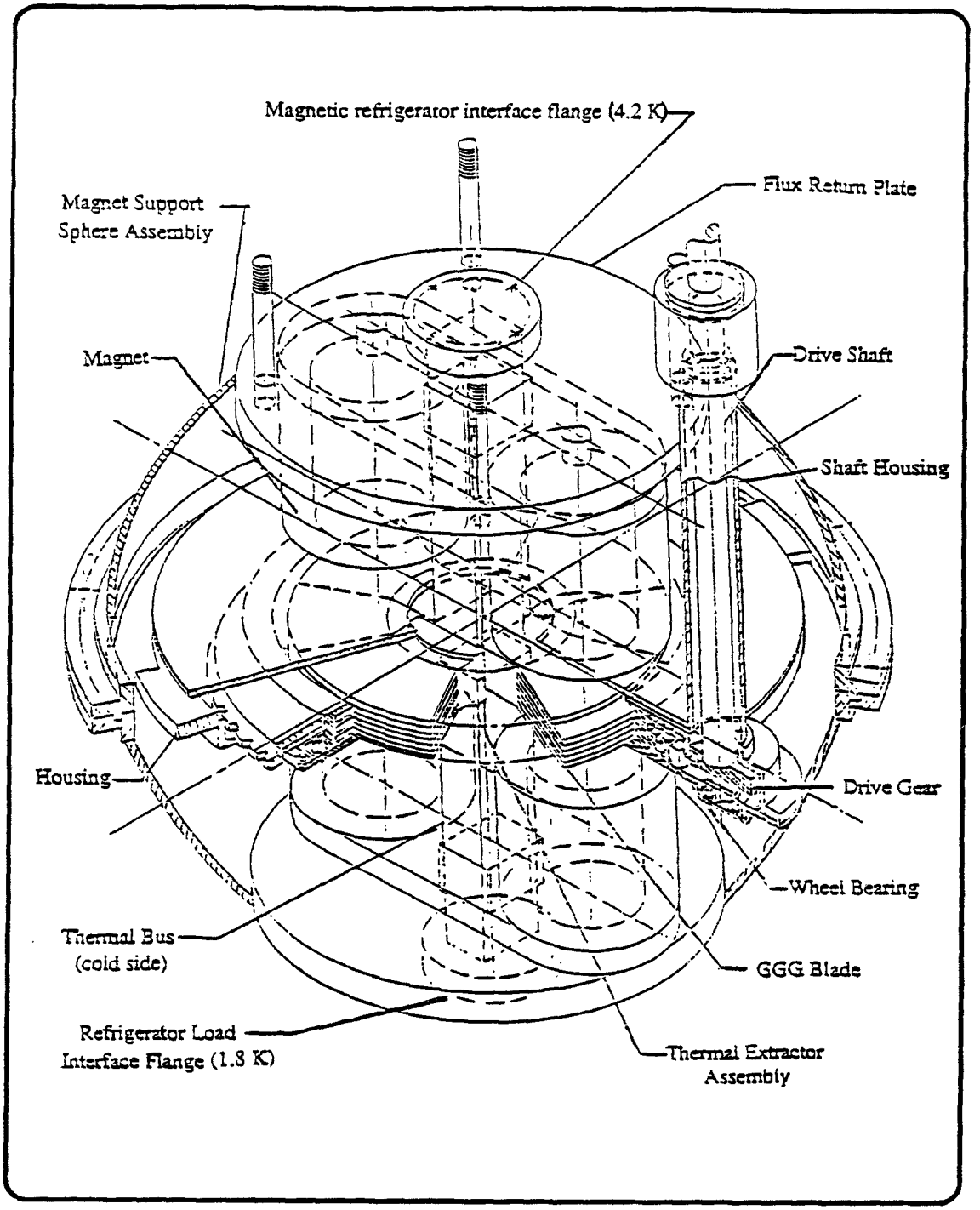

Fig. 2. The Astronautics magnetic refrigerator for 1.5 K to 4.5 K operation.

TABLE I.
SPECIFICATIONS AND CHARACTERISTICS OF TMD 1.5-4.5-0.5

Refrigeration capacity	- 0.5W
Load temperature	- 1.8 K
Heat rejection temperature	- 4.2K
Heat rejection method	- Nucleate boiling
Refrigeration cycle	- Carnot cycle with refrigerant cycling between 1.5 K and 4.5 K
Magnetic material	- Gadolinium Gallium Garnet
Heat Exchange	- Helium gas conduction between parallel plates
Magnetization/demagnetization	- Rotary motion of magnetic material at ~1 rad/sec
Magnet configuration	- Two NbTi Helmholtz pairs
Source/sink connection	- Conduction through copper busses

III. THEORETICAL PREDICTIONS AND EXPERIMENTAL RESULTS

There are four basic subsystems of the magnetic refrigerator: magnetic, structural, mechanical, and thermal. Each of these subsystems is coupled to the others and iteration is required to achieve an optimum design. Examples of design calculations and experimental results from each area are now presented.

Magnetic Subsystem

This consists of the magnets, joints, persistent mode switch, leads, power supplies, protection circuit and control units. The chief components in this subsystem are the magnets. They were designed for a peak field of 4.5T in the gap between the magnets where the GGG rotates. The fields and forces within each magnet were calculated and used in the coil design. The net forces among the magnets and detailed forces on the GGG were then calculated.[13] The magnets were wound with 0.85mm diameter multifilamentary (54 filaments) twisted NbTi wire with a 1.35:1 copper to superconductor ratio and formvar insulation (obtained from Oxford Superconducting Technology, Inc.). The current carrying capacity of a short sample of the wire as a function of external magnetic field was directly measured in our labs and used in the design calculations. The magnets were fabricated in our shops and tested at 4.2 K. A typical coil achieved 92-95% of short sample performance. The short sample data, the design load line, and the experimental results are shown in Fig. 3.

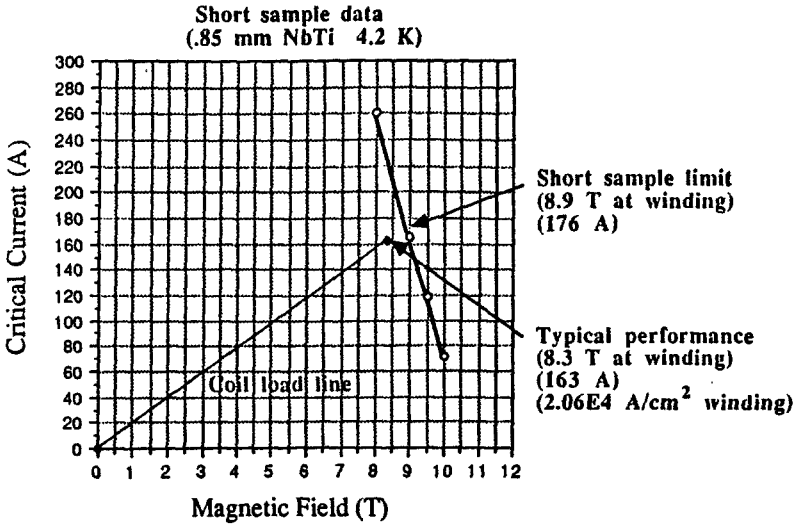

Fig. 3. Characteristics of the NbTi magnets used in the Astronautics magnetic refrigerator for 1.5 K to 4.5 K operation.

Structural Subsystem

This consists of the housing, the external shell, wheel hub, the LHe heat exchanger, gas refrigerator, and external support rods. The housing and external shell are two key elements of this subsystem in the MR. The housing contains the only moving parts of the refrigerator and the helium heat exchange gas. It must be shaped in a pancake like geometry to keep the gap between the magnets as small as possible. This geometry is susceptible to "oil canning" when the helium gas pressure changes. Therefore it must be carefully modeled to insure proper cold operation. Finite element codes have been used to calculate the deflection expected as a function of helium gas pressure. The predicted deflection and the measured results are shown in Fig. 4 for two different radial locations on the stainless steel housing. These were measured at about 10 K using the gas refrigerator to cool the housing. Note that the measured and predicted deflections agree very well. The 7 cm measurements are near the maximum predicted deflection for the housing and the 10.4 cm measurements are near the bearing location.

Similar calculations and measured results have been obtained for most of the other structural components. In high tolerance systems these motions along with those from thermal contractions are critical to the successful warm assembly and subsequent cold operation.

Drive Subsystem

This consists of the cryogenic bearings, drive gears and shaft, rotary seals, drive motor, and controller. One of the key aspects of these components is that they have to transmit power from near room temperature to the cryogenic region of the MR. In the case of the present cryocooler, the input power is transmitted down a stainless steel drive tube sealed at room temperature. The shaft drives a spur gear that engages the large gear on the wheel hub. The wheel hub is supported on a dry-lubricated ball bearing. The frictional dissipation in the bearing is a thermal load that directly reduces the net cooling power and

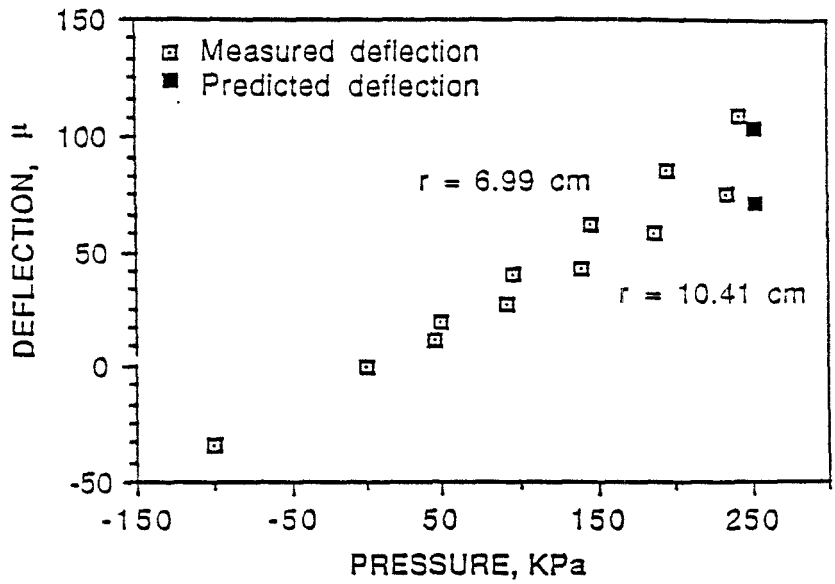

Fig. 4. The measured and predicted deflections of the housing at two locations as a result of internal pressurization with helium gas.

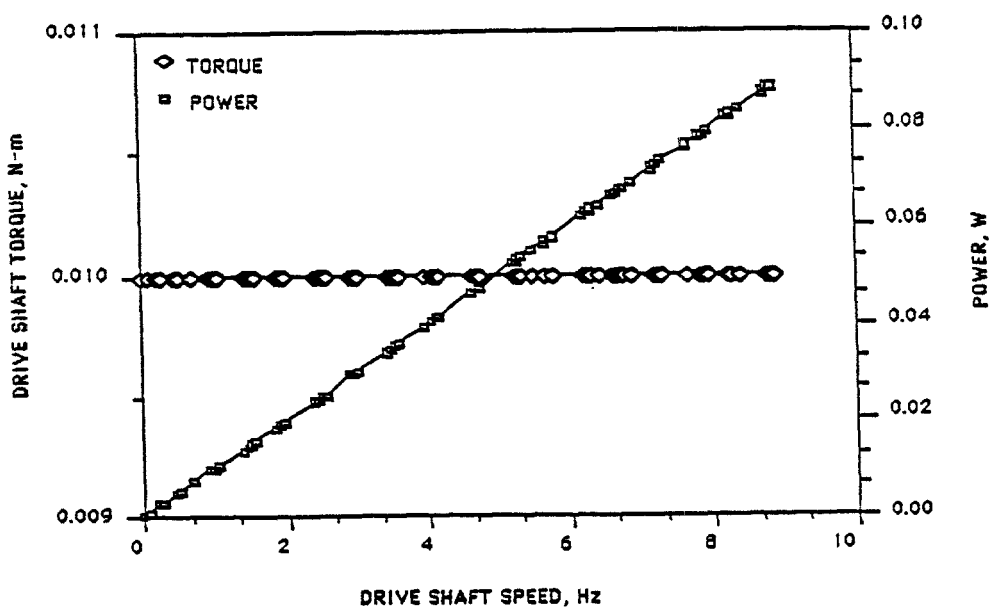

Fig. 5. The torque and power dissipation produced by the drive shaft and associated bearings. The bearings were at 10 K. The main wheel hub bearing is not included in this test.

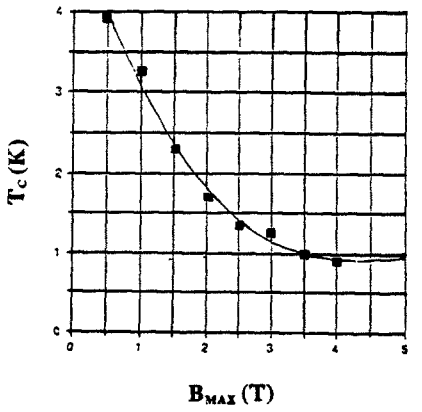

Fig. 6. Model calculations of the cold sink temperature of the MR at zero thermal load.

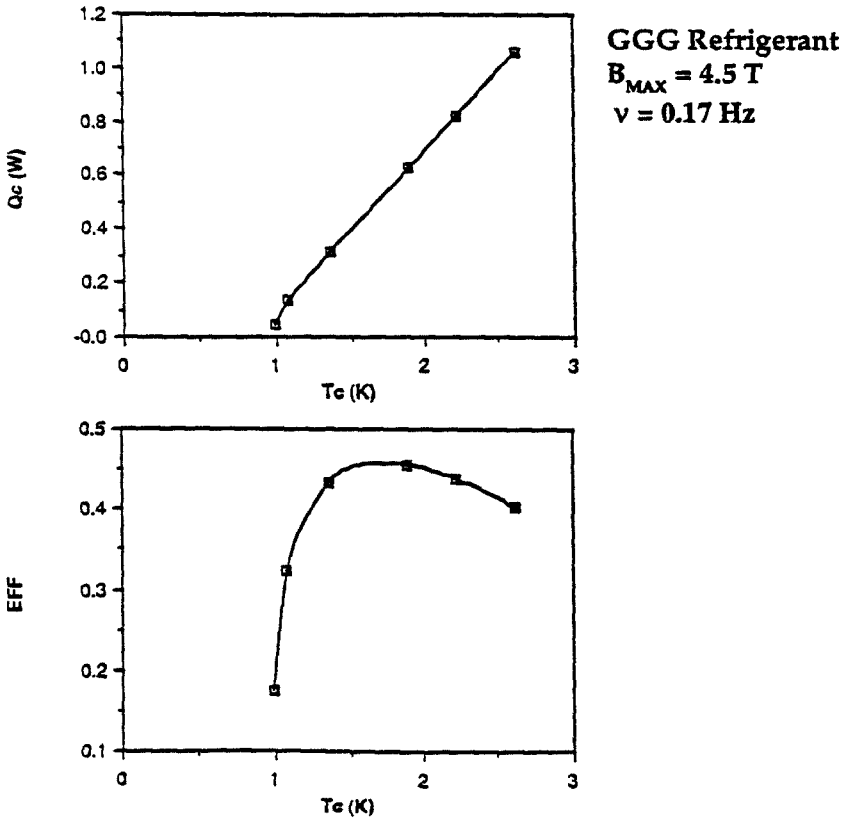

Fig. 7. Model calculations of the cooling power and efficiency relative to Carnot of the Astronautics MR at a fixed wheel rotation frequency and magnetic field.

hence efficiency. Although difficult to calculate, the bearing friction can be readily measured by using torque meters. Figure 5 illustrates the frictional power produced by the drive assembly at about 10 K.

Thermal Subsystem

This consists of the GGG, the copper fins and buses, the hot and cold heat exchangers, the helium exchange gas, and the gas cycle refrigerator. The performance of the MR with a complete thermal network including adiabatic temperature changes in the GGG due to magnetic field magnitudes and profiles has been done using MITAS (TSAP). The predicted achievable temperature as a function of peak magnetic field is shown in Fig. 6. Note that a field of less than 2T will reach the λ-point (2.18 K) at zero thermal load.

The predicted cooling power and efficiency relative to Carnot are shown in Fig. 7 for $B_{MAX} = 4.5T$ and $\nu = 0.17\ H_Z$. At 1.8 K, a cooling power of about 0.65 W is indicated with an efficiency of about 45% of Carnot. These predictions will soon be put to the test as the complete refrigerator is operated.

IV. SUMMARY AND CONCLUSIONS

A magnetic refrigerator capable of about 0.5W of cooling at 1.8 K with a peak field of 4.5T while rotating at 0.17 H_Z (10 RPM) has been described. Many subassembly tests have been successfully performed and the results have validated many of the design calculations. A few questions still remain to be answered including helium gas motion in the housing and the ultimate validity of the overall thermal model. Experiments to answer these questions are in progress.

V. ACKNOWLEDGEMENTS

The considerable effort and ingenuity exerted by T. Servais, J. Laatsch, M. Bordson and R. Syphard in the assembly of the Astronautics magnetic refrigerator is gratefully acknowledged.

VI. REFERENCES

1. W.P. Pratt, Jr., S.S. Rosenblum, W.A. Steyert, and J.A. Barclay, Cryog. 17, 689 (1977).

2. J.A. Barclay, O. Moze, and L. Paterson; J. Appl. Phys. 50, 5870 (1979).

3. C. Delpuech, R. Beranger, G. Bon Mardion, G. Claudet, and A.A. Lacaze, Cryog. 21, 579 (1981).

4. A.F. Lacaze, A.A. Lacaze, R. Beranger, and G. Bon Mardion; Proc. ICEC-9, Kobe, Japan (Butterworth and Co., Guildford, UK 1982), pg. 14.

5. A.F. Lacaze, R. Beranger, G. Bon Mardion, G. Claudet, C. Delpuech, A.A. Lacaze, and J. Verdier; Adv. Cryog. Eng. 27, 703 (1982).

6. A.F. Lacaze, R. Beranger, G. Bon Mardion, G. Claudet, and A.A. Lacaze; Cryog. 23, 427 (1983).

7. A.F. Lacaze, R. Beranger, G. Bon Mardion, G. Claudet, and A.A. Lacaze; Adv. Cryog. Eng. 29, 573 (1984).

8. Y. Hakuraku and H. Ogata; Jap. J. Appl. Phys. 25, 140 (1986).

9. Y. Hakuraku and H. Ogata; J. Appl. Phys. 60, 3266 (1986).

10. Y. Hakuraku and H. Ogata; Jap. J. Appl. Phys. 24, 1111 (1985).

11. Y. Hakuraku and H. Ogata; Cryog. 26, 171 (1986).

12. J.A. Barclay, W.F. Stewart, W.C. Overton, Jr., R.J. Candler, and O.D. Harkleroad; Adv. Cryog. Eng. 31, 743 (1986).

13. J.A. Barclay, M. Shnaider, C.R. Cross, F.C. Prenger, W.F. Stewart, and C.B. Zimm; Proc. 4th Int'l Cryocooler Conf., Easton, MD, Sept. 25-26, 1986, pg. 89.

A FINITE ELEMENT MODEL OF AN EXPERIMENTAL MAGNETOCALORIC REFRIGERATOR

Geoffrey Green
Erwin Schroeder

David Taylor Research Center, Bethesda, MD 20084

ABSTRACT

The David Taylor Research Center is developing superconducting electrical machinery for use in Navy ships. This machinery requires cryogenic refrigeration to maintain temperatures that permit superconductivity, and for shipboard use the refrigeration equipment must be rugged, dependable and efficient. To meet this need, the Electrical Systems Division is developing a refrigeration cycle that uses ferromagnetic materials that undergo large adiabatic temperature changes when subjected to a magnetic field. To cool from room temperature, several types of magnetic materials with successively lower Curie temperatures will be used. This type of cycle promises to produce a very efficient refrigeration process while avoiding many of the problems associated with the valves, seals, and compressors in gas cycle refrigerators.

To aid in selecting effective designs of the apparatus and determining effective configurations of the magnetic materials, a mathematical model of the experimental refrigerator was developed. To implement the model quickly and economically, a finite element model was selected and implemented using the NASTRAN program. Results obtained from the mathematical analysis are compared with the measured performance of a prototype experimental apparatus. Starting from 296 K, this refrigerator produced a 50 K temperature difference across the active regenerator.

INTRODUCTION

The U.S. Navy at the David Taylor Research Center (DTRC) has been investigating a magnetic refrigerator to provide cooling from 300 to 4.2 K. A magnetic refrigerator has the potential of greater efficiency, higher reliability, and more rugged construction than the present liquid helium gas cycle refrigerators. The fact that this type of refrigerator has no compressor, no cold valves or seals, and makes use of a rugged regenerative type of heat exchanger makes this concept very attractive for a shipboard environment. The magnetic refrigerator uses the magnetocaloric effect of a ferromagnetic or paramagnetic solid to produce an adiabatic demagnetization temperature change or an isothermal entropy change. This property was measured by Benford and Brown [1] using gadolinium as the ferromagnetic material. This principle can then be used to extract heat from a low-temperature source and transfer it to a higher temperature sink, resulting in a magnetic refrigerator.

The Navy has pursued a reciprocating, active regenerative magnetic refrigerator concept, shown schematically in Figure 1. This concept consists of five major parts: (1) the high magnetic field system, consisting of a superconducting magnet surrounded by a pool of liquid helium and contained in a vacuum-insulated Dewar flask; (2) the ferromagnetic material, gadolinium, a rare earth metal having a Curie temperature of 293 K; (3) the displacer, which moves the fluid through the ferromagnetic material to perform the heat exchange; (4) the warm heat exchanger, which removes the heat produced in the adiabatic magnetization process; and (5) the passive regenerator, which isolates the cold section of the refrigerator from the warm mixing chamber of the displacer.

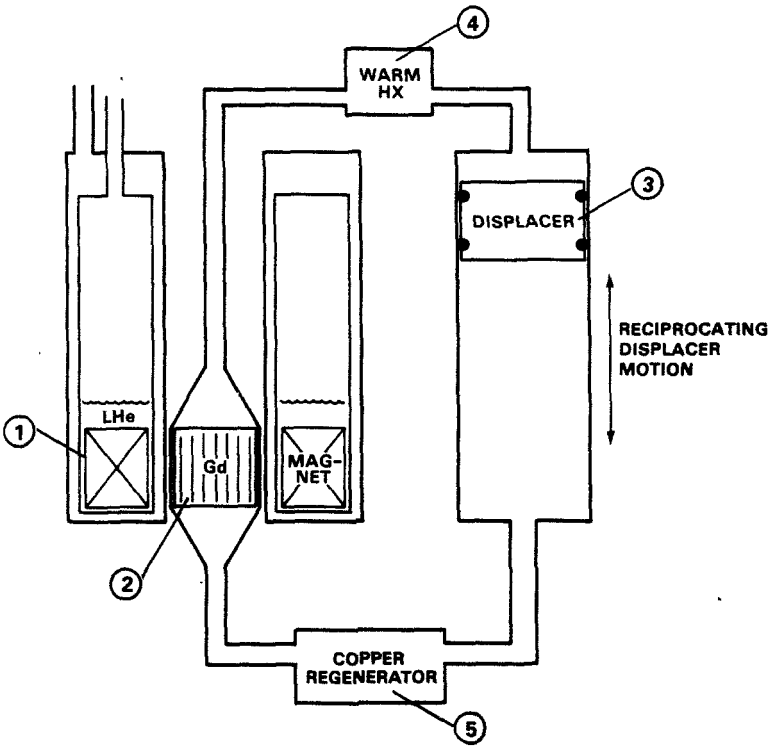

Fig. 1. The Magnetic Refrigerator

A magnetic refrigerator of this type undergoes the following cycle to produce cooling: (1) The magnet is ramped up to full field, causing the ferromagnetic material to heat up. (This step is equivalent to the compression process in a gas cycle.) (2) The displacer moves down, pushing the working fluid through the ferromagnetic material and removing the heat of the magnetization process. This heat is carried to the warm heat exchanger and carried off by the counterflowing water circuit. (3) The magnetic field is removed, cooling the gadolinium through an adiabatic demagnetization process. (4) The displaces is moved up, and the fluid is cooled as it passes through the ferromagnetic material and then it passes through and cools the passive regenerator. In the computer analysis of the cycle, the preceding steps (1) and (2) are referred to as the exhaust stroke and steps (3) and (4) are referred to as the intake stroke.

EXPERIMENTAL APPARATUS

The experimental apparatus required to measure the thermal performance of the magnetocaloric effect in an active regenerator was designed and fabricated at DTRC. [2]

The essential components of the magnetic refrigerator apparatus are shown schematically in Figure 2.

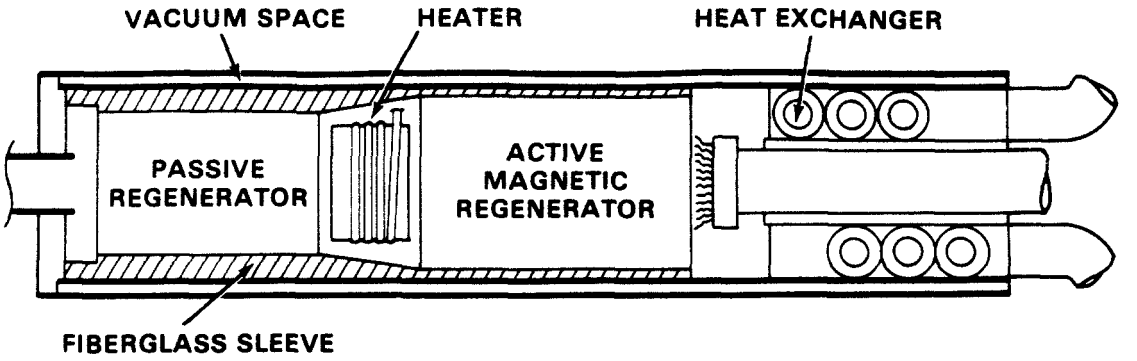

Fig. 2 Magnetic Refrigerator Apparatus

The essential components of the magnetic refrigerator apparatus are shown schematically in Figure 2.

The magnetic material was centered in the almost uniform 7 tesla magnetic field by placing the apparatus through the warm bore of the magnetic Dewar flask. The material in both the passive and active ferromagnetic regenerator were formed into a narrow embossed metal ribbon, wound into discrete sections ("pancakes"), and stacked into G-10 fiberglass sleeve (see Figure 3). The passive regenerator was fabricated with copper, the magnetic regenerator with gadolinium. The gadolinium ribbon was embossed using a rolling mill and sheared into 0.317 cm. widths and lengths of it were wound into the pancake sections. These pancakes could then be placed into the fiberglass cylinder as illustrated in Figure 3.

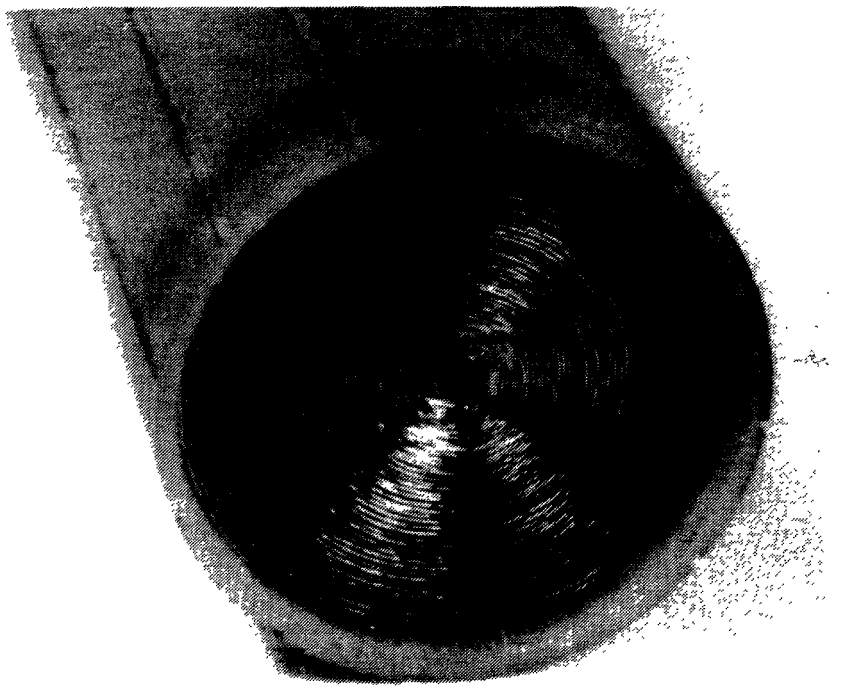

Fig. 3. Gadolinium Ribbon Regenerator Section in the G-10 Fiberglass Sleeve

The passive regenerator used a copper wire that also was formed into a ribbon, wound into a pancake, and inserted into a fiberglass cylinder. The embossed bumps on the metal ribbons provided a set of uniformly spaced flow channels separated by a high heat capacity material to provide the regeneration. The copper regenerator had 0.0178 cm embossed bumps on a ribbon 0.0254 cm thick. This provided a packing factor of 65% and a total copper mass of 2.47 kg. The gadolinium, in contrast, had 0.0127 cm embossed bumps on a ribbon 0.0127 cm thick, which produced a packing factor of 50% and a total mass of 0.730 kg.

A finned tube heat exchanger (Figure 4) was placed at the warm end of the refrigerator to remove the heat of the magnetization process and to maintain a constant temperature at that point. Water flowing through the tube intercepts the heat from the working fluid that passes through the fins of the shell portion of the heat exchanger. The outlet portion of the finned tube heat exchanger and the copper regenerator were connected to the displacer cylinder on either side of the piston. This displacer was a hydraulic cylinder with a 12.7 cm diameter piston and a 22.86 cm stroke. Coupled directly to the displacer was a hydraulic cylinder with a 5.08 cm bore and 22.86 cm stroke. This cylinder drove the displacer back and forth under electronic control, thus moving the gaseous working fluid (pressurized N_2 gas) back and forth through the magnetic refrigerator.

Temperatures were measured in the refrigerator components with type T (copper-constantin) thermocouples. These thermocouples were inserted through small holes drilled in the fiberglass tube and into the component material. Number 36 thermocouple wire was used to minimize heat conduction and response time. The thermocouple wire was placed in

Fig. 4. Finned Tube Heat Exchanger

grooves machined in the outside of the fiberglass tube. A total of 13 thermocouples were used as follows:

- 3 in the passive regenerator
- 1 on the heater
- 1 in the gas space between the regenerator and the magnetic material
- 7 in the active magnetic regenerator
- 1 in the gas space between the magnetic material and the heat exchanger

The mass flow of the working fluid, N_2 gas, was varied as a function of temperature to maintain equivalent changes in the energy per mass of the gas and the magnetic material. The refrigerator was controlled and the data recorded using a small digital laboratory computer. Several experimental tests were conducted starting at or near room temperature and cooling down to 250 to 246 K. The temperatures through the active regenerator were measured in addition to the cool down rate for each cycle.

THE FINITE ELEMENT ANALYSIS

Changes in the size and design of components and in the operating characteristics produce significant changes in the temperature span achieved and the efficiency of the refrigerator. Designing, building, and testing an experimental refrigerator is expensive and time consuming. Therefore, it is desirable to explore various configurations using a computer model to determine promising refrigerator configurations for experimental tests.

In order to keep the time needed to produce a computer model to a minimum, and since DTRC has considerable experience with the NASTRAN program, it was decided to use the NASTRAN transient heat transfer capability for this problem. However, several aspects of the problem make it a non-routine NASTRAN application. The material properties of the refrigerant are temperature-dependent in the temperature range used and make the problem nonlinear. Also, each test run of the refrigerator consists of many strokes. In the mathematical simulation, each stroke corresponds to a time segment with initial conditions different from, but determined by, the final conditions of the previous segment. NASTRAN provides for neither nonlinear material properties nor prescribing temperature values during a transient analysis. To overcome these restrictions, a sequence of NASTRAN analyses is used, one for each stroke. This approach is practical because the model has few degrees of freedom, so the time for each analysis is short. Also the temperature change during one stroke is small enough to permit the use of constant material properties during the analysis of that stroke. An auxiliary program uses results from the NASTRAN analysis of one stroke to compute initial conditions, and prepare NASTRAN data for the next stroke.

Several simplifying assumptions for the mathematical model keep the analysis manageable. Only the active and passive regenerators, and the fluid passing through the refrigerator are modeled. In each regenerator, the chamber walls and the material in the chambers are modeled. Since the layers of refrigerant, copper, and fluid are thin, it is assumed that there is no significant temperature variation through these layers. It is also assumed that there is no significant temperature variation across the chamber. Therefore, the temperature of each type of material is assumed to vary only along the length of the chambers, that is, the problem is one-dimensional. The magnetic field was designed to be as uniform as possible along the length of the gadolinium, therefore the field is assigned a uniform value of 7 tesla. Since several seconds are required to apply or remove the magnetic field, at the beginning of each stroke, the temperature of the fluid is set equal to the temperature of the refrigerant or copper at each position along the length of the regenerators. The temperature distribution in the chamber walls is not changed while the magnetic field is changing. The refrigerant coils are stacked one on top of another. Since the thermal connection between coils is relatively small, and each finite element represents several coils, the thermal conductivity of the material is replaced by a value that accounts for the conductivity of the material modified by the much smaller conductivity between coils.

The heat exchanger is very efficient and lowers the temperature of the fluid flowing through it to the ambient temperature. The passive regenerator has both a large mass and a large area to transfer heat, so that the fluid flowing from the regenerator into the displacer is also at the ambient temperature. Therefore, during the intake stroke, the fluid flowing from the heat exchanger into the active regenerator, and during the exhaust stroke, the fluid flowing from the displacer into the regenerator, are assumed to have constant temperatures. Since temperature-dependent material properties are not changed during one stroke, they are determined for a temperature projected for the middle of the next stroke.

The partial differential equations that describe heat conduction in the gadolinium, in the copper, or in the chamber walls are one-dimensional heat equations with load terms that represent heat transfer from the fluid.

$$\rho_m c_m \frac{\partial T_m}{\partial t} - k_m \frac{\partial^2 T_m}{\partial^2 x} = \frac{A_m h}{V_m}(T_f - T_m)$$

for m = g, c or w for gadolinium, copper, or chamber wall and where

ρ_m = density of material

c_m = heat capacity of material

k_m = conductivity of material

A_m = area of the surface between the material and fluid

V_m = volume of material

T_m = temperature of material

h = convection coefficient

The partial differential equation that describes heat conduction in the fluid, heat carried by the flowing fluid, and heat transferred to the fluid from the gadolinium, copper, or chamber wall is

$$\rho_f c_p \frac{\partial T_f}{\partial t} - k_f \frac{\partial^2 T_f}{\partial^2 x} = -\rho_f c_p v \frac{\partial T_f}{\partial x} + \frac{A_m h}{V_f}(T_m - T_f) + \frac{A_w h}{V_f}(T_w - T_f)$$

The problem is solved using a finite element transient thermal analysis with the NASTRAN program. The refrigerant, copper, chamber walls, and fluid are modeled by one-dimensional heat conduction elements. Transfer of heat between the fluid and the refrigerant, copper, and the chamber walls is modeled using surface conduction elements. Figure 5 is a schematic representation of the finite element model.

The term in the fluid differential equation containing the spatial derivative of the fluid temperature is obtained by using a finite difference approximation that is implemented by a transfer function. This term is included in the differential equation by applying loads to appropriate nodes using a capability for nonlinear loads.

To model the successive strokes of the magnetic refrigerator, a series of NASTRAN runs is made, one for each stroke in the simulation. These NASTRAN runs are made in a loop in which an auxiliary program, developed by DTRC, is run after each NASTRAN analysis to prepare data for the next NASTRAN run and to print the initial and final temperatures for each stroke. To obtain the temperatures at the end of a stroke, the auxiliary program reads a file of nodal temperatures produced by NASTRAN. With this information, it computes the temperature drop or rise at each refrigerant node depending on whether the next stroke is an intake

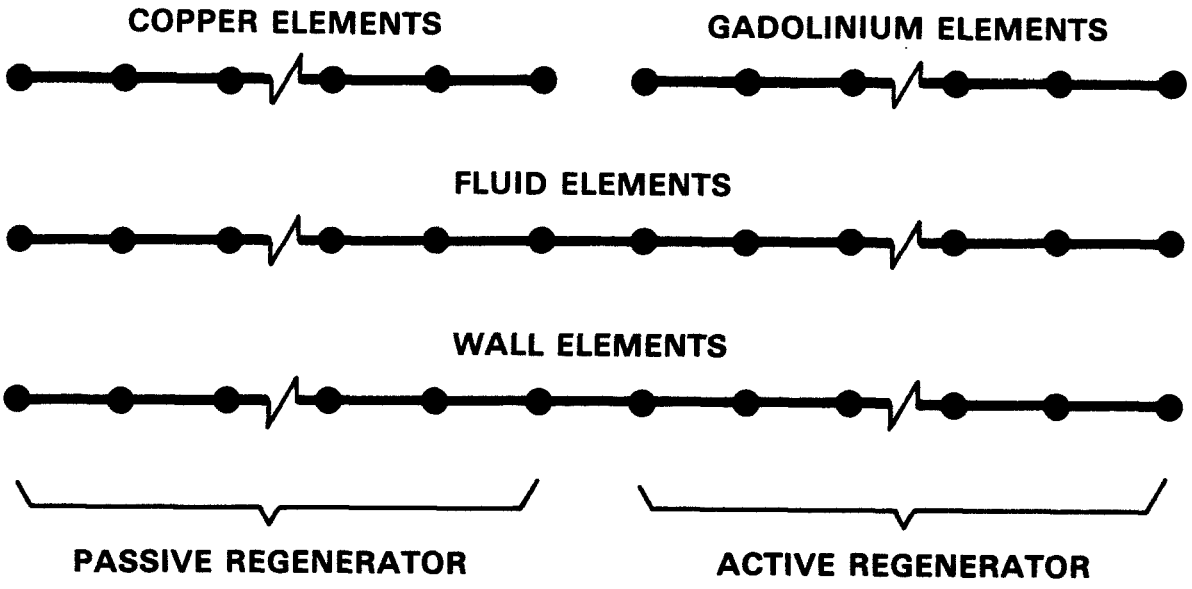

Fig. 5. The Finite Element Model

or exhaust stroke. The program then determines the initial temperature of each refrigerant, copper, fluid, and wall node for the next stroke. The program also computes the heat capacity for each refrigerant element, and the heat capacity and conductivity for the fluid elements. The time for the next stroke is determined by the temperature at the cold end of the active regenerator and is used to set the number of integration steps for the transient analysis.

The program prints the initial and final temperatures for each stroke; this output provides a temperature history of the simulation run. Finally, the program prepares a NASTRAN input file incorporating the new data for the next NASTRAN run.

RESULTS AND DISCUSSION

The measurements obtained from the experimental apparatus were compared to the performance of the computer model. Figure 6 indicates the cool-down characteristics of the cold portion of the active regenerator for various cycles. This comparison gives reasonably good agreement between the model and the measured temperature. However, the numerical model predicts a slightly lower cool-down rate between the 10th and 20th cycles than was measured in our experimental apparatus. No explanation for this variance is given at this

time. A plot of the temperature distribution of the four separate steps of the magnetic refrigeration cycle is shown in Figure 7. This comparison shows good agreement except for the magnetization and demagnetization of the magnetic material. This may be largely due to the experimental apparatus requiring 30 seconds to ramp the field up or down which may allow a significant amount of heat transfer. Where as, the computer model assumed an instantaneous change in the field resulting in no heat transfer. In addition, the thermocouples located at the ends of the active regenerator were sandwiched between the gadolinium ribbon and a series of copper screens. This may have caused a slight reduction in the measured adiabatic temperature change during the magnetization and demagnetization processes.

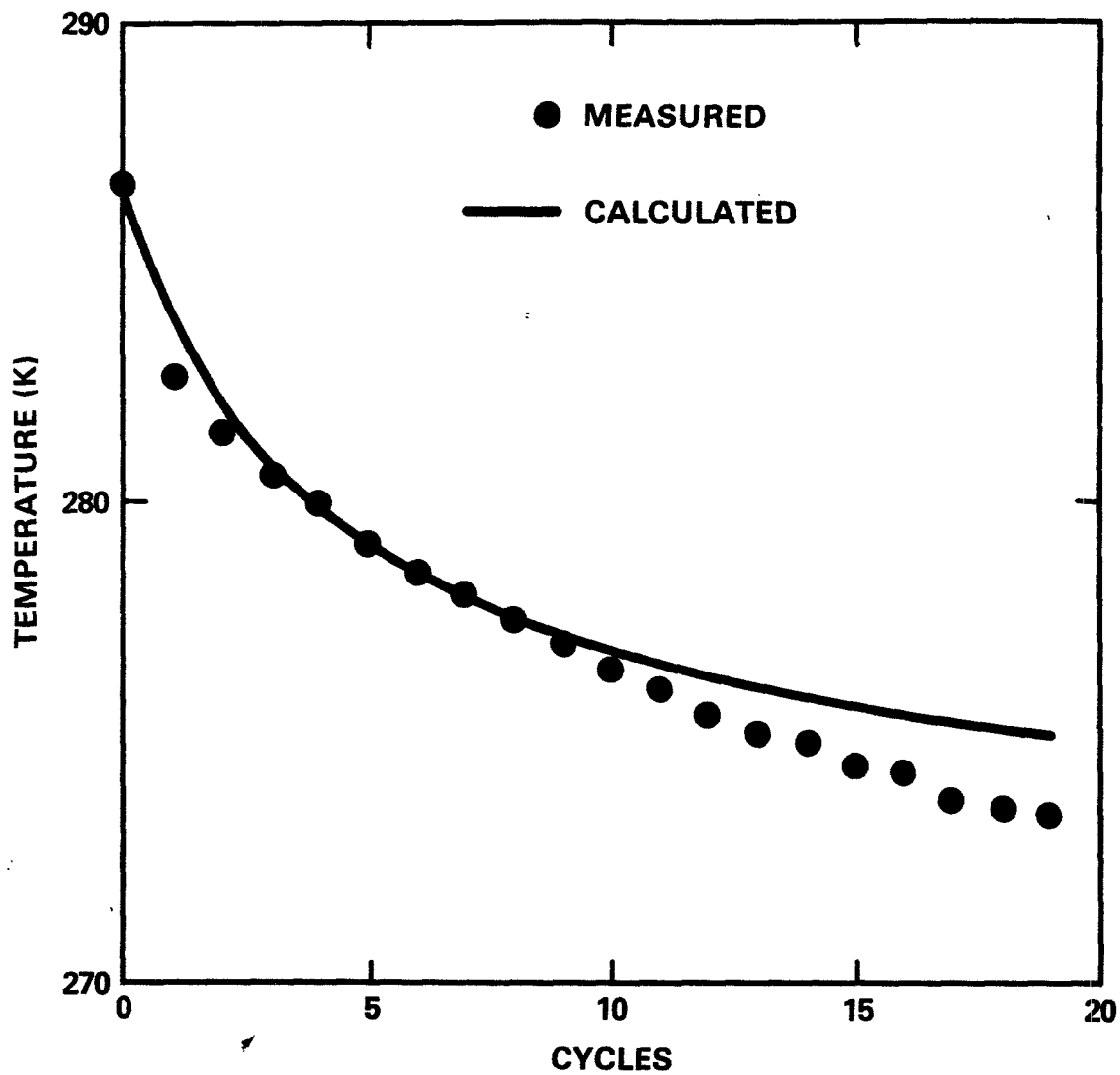

Fig. 6. Temperature Comparisons for 20 Cycles

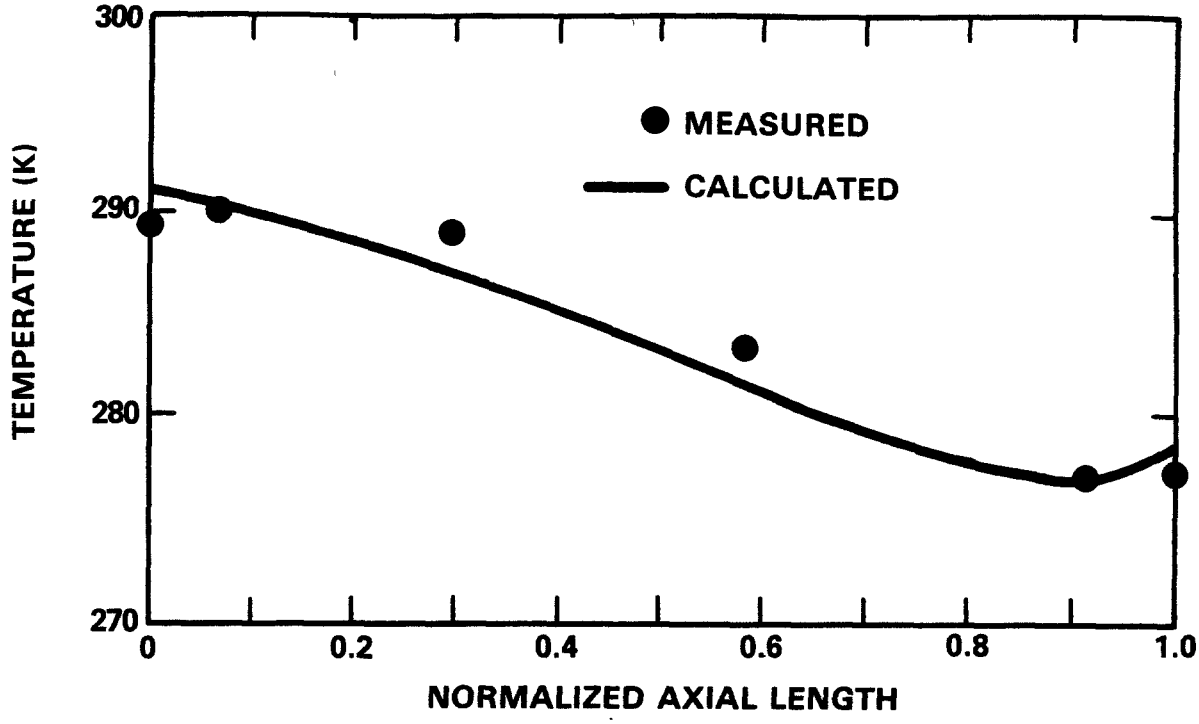

7a. Temperature Distribution of Active Regenerator Cycle, Start or End of Intake Stroke

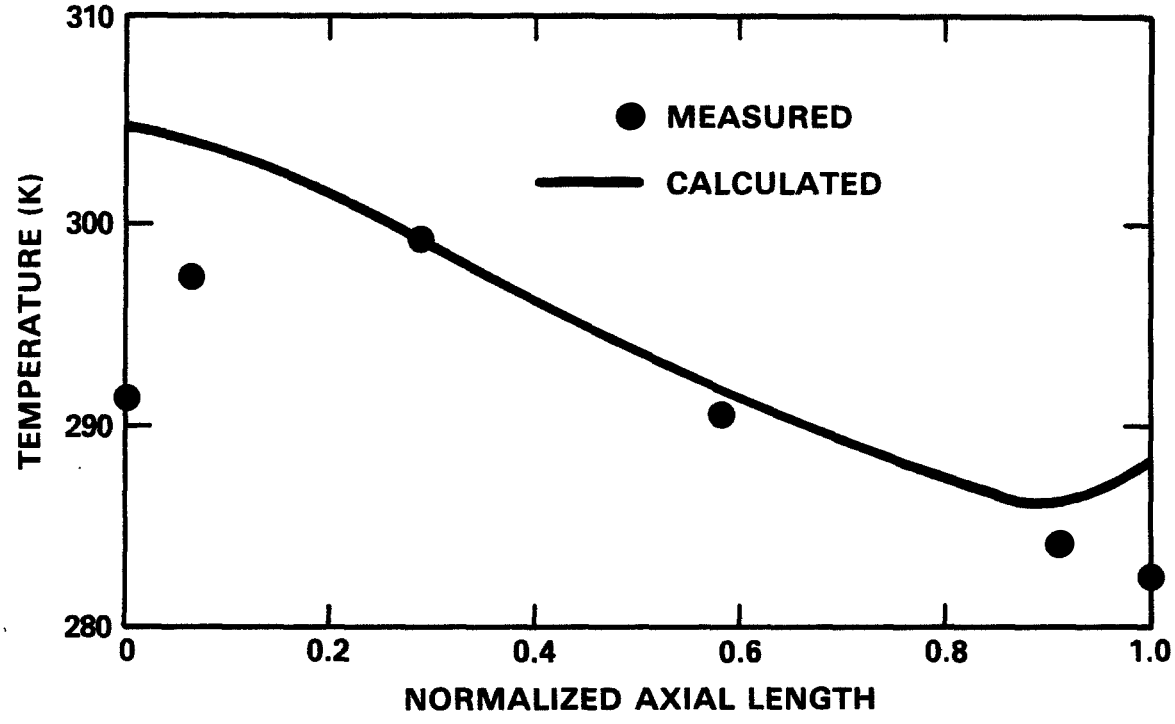

7b. Temperature Distribution of Active Regenerator, End of Magnet Charging Cycle

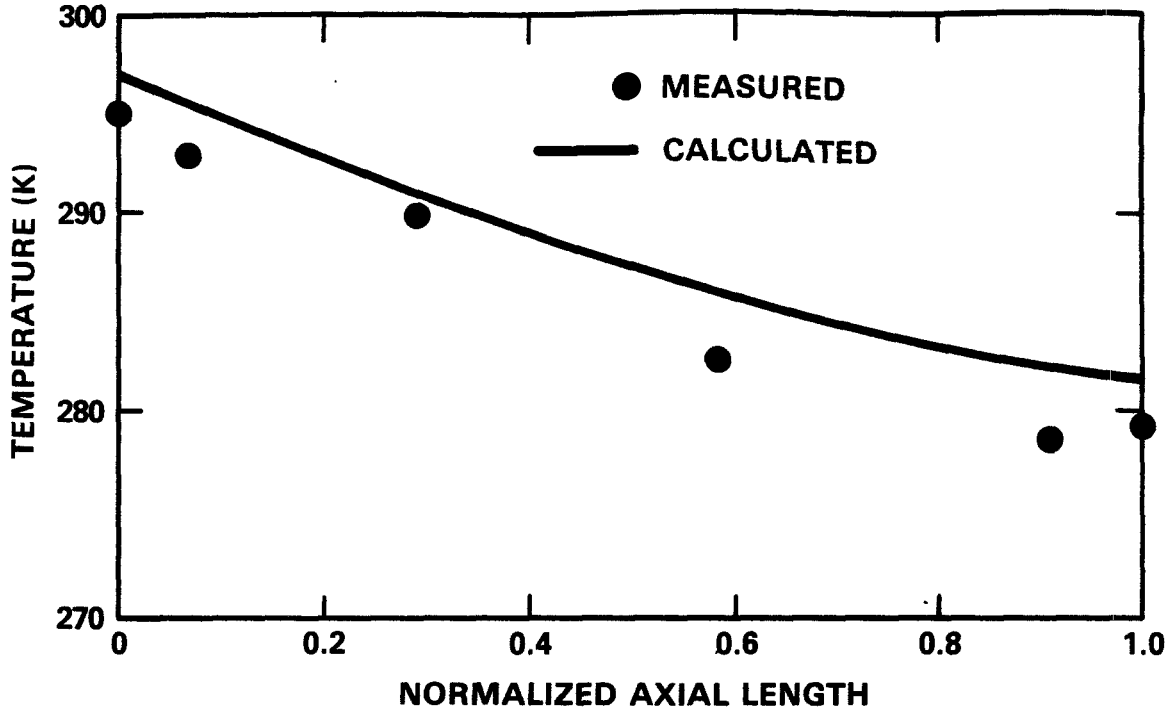

7c. Temperature Distribution of Active Regenerator, End of Exhaust Stroke

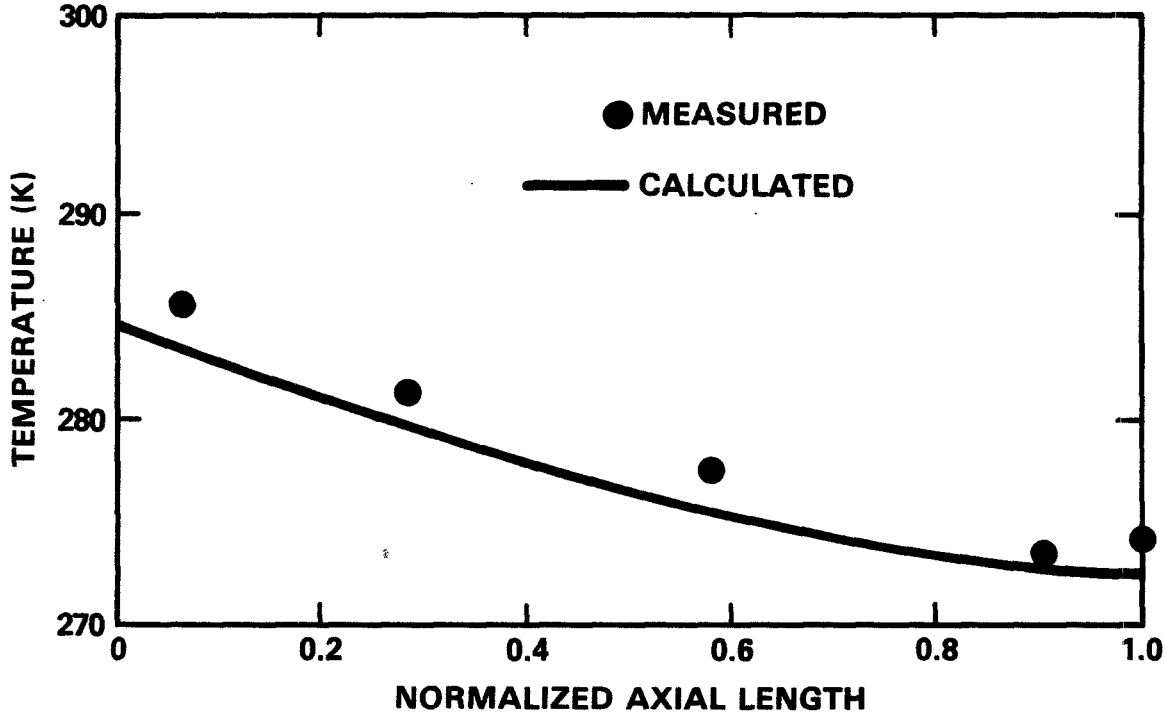

7d. Temperature Distribution of Active Regenerator, End of Magnet Discharging Cycle

An important parameter of some concern is the axial thermal conduction in the active and passive regenerators. This property of the ribbon regenerator configuration was not measured and a value was calculated based on an assumed contact area. However, the numerical model indicated that the magnetic refrigerator's performance was relatively insensitive to changes in this parameter. Thus, it was concluded that an error in estimating this parameter would not have an important effect on the results produced by the numerical model.

The effect of the ferromagnetic material being assigned a constant heat capacity over the temperature span encountered during one stroke needs to be examined. The differences in heat capacity are small, but not insignificant and it is not known how much this affects the results. Also, the small non-uniformity of the magnetic field profile was considered to be insignificant, however, this assumption needs to be examined in more detail. In fact, the sensitivity of the performance of the magnetic refrigerator to the values and profile of the magnetic field may be larger than anticipated.

Another parameter of critical importance is the mass flow of the working fluid. The heat capacity of the quantity of fluid that flows through the active regenerator must be properly matched to the heat gained or lost by the magnetic material during the magnetization and demagnetization processes. The sensitivity of the mass of fluid displaced to the performance must be evaluated.

In future work, the computer model will be used to evaluate the model's sensitivity to changes in several of these parameters. In addition, the refrigerator load characteristics will be evaluated for various temperatures. The model will also be used to predict the preformance characteristics for an active regenerator that may consist of several different ferromagnetic materials, each operating at progressively lower temperatures. Rare earth elements gadolinium, terbium, and dysprosium are three possible refrigerants; each has a temperature range at which it works most effectively. The largest temperature change with a change in magnetic field occurs near 293, 235, and 180 K for the three elements, respectively.

REFERENCES

1. Benford, S.M. and G.V. Brown, "T-S Diagram for Gadolinium Near the Curie Temperature," J. Appl. Phys., Vol 52 (1981).

2. Green, F.G., W.G. Patton, J. Stevens, and J. Humphrey, "Magnetocaloric Refrigeration,:" DTNSRDC Report 87/032 (1987).

REGENERATIVE MAGNETIC REFRIGERATION OVER THE TEMPERATURE RANGE OF 4.2 TO 15 K*

F.J. Cogswell, J.L. Smith, Jr., and Y. Iwasa

Cryogenics Engineering Laboratory, Massachusetts Institute of Technology
Cambridge, MA 02139

I. Introduction & Background

Magnetic Refrigeration

In a magnetic refrigerator, the working fluid is replaced by magnetic salts, and property swings are accomplished by magnetization. In theory magnetic refrigerators can perform more closely to the Carnot machine than the compressor-expansion systems. A few magnetic refrigerators have been built and tested.[1-5]

Thermally active regeneration has several advantages over other methods.[6,7] One advantage is that the active element remains stationary, and therefore the cold space need not contain any moving parts. Magnetization of the element is accomplished with a time-varying magnetic field. Because of recent advances in superconductor design, time-varying-field-induced losses can now be made acceptably small. Another advantage of active regeneration is that the regenerator core can be made to span a relatively large temperature range between the warm and cold reservoirs. This is because the individual segments in the core each cycles through a relatively small temperature range, while the total effect of all the segments is to cascade over a large temperature range. One potential disadvantage is that it may be difficult to directly control the temperature of a core region which is far from the core's inlet. Proper control of the thermodynamic cycles is therefore essential for the successful operation of a refrigerator based on thermally active regeneration.

Experimental System

Our experimental system is shown schematically in figure 1. The key components of this apparatus are the regenerator core, the displacer, the temperature control reservoirs, and the superconducting solenoids.

The GGG (gadolinium gallium garnet) is ideal as a core element for magnetic refrigerators operating over the temperature range of 4 to ~15 K. The core was designed to minimize the losses by axial conduction, fluid friction, irreversible heat transfer, and helium entrainment.[6]

The displacer forces supercritical helium (3 ~ 5 atm) through the core. As the core is magnetized the displacer moves down, pushing helium from the cold-end reservoir, up through the core, and out into the warm-end reservoir. As the core is demagnetized the displacer moves up, reversing the helium flow.[7].

* Sponsored by Sumitomo Heavy Industries.

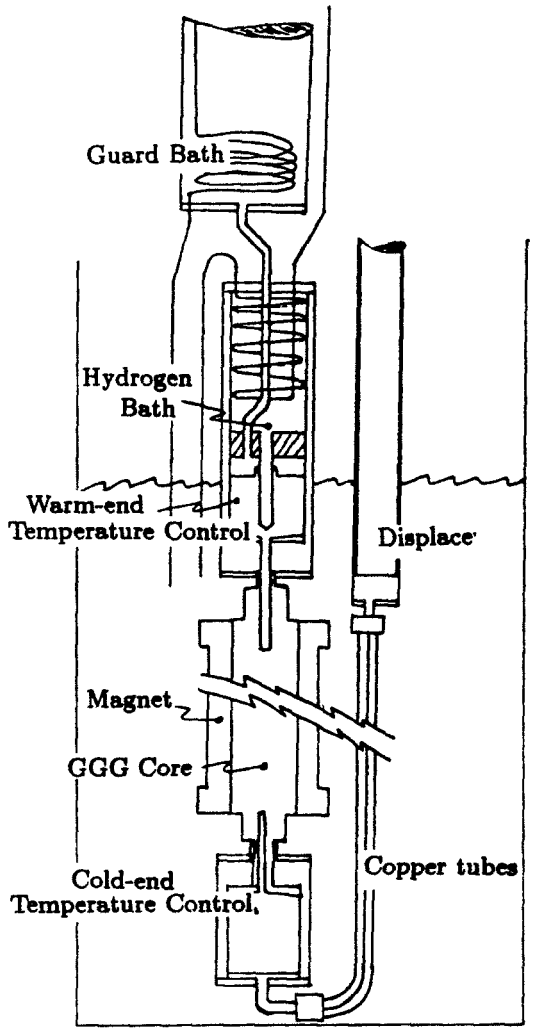

Fig. 1. Experimental System

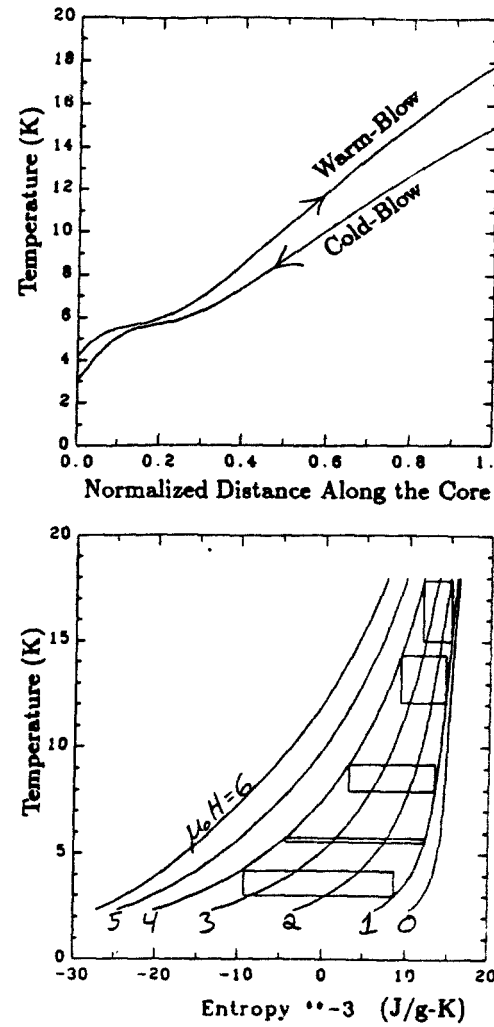

Fig. 2. Temperature Profiles and T–S Diagram for Ideal Carnot Device

The warm-end reservoir temperature is fixed by a hydrogen bath, while the cold-end reservoir temperature is fixed by electric heaters which match the refrigeration load. The temperature control modules control the temperature of the helium as it enters the core. They also measure the refrigeration and heat of rejection.[7]

The superconducting solenoids have been recently modified. The original system contained a single coil which produced a uniform 4-T magnetic field over the length of the core. A secondary coil has been added and its role will be discussed later in this paper.

Original Design Goal

The original analysis modeled the system as a series of "differential" Carnot refrigerators cascaded between the two reservoirs.[6] Each Carnot refrigerator at a given point in the core works between a different temperature range. There are four steps to a complete cycle.

1. An adiabatic magnetization raises the temperature profile of the core from the cold-blow profile to the warm-blow profile. No helium is displaced.
2. An isothermal warm-blow occurs as the magnetization continues while the proper amount of helium is forced to flow from the cold-end to the warm-end. The helium cools the core as the magnetic interaction heats it. The process is isothermal if these two effects match.
3. An adiabatic demagnetization lowers the temperature profile of the core from the warm-blow profile to the cold-blow profile.
4. An isothermal cold-blow occurs as the demagnetization continues with helium flow from the warm-end to the cold-end.

Even if Carnot cycles could be obtained within the core, the overall process still would not be reversible. Refrigeration is obtained when helium colder than 4.2 K enters the cold-end reservoir; thermal mixing also occurs in the warm-end reservoir as heat is rejected. Entropy is thus generated in both reservoirs.

Why Can't We Produce Carnot Cycles?

There are three reasons why Carnot cycles can never be realized by the original device: 1) system irreversibilities, 2) helium void and the breathing effect, and 3) improper field-flow phasing. The last one seems most crucial.

1. System Irreversibilities The primary cause of irreversibility within the core is nonzero heat transfer ΔT between the GGG and helium. This causes the helium temperature profile to deviate from the GGG temperature profile. The magnitude of the temperature deviation can be estimated as a function of the temperature gradient, the helium flow rate, and the type of path, i.e.: adiabatic, isothermal or in between.

2. Helium Void and the Breathing Effect Helium void within the core has two major effects. First it adds zero-field specific heat to the core, reducing the temperature swing available from a given adiabatic path. Second it gives rise to what we call the breathing effect. The density of supercritical helium varies significantly as it is heated over its critical point at 5.6 K. As the GGG is magnetized, the entrained helium is heated and it expands, thus expelling helium from the core. As the GGG is demagnetized, helium is pulled back in. The breathing effect prohibits true adiabatic paths.

3. Improper Field-Flow Phasing A field-flow mismatch results since the rate of magnetic interaction and the helium flow rate cannot be adequately matched over the length of the core to allow for an isothermal path. If it is matched at one end of the core then it will not be in general matched at the other end.

II. Preliminary Experimental Results

The device was tested several times in 1987 and 1988. No steady-state refrigeration was achieved over the temperature range of 4.2 to 15 K. The results did however match closely to that predicted by a computer simulation program which was developed during the testing program. This program is discussed in the next section.

III. Analysis

There are three types of analysis which have been performed for this project. The first analyzes an Ideal Carnot Device. Though the efficiency of a ideal device (irreversibilities generated only in the reservoirs) can be determined from simple thermodynamic relations, the refrigeration power can only be determined by properly matching the helium properties to the GGG properties. The maximum refrigeration power per mass of GGG is found as a function of cycle parameters. This value can then be used as a standard of comparison for our actual device.

The second analysis is done by computer simulation. The computer simulation program includes real properties of the core such as finite heat transfer coefficient and a helium void of about 5%, and more importantly it follows the same parameter dependence as the real system. In general, it is not possible to prescribe exactly what thermodynamic cycle each segment along the core will experience. As we vary the magnetic field and helium flow in order to control the temperature of one core region, we cannot control the other regions. The independent variables are rate of magnetic field change, $\dot{H}$, and rate of helium flow, $\dot{m}$. The steady-state temperature profiles cannot be directly prescribed. Note that though the helium flow rate is not the same throughout the core due to the breathing effect, it is not independently controlled as a function of position either.

The final method of analysis tries to explain cycle imperfections from a convection wave point of view. To do this it looks in detail into various limiting cases of the governing equation. With a more fundamental understanding of how steady state cycles develop we can determine a criterion for when refrigeration is possible.

Analysis of an Ideal Carnot Device

A model core with no irreversibilities and no helium entrainment (and therefore no breathing effect) was studied to see if it would be possible to obtain a series of Carnot refrigerators in this ideal limit. This method iteratively chose the isothermal cold-blow temperature profile and then constructed the resulting match between the helium and GGG thermodynamic properties. The iteration was successful when a match was found which used the available field swing of our superconducting magnet (1 to 4 T). It was found that:

- The field must be a function of both time and position if Carnot cycles are to be achieved. This result is true even in this ideal case.
- If the field could be prescribed as any arbitrary function of time and space, then refrigeration over the temperature range of 4.2 to 15 K should be easily achieved, even with the inclusion of irreversibilities in the core.

- This analysis does not predict the degree of perturbation from the ideal Carnot cycles that will result from our system, which applies the magnetic field uniformly over the core, and which has a helium void of about 5% within the core.

A temperature-entropy diagram of one successfully matched ideal-Carnot cycle is shown in figure 2. The corresponding temperature profile is also shown.

A Two-Stage Ideal Carnot System

In this part of the analysis we forced a match between 1) the net helium flow, and 2) the net heat flow between a two-stage ideal Carnot system. The lower stage refrigerates between 4.2 and 10 K, while the upper stage refrigerates between 10 and 15 K. We found that if both stages were optimized, then a two-stage match required that the upper stage use different cycle parameters than the lower stage. That is:

- In order to design a two-stage system with ideal Carnot stages, the upper stage must use more of the available field swing for the adiabatic part of the cycle.

Analysis by Computer Simulation

A computer simulation program was developed in order to help study the behavior of our refrigeration system. This program breaks the core into segments. For each segment and for each step in time it iteratively solves an energy balance. The helium is kept at constant pressure, and therefore in order to conserve helium mass, the flow rate must be adjusted from segment to segment. This inclusion of the breathing effect is necessary in order to properly model our system.

Once the program has reached a cyclic steady-state, information is recorded. Some of the graphs produced by this program include:

1. Temperature profiles at any pre-selected field increments. Approximately 20 profiles may be plotted on four different graphs for one complete cycle.
2. Selected segments plotted on a T-S diagram of the GGG.
3. The net enthalpy flux along the core over a complete cycle, calculated at each segment boundary, is plotted as a function of position along the core. Enthalpy flow is taken to be positive if the mass flow is from the cold-end to the warm-end, and negative for reverse flow. The derivative of this graph is the net work into the corresponding segment. The value of this graph at the cold-end is the refrigeration, and the value at the warm-end is the heat of rejection.
4. The net entropy flux along the core over a complete cycle is also plotted. It is defined in the same way as the enthalpy flux in item 3. The derivative of this graph is the net irreversibility generated by the corresponding segment. Steep sections in this curve represent inefficient regions in the core. In a good overall cycle the percent increase in this curve will be small.
5. The net entropy flux at several selected segment boundaries, recorded at each time step of the cycle, is plotted against the corresponding temperature of the upstream segment. This curve shows in detail what went into making the graphs described in item 4. It also helps show why a segment is inefficient.

The computer program was run for many cycle parameters. The results can be

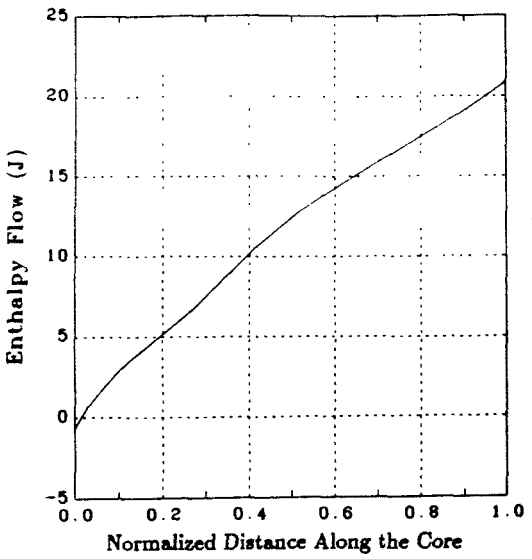

Fig. 3a.

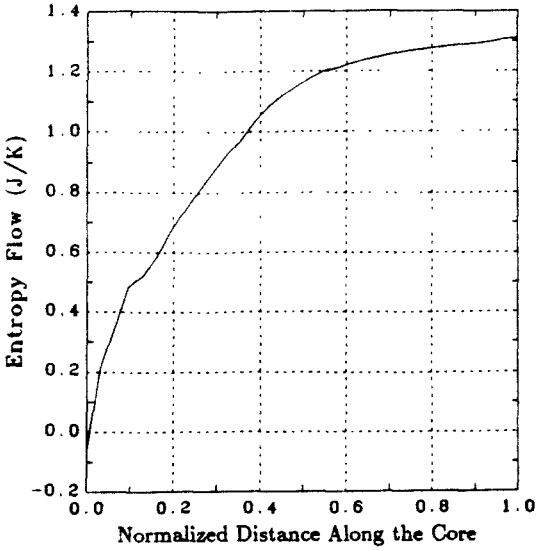

Fig. 3b.

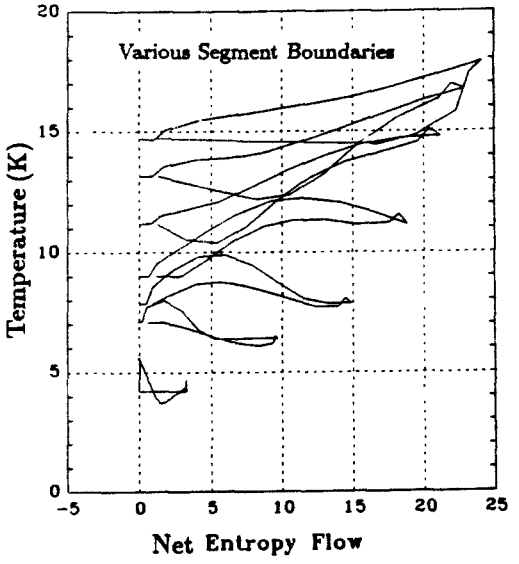

Fig. 3c.

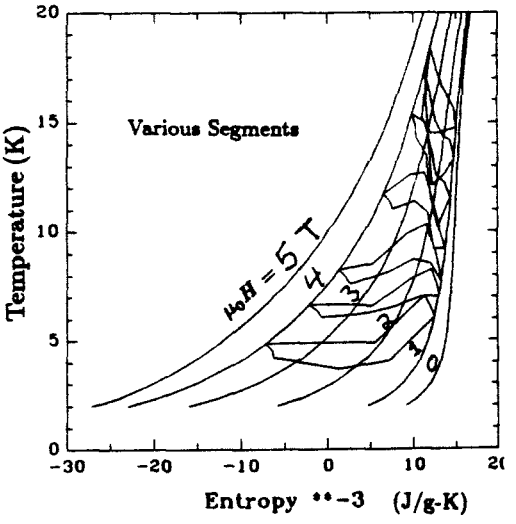

Fig. 3d.

Fig. 3a-d. Computer Simulation Output.

summarized as:

- Net refrigeration is not achieved for any cycle parameters when the temperature range was 4.2 to 15 K.
- The cold-end seems to be insensitive to variations in cycle parameters.
- The warm-end responds to variations in cycle parameters.
- For smaller temperature ranges of 4.2 to 10 K, and 10 to 15 K, refrigeration is achieved, and the efficiency is optimized.

Some of the graphs produced by the program for operation over the temperature range of 4.2 to 15 K are shown in figure 3. From these graphs we can see that the cold-end is not being cycled as a refrigerator, that figure 3-c shows a cross-over on the temperature-entropy curve which cancels refrigeration. Most of the irreversibility is generated in the cold-end. It seemed that there should be a way to modify the thermodynamic cycle in such a way to help the cold-end (perhaps at the expense of the warm-end) to even out the irreversibilities and produce refrigeration. All attempts to do this failed.

Data from our computer simulation program matched the test data well. We knew that the breathing effect and improper field-flow phasings were causing a bad thermodynamic cycle to develop, but we still did not have a method for correcting the problem.

Computer Simulation: A Two-Stage System

As in the previous two-stage Ideal Carnot system, we also forced the net helium flow and the net heat flow to match between the two computer simulated stages, and again we found that:

- If we are to match the helium flow and the heat flow of a two-stage system, then the upper stage must use more of the available field swing for the adiabatic part of the cycle than the lower stage.

Computer Simulation: Single-Stage, Two Independent Solenoids

After looking at the above analysis, and noting some of the problems with our device, we found that simple field modifications could remove most of the short comings. When the computer simulation program was tested with two independent fields over a single core, it was found that refrigeration could be produced. The field profile of one such computer run is shown in figure 4.

Analysis of the Governing Equation in Various Limits

The above analysis produced a solution to our cycle selection problem, but it left unanswered some basic questions:

1. Is it possible to obtain proper thermodynamic cycles with a single solenoid, if so how should the field profile be shaped?
2. Can other non-Carnot-type cycles be used with equal or better success? After all, a regenerator can store heat reversibly at any temperature, and in so doing allows for other reversible thermodynamic cycles.

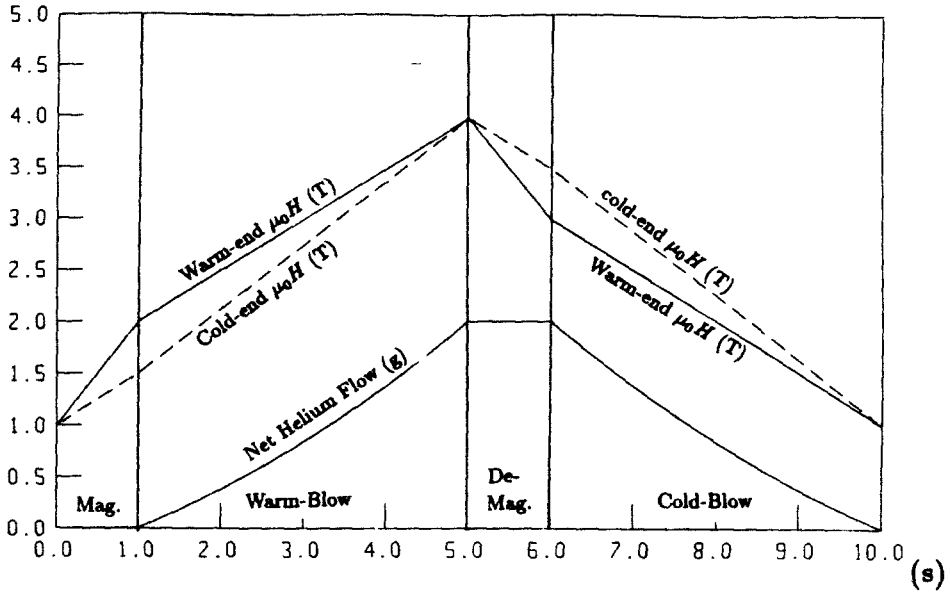

Fig. 4. Cycle Parameters Predicted to Produce Refrigeration

3. Smaller temperature ranges can accommodate improper field-flow phasing without significant loss of refrigeration . What is the largest temperature range which can be successfully refrigerated over for a single solenoid device?

In order to better understand some of the phenomena involved in active regeneration, we have analysed the basic governing equation for our device in its various limiting cases. These cases include: 1) the isothermal limit, 2) the adiabatic limit, and 3) step-wise-constant-parameter convection wave solutions. One of the key parameters of active regeneration comes from the isothermal limit. In this limit the temperature of the core is governed by:

$$\frac{dT}{dx} = \frac{(1-por)\,A\,\rho_g}{c_p}\left(-T\frac{\partial S_g}{\partial H}\Big|_T\right)\frac{\dot{H}}{\dot{m}} \quad \text{(K/m)}$$

where por is the helium void fraction, A is the core cross section, ρ_g is the GGG density, and c_p is the helium specific heat. It is important to note that the independent parameters appear as the ratio $(\dot{H}/\dot{m})$, where $\dot{H}$ is the rate of change of the applied magnetic field, and $\dot{m}$ is the helium mass flow rate. For a given field, H, and a given temperature profile within the core, there is a value of $(\dot{H}/\dot{m})$ which will allow for a solution to the above equation and therefore for a locally isothermal region in the core.

When the above equation is not satisfied, isothermal imbalances result and other terms must be included in the governing equation. The details of this analysis are not presented here. Some of the main results are:

- Deviations from the Carnot-type thermodynamic cycle will result in excess helium

flow on the cold-blow, which will in turn cause thermal pollution of the cold-end reservoir and a loss of net refrigeration. The Carnot-type cycle is best.

- Larger temperature ranges allow for less total helium flow. Less total helium flow results in greater accumulation of isothermal imbalances.
- When the temperature range is low, the helium flow rate may be great enough to allow the convection wave to travel the length of the core during a flow process. When this happens, isothermal imbalances may be pushed out of the end of the core and need not accumulate.
- The proper adiabatic path must both raise (or lower) the temperature profile, and adjust its gradient. The average temperature gradient must be steeper during the warm-blow, and less steep during the cold-blow.
- The breathing effect causes unwanted flow during the "adiabatic" processes. The net effect of an adiabatic magnetization with our device is to raise the temperature of the core fairly uniformly.

From the above results two conclusions can be made on oor device.

1. Since the convection wave will not travel the length of the core during a process which spans the temperature range of 4.2 to 15 K, we must therefore have proper spatial control of the ratio $(\dot{H}/\dot{m})$.
2. We cannot obtain proper adiabatic paths with a single uniform magnetic field. We do not have proper spatial control of $(\dot{H}/\dot{m})$.

These problems could be solved by two different methods. Either we can cover the desired temperature range in two stages, each stage satisfying the small temperature range criteria, and therefore not requiring proper control of $(\dot{H}/\dot{m})$, or we can modify our present device to obtain better field-flow phasing. We decided to gain better control of $(\dot{H}/\dot{m})$ by modifying our magnetic field system.

A parallel project has been underway in France.[8] This project has used the same basic system designs as appeared in our earlier papers. Being a second generation device, certain improvements have been made to help obtain better field-flow phasing, but a single solenoid is used. Data from this device still indicates difficulty in controlling the thermodynamic cycle. The basic behavior predicted by our computer simulation program holds true for the French device.

IV. Modification to Our Device

Figure 4 shows the magnetic field as a function of time for both the (upper) warm-half and the (lower) cold-half of the core. This pattern was found by the computer simulation program to produce refrigeration over the 4.2 to 15 K range consistent with the device limitations. Note that the greatest difference between the two fields at any given time is only 0.5 T.

A perturbation (secondary) coil is wound over the length of the core, with the (upper) warm-half windings in the same direction as the primary coil, and the (lower) cold-half windings in the opposite direction. This coil, driven by its own supply separate from the one for the main coil, adds 0.25 T to the warm-half while it subtracts 0.25 T from the cold-half. It is controlled by the same computer program which controls the

primary current and the displacer position.

VI. Conclusions

One major cycle parameter is the percent of the available field swing used for the "adiabatic" paths. As the adiabatic percent is increased from zero, more heat is pumped, and the cycle efficiency is reduced. The GGG and helium properties are such that a field-flow mismatch occurs between the cold-half and the warm-half of the core. In order for the warm-half to pass the proper amount of heat out to the warm-end reservoir, it must have a larger adiabatic percent than the cold-half. If a single coil is used, then the adiabatic percent is the same everywhere; heat will "pile up" within the core.

As the overall temperature span becomes smaller, the field-flow phasing becomes less critical. One reason for this is that the increased helium flow rate associated with a smaller temperature range may allow the convection wave associated with the isothermal perturbations to travel the core's length during a single cycle path. When this happens, past cycle imperfections are pushed out of the core.

References

1. J.R. Van Geuns, "A Study of a New Magnetic Refrigerating Cycle," *Philips Res. Rept. Suppl.* **6**, (1966).
2. A.F. Lacaze, R. Béranger, G. Bon Mardion, G. Claudet, and A.A. Lacaze, "Efficiency improvements of a double acting reciprocating magnetic refrigerator," *Cryogenics*, **23**:427–436, (1983).
3. J.A. Barclay, W.F. Stewart, W.C. Overton, R.J. Candler, and O.D. Harkleroad, "Experimental results on a low-temperature magnetic refrigerator," *Advances in Cryogenic Engineering*, **31**:743–752, (1985).
4. H. Nakagome, T. Kuriyama, H. Ogiwara, T. Fujita, T. Yazawa, and T. Hashimoto, "Reciprocating magnetic refrigerator for helium liquefaction," *Advances in Cryogenic Engineering*, **31**:753–762, (1985).
5. Y. Hakuraku and H. Ogata,"Thermodynamic analysis of a magnetic refrigerator with static heat switches," *Crogenics*, **26**, (1986).
6. C.P. Taussig, G.R. Gallagher, J.L. Smith, Jr., and Y. Iwasa, "Magnetic Refrigeration Based on Magnetically Active Regeneration," *Proc. of the Fourth International Cryocoolers Conference,"* 79–88, (1986).
7. F.J. Cogswell, Y. Iwasa, J.L. Smith, "A Regenerative Magnetic Refrigerator Operating Between Liquid Helium and Liquid Hydrogen Reservoirs," *IEEE Transactions on Magnetics*, **24**:1011–1014, (1988).
8. P. Seyfert, P. Brédy, G. Claudet, "Construction and testing of a magnetic refrigeration device for the temperature range of 5 to 15 K," *Presented at ICEC12*, South Hampton, July 12-15, (1988).

SESSION III

PULSE TUBE REFRIGERATORS

CHAIRPERSON: R. LONGSWORTH
VICE CHAIRPERSON: P. KITTEL

CONCEPTS FOR THERMOACOUSTIC REFRIGERATION AND A PRACTICAL DEVICE

Thomas J. Hofler

ONT/ASEE Postdoctoral Fellow
Naval Postgraduate School, Monterey, California 93943

A brief overview of the principals of thermoacoustic refrigeration is given, in the context of a comparison to Stirling cycle coolers and pulse tube coolers. A practical cooling engine is described which is an electrically driven cooler having one moving part (at room temperature) and no sliding seals. Some experimental results and a comparison to a thermoacoustic theory are presented. Also, monatomic gas mixtures having low Prandtl number will be discussed. These mixtures improve the experimental efficiency of our refrigerator which can also be seen from a qualitative examination of the theory. Thermoacoustic refrigerators offer potential advantages for high-reliability and low vibration which make it well suited for applications in space.

INTRODUCTION

This work began at Los Alamos National Laboratory with G. W. Swift and J. C. Wheatley and was motivated by an article by P. H. Ceperley,[1] which suggested some acoustic variations of the Stirling cycle engine, and an article by Gifford and Longsworth[2] which discussed a new class of heat pumping engine known as the pulse tube. Later at Los Alamos, the thermoacoustic theory of N. Rott and coworkers[3-5] was discovered and incorporated in to our research. Rott is responsible for using the term "thermoacoustic" in the restricted sense of acoustic heat engine effects, and we use this term since the Rott theory is the best available at this time. References 6-9 are a selected overview of the Los Alamos work. Part of this work has moved to the Naval Postgraduate School with collaboration from Steve Garrett, Anthony Atchley, and Steve Baker.

I. SOME THERMOACOUSTIC CONCEPTS

A. The Stirling Refrigerator

The following discussion revolves around what happens in a stack of parallel plates (having adjacent plates spaced apart by a uniform amount) when placed in a gas having an oscillatory pressure and velocity. Although other geometries are possible, this geometry is suitable for thermoacoustic engines (where it is usually referred to as the "stack") as well as Stirling engine regenerators. The main purpose of this discussion is to make a distinction between the function of a regenerator in a Stirling engine refrigerator and the "stack" of a thermoacoustic refrigerator, and to indicate the roles these two heat transport mechanisms play in pulse tube operation. A highly simplified schematic of a Stirling cycle refrigerator is shown in Fig. 1.

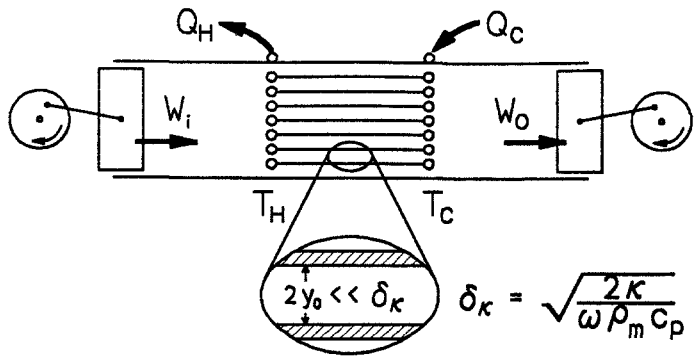

FIG. 1. A simplified schematic of a Stirling cycle refrigerator.

The regenerator is shown in the center of the tube in Fig. 1. The separation between these regenerator plates is much less than δ_κ, the thermal penetration depth as defined in the figure, where κ is the thermal conductivity, ρ_m is the mean density, and c_p is the specific heat at constant pressure. Roughly, δ_κ is the distance heat can diffuse through the gas during one cycle. Thus temperature gradients can only occur in the x direction along the plates and the gas is isothermal in the y direction transverse to the plates. The oscillatory component of the gas temperature T_1 at any point in the regenerator is approximately zero. The 1 subscript denotes a quantity as first order in a small amplitude expansion (eg. $T=T_m+T_1+T_2+\cdots$). The other major feature of a Stirling refrigerator is the nature of the work flow in the gas. The local work flux is given by the time averaged product of pressure p_1 and velocity u_1. Typically, there is an input work flow W_i that is supplied to the regenerator and an output work flow W_o which is removed from the system. W_o is a substantial fraction of W_i so $|W(x)| >> 0$, and there is a substantial in-phase component between the pressure and velocity at any point in the regenerator. To use acoustics jargon, we would say that there is a substantial travelling wave component in the regenerator.

If we make certain approximations (ie. ideal gas, small amplitude, and no thermal conductivity in the x direction), then a simple expression for the total enthalpy flow H_2 can be obtained,[4,10]

$$H_2 = \Pi \rho_m c_p \int_0^{y_o} T_1 u_1 dy = W_2 + Q_2 \approx 0, \qquad (1)$$

where Π is the total plate perimeter of a cross section through the plates and y_o is half the plate separation. The 2 subscript denotes quantities that are accurate to second order in the small amplitude. So, the enthalpy flow, which is the sum of the work flow W_2 and heat flow Q_2, is approximately zero because $T_1 \approx 0$. The result is that there is a heat flow Q_2 that is equal and opposite in direction to the substantial work flow W_2 discussed above.

B. The Thermoacoustic Refrigerator

A simple schematic of a thermoacoustic refrigerator is shown in Fig. 2, where an acoustic driver is exciting a quarter wavelength standing wave in a gas filled tube containing a "stack" placed near the closed end of the tube.

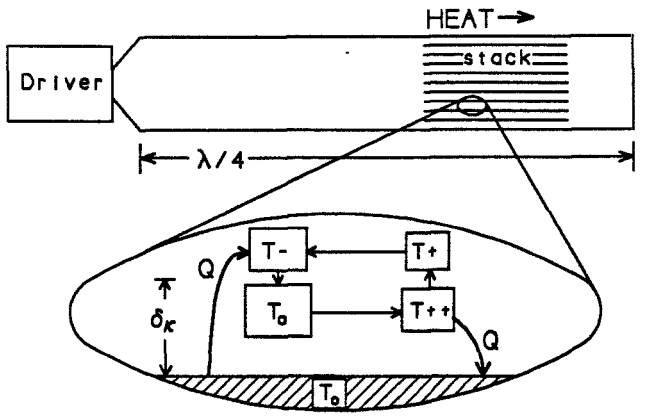

FIG. 2. Schematic of a thermoacoustic refrigerator.

Note that the resonance condition of a quarter wavelength is not essential, but it is a means of obtaining high pressure amplitudes with minimal mechanical demands on the driver. The plates in the stack are typically spaced a few thermal penetration depths δ_κ apart and we assume that initially the plates have a uniform temperature distribution. A magnified view of the gas near a plate shows a gas parcel oscillating back and forth above the plate and conducting heat to and from the plate, through a layer of gas about δ_κ thick. (The vertical displacement of the parcel in the figure is used for graphical simplicity and does not physically occur in this simple model. A detailed discussion of the thermodynamic cycle for this parcel will not be given, and can be found elsewhere.[11]) This layer of gas, called the thermal boundary layer, represents a thermal impedance and conducting heat through it takes a finite amount of time. This results in a time phase lag between the pressure p_1 and the temperature T_1.

Another way of looking at this is to realize that gas parcels located half between adjacent plates are undergoing nearly adiabatic compressions (with correspondingly large T_1 temperature variations) and that parcels located very close to the plates are undergoing nearly isothermal compressions (with correspondingly small T_1). Not only is there a great deal of temperature stratification in the transverse direction, but there is also a large variation in the phase of the local temperature relative to the pressure. This is in contrast to a Stirling regenerator where $T_1 \approx 0$.

The other major physical difference between a regenerator and a thermoacoustic "stack" is that p_1 and u_1 are very nearly in quadrature, since the "stack" is in a standing wave having a moderately high quality factor and $W_2 \approx 0$. This results in a substantial component of T_1 that is in-phase with u_1. Going back to the integral of Eq. 1 for local enthalpy flow, we can see that $|H_2| \gg 0$, thus $|Q_2| \gg 0$. The direction of Q_2 is always towards the nearest pressure antinode (ie. local maximum) of the standing wave which, in Fig. 2, is located at the closed end of the tube.

C. The Orifice Pulse Tube Refrigerator

The article "Surface Heat Pumping" by Gifford and Longsworth[2] describes the original pulse tube refrigerator. The title of the article is the term the authors coined for the heat transport effect occurring in the pulse tube. Their qualitative description of this effect was entirely correct and this effect is equivalent to the thermoacoustic heat transport discussed in the previous section. Much later, a significant improvement to this engine was discovered by Mikulin et. al.[12], which was called the orifice pulse tube refrigerator. Today, some of the most highly developed orifice pulse tubes are made by Radebaugh and coworkers,[13,14] and Fig. 3 is due to Radebaugh. The purpose of this section is to indicate the role thermoacoustic heat transport has in the operation of practical pulse tube engines and discuss other possible mechanisms at work in these engines.

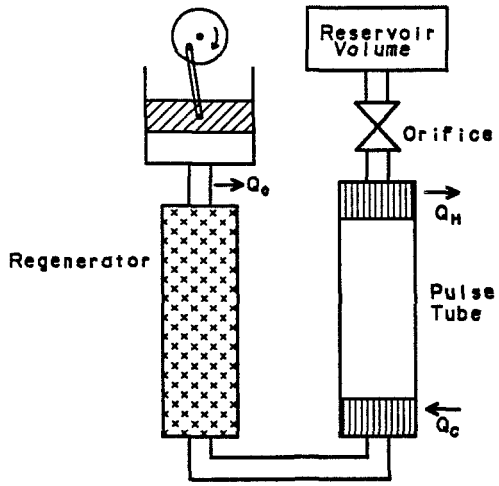

FIG. 3. Schematic of an orifice pulse tube refrigerator.

The original pulse tube is the same device as the orifice pulse tube shown above except that the orifice is closed, which we will assume at the start. The pulse tube portion is typically an empty tube having a diameter that is several times larger than δ_κ. The empty tube then transports heat in a manner similar to the "stack" of Sec. B. The physics is the same, but some of the practical details are different. In the pulse tube the frequencies are much lower, δ_κ is much larger, and the pressure amplitudes are much greater than in a thermoacoustic refrigerator. The function of the regenerator of Fig. 3 is somewhat less clear.

One of the problems of the device of Fig. 2 and of a pulse tube driven without a regenerator is that the ambient temperature driver or compressor conducts heat to the cold end of the "stack" or pulse tube. A brief review of the pulse tube literature gives no explanation for the existence of the regenerator and the reader is left to assume that its function is to passively isolate the warm compressor from the cold pulse tube. This would be entirely true if the pulse tube adsorbed no work and the pressure and velocity time phase were in exact quadrature. However, the pulse tube and its heat exchangers do adsorb some small amount of work $\dot{W}$, and this work must flow through the regenerator from the compressor. From the discussion of Sec. A, we know that the regenerator must transport some heat in the

direction opposite to the work flow. So, the basic pulse tube refrigerator is perhaps a hybrid engine with a thermoacoustic part and a Stirling cycle part.

The main function of the orifice and reservoir is to dissipate work by allowing the gas to flow through the flow-resistance of the orifice. Increasing the work flow (or traveling wave component) through the pulse tube portion has little effect on the thermoacoustic heat transport in the tube. Wheatley has shown[15] that the heat transport due to a pure traveling wave in such a case is about an order of magnitude less than the heat transport for a pure standing wave, and that the two transport effects are *opposite* in direction. The added work dissipation must also flow through the regenerator from the compressor and this causes a great deal of heat to be pumped by the regenerator. Thus, the orifice pulse tube engine may operate primarily as a Stirling refrigerator, with the pulse tube portion serving as a means to thermally isolate the heat generating orifice from the cold end of the regenerator.

II. AN EXPERIMENTAL THERMOACOUSTIC REFRIGERATOR

A. The Apparatus

The thermoacoustic refrigerator design and measurements discussed in this section were motivated by a desire to measure the intrinsic thermodynamic efficiency of the heat transport that occurs in the "stack" and separate this from any other system inefficiencies or parasitic losses. This goal has been successfully achieved with an experimental apparatus that is a fully functional refrigerator and a nearly practical device, shown in Fig. 4.

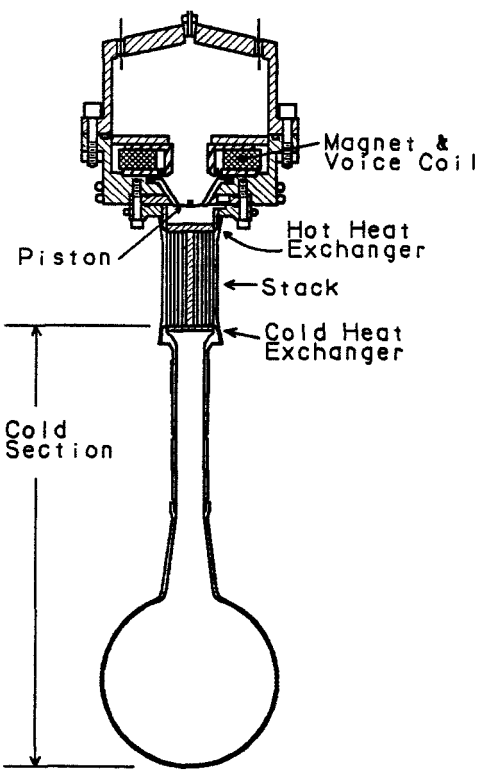

FIG. 4. Cross section of an experimental thermoacoustic refrigerator.

The overall quarter wavelength resonator geometry shown in Fig. 2 is used here as well, with a few modifications. Since moderately high Q standing waves are used in these systems, it does not matter where the acoustic driver is located in the system. The large volume-displacement driver of Fig. 2 is located at the velocity antinode of the standing wave and the small volume-displacement driver piston of Fig. 4 is located at the pressure antinode of the standing wave. This allows the cold end of the system to be isolated from the driver, and a regenerator is not required. The spherical volume at the bottom simulates an open end to the tube, and the overall length of the system is 60 cm.

The driver is a permanent magnet linear motor having one moving part and no sliding seals. The piston assembly has a 2 in. diameter at the voice-coil and a 1 in. diameter where it mates to the resonator via a flexible plastic seal, and has a total moving mass of 5 g. A capillary leak eliminates any static pressure differences across the flexible seal. A subminiature accelerometer mounted on the piston, and a pressure transducer installed in the resonator near the piston, allow accurate measurement of the acoustic power delivered to the resonator irrespective of driver inefficiencies.[16] These transducers also allow the drive frequency to be dynamically controlled to maintain resonance.

The maximum driver amplitude is usually determined by the limits of the flexible plastic seal and the following are measured levels associated with a functional maximum drive amplitude which has been sustained for months of operation without repair. The peak-to-peak piston displacement is 760 microns with a swept volume of 0.45 cm^3 and a dynamic pressure ratio of p(max)/p(min) = 1.06. The acoustic power delivered to the resonator is typically 10 watts for He.

The resonator contains hot and cold heat exchangers which butt up against a "stack" and He gas (or gas mixtures) at 10 bar absolute pressure. The resonant frequency varies from a maximum of 650 Hz with He gas to a minimum frequency of 250 Hz with He-Xe mixtures. An electrical resistance heater provides a heat load near the cold heat exchanger. The resonator vessel is constructed of heavy gauge copper except in the stack region where the tube is fiberglass. The "stack" is a spiral roll of plastic film and spacers that is 3 in. long and has a 1.5 in. diameter with 70 layers across a diameter. The heat exchangers consist of 50 parallel copper strips. The resonator is thermally insulated by a vacuum space and either a temperature controlled radiation shield or superinsulation. The cool down time is slow because of the large heat capacity of the resonator and all of the measurements are taken in steady state.

This refrigerator design has potential advantages for high reliability and low vibration applications and we at NPS are currently fabricating a new version that will be flown as a space shuttle GAS experiment (NASA G-337). We hope to demonstrate the feasibility of using this refrigerator for space applications.

B. Experimental Results

The coldest temperature achieved to date with the above refrigerator is 193 K with an ambient temperature of 293 K. The experiment can be run with a known electric heat load, the acoustic power delivered to the resonator can be measured, and the temperatures measured in steady state. Various small parasitic loads and losses can be measured and included in the analysis. These effects include an external heat leak, cold resonator losses, and heat exchanger losses. These data can then be analyzed to

determine the thermoacoustic efficiencies intrinsic to the "stack". Some of these results are shown in Fig. 5 and Fig. 6, along with comparisons to the theory of N. Rott.[17]

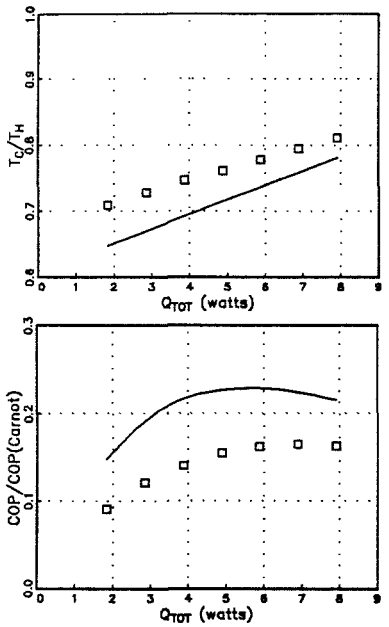

FIG. 5. A comparison of experimental data and theory, for He gas and a pressure ratio of 1.06. The upper plot is temperature ratio vs. heat load and the lower is relative COP vs. heat load. Solid curves represent the theory.

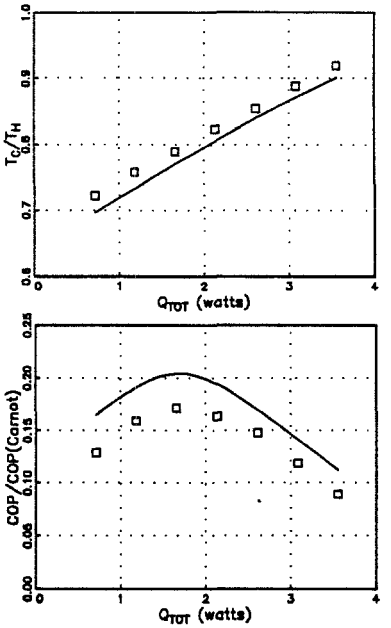

FIG. 6. A comparison of experimental data and theory, for a pressure ratio of 1.03.

These results show temperature ratio T_{COLD}/T_{HOT} and relative coefficient of performance COPR=COP/COP(Carnot) versus Q_{TOT}, the heat load *external* to the "stack". Figure 5 indicates a substantial cooling power of 7 watts at maximum COPR with a moderately large discrepancy between experiment and theory, and Fig. 6 indicates much better agreement with theory at a reduced power level. The smallest heat load data point on these plots represents zero electric heat load and its value is an indication of the relative size of the parasitic load.

III. MONATOMIC GAS MIXTURES

The Prandtl number σ of a fluid is a dimensionless quantity given by the ratio of kinematic viscosity ν to thermal diffusivity χ and is equal to 2/3 for noble gases. Prandtl number can also be thought of as the amount of momentum diffusion relative to thermal diffusion. This is an important quantity in any heat engine where viscous scrubbing losses are significant. In thermoacoustic engines it also affects the basic transport mechanism where the details of gas motion, thermal conduction, and phasing near a solid surface are important.

While the Prandtl number for most gases is roughly unity and does not vary much, the Prandtl number for liquid metals, such as mercury and sodium, can be orders of magnitude smaller. The reason for this is that the momentum diffusion for a liquid metal is dominated by the massive metal atoms and the thermal diffusion is dominated the mobile, low-mass electrons. This effect can also be seen, to a

lesser extent, in gases where a light gas is mixed with a heavy gas. The Prandtl number can be calculated as a function of mixture concentration using kinetic gas theory[18] and some results are shown in Fig. 7.

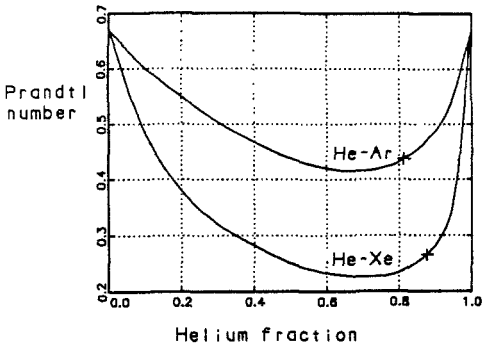

FIG. 7. Theoretical dependence of Prandtl number on He concentration, for He-Ar and He-Xe gas mixtures.

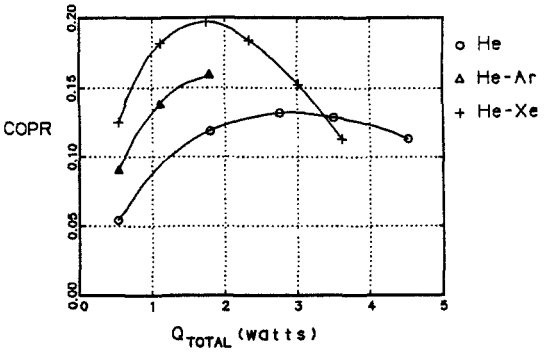

FIG. 8. Comparing experimental COPR for three different gases.

We also hope to measure these variations in Prandtl number by means of acoustic quality factor measurements in a double Helmholtz resonator. The losses in spherically symmetric resonant modes of the volume are dominated by thermal conduction from the gas to the resonator walls, and the losses in the Helmholtz modes are dominated by viscous scrubbing at the tube joining the two volumes.

A mixture of He-Ar and a mixture of He-Xe have been tried in the thermoacoustic refrigerator of Sec. II without any other modification. The concentration and value of Prandtl number for these mixtures is shown by the curve markers in Fig. 7, and the refrigerator results are shown in Fig. 8 along with pure He for comparison. The continuous curves in Fig. 8 are only to guide the eye and do not represent theoretical predictions. The data for He-Xe represent a 50% improvement in COPR relative to pure He. These results only have the external heat leak included in the Q values, and so the values of COPR for a practical refrigerator are roughly 10% lower than the plotted values and the values of COPR intrinsic to the "stack" are roughly 10% higher than those plotted.

The value of using low σ gas mixtures in thermoacoustic refrigerators can also be examined with the Rott theory.[17] Figure 9 is a plot of these calculations for three different temperature ratios.

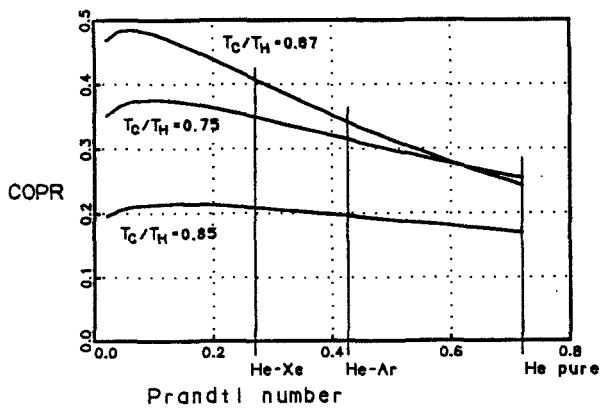

FIG. 9. Theoretical dependence of COPR on Prandtl number for three different temperature ratios.

The smaller temperature ratios represent greater heat loads on the cold end of the refrigerator. The vertical lines indicate the Prandtl numbers of the gases used in the experiments. These calculations indicate that substantial gains in COPR can be had with low Prandtl number gas mixtures, but only at small heat loads. Furthermore, these calculations support the contention of Gifford and Longsworth that viscosity may actually improve the performance of surface heat pumping[2] although the optimum value of Prandtl number may be $\sigma = 0.1$ or less.

ACKNOWLEDGMENTS

The author wishes to thank Greg Swift and Albert Migliori of Los Alamos National Laboratory and Steve Garrett of the Naval Postgraduate School for their support and guidance. Also, thanks are extended to Lt. Mike Suzalla for his work on gas mixtures and their performance. This work has been funded by the Division of Materials Science in the DOE's Office of Basic Energy Sciences and the Office of Naval Research.

1. P. H. Ceperley, "A pistonless Stirling engine - the traveling wave heat engine", J. Acoust. Soc. Am. 66, 1508 (1979).
2. W. E. Gifford and R. C. Longsworth, "Surface Heat Pumping", Adv. Cryogenic Eng. 11, 171 (1966).
3. N. Rott, "Damped and thermally driven acoustic oscillations in wide and narrow tubes", Z. Angew. Math. Phys. 20, 230 (1969).
4. N. Rott, "Thermally driven acoustic oscillations, part III: Second-order heat flux", Z. Angew. Math. Phys. 26, 43 (1975).
5. N. Rott, "Thermoacoustics", Adv. Appl. Mech. 20, 135 (1980).
6. J. C. Wheatley, T. Hofler, G. W. Swift, and A. Migliori, "An intrinsically irreversible thermoacoustic heat engine", J. Acoust. Soc. Am. 74, 153 (1983).
7. J. C. Wheatley, T. Hofler, G. W. Swift, and A. Migliori, "Understanding some simple phenomena in thermoacoustics with applications to acoustical heat engines", Am. J. Phys. 53, 147 (1985).
8. J. C. Wheatley, G. W. Swift, and A. Migliori, "The natural heat engine", Los Alamos Science 14, 2 (1986).
9. G. W. Swift, "Thermoacoustic engines", J. Acoust. Soc. Am., to be published in late 1988.
10. Ref. 9, Section V.
11. Ref. 7, Section V. A.
12. E. I. Mikulin, A. A. Tarasov, and M. P. Shkrebyonock, "Low temperature expansion pulse tubes", Adv. Cryogenic Eng. 29, 629 (1984).
13. R. Radebaugh, J. Zimmerman, D. R. Smith, B. Louie, "A comparison of three types of pulse tube refrigerators: new methods for reaching 60 K", Adv. Cryogenic Eng. 31, 779 (1986).
14. R. Radebaugh, "Pulse tube refrigeration - a new type of cryocooler", Proc. 18th Int. Conf. on Low Temperature Physics, Kyoto, 1987, Jpn J. Appl. Phys. 26, Suppl. 26-3, 2076 (1987).
15. Ref. 6, Eq. (11).
16. T. Hofler, "Accurate acoustic power measurements with a high intensity driver", J. Acoust. Soc. Am. 83(2), 777 (1988).
17. Ref. 6, Eqs. (26)-(43).
18. J. O. Hirschfelder, C. F. Curtiss, and R. B. Bird, *Molecular Theory of Gases and Liquids*, (John Wiley & Sons, 1954).

THERMALLY ACTUATED PULSE TUBE REFRIGERATOR

M.Kaneko*
Y.Matsubara

College of Science and Engineering
Department of Atomic Energy Research Institute
Nihon University
Tokyo 101, Japan

1 Introduction

The deveropment of reliable and low cost cryocoolers which meet the requirement of the application fields is coming to be an important subject. The pulse tube refrigenarator has the potentiality of the low cost and the reliability, because it has no moving parts except the gas compression part [1]. Therefore the design of the compression system is the most important subject in the view point of the reliability. In the case of producing a mechanical compressor, the high reliability will cause the cost to be high. The thermally actuated gas compression system, however, which is similar to the compressor part of Vuilleumier cryocoolers may be produced at a low cost with a high reliability.

This paper describes the feasibility of the thermally actuated gas compression system for the pulse tube refrigerator.

2 Fundamental Model

Thermal compressors can be classified into three types shown in the Figure 1. Type (a) is abailable for such uses as a thermal compression part of the Vuilleumier cryocooler. In this case, the hot displacer which is conected to the cranke mechanism is actuated by force using such as an electric motor. This system works in smooth motion. The expensive and the complex mechanism may be used in the system, however.

In the case of type (b), no external force is used to operate the system. Therefore the system is a kind of heat engin. This system has the drive shaft with a shaft seal. The displacer is actuated by the force which is generated by the pressure difference between two chambers separated by the shaft seal. It is possible to operate the system in the hermonic motion by using such as a large flywheel. The origin of the position is the center of the cylinder on the axis. This system needs the work which is given by

*Research associate from Suzuki Shokan Co., Ltd.

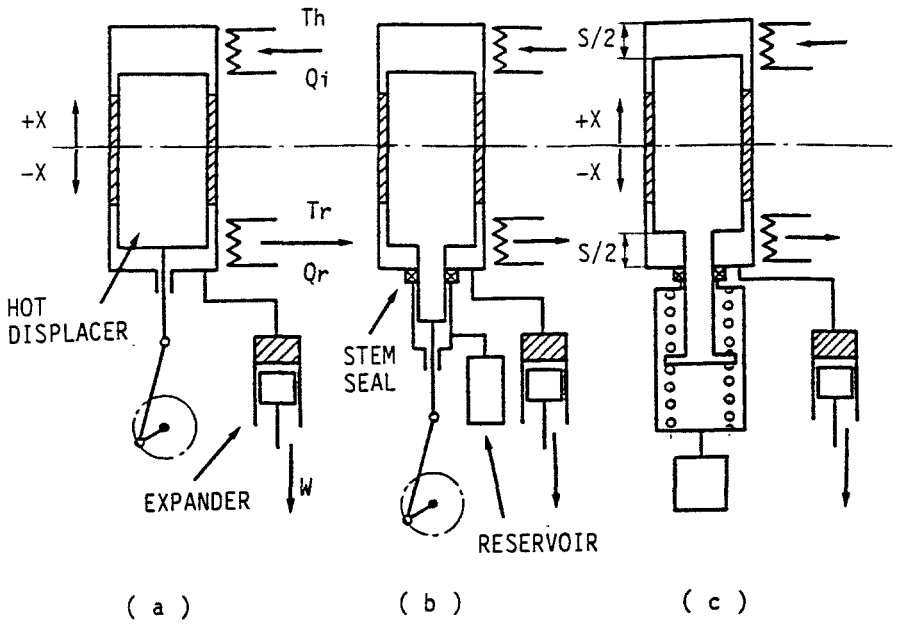

Fig.1. Three fandamental type of thermal compressor.
(a) Actuated by force with crank mechanism.
(b) Thermally actuated with crank mechanism.
(c) Thermally actuated without fixed stroke.

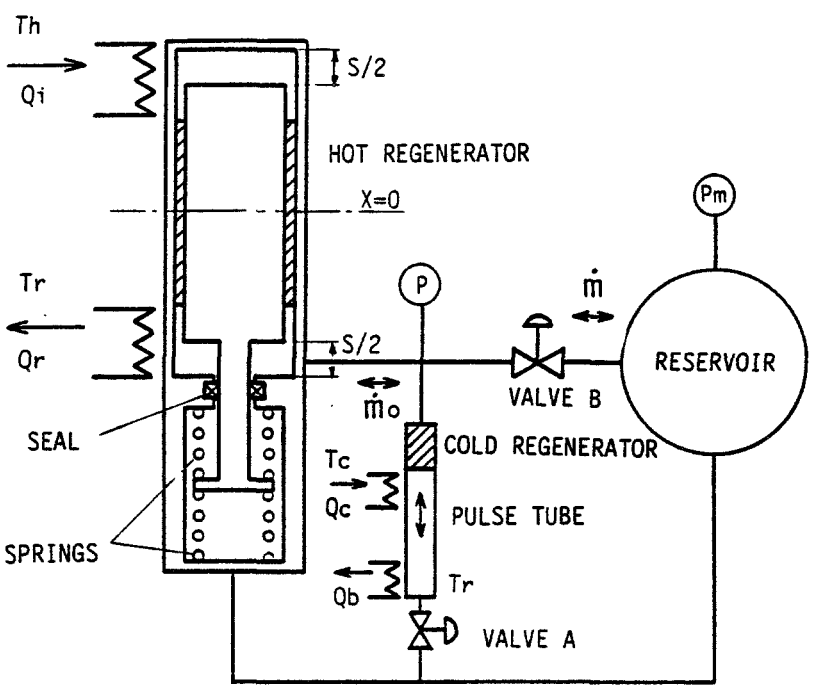

Fig.2. Schematic diagram of thermally actuated Pulse tube refrigerator.

$$\oint (P-P_m)\, A\, dx > 0, \qquad \text{---------- (1)}$$

where P is the working pressure which changes with the motion, P_m is the pressure of reservoir, A is the cross sectional area of the shaft and x is the position. In the negative x value position, the working pressure is higher than the reservoir pressure. In the opposite case the working pressure is lower than reservoir. Therefore the system needs such as a flywheel to make the motion continue. In the case of the isothermal process as well as the adiabatic process, the force which is the product of the pressure difference and the area of the stem has the same value at any position. This means that the system can not be operated because it produces no work.

By using the expander with the proper motion, however, the positive value of work can be produced. In that case the pressure at some position in a downward motion is higher than that in a upward motion. Therefore the system can be operated by using only heat energy. The crank mechanism may be used between the hot displacer and the expander. The shortage of moving force which is caused by the pressure difference makes the motion to be the swing motion. The moving force will be decreased in the swing motion because the pressure difference decreases with reducing the stroke of motion.

The type (c) is also operated by only heat energy. This self actuation mechanism is almost the same as the type (b) except using spring and having no fixed stroke. This type of thermal compressor would not be unstable because the system of a spring and mass will acts such as a flywheel used in the type (b).

In order to operate the system, the work which is produced by using the drive shaft should be a positive value. The cyclic motion is also realized by replacing the expander to the throttle valve and reservoir because the pressure change of working gas do not trace on the oposite process. If the work produced by the expander may not be used as the driving energy, the throttle valve methord is the most simple system. Therefore the thermally actuated compression system having a valve has been selected for the pulse tube refrigerator.

Figure 2 shows the schematic diagram of thermally actuated pulse tube refrigerator. The refrigerator consists of a thermal compressor and a pulse tube. The pressure of a spring chamber is equall to the pressure of reservoir. Those pressure is almost constant because of a large volume of the reservoir.

At the start of the motion, the position of the displacer x equall to -s/2 and the valve B is slightly opened. The high pressure gas flows into the reservoir through the valve B. Reducing the pressure difference between the cylinder and the spring chamber, the displacer start to move upward by spring force. The displacer moves with increasing speed by the increment of pressure. When the pressure becomes lower than the pressure

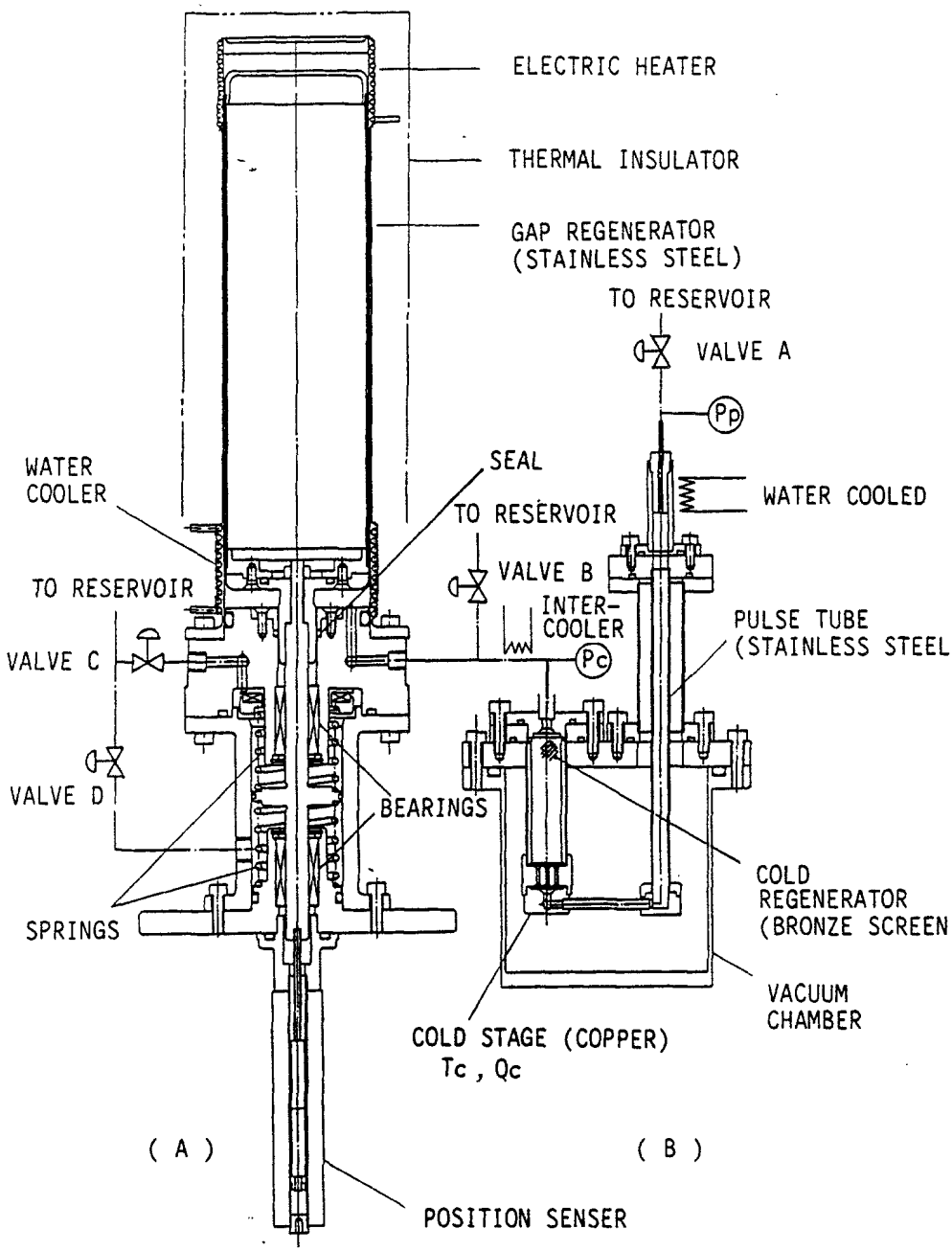

Fig.3. Thermally actuated pulse tube refrigerator.
(A) Thermal compression part.
(B) Pulse tube refrigeration part.

of reservoir, working gas coming from the reservoir flows into the cylinder through the valve B. The motion continues by its momentum untill the force ballance becomes the reverse. The P-V work of this cycle is the positive value, that is, the displacer motion becomes cyclic.

When the valve A is closed, it is the basic pulse tube refrigerator. The motion is also controlled by the valve A. When the valve A is opened, this system is called the orifice pulse tube refrigerator [2]. In order to obtain the high efficiency, reducing the ratio of the mass flow rate (m/m_0) is important. Decreasing the temperature of the pulse tube increases the mass flow. It causes the degradation of the pressure ratio.

3 Experiment

Figure 3 shows the test machine of the thermally actuated pulse tube refrigerator. In the compression part, a gap regenerator is used and the displacer is made of 304 stainless steel. It is 63.4 mm in diameter and about 230 mm in length. The cylinder is also made of 304 stainless steel. The components have been welded. The radial clearance of the displacer section is about 0.3 mm. The heat injection part, which has the heat transfer area of about 0.01 m^2, is covered by electrical heater. The heat rejection part is covered by cooling water tube. The mass of the moving part except the springs is 0.87 kg. The caractristic of the spring is linear and its constant is 4.1×10^3 N/m. Opening the valve C and D, the pressure of spring chamber has become equall to the pressure of reservoir which has about 2 litters (2×10^{-3} m^3) of volume. The pressure variation of the reservoir has been small as compared with that of working gas. The ratio is about 1 to 2 %. The shaft which is sealed by cap seal has a diameter of 16 mm. The possible maximum stroke is about 14.2 mm.

The matrices of the cold regenerator are made of layers of phosphor-bronze mesh which is about 200 mesh. The regenerator has a diameter of 13 mm and a length of 50 mm. The pulse tube which is made of stainless steel has an inner diameter of 7 mm, a length of 140 mm and a thickness of 0.5 mm. The hot end of pulse tube which is made of copper has been cooled by water at room temperature. it has a length of about 30 mm and heat transfer area of 6.6×10^{-4} m^2.

For the first step of the experiment, the pulse tube refrigeration part were replaced by the external volume V_x to know the performance of the compressor. That thermally actuated gas compression system has been operated by only the heat energy.

Figure 4 shows some experimental data of pressure and displacement variations. The external volume is 13.6 cc (13.6×10^{-6} m^3) of volume and the pressure of reservoir is about 2.9 MPa. To increase the operating frequency the orifice setting of valve B was at a slightly higher value. The position of the displacer was measured by using a linear variable differential transformer which was adjusted to the bottom position of the displacer.

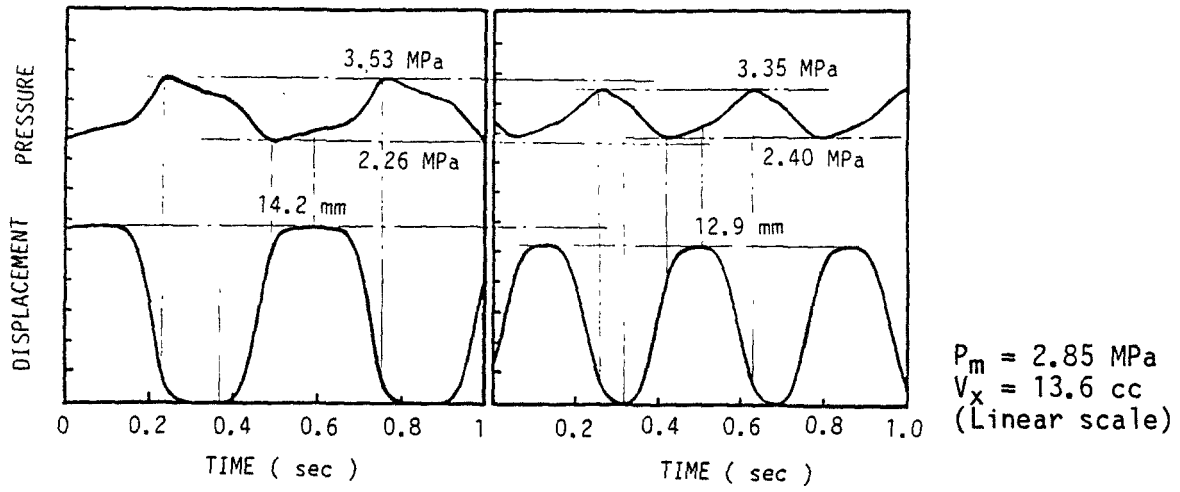

(a) f = 1.9 Hz (b) f = 2.7 Hz

Fig.4. Experimental data of pressure and displacement variations.

In the case (a) of Figure 4, the stroke of the displacer is a maximum possible value of 14.2 mm. This shows that increasing the cycle speed decreases stroke, pressure difference and compression ratio. In the case (b) the stroke of the displacer is smaller than the case (a). It has been confirmed that the P-V work of this system was positive by this chart. In the case that the displacer did not reach either end, the displacer motion had been stopped. We suppose that the phenomena was caused by a unstable frictional force.

Figure 5 shows the experimental results of the thermal actuated compressor. In case (B), the external volume V_x was 13.6 cc of volume and the pressure of reservoir is about 2.9 MPa. Increasing the frequency by increasing the orifice setting of valve B decreases the pressure ratio defined as P_{max}/P_{min}. The available frequency was about 2.6 Hz. The result suggests the compressor needs the pressure difference of 0.45 MPa at least to continue the motion. In such a valve setting, the compressor is short of the moving force caused by pressure difference. The change of the degradation of pressure ratio is caused by the shortage of stroke. Operating just below the frequency of the point C may be the efficient operation. The result also shows that decreasing the external volume increases the pressure ratio as well as the optimum operating frequency. The heat injection part, the gap regenerator, and the heat rejection part have a dead volume of 2.5 cc,13.8 cc and 5.0 cc, respectively.

Figure 6 shows the cooling capacity of the paticular pulse tube refrigerator. The temperatures of the electric heater portion and the water cooling portion were about 700 K and 300 K, respectively. The pressure of the reservoir was about 2.9 MPa. To keep the frequency at about 1.9 Hz the valve B has been adjusted. For the orifice pulse tube the valve A was slightly opened. In the case of the optimum orifice setting for the pulse tube, the operating frequency became low and the

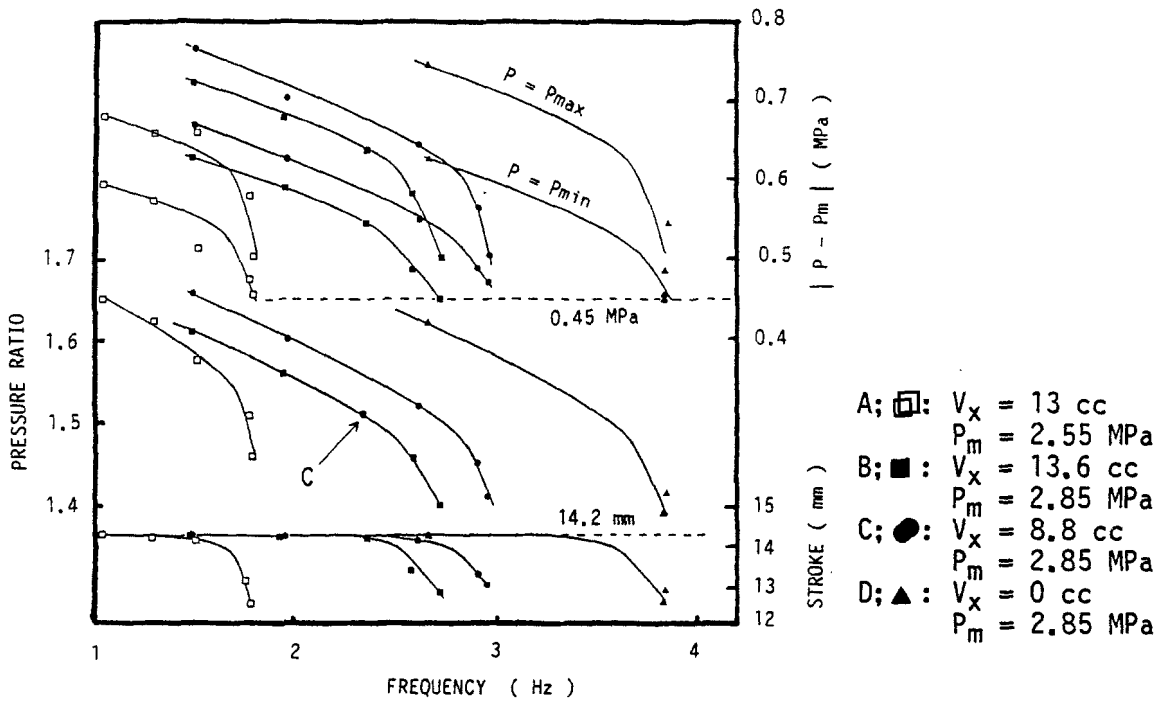

Fig.5. Experimental results of the thermally actuated compressor.
Hot temperature T_h=700 K, Room temperature T_r=300 K
Working pressure P, Reservoir pressure P_m
Pressure ratio = P_{max}/P_{min}, External volume V_x.

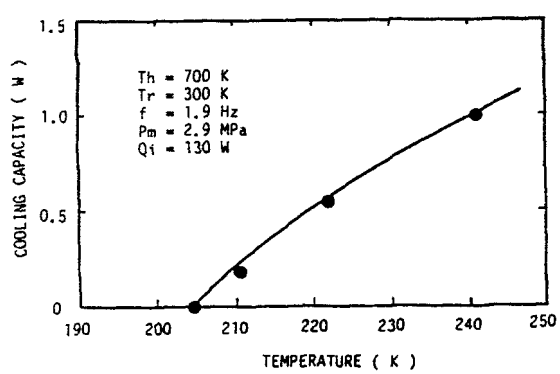

Fig.6. Cooling capacity of the test aparatus

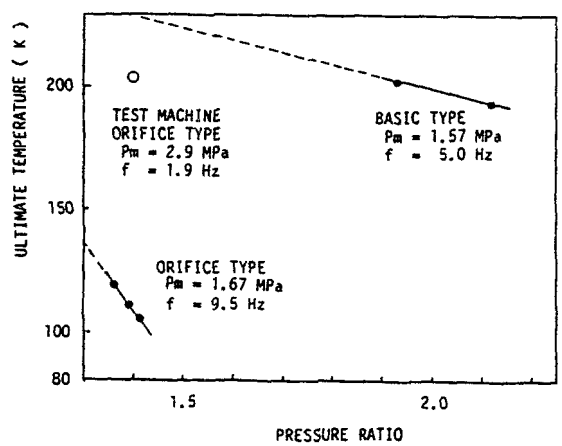

Fig.7. Performance of the pulse tube refrigerator using the mechanical compressor

cold end temperature was high. The pulse tube refrigeration part has the total volume of about 11 cc. Considering the temperature level, it is 13.4 cc which value is nearly equall to the external volume of 13.6 cc in the Figure 5. The pressure ratio was about 1.4. This results suggests that the amount of gas passing through the cold regenerator is larger than the case B of Figure 5, or the required level of the pressure difference become high because of the frictional force. The working pressure and the temperature was decided by the property of 304 stainless steel.

Figure 7 shows the performance of the particular pulse tube refrigerator using the mechanical compressor. The result of the thermally actuated pulse tube refrigerator is plotted in the diagram.

4 Discussion

According to the experimental results of the thermal actuated compression part of the refrigerator, the cycle speed seems to be limitted by the frictional force. Owing to the frictional force in the motion, the large pressure difference which causes the moving force has been required. The pressure ratio has been decreased by the dead volume of the system by increasing an external volume. That results suggests that the large swept volume of the compression part with the same stroke and the drive shaft is required for the high frequency operation. In this experiment the amount of gas passing through the valve B has not been measured. Decreasing that amount of gas, however, increases the total efficiency because the work is not produced by the valve.

The motion of the displacer is the forced oscillation with a dampping effect. The driving force depends on both the position and the direction of the motion because the force is proportional to the pressure difference between the working gas pressure and the almost constant pressure of the reservoir. Therefore there exist two kind of force which depend on the position x. Those are the force of spring and the force of pressure. The amount of lost energy which is caused by the friction is given by the work caused by the force of pressure. The equation of the motion is expressed as follows,

$$M\ddot{x} + A\dot{x}/|x| + B\dot{x} + Kx + S(P-P_m) = 0, \qquad \text{-------- (2)}$$

where M is the mass of the moving parts, A is a drag force caused by seal resistance, B is a coefficient caused by the viscosity of the working gas, K is a spring constant and S is the area of the drive shaft. The pressure P which is a function of the position, calculated for the isothermal model using the ideal gas property. The effect of the valve is given by

$$\dot{m} = C(P^2-P_m^2), \qquad \text{---------- (3)}$$

where $\dot{m}$ is a mass flow rate through the valve, C shows the setting value of the valve orifice. The calculation has been carried out by a computer using the Runge-Kutta method.

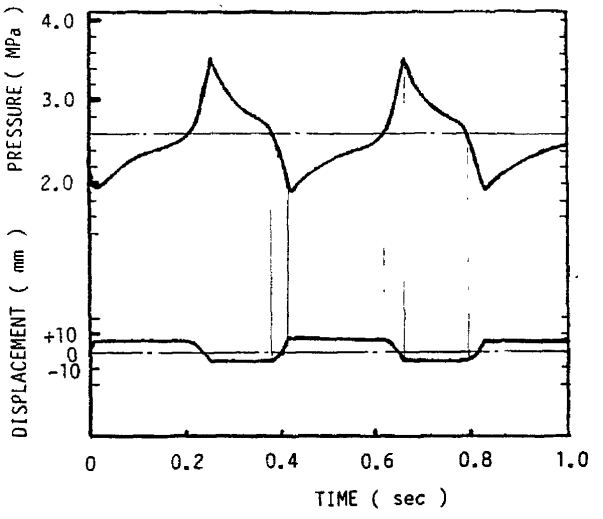

Fig.8. Pressure and movement variation thermally actuated compressor from computer analysis;
P_m=2.6 (MPa), K=8.2x10^3 (N/m)
M=0.87 (kg), f=2.5 (Hz)
P=P_{max}-P_{min}=0.31 (MPa)

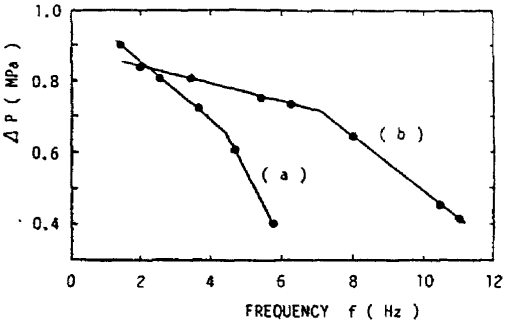

Fig.9. Effect of the friction term from computer analysis;
P_m=2.6(MPa), K=8.2x10^3(N/m)
M=0.87(kg), Vx=6.2(cc)
(a) a=26(N), B=87(N s/m)
(b) A=8.7(N), B=44(N s/m)

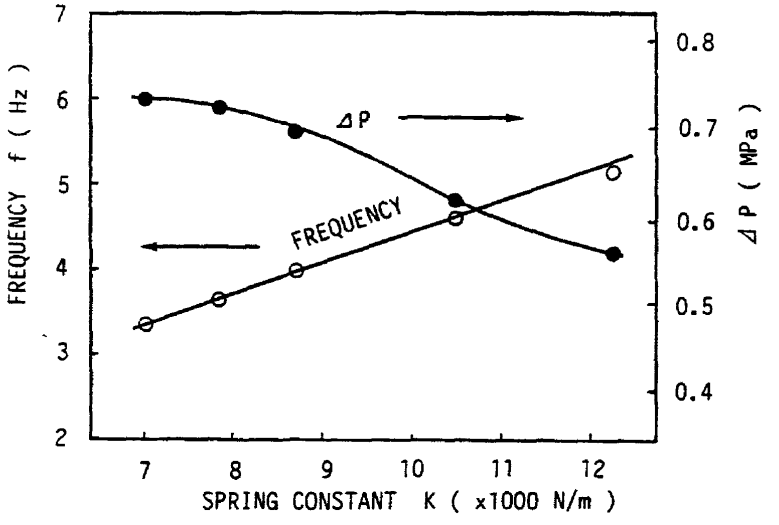

P_m=2.6 (MPa)
M =0.87 (kg)
V_x=6.2 (cc)
C =0.0035

Fig.10. Effect of spring constant from computer analysis.

Figure 8 shows the result of computer analysis. Since the heat is transfered instantaniously in this calculation model, the change of pressure is more sharp as compared with experimental results in Figure 4.

Figure 9 suggests that to decrease the friction is effective for obtaining the high operating frequency. Figure 10 shows the effect of the spring constant. By choosing the high value of the spring constant with the same mass, the available potential energy of spring increases. That causes the frequency to increase and also the stroke of motion to decrease.

It is nesessary to consider the real heat transfer in order to obtain the good computer simulation. The estimation of the flow passing through the valve and the effect of using spring which has a non linear charactristics are interesting for new design. The frequency of the particular pulse tube refrigerator was very low. The pressure ratio was also small. In spite of such conditions, the ultimate temperature of about 200 K was obtained. We suppose that the orifice type pulse tube do not require the high compression ratio as shown in Figure 7 [3].

5 Conclusion

The thermally actuated pulse tube refrigerator has been operated at the temperature of about 200 K. The possibility of reaching 100 K has been presented under the condition of a low pressure ratio (about 1.4) and high frequency (about 10 Hz). The possibility of the high frequency operation has been suggested by the calculated results as well as the experimental results. Cryogenic refrigerators are required to be a reliable and a low cost. This particular refrigerator has a potential reliability with a low cost. To investigate both the effect of the valve flow and the effect of the non-linear spring are the interesting for new design because the motion and the efficiency depend on both the valve flow and the springs which promote the oscillating motion.

6 References

[1] Gifford,W.E. and Longsworth,R.C.,"Pulse tube refrigeration progress", Advances in Cryogenic Engineering, Vol. 10B, Plenum Press, New York, (1965), p. 69.

[2] Radebaugh,R., Zimermann,J.,Smith,D.R. and Louie, B., "A Comparison of Three Types of Pulse Tube Refrigerators:New Methods for Reaching 60 K", Advances in Cryogenic Engineering, Vol. 31, Plenum press, New York, (1986), p.779.

[3] Matsubara,Y. and Miyake,A., "Alternative Methods of The Orifice Pulse Tube Refrigerator", Proceedings of The 5th International Cryocoolers Conference,

OPTIMIZATION OF A PULSE TUBE REFRIGERATOR FOR A FIXED COMPRESSOR SWEPT VOLUME*

Ray Radebaugh, Kanchan Chowdhury, and James Zimmerman

Chemical Engineering Science Division
National Bureau of Standards, Boulder, CO 80303

This paper discusses experiments which were done to determine the minimum temperature and the maximum refrigeration power available with an orifice pulse tube refrigerator driven by a compressor with a fixed swept volume of 25 cm^3. The frequency of the compressor motion could be varied between 10 and 25 Hz. Only screen regenerators were studied but several mesh sizes and regenerator volumes were used. The screen materials tested were phosphor bronze, stainless steel, and nylon. Three different pulse tube volumes were investigated for most regenerators. The lowest temperatures achieved were about 67 K with the following conditions: pulse tube volume of 7.9 cm^3, regenerator gas volume of 9.2 cm^3, regenerator screen of 250 mesh stainless steel, frequency of 10-15 Hz, and average pressures of 1500-2000 kPa. These optimum volumes resulted in a pressure ratio of about 1.3. A net refrigeration power of about 2 W at 80 K could be achieved with those conditions. Comparisons with theory and design guidelines are discussed.

1. Introduction

The pulse tube refrigerator is a variation of the Stirling refrigerator [1] with the advantage that the moving displacer is eliminated. The result is less vibration at the cold end and a potential for increased reliability. A single stage Stirling refrigerator achieves 40-50 K with no load. At present the best no-load temperature achieved with a single stage pulse tube refrigerator is 60 K [2]. This temperature was achieved with an orifice pulse tube [2,3] that was not fully optimized. A large laboratory compressor with a swept volume of 290 cm^3 was used in those experiments. The intrinsic cooling efficiency of the orifice pulse tube itself is nearly as high as that of a Stirling cycle expansion space [4].

The object of our experiments was to start with a much smaller compressor of the type typically used for a split Stirling cryocooler and determine the lowest temperature and maximum refrigeration power that can be achieved with this fixed compressor volume. From these studies design

*Research funded by NASA/Ames Research Center.

guidelines regarding the optimum regenerator and pulse tube sizes could be generated. The overall system efficiency is not optimized in such an approach and was not studied in any detail.

2. Theory

Figure 1 shows a schematic of the orifice pulse tube refrigerator. Previous experiments [5] have shown that in the orifice pulse tube, heat transfer between the gas and the wall is detrimental to the performance. The basic pulse tube (no orifice), however, relies on heat transfer to achieve a proper phase shift between the pressure and the mass flow rate. In the orifice pulse tube the proper phase shift is brought about by the additional expansion of the gas in the pulse tube due to gas flow out through the orifice and the compression caused when gas flows back into the pulse tube. The gas pressure in the reservoir volume remains at the average pressure, P_o, whereas the pressure in the pulse tube varies nearly sinusoidally between P_{max} and P_{min}.

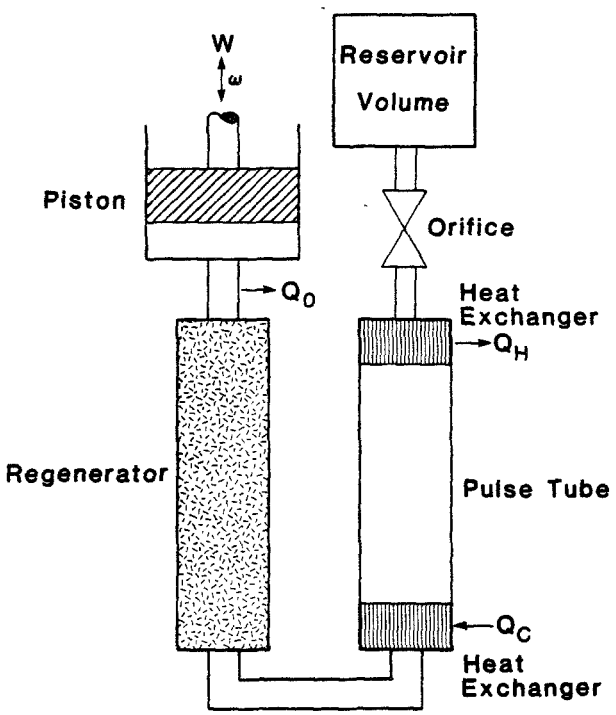

Figure 1. Schematic of the orifice pluse tube refrigerator.

The model we choose assumes the gas in the pulse tube is adiabatic with heat transfer occurring only in the heat exchangers at the hot and cold ends of the pulse tube. In addition, the model assumes that the dynamic pressure and temperature are small compared with the average values. With such small variations we can assume that the variations in the mass flow rate, pressure, and temperature are sinusoidal. Some details of this harmonic model have been discussed previously [6]. When various void volumes are considered the gross refrigeration power is calculated to be

$$\dot{Q}_c = \frac{\omega T_c P_o (V_{co}/T_{co})^2}{16 (V/T)_{eff}} , \qquad (1)$$

where ω is the angular frequency, T_c is the cold end temperature, P_o is the average pressure, V_{co} is the compressor swept volume, T_{co} is the average temperature of the gas in the compressor, and $(V/T)_{eff}$ is the sum of the effective volume-to-temperature ratios of all the volumes in the system including the pulse tube and compressor volumes. For the pulse tube, that ratio should be $V_t/\gamma T_c$, where the specific heat ratio γ is included because of the adiabatic behavior in the tube.

With the additional assumption that most of the temperature gradient within the pulse tube occurs in the center one-third of the gas that must always remain in the tube as a buffer between the hot and cold ends, the model gives the optimum pulse tube volume as

$$V_t/V_{co} \approx (3/\sqrt{2})(T_c/T_{co}) . \qquad (2)$$

For T_c = 70 K and T_{co} = 350 K, we have V_t/V_{co} = 0.42. The optimum regenerator volume is not calculated by this model since it assumes a perfect regenerator.

3. Experimental Apparatus

Figure 2 is a photograph of the pulse tube refrigerator used for these experiments. The crank driven compressor has two opposed pistons to decrease vibration. The total swept volume is 25 cm^3. Measurements made with known isothermal volumes suggest the effective swept volume is about 22.3 cm^3 due to some leakage by the filled Teflon piston rings. This compressor was originally built for a two-stage split Stirling refrigerator to provide 1 W at 25 K. The operating frequency was varied between 10 Hz and 25 Hz with a variable frequency power supply. The hot ends of the pulse tube and the regenerator were bolted to a large aluminum base using a lead gasket to provide a seal. This arrangement made it easy to remove one pulse tube or regenerator and replace it with a different one. The cold ends of the regenerator and pulse tube were connected with a 3 mm o.d. x 0.4 mm wall soft copper tube. Copper screens placed in the cold end of the regenerator constituted the cold heat exchanger. About 30 copper screens of 80 mesh were placed in the copper reducing

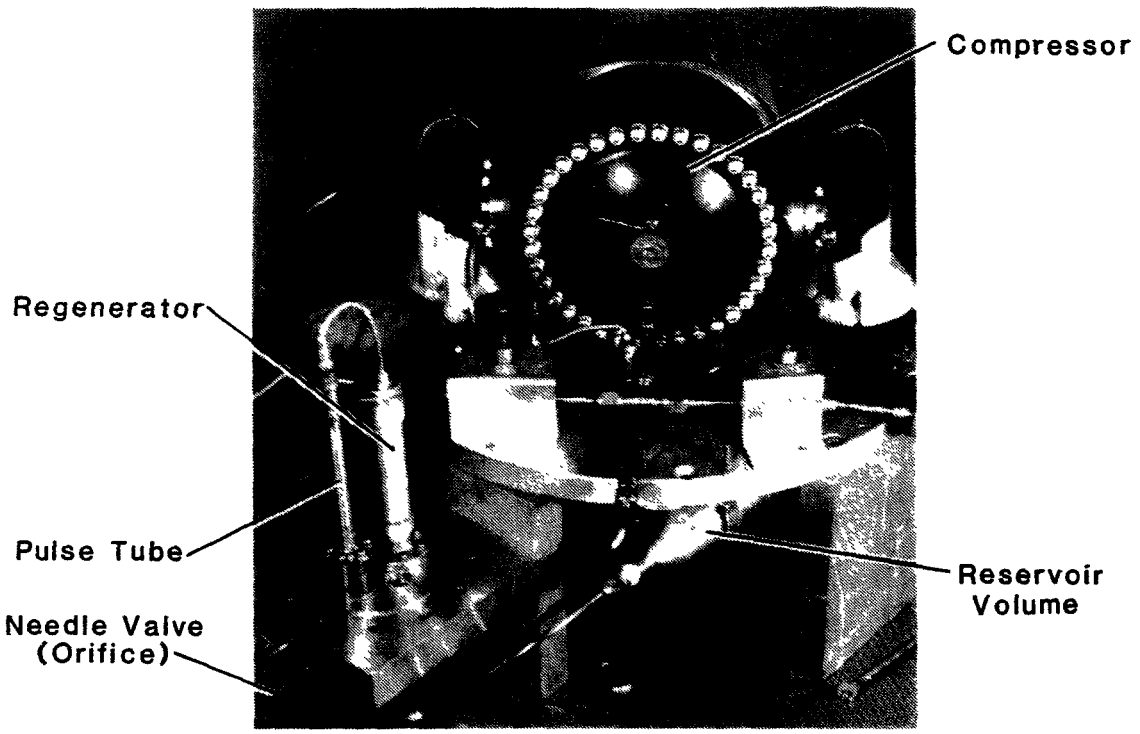

Figure 2. Photograph of pulse tube refrigerator.

fitting at the cold end of the pulse tube to provide for flow straightening. Without the flow straighteners the temperature could be 10-15 K higher. The hot heat exchanger was made with 80 mesh copper screen and occupied about 10% of the pulse tube volume. A valve with a 1.4 mm orifice was used for the orifice and the reservoir volume was 500 cm^3.

Small piezoresistive pressure transducers measured the gas pressure near the compressor, at the hot end of the pulse tube, and in the reservoir volume. The pressure in the reservoir volume varies only slightly and was measured sometimes to determine the mass flow rate, $\dot{m}_o$, through the orifice. A commercial diode thermometer accurate to ± 1 K was bolted to a copper bracket soldered to the cold end of the regenerator. A heater was also attached to the same copper bracket. About 5 layers of aluminized polyester were wrapped around the cold parts before bolting on the vacuum can and evacuating to a pressure of 10^{-3} Pa (10^{-5} torr).

Heat dissipation from the compressor housing and the two cylinders was aided by fans that directed air over the fins. Heat dissipation from the hot end of the pulse tube was by conduction through the copper screen and into the copper block in which the screens were pressed. From the copper block the heat was conducted through the lead gasket to the aluminum base and the frame of the compressor. No fins or fans were used to

enhanced the heat dissipation from the pulse tube. As a result the aluminum base was usually at a temperature of 40-45 °C during normal operation of the refrigerator. We estimate that a base temperature of 25 °C would have lowered the pulse tube cold end temperature by about 5-8 K.

Void volumes associated with the compressor and connecting tubes are as follows: Clearance volumes within each cylinder, 2 cm^3; connecting tube volume from compressor to hot end of regenerator, 3.83 cm^3. The total external void volume is then 7.83 cm^3. That void volume is fairly large for a compressor swept volume of 25 cm^3 and resulted in low pressure ratios and reduced refrigeration power.

4. Description of Regenerators, Pulse Tubes, and Experimental Conditions

Most regenerators were constructed of stainless steel screen, though some used nylon screen. A few preliminary measurements were done early in the program with 150 mesh phosphor bronze screen. A lowest temperature of 138 K was achieved with the phosphor bronze screen regenerator, which was replaced with stainless steel. The stainless steel screen produced much lower temperatures due to the reduced conduction loss. Table 1 lists the characteristics of the regenerators studied. Figure 3 is a plot of the regenerator void volume and mesh size used in these studies, though regenerator VIII, which used combinations of sizes, is not shown. Various lengths and diameters were used to minimize the sum of the loss terms due to the conduction, imperfect regenerator, and pressure drop.

Almost all the pulse tubes tested were thin walled stainless steel tubes with an outer diameter of 9.53 mm and a wall thickness of 0.254 mm. Only the length was varied to obtain different volumes for the pulse tube. Generally the pulse tube volumes varied from 5 cm^3 to 12.5 cm^3. For a frequency of 10 Hz the thermal penetration depth in a semi-infinite slab

Table 1. Regenerators Tested

#	wall material*	L (mm)	O.D. (mm)	wall thickness (mm)	screen material	screen mesh	porosity	void volume (cm^3)
I	s.s.	127	12.7	0.254	s.s.	150	0.69	10.2
II	s.s.	76	12.7	0.254	s.s.	150	0.69	6.1
III	s.s.	100	15.9	0.30	s.s.	200	0.63	10.2
IV	s.s.	127	15.9	0.30	s.s.	200	0.63	14.63
V	s.s.	178	15.9	0.30	s.s.	200	0.63	20.5
VI	G-10	28	14.3	0.78	nylon	210	0.56	2.0
VII	G-10	89	18.2	0.78	s.s. & nylon	200 & 210	0.58	11.3
VIII	G-10	69	20.7	0.82	s.s. & nylon	250 & 210 200 & 210 150 & 140	0.60	11.7
IX	G-10	68	18.2	0.78	s.s.	250	0.62	9.2

*s.s. = stainless steel

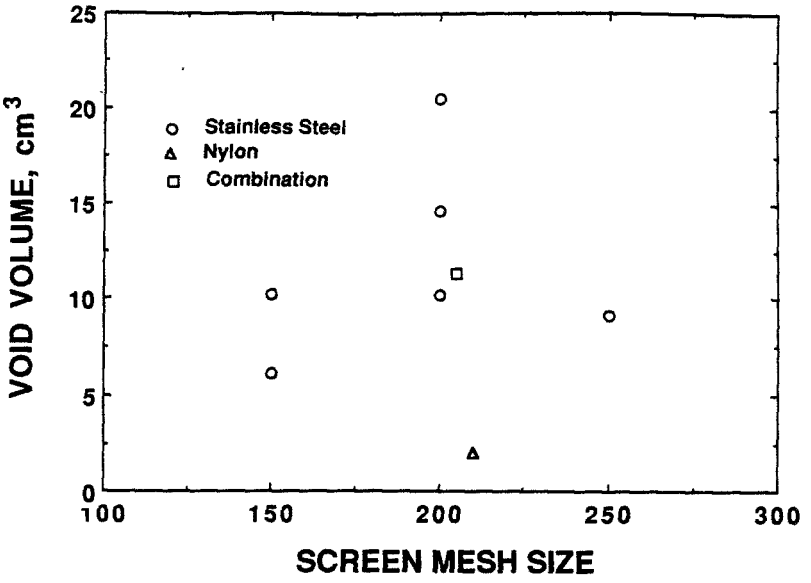

Figure 3. Void volumes and mesh size used in the regenerators.

of helium gas is about 0.8 mm at 1 MPa and 300 K. It is less for lower temperatures, higher pressures, and higher frequencies. We conclude that in all of our experiments the pulse tubes behaved nearly like adiabatic tubes.

Most regenerators were tested with different sizes of pulse tubes. For each pulse tube the performance was measured with at least 3 different frequencies. For each frequency the orifice opening was varied in order to achieve the lowest temperature for a given refrigeration power. The refrigeration powers were measured generally up to a maximum temperature of 160 K and ranged from 0 W to 9 W. For each run the maximum and minimum in the pressure oscillation were recorded at two points: before the regenerator (after the compressor) and after the regenerator (at the hot end of the pulse tube). The ratio of maximum to minimum pressure in the pulse tube varied between 1.12 and 1.75 in these experiments.

For a perfect regenerator the optimum pulse tube size, according to theory, depends only on the compressor swept volume and the temperatures of the pulse tube and compressor. For imperfect regenerators the optimum pulse tube size will be reduced in order to lower the regenerator loss term caused by the large mass flow passing through the regenerator and on to the pulse tube. A smaller pulse tube reduces the mass flow through the regenerator.

5. Results and Discussion

5.1 Regenerator I

This regenerator was used with a pulse tube of 7.0 cm^3. Various average pressures were used at each of three different frequencies to determine the best pressure for this series of measurements. The results are shown in Figure 4. Only the no-load temperatures were measured. The best pressure according to Figure 4 is 1500 kPa. This pressure was used for the rest of the regenerators except for regenerator IX when the pressure was varied again. The lowest no-load temperature was 82 K at a frequency of 15 Hz.

5.2 Regenerator II

To search for the optimum regenerator size some change in size was made and the change in performance noted. Regenerator II was made smaller than Regenerator I by reducing the length from 127 mm to 76 mm. Pulse tube volumes of 5 cm^3, 7 cm^3, and 9 cm^3 were tested with this regenerator. The lowest no-load temperature was 94.6 K at 10 Hz with the 7 cm^3 pulse tube. Since the optimum frequency was less than that with Regenerator I the results suggest the regenerator loss term is relatively large and offsets the increased refrigeration due to the higher pressure ratio.

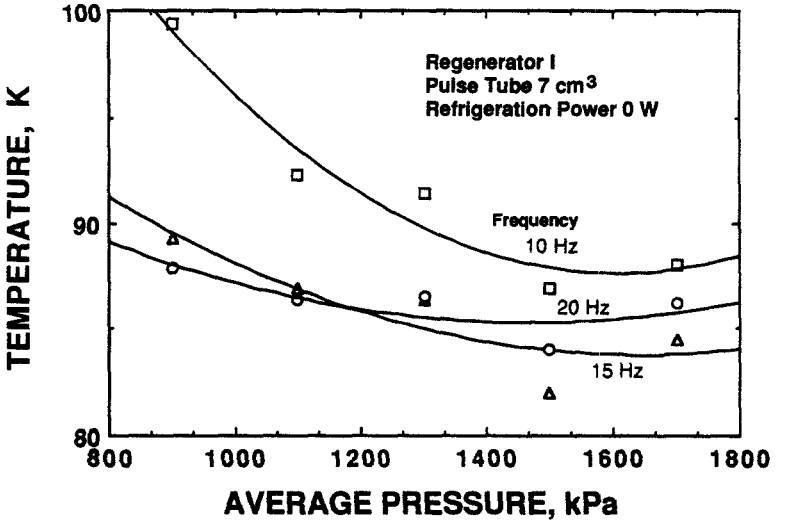

Figure 4. Variation of temperature with average pressure for 7 cm^3 pulse tube with Regenerator I.

5.3 Regenerator III

Approximate calculations showed that the conduction loss with Regenerator I was not dominant. To decrease the regenerator loss term, 200 mesh screen was used for Regenerator III instead of 150 mesh used previously. The diameter was increased and the length shortened to keep the volume and the pressure drop about the same as with Regenerator I. Pulse tube volumes of 5 cm^3, 7 cm^3, 7.85 cm^3 and 9 cm^3 were used. Figure 5 shows the linear behavior of refrigeration power on temperature for various orifice settings. The optimum orifice opening increases with increasing refrigeration power. The pulse tube with 7.85 cm^3 gave the lowest no-load temperature of 71 K. Figure 6 shows how the temperature varies with frequency for different loads using the 7.85 cm^3 pulse tube. The optimum frequency varies from 15 Hz for 0 W to 20 Hz at 3 W. At the higher temperatures that occur when a load is applied the regenerator loss term is not as important, so higher frequencies can be used to increase the refrigerator power.

Figure 7 shows how the temperature varies with pulse tube volume for various loads and frequencies. With no load at 71 K the optimum pulse tube volume is 7.85 cm^3, or $V_t/V_{co} = 0.35$. This result is in fair agreement with the value 0.43 calculated from eq. (2) with $T_{co} = 350$ K. The slightly lower experimental value is expected because of the regenerator loss term. At 94 K with 2 W refrigerator power the optimum pulse tube volume is about 9 cm^3, which gives $V_t/V_{co} = 0.40$. Equation (2) gives $V_t/V_{co} = 0.56$.

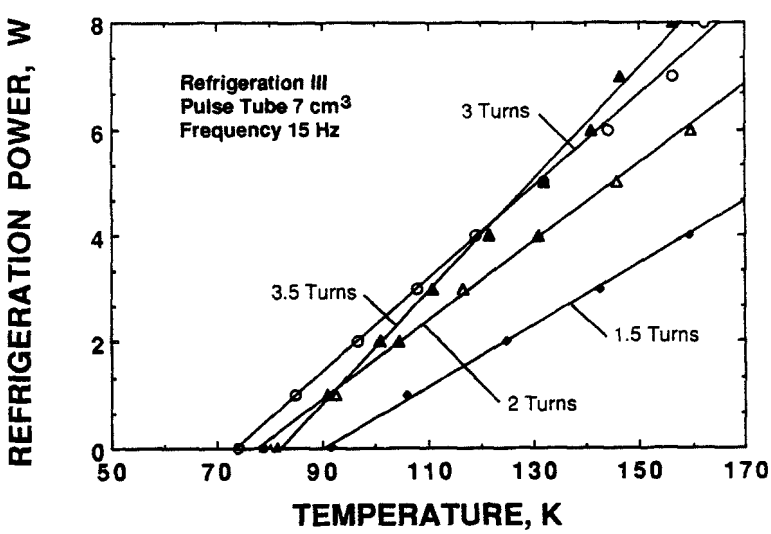

Figure 5. Refrigeration power of 7 cm^3 pulse tube and Regenerator III for various ofifice settings.

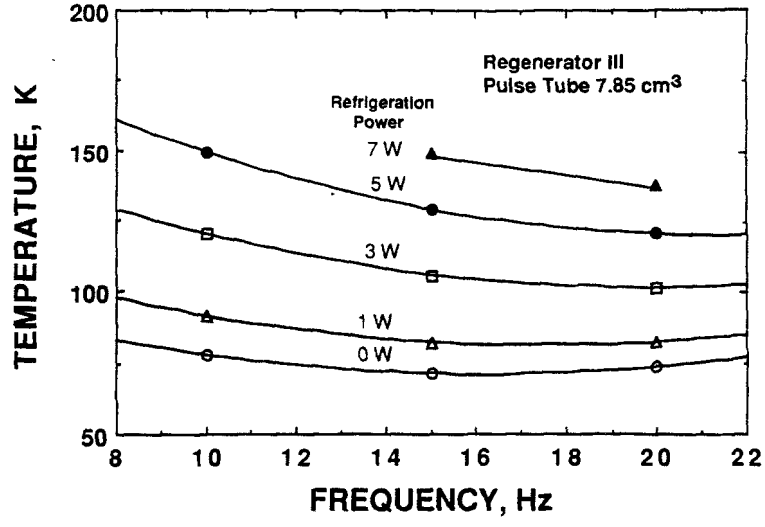

Figure 6. Temperature vs. frequency for different loads with 7.85 cm^3 pulse tube and Regenerator III.

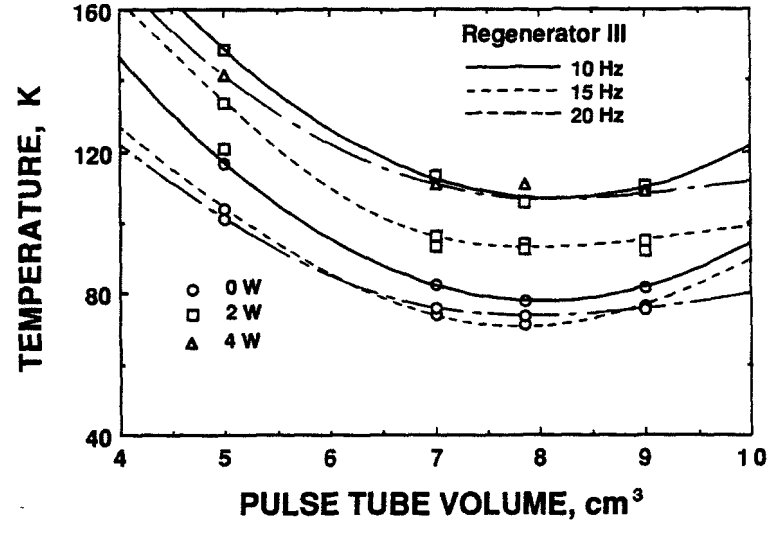

Figure 7. Temperature vs. pulse tube volume for Regenerator III.

The pressure ratio at 71 K with the 7.85 cm^3 pulse tube was 1.27 in the pulse tube and 1.47 near the compressor. These ratios increased to 1.32 and 1.51 at 94 K with 2 W power applied.

5.4 Regenerator IV

Regenerator III produced good results. We then decided to increase only the length; this would decrease conduction and the regenerator loss, but at the expense of greater void volume and pressure drop. Regenerator IV was made 27% longer than Regenerator III. The best no-load temperature was 81.3 K at 15 Hz with a 7.35 cm^3 pulse tube volume. Regenerator III gave 71 K at no load. It is interesting, however, that even with a pressure ratio of 1.16 a no-load temperature of 105 K was reached with a 11.35 cm^3 pulse tube volume at 20 Hz.

5.5 Regenerator V

This regenerator was made longer than Regenerator IV even though Regenerator IV did not perform as well as Regenerator III. The object of the tests with this regenerator were to study the performance at low pressure ratios. The best no-load temperature was 81 K with a 12.5 cm^3 pulse tube at 10 Hz. The pressure ratio was 1.19. At 20 Hz a no load temperature of 88 K was achieved with a pressure ratio of 1.14.

5.6 Regenerator VI

This regenerator was made with a volume much less than the others to investigate the behavior in this region. Because of the short length, conduction would be fairly large, so we decided to use nylon screen and G-10 fiberglass-epoxy for the tube. The void volume was only 2.0 cm^3.

The lowest no-load temperature was 104 K at 10 Hz with a 7 cm^3 pulse tube. The pressure ratio was 1.47. We observed that nylon screen appears to give a higher pressure drop than does stainless steel screen. We are investigating this effect further. The low frequency of 10 Hz where the optimum occurred is indicative of a large regenerator loss term.

5.7 Regenerator VII

This regenerator also used a G-10 fiberglass-epoxy tube, but the packing was alternate layers of 200 mesh stainless steel and 210 mesh nylon. The alternating nylon layers tend to reduce the thermal conduction of the packing, and the rigidity of the stainless prevents the nylon from packing together too tightly and increasing the pressure drop. The void volume was about the same as Regenerator III but this regenerator was shorter and larger in diameter.

Only a 7.85 cm^3 pulse tube was tested with this regenerator. The lowest no-load temperature of 71 K was achieved at 15 Hz with a pressure ratio of 1.259. The same pulse tube volume with Regenerator III gave the same temperature but with a pressure ratio of 1.267.

5.8 Regenerator VIII

This regenerator used a G-10 tube and was packed with different mesh sizes. The fine mesh (250 mesh stainless + 210 mesh nylon) was used for the coldest
18 mm. The next 34 mm were packed with medium mesh (200 stainless + 210 mesh nylon) and the 17 mm on the hot side were packed with course mesh (150 stainless + 140 mesh nylon). This grading of mesh size was to make use of the fact that the majority of the pressure drop occurs near the hot end of the regenerator where the viscosity is highest and the density is lowest.

Only a pulse tube volume of 7.85 was tested with this regenerator. A temperature of 77 K was reached with 15 Hz. The pressure ratio was 1.292. Regenerator III had a slightly higher pressure drop at this same temperature. The poorer performance of Regenerator VIII is attributed to a lower heat transfer coefficient caused by the lower Reynolds number in the larger diameter.

5.9 Regenerator IX

Since nylon screen did not seem to improve the performance of the regenerators, we went back to using stainless steel screen for this regenerator. This time a mesh size of 250 was used. With the finer mesh a larger diameter had to be used to keep the pressure drop from being too large. A G-10 tube was used to reduce thermal conduction in the regenerator. The void volume was about 21% smaller than that of Regenerator III and the effective surface area was about 5% greater.

A pulse tube volume of 7.85 cm^3 was used with this regenerator. A no-load temperature of 69 K was achieved at 15 Hz and 1400 kPa pressure. This result is slightly better than that achieved with the previous regenerators and may be due to the reduced conduction in the G-10 wall and a slightly lower regenerator loss term. Additional measurements were made at 1000 kPa, 1600 kPa, and 2000 kPa. Figure 8 shows the temperature as a function of frequency for a pressure of 2000 kPa. With the higher pressure the optimum frequency is reduced. At no load, 11 Hz is the best frequency; at 5 W a frequency of 16 Hz is best. The lowest no-load temperature of 67 K at 9 Hz for 2000 kPa was the lowest temperature achieved in these experiments. At 15 Hz about 2 W of net refrigeration were achieved at 80 K.

Figure 9 shows the temperature as a function of pressure. Note that 2000 kPa may be best for the no load case, but higher pressures would be better for the higher loads. Overheating of the compressor prevented us from doing tests at higher pressures.

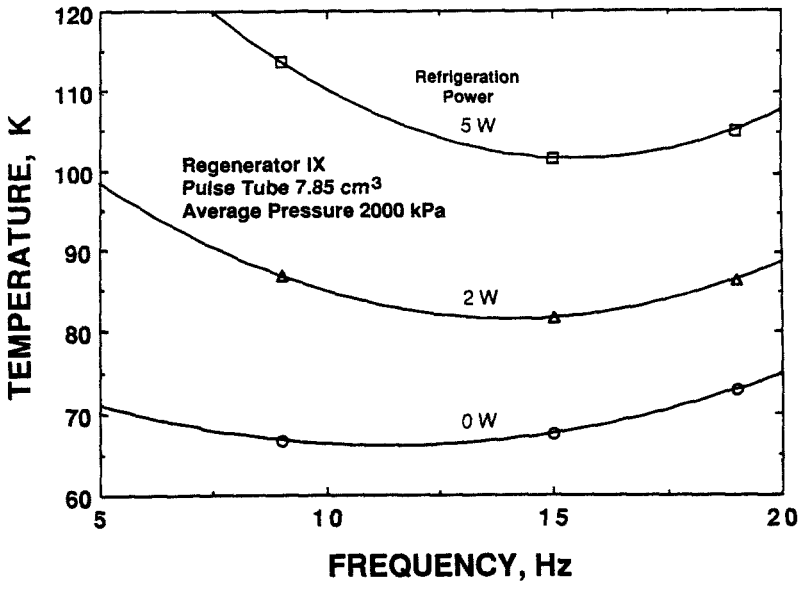

Figure 8. Temperature vs. frequency for 7.85 cm³ pulse tube and Regenerator IX at 2000 kPa.

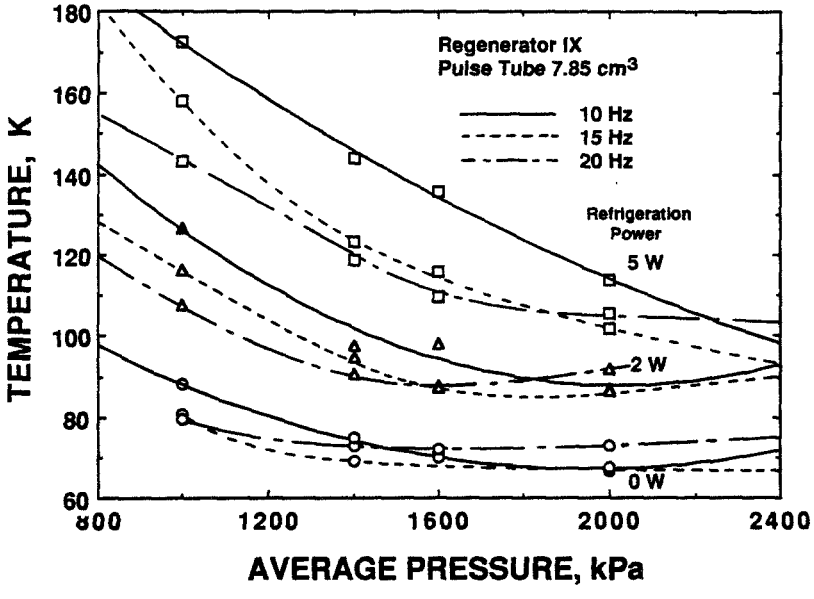

Figure 9. Temperature vs. pressure for 7.85 cm³ pulse tube and Regenerator IX.

6. Conclusions

We have found that the best pulse tube size for minimum temperatures with this compressor is about 7.85 cm^3, which corresponds to V_t/V_{co} = 0.35. At 94 K the value becomes V_t/V_{co} = 0.40. These results are only slightly lower than the calculated values of 0.43 and 0.56. The difference is presumably due to regenerator losses.

Stainless steel is a much better screen material for the regenerator than phosphor bronze because of reduced conduction. Nylon does not appear to be an improvement over stainless steel. A mesh size of 250 gave the best performance, but only with a G-10 tube to reduce tube conduction in the short length required for the fine mesh. A regenerator void volume of about 9.2 cm^3 gave the best performance. In reduced units we find V_{rg}/V_{co} = 0.41. This void volume applies only to a screen matrix. An improved configuration such as gaps should result in a lower regenerator void volume.

A low temperature of 67 K was achieved at 9 Hz with 2000 kPa, and 2 W of refrigeration at 80 K were obtained at 15 Hz with the same pressure. Further improvements could be made by lowering the hot end temperature from 40-45°C to about 25°C by the use of fins and a fan.

We acknowledge the generous contribution made by Hughes Aircraft Company, Torrance, California, for providing the compressor to us on a long term loan.

7. References

[1] Radebaugh, R., Pulse Tube Refrigeration-A New Type of Cryocooler, Japanese J. Appl. Physics 26, Suppl. 26-3, 2076 (1987).

[2] Radebaugh, R., Zimmerman, J., Smith, D.R., and Louie, B., A Comparison of Three Types of Pulse Tube Refrigerators: New Methods for Reaching 60 K, Adv. Cryog. Eng. 31, 779 (1986).

[3] Mikulin, E. L., Tarasov, A. A., and Shkrebyonock, M.P., Low Temperature Expansion Pulse Tubes, Adv. Cryog. Eng. 29, 629 (1984).

[4] Radebaugh, R., and Herrmann, S., Refrigeration Efficiency of Pulse Tube Refrigerators, Proc. 4th Int'l Conf. Cryocoolers, p. 119 (1987).

[5] Herrmann, S., and Radebaugh, R., Measurements of the Efficiency and Refrigeration Power of Pulse Tube Refrigerators, NBS Tech. Note 1301 (1986).

[6] Storch, P.J., and Radebaugh, R., Development and Experimental Test of an Analytical Model of the Orifice Pulse Tube Refrigerator, Adv. Cryog. Eng. 33, 851 (1988).

ALTERNATIVE METHODS OF THE ORIFICE PULSE TUBE REFRIGERATOR

Y.Matsubara
A.Miyake

Department of Atomic Energy Research Institute
College of Science and Engineering
Nihon University
Tokyo 101, Japan

1 Introduction

The lowest attainable temperature of the pulse tube refrigerator is greatly improved by use of an orifice and buffer volume [1,2]. However the refrigeration power per unit mass flow is still small in comparison to that of Stirling or G-M coolers. The small refrigeration power per unit mass flow induce the low overall performance as the cryocooler due to the high regenerator loss and the mechanical loss of the compressor system.

This paper describes the alternative methods to the orifice pulse tube refrigerator for the purpose of the improvement of the refrigeration power per unit mass flow rate.

2 Fundamental Model

According to the works developed by Radebaugh and coworkers, it is known that the refrigeration capacity of the orifice pulse tube increased as compared with that of basic pulse tube [3].

As one of the reason of this effect, we considered the pressure drop due to the mass flow across the orifice. The gas compression work must be increased when the mass flow exist at the orifice. This increased work is dissipated at the hot end of the pulse tube, which may induce the increased refrigeration capacity at the cold end of the pulse tube.

As an alternative method, which may also dissipate the gas compression work at the hot end of the pulse tube, we introduced the moving plug instead of the orifice as shown in figure 1. The difference between this moving plug and the expander or displacer of Stirling or G-M cycle is that the moving plug is operated at the room temperature. The movement of the plug must be controlled as it produce the optimum phase shift between the pressure and the volume change.

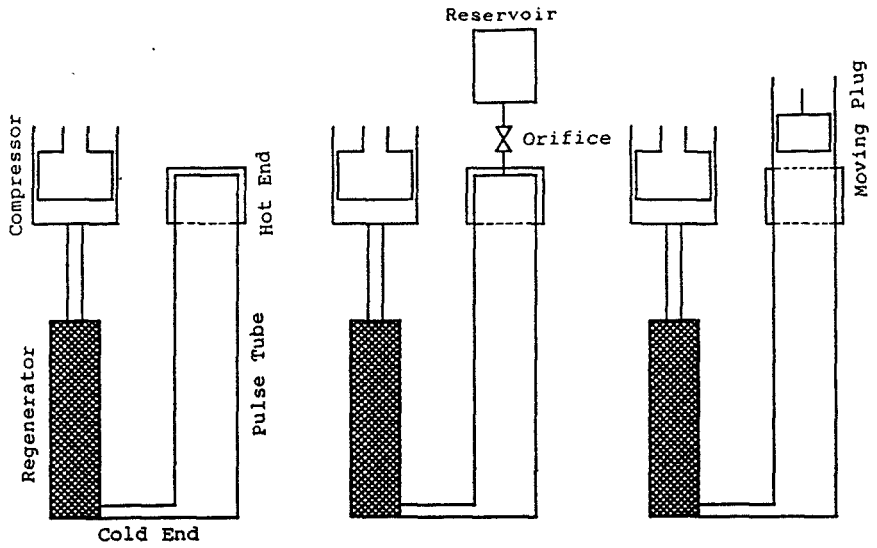

Fig.1 Schematic of pulse tube.

Typical controll methods are given in figure 2, schematically. A pair of check valves instead of moving plug is also applicable as shown in figure 2(d). In this case, the gas compression work may be dissipated by the circulating gas flow obtained at the hot end of the pulse tube, which is controlled by a valve installed between these check valves.

At first, we considered the orifice pulse tube. The sinusoidal change of the compressor volume, V_c, is given as,

$$V_c = 0.5\ V_{co}(1+\cos 2\pi ft) \quad \text{---------- (1)}$$

where, V_{co} is the maximum compressor volume, f is cycle frequency and t is time. Assuming the ideal gas and no pressure drop across the regenerator, constant volumes including the regenerator void, pulse tube and the hot end volume are summarized to an equivalent volume, V_{eq}, which gives the same total mass of the working gas at 300 K. The mass flow rate at the orifice, m_b, is given as

$$m_b = \alpha\ (P^2-P_b^2) \quad \text{---------- (2)}$$

where P is the pressure at the pulse tube, P_b is the pressure at the buffer volume and the constant α is assumed which may proportional to the orifice opening. Then the pressure equation is given as follows,

$$P = \frac{(m - m_b)}{(V_c+V_{eq})} RT \quad \text{---------- (3)}$$

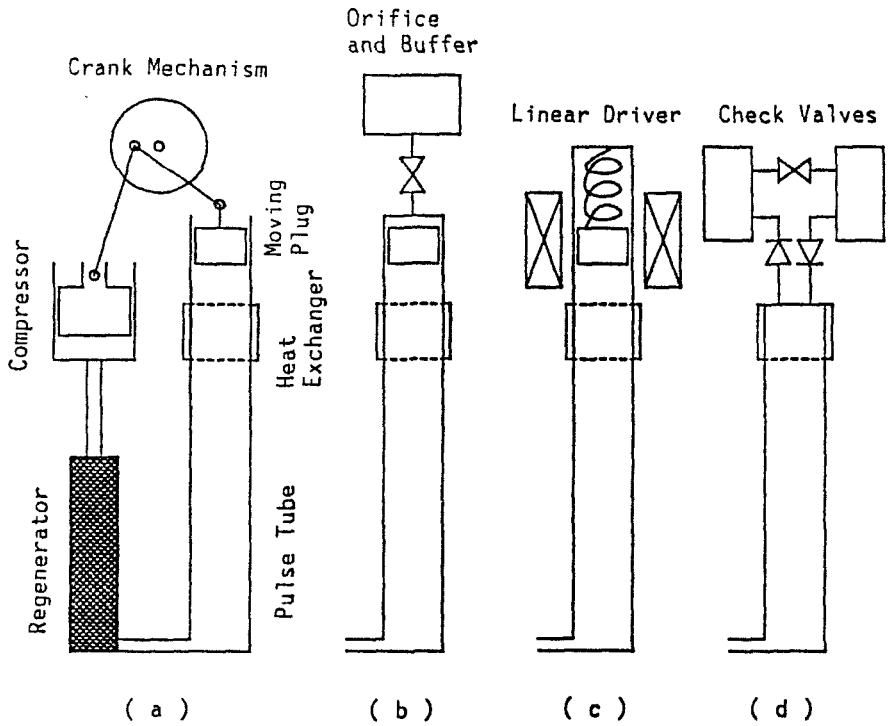

Fig.2 Typical controll methods of the moving plug.

$$m_1 = \frac{P_o}{RT}(0.5\ V_{co}+V_{eq}+V_b) \qquad \text{---------- (4)}$$

where, R is gas constant, P_o is initial pressure V_b is buffer volume and T is the equivalent temperature (= 300 K).

Equations (1)∿(4) were solved by Runge-Kutta method. Figure 3 shows one of the calculated results. After two cycles, we get almost stable oscillations. It is noted that the oscillation of m_b and P is almost in phase where the values of parameters listed on figure 3 are used. If the increasing entropy caused by the pressure drop at the orifice, due to the mass flow to and from the buffer volume, is given by the isothermal compression work, the following equation will be derived.

$$Q_b = m_b RT\ \ln(P/P_b) \qquad \text{---------- (5)}$$

The time integration of Q_b through one cycle may defined as the equivalent work at the orifice.

Figure 4 shows this equivalent work, Q_b, mass flow at the orifice and pressure ratio at the pulse tube. Increasing orifice opening increase the mass flow and decrease the pressure ratio. As the results, maximum Q_b is appeared.

Figure 5 shows the relation between m_b and Q_b. This figure also shows the same relation of the moving plug pulse tube, which is derived as follows. Consider the sinusoidal change of the moving plug, V_m,

$$V_m = 0.5\ V_{mo}[1+\cos(2\pi ft+\theta)] \quad \text{---------- (6)}$$

where V_{mo} is maximum volume and θ is the phase shift angle between V_m and V_c of equation (1). The pressure equation instead of equation (3) and (4) is expressed as,

$$P = \frac{m_1}{V_c+V_{eq}+V_m} RT \quad \text{---------- (7)}$$

$$m_2 = \frac{Po}{RT}(0.5\ V_{co}+V_{eq}+0.5\ V_{mo}) \quad \text{---------- (8)}$$

The cyclic integration of $P\ dV_m$ using equation (1),(4) and (7) gives the work extracted from the moving plug, Q_m. The curve in figure 5 was obtained for the variable V_{mo} when the $\theta=\pi/2$.

In comparison with the moving plug and orifice pulse tube, it is noted that the Q/m of the moving plug is greater than the orifice , however, it is almost same when the relatively small opening of the orifice or small displacement of the moving plug has been used.

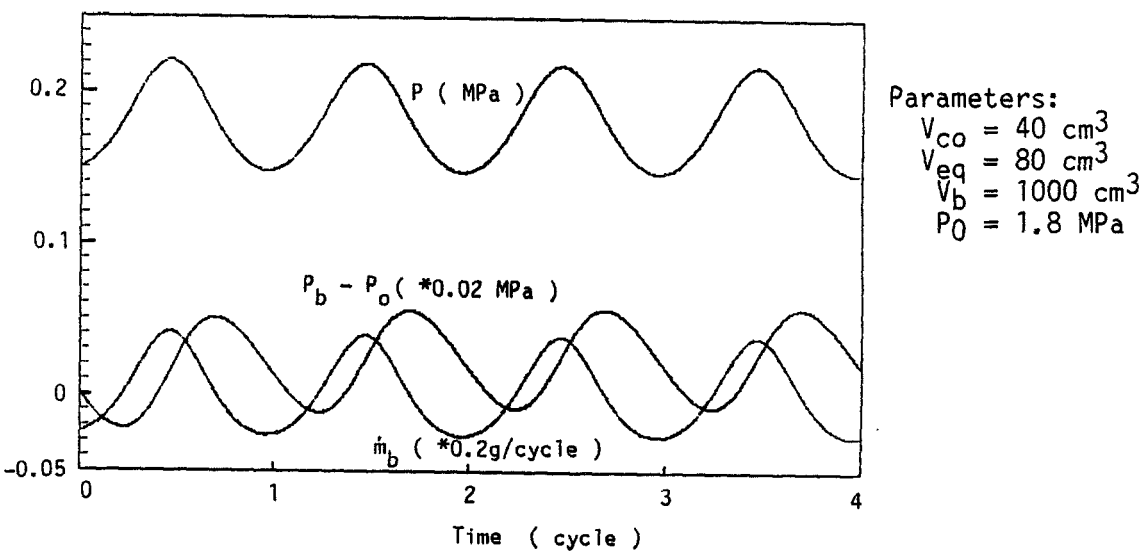

Fig.3 Pressure and mass flow trace of the orifice pulse tube

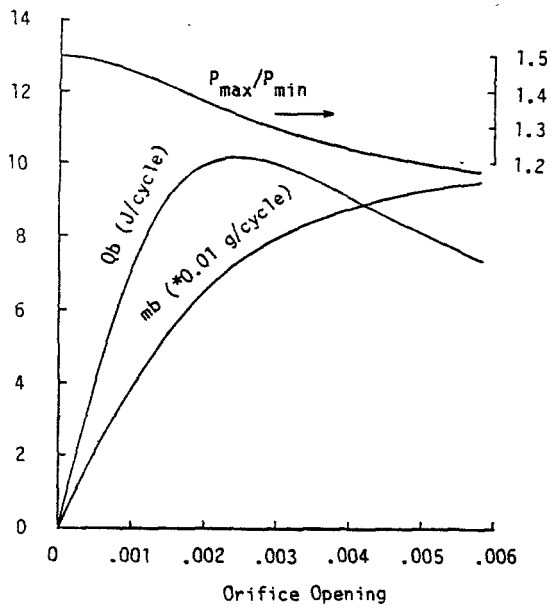

Fig.4 Equivalent work at the orifice.

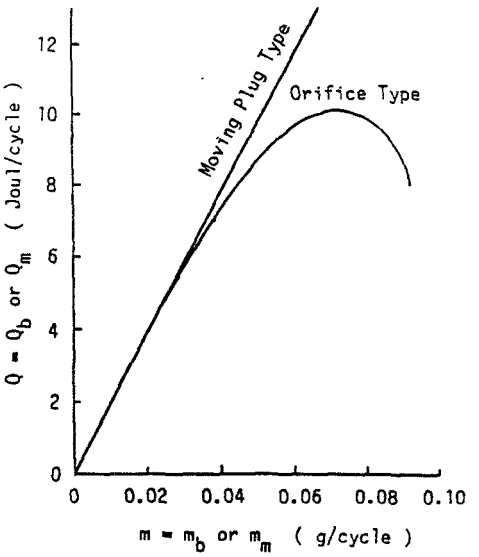

Fig.5 Comparison of Q/m.

3 Experimental Results

The experiments have been done by the apparatus as shown in figure 6 schematically. The oscillating pressure was supplied by the switching valves and the compressor for the G-M cycle cryocooler. The pulse tube is a stainless steel tube of 11 mm I.D., 0.5 mm thickness and 228 mm length. The copper isothermal region of 11 mm I.D. and 40 mm length was attached at the hot end of the pulse tube. Inside of the isothermal region, no heat transfer materials such as copper screen are installed. The water cooling channel was soldered at the isothermal region. A throttle valve as the orifice or a volume for the moving plug was connected by the copper tube of 2 mm I.D. and 180 mm length. The regenerator is a stacked 200 mesh copper screen of 36 mm diameter and 125 mm length.

Figure 7 shows the experimental results obtained by a same pulse tube with different hot end condition. In case of basic pulse tube, minimum temperature of 163 K was obtained at the cycle frequency of 3.5 Hz. The optimum orifice opening decrease the minimum temperature down to 78 K with increasing frequency of 6.5 Hz. On the other hand, the minimum temperature of the pulse tube with the moving plug was 73 K at 10 Hz.

This plug was made by the phenolic resin of 20 mm length having two cap seals and was installed in the stainless steel tube of 14 mm I.D.. The maximum displacement volume is 4.6 cm^3 which is 17 % of the pulse tube volume including the isothermal region. The displacement transducer was attached at the plug end. The pressure of this side of the plug end is

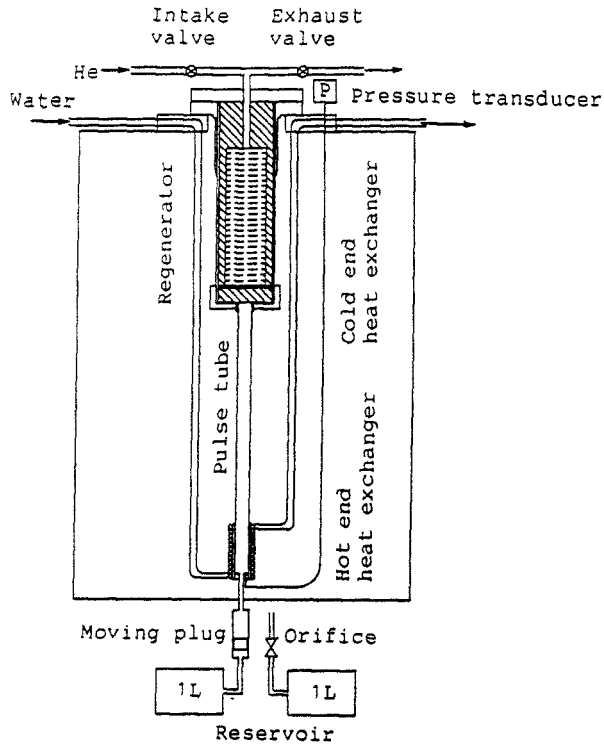

Fig.6 Schematic of test apparatus.

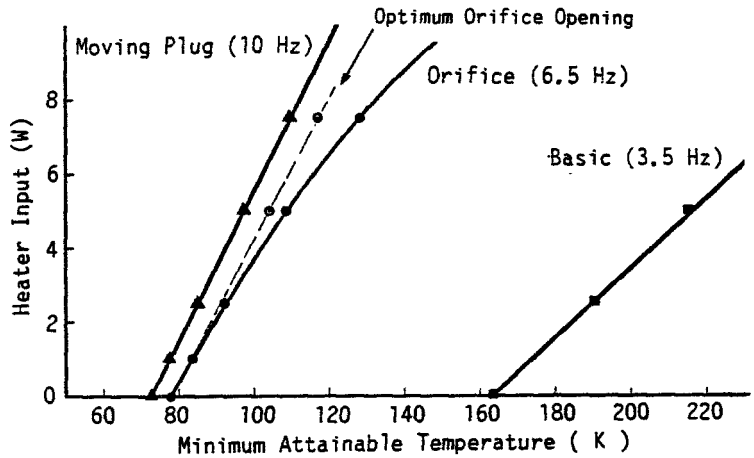

Fig.7 Refrigeration performance.

maintained at the mean pressure of the oscillating pressure in the pulse tube. The friction force of the cap seals was used as the phase shifter of the plug. The actual displacement volume of the plug at 10 Hz was not obtined at the full stroke condition and was decreased to 3.4 cm^3.

During the experiment of the moving plug pulse tube, the temperature of the isothermal region has been maintained near room temperature without cooling water. This result indicates the isothermal region may not required for the case of moving plug pulse tube.

Figure 8 shows the pressure waves of the orifice type and figure 9 shows the pressure wave and plug movement of the moving plug type when the cold end temperature was minimum. In the case of the orifice type, the pressure ratio was 1.49 and the maximum pressure difference at the buffer volume was 0.012 MPa. the mean pressure was 1.8 MPa. Assuming the isothermal condition, the mass flow at the orifice will be 0.019 g/cycle or 0.12 g/sec. In the case of the moving plug type, the pressure ratio was 1.27 and the mean pressure was 1.7 MPa. The phase angle, ψ, between the pressure and the plug displacement was about 52 degrees. Using these values, the mass flow increased by the moving plug was calculated below about 0.01 g/cycle or 0.1 g/sec.

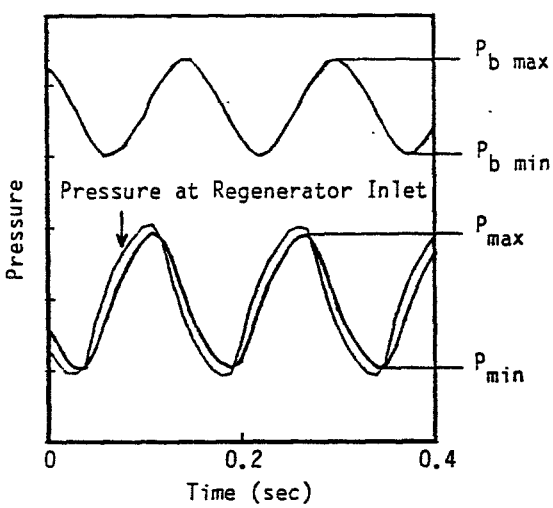

Fig.8 Pressure wave of orifice pulse tube.

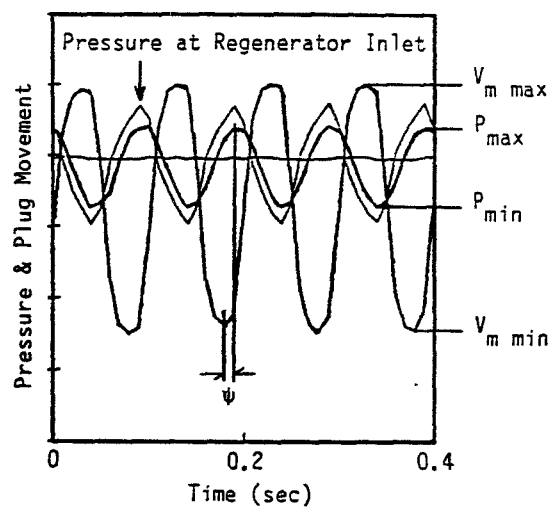

Fig.9 Pressure wave of moving plug pulse tube.

Figure 10 shows the relation between the pressure ratio and the minimum attainable temperature. These results indicate that the orifice type can be operate with the lower pressure ratio than the basic type, and the moving plug type can be operate with further reduced pressure ratio compared to the orifice type.

In the case of the moving plug type, the maximum frequency of 10 Hz was limmited by the pressure drop caused by the flow switching valve (rotary valve was used). As the results, the pressure ratio at the pulse tube was decreased to 1.27 which induce the small displacement of the plug. Therefore the possible operation at the higher frequency than 10 Hz may not be denied.

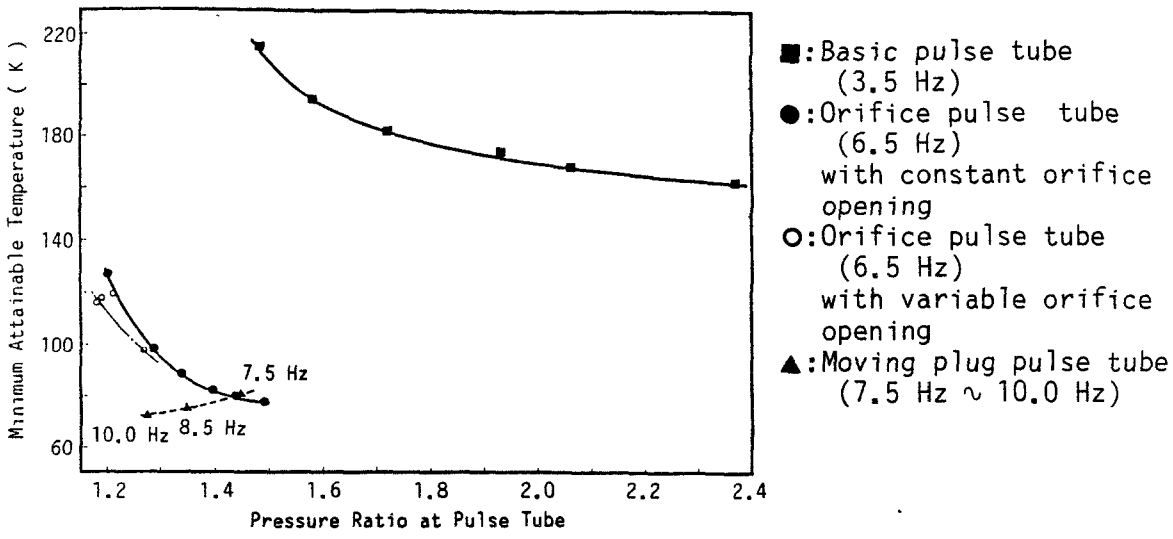

Fig.10 Minimum attainable temperature as a function of pressure ratio.

4 Conclusion

The reason of that the pulse tube refrigerator using ideal gas has the ability of the cryogenic temperature refrigeration will be based on the surface heat pumping effect through the pulse tube wall which is introduced by Gifford and Longsworth [4]. The pulse tube with orifice may be considered as the method having the ability of enhanced heat pumping effect. However the "orifice" is not an active device. Therefore there will be a limit to obtain the reasonable phase shift between the pressure and the temperature of the total mass in the pulse tube.

The moving plug instead of orifice is an active device, therefore it can be change the phase and the speed of the movement independently. The moving plug we used for this experiment is a simple plug only having the constant seal friction. Even though we have obtained the lower minimum temperature than the orifice type with same pulse tube. The quantitative discussion between the calculation and the experimental results is not performed so far. Further experiments using the controllable moving plug and the exact calculations should be performed to obtained the performance of the moving plug pulse tube refrigerator.

The merit of the simplicity of the pulse tube is decreased by adding the another moving parts, however, it may not serious problem because the moving components are still at room temperature. In the case of the refrigeration temperature higher than about 80 K, the Type (a) in figure 2 has another merit to improve the overall performance as the refrigerator, due to the recovering expansion work done by the moving plug.

Construction of much of the apparatus was done by M. Kaneko and is greatly appreciated.

5 References

[1] Mikulin, E.I., Tarasov, A.A. and Shkrebyonock, M.P., "Low temperature expansion pulse tubes", Advances in Cryogenic Engineering, Vol. 29, Plenum Press, New York, (1984), p. 629.

[2] Radebaugh, R., Zimermann, J., Smith, D.R. and Louie, B., "A Comparison of Three Types of Pulse Tube Refrigenerators: New Methods for Reaching 60 K", Advances in Cryogenic Engineering, Vol. 31, Plenum Press, New York, (1986), p. 779.

[3] Radebaugh, R. and Herrrmann, S. , "Refrigeneration Efficiency of Pulse Tube Refrigenerators", Proceeding of 4th International Cryocooler Conference, David Taylor Naval Ship, (1987), p. 119.

[4] Gifford, W.E. and Longsworth, R.C., "Surface heat pumping", Advances in Cryogenic Engineering, Vol. 11, Plenum Press, New York,(1966), p. 171.

TWO-STAGE PULSE TUBE REFRIGERATOR

Yuan Zhou, Wenxiu Zhu and Jingtao Liang
Cryogenic Laboratory, Chinese Academy of Sciences
Beijing, People's Republic of China

ABSTRACT

Experimental investigation of two-stage pulse tube refrigerator has been carried out in our lab recently in order to achieve lower temperature. Both stages are composed of the same type of orifice pulse tube, they are connected to two pressure wave generators separately. The first stage pulse tube being 19mm in diameter by 400mm in length, provides precooling through two small heat exchangers for the second stage pulse tube, being 11mm in diameter by 300mm in length, the helium gas reservoir for the second stage is connected to the hot end of the second stage pulse tube via a regenerator and an orifice. The experimental results showing the temperature ratio between the two ends of the second stage pulse tube versus the pressure swing ratio and the orifice flow area in the second stage will be presented in this paper.

INTRODUCTION

Recently a low temperature of 60K using helium gas in a one stage orifice pulse tube has been achieved a NBS. [1] And the investigation of pulse tube with axial curvature shows the possibility of constructing a pulse tube refrigerator within a compact space with good performance. [2] Because the pulse tube refrigerator has no moving part at low temperature, it has the potential for high reliability and, with multiple stages it may replace Stirling, Gifford-Mcmahon and Joule-Thomson refrigerators in some cases for temperatures down to about 15K. It is even possible to build a small-sized or medium-sized helium liquefier by adding a J-T stage to a mul-ti-stage orifice pulse tube refrigerator. Since the temperature that can be reached with a single-stage orifice pulse tube refrigerator is limited, we turn to two-stage orifrice pulse tube refrigerator for lower temperatur, One approach to form a two-stage orifice pulse tube refrigerator is to add an orifice and gas reservoir to each stage of a two-stage basic pulse tube[3], as shown in Fig.1. This arrangement is not practically feasible in two reasons:

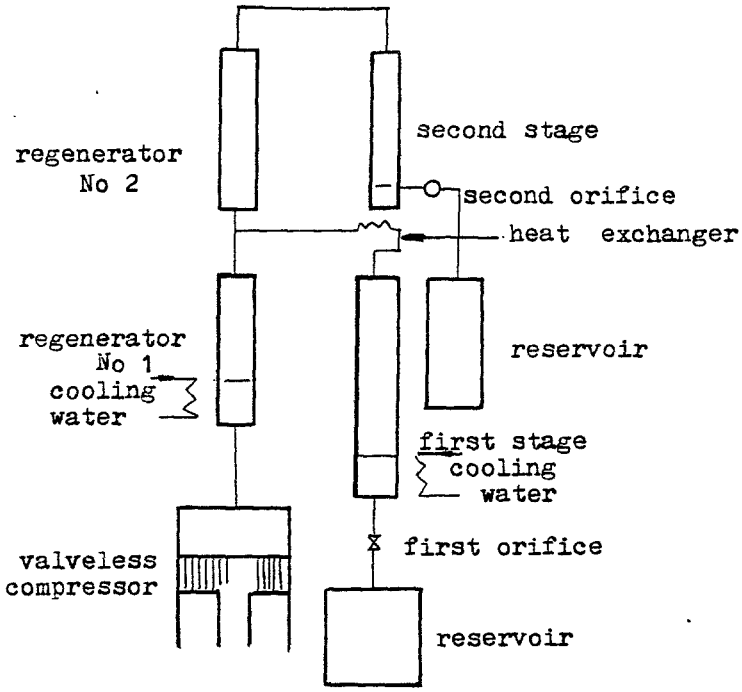

Fig. 1 Two-stage pulse tube schematic

i] The gas reservoir in the second stage is placed at low temperature and needs a large amount of refrigeration power to precool it.

ii] The hot end of the first stage is no longer closed, and the flow resistance of the second stage regenerator which is packed with small lead pills is much larger than that of the orifice of the first stage, therefore very little helium gas can get into or out of the pulse tube of the second stage.

To our knowledge, no construction and testing of such a two-stage orifice pulse tube refrigerator have been reported so far. This paper presents the propositions and results of experimental investigation of two-stage pulse tube refrigerator of different design. A lowest temperature of 31K has been achieved in second stage pulse tube, being of 9.5mm in diameter by 300mm in length with maximum and minimum pressures of 0.95MPa and 0.6MPa respectively at a frequency of 5Hz,while the first stage pulse tube is of 19mm in diameter by 400mm in length with a cold end temperature of 98K.

PROPOSITION FOR A PRACTICAL TWO-STAGE REFRIGERATOR

To improve the system shown in Fig.1, we propose two-stage orifice pulse tube refrigerator as shown in Fig.2. The large gas reservoir of the second stage with volume of 1.2 liters can be placed at room temperature by inserting a regenerator between the orifice and this gas reservoir. Thus

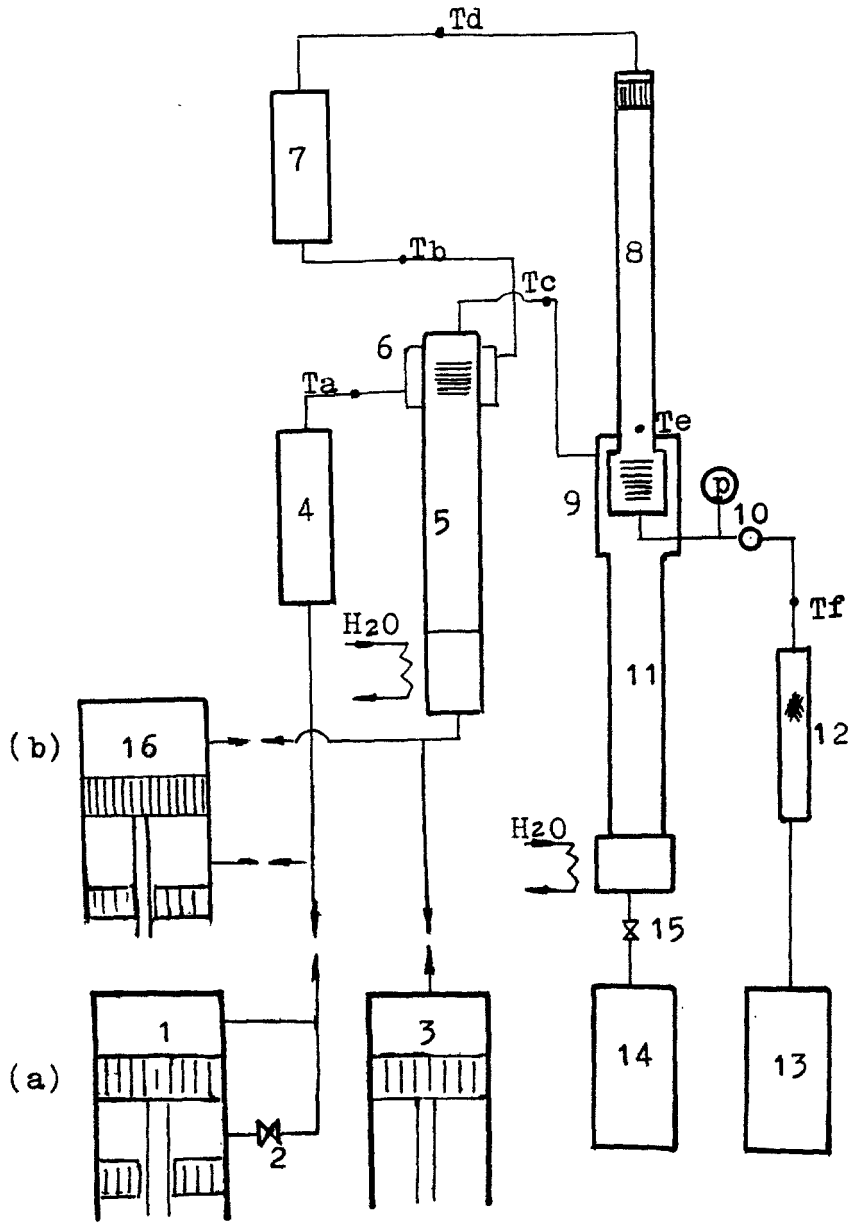

Fig. 2 Two-stage orifice pulse tube schematic, in which: 1 valveless compressor for second stage 2 by-pass valve 3 valveless compressor for first stage 4 warm regenerator for second stage 5 regenerator for first stage 6 heat exchanger 7 cold regenerator for second stage 8 second stage pulse tube 9 heat exchanger 10 second stage orifice 11 first stage pulse tube 12 regenerator for second stage 13 second stage reservoir 14 first stage reservoir 15 first stage orifice

the starting time of the first stage can be greatly reduced. The gas distribution problem can be solved by providing pressure waves separately for each stage. In Fig.2 (b) the compression volume of the pressure wave generator is divided into two by the piston which oscillates back and forth and produces pressure waves for the two stages. In Fig.2 (a) two pressure wave generators are used to produce pressure waves for the first stage and the second stage respectively. In both cases, the hot end of the second stage pules tube is linked to the cold end of the first stage by heat exchanger 9 packed with 25 layers of copper discs with 20 punched holes on each, and heat exchanger 6 being disposed between the warm regenerator and cold regenerator of the second stage is used to compensate for the warm regenerator loss with part of the refrigeration power of the first stage and is packed with 30 layers of copper discs with 25 punched holes on each. The other side of both exchanger 6 and exchanger 9 is screw surface for increasing the area of heat transfer. Instead of using a needle valve as in the first stage, we use a brass plate being 2mm in thickness with a small hole that is welded into the connecting tube as the second stage orifice, which can be changed to observe the influence of the flow area of the second stage orifice on the lowest temperature that can be achieved by the system (as shown in Fig. 3).

The dimensions of the pulse tube and regenerators of the two stages used in the experiments are listed in Table 1.

Table 1 Dimensions of two-stage pulse tube.

Items	Length (mm)	Internal dia.(mm)	Wall thickness (mm)	Volume $(cm)^3$
First stage pulse tube	400	19.0	0.5	113.4
Second stage pulse tube	300	11.0	0.5	28.5
		9.5	0.25	21.3
Regenerator 5	180	24.0	0.5	81.4
Regenerator 4	160	24.0	0.5	72.3
Regenerator 7	80	21.0	0.5	27.7
Regenerator 12	140	15.0	0.5	24.7

GENERAL DESCRIPTION OF EXPERIMENTS

Most experiments were done with the two-stage system shown in Fig.2. We varied the pressure ratio of the

second stage by adjusting the by-pass valve disposed between the compression volume and the crankcase of the compressor to observe the change of the ratio of the hot end temperature to the cold end temperature of the second stage pulse tube. We also investigated the relationship between the above temperature ratio and the ratio of orifice diameter to pulse tube diameter for the second stage by changing the orifice diameter. The average pressure used in these experiments was approximately 0.8MPa with a pressure range of 0.65 - 1.0MPa for the second stage. The pressure of the second stage pulse tube was measured with an absolute pressure transducer of the variable reluctance type attached to the hot end of the second stage pulse tube.The displacement volume of the valveless compressor of the second stage with a fixed frequency of 5Hz is 400cm^3. Temperatures at different points of the system illustrated in Fig.2 were measured with copper vs constantan and gold-iron vs nickel-chromium thermocouples. The low temperature part was thermally insulated from the surroundings with avacuum of $3x10^{-5}$ torr, but no radiation shield was used. Helium gas was used for all runs. About one and a half hour was required for the two stage orifice pulse tube refrigerator to reach the lowest temperature.

Then we substituted the pulse tube of the second stage with a smaller tube which was 9.5mm in diameter by 300mm length to observe the influence of the ratio of the first stage pulse tube volume to the second stage pulse tube volume on the lowest temperature.

We experimentally tested the two-stage orifice pulse tube refrigerator shown in Fig.2(b) only to demonstrate the possibility of using only one moving part at room temperature for a two-stage orifice pulse tube refrigerator.

EXPERIMENTAL RESULTS AND DISCUSSION

Fig. 3 shows the ratio of the hot end temperature to the cold end temperature as a function of the pressure ratio for the second stage. We can see that the temperature ratio increases almost linearly with the increase of pressure ratio, this is consistent with the analytical results[4].

Fig. 4 shows the temperature ratio varying with the ratio of the orifice diameter to the pulse tube diameter for the second stage. When the diameter ratio is 0.08, the temperature ratio reaches a maximum. But when the hot end is closed (zero orifice diameter) and the pressure ratio is less than 1.3, the temperature ratio becomes less than 1, that is the "hot" end temperature becomes lower than the "cold" end temperature. One possible explanation for this phenomenon is that the regenerator loss due to the heat generated by the friction between helium gas and the matrix at the cold end of regenerator surpasses the refrigeration capacity of second stage pulse tube, This problem needs to be further investigated.

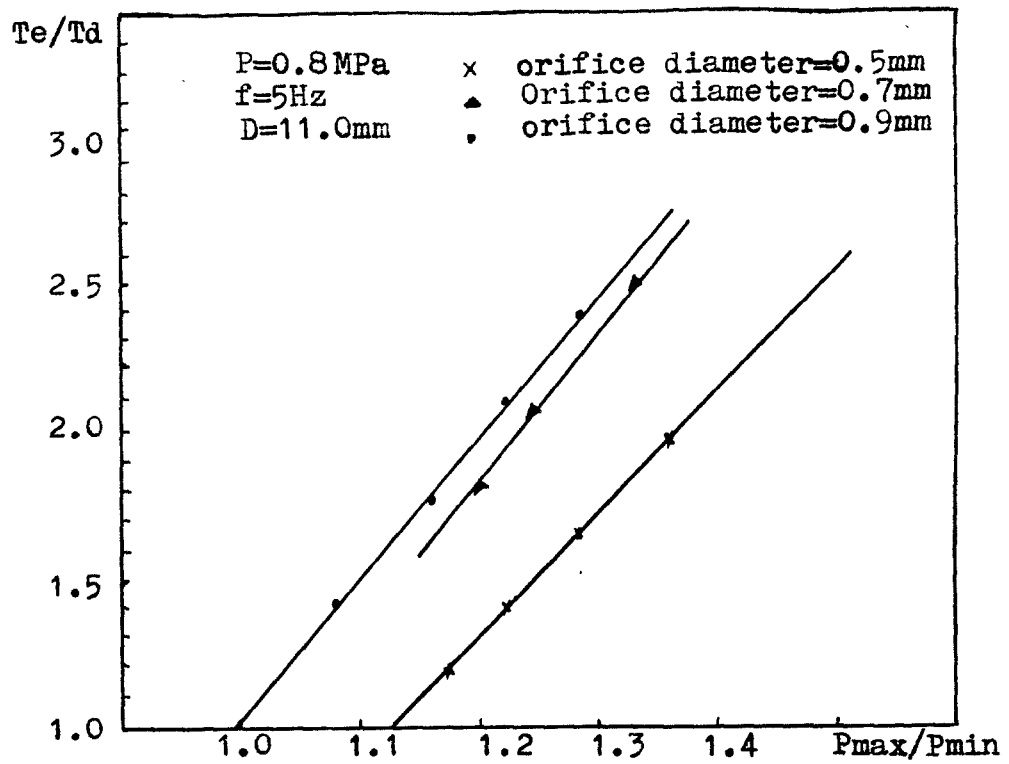

Fig. 3 Temperature ratio vs the pressure ratio for second stage

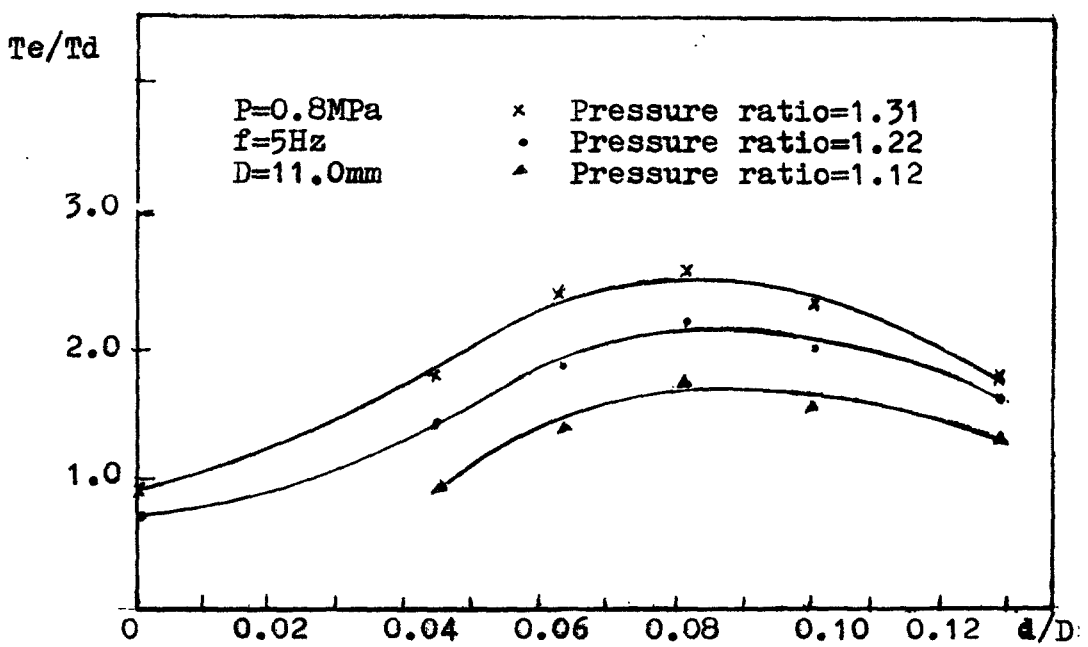

Fig. 4 Temperature ratio vs the ratio of the orifice diameter to the pulse tube diameter for second stage

Table 2 Temperature of different points in the two-stage pulse tube refrigerator

Items	The system in Fig.2(a)	The system in Fig.2(a)	The system in Fig.2(b)
Ta (K)	108	103	109
Tb (K)	103	102	107
Tc (K)	98	98	104
Td (K)	44	31	53
Te (K)	106	103	105
Tf (K)	110	104	114
Te/Td	2.4	3.3	2.0
Dia. of 2nd stage (mm)	11.0	9.5	11.0
Orifice dia. (mm)	0.9	0.7	1.1
Frequency (Hz)	5	5	8
Pmax/Pmin (MPa/MPa)	0.7/0.92	0.6/0.95	0.9/1.05

The lowest temperature of 31K achieved with the system shown in Fig.2(a) by substituting the 11.0mm diameter tube of the second stage with a 9.5mm diameter tube and the temperature at different points of the system when it is in operation are listed in Table 2. From Table 2. losses of regenerators and heat exchangers are rather large with the dimensions and constructions adopted in our experiments. To obtain lower temperature at the cold end of the second stage, it is necessary to improve the regenerators and heat exchangers to reduce the heat load at the cold end of the first stage and thus lower the hot end temperature of the second stage pulse tube. From Table 2 we can also see that a smaller second stage pluse tube cooperates better with the first stage, in other words, a larger ratio of the pulse tube volume of the first stage to the pulse tube volume of the second stage is more suitable in this case. With a smaller second stage pulse tube the pressure ratio of the second stage can be increased and thus lower temperature can be achieved.

The test apparatus were not operating at optimum working conditions. It may be possible to reach 25K or lower if the pressure ratio of the second stage is increased and better regenerators and heat exchangers can be made as well.

CONCLUSIONS

i] Due to the flow resistance in two-stage pulse tube, special difficulties are met in constructing a practical two-stage

machine. A practical two-stage orifice pulse tube refrigerator is proposed and experimentally tested, and prove to be practical feasible and effective.

ii] Experiments show that the temperature ratio of the second stage increases almost linearly with the increase of the pressure ratio of the second stage and that it becomes maximum at a certain diameter ratio between the orifice and pulse tube of the second stage. A lowest temperature of 31K was achieved. This two-stage system has the potential for reaching lower temperatures.

ACKNOWLEDGMENTS

The authors wish to thank Prof.C.S. Hong for his help and discussion to this paper.

REFERENCE

1 S.Herrman and R.Radebanugh "Measurments of the efficiency and Refrigeration power of pulse tube refrigerators" NBS Thchnical Note 1301 (1986).

2 Yuan Zhou,Wenxiu Zhu and Yen sun "Pulse tube with axial curvature". "Advances in Cryogenic Engineering" Vol. 33 Plenum Press, New York, (1987)

3 W.E.Gifford and R.C.Longsworth "Pulse-Tube Refrigeration" Transactions of the ASME 264 (1964)

4 Peter J. Storcth and Ray Radebaugh "Development and experimental test of an analytical model of the orifice pulse tube refrigerator". "Advances in Cryogenic Engineering" Vol. 33 Plenum Press, New York, (1987)

SESSION IV

STIRLING REFRIGERATORS I

CHAIRPERSON: A. DEVILLIERS
VICE CHAIRPERSON: G. WALKER

LONG LIFE STIRLING CRYOCOOLER FOR SPACE APPLICATIONS

R. McFarlane, C. S. Keung, M. A. Shaik, M. Starr
Philips Laboratories
Briarcliff Manor, New York

The 5 W 65 K first generation refrigerator developed by Philips Laboratories in the early 1980's for NASA is continuing on life test with over four years of operation logged. This paper reviews the design innovations incorporated into the second generation refrigerator of the same cooling specifications, now nearing completion. Among the new features described are high efficiency linear motors with magnetic springs and closed loop digital control, magnetic bearing suspension with fiber-optic position sensors, active counterbalancing with linear motor and gas spring combination. The above features, together with clearance seals and hermetic containment of outgassing materials, result in a long-life highly efficient cryocooler.

1. Introduction

Philips Laboratories completed and put into operation in 1983 a laboratory model of a unique 5 Watt 65 K linear resonant Stirling cryocooler [1], intended to prove the feasibility of continuous unattended operation in space over a period in excess of 5 years, without degradation of performance. Long life is achieved by eliminating contact and the associated wear and by simplification of the mechanical drive. The moving compressor and displacer elements are driven by electronically controlled linear motors and are suspended by closed loop controlled active magnetic bearings, permitting the use of clearance seals. The laboratory model continues to function under life test, having exceeded 38,000 hours of operation without degradation of performance.

In this paper, we describe the additional innovations incorporated into a flight qualified cryocooler under construction, capable of withstanding launch loads. During the launch period, the magnetic bearings are active and must have sufficient stiffness to maintain the clearance seal without touchdown. The gap between bearing surfaces was reduced to 20 microns to improve bearing stiffness and thermodynamic efficiency. In order to conserve electrical energy, the linear motors, bearing electromagnets and the electronic circuitry for driving them were designed for optimum efficiency by the use of rare earth cobalt magnets, high permeability magnetic materials and pulse width modulated amplifiers. Fiber-optic sensors were designed for monitoring shaft radial position to provide closed loop control of the magnetic bearings. These sensors offer a combination of high sensitivity, simplicity and hermeticity. Custom designed linear position sensors ensure precise phase control between compressor and displacer and reduction of vibration by an active counterbalancing system. The operating point of the cryocooler is established and monitored by a system controller which also provides graceful startup and shutdown, safety interlocks and the option of local or remote control.

Section 2 of this paper gives an overall description of the refrigerator; Section 3 describes radial position sensors used in the magnetic bearings; Section 4 describes the active counterbalance used to cancel vibrations; Section 5 the axial controller used to control reciprocatory motion of the pistons; Section 6 the system controller; and Section 7 describes some structural analysis including natural frequency calculations. In Section 8 the current status of the refrigerator program is given.

2. System Description

The cryogenic refrigerator described here is a single expansion stage machine operating on the closed Stirling cycle. The refrigerator will provide 5-Watt cooling at 65 K. All three of the moving parts are linearly reciprocated within their cylindrical housings and are radially

supported by active magnetic bearings.

The refrigerator is comprised of a compressor, a single stage expander, and a counterbalance (Figure 2.1). The expander section contains the displacer with a built-in regenerator and the cold and warm side heat exchangers. The compressor contains the compressor piston and piston linear motor. The counterbalance contains the countermass, which is part of the motor armature, and the two gas springs designed to resonate the countermass at the refrigerator reciprocating frequency. All the gas seals are clearance type provided by the magnetic bearing clearance. The piston (compressor) and the countermass are reciprocated with a moving magnet linear motor (no flexing leads). The displacer is reciprocated with an integrated magnetic spring/motor [2].

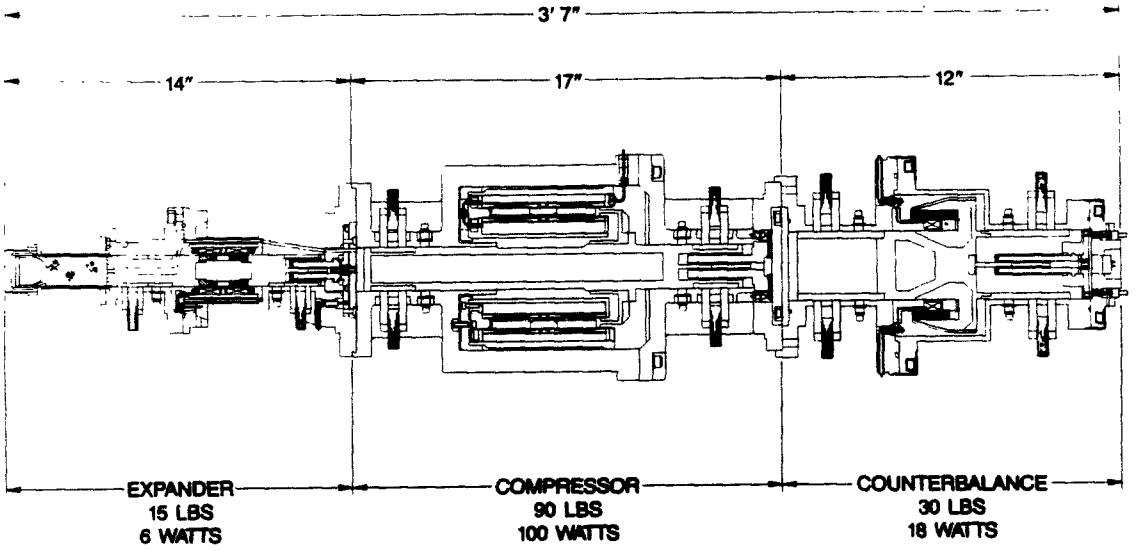

Figure 2.1. Philips/NASA Stirling Refrigerator

Since last reported [3], design changes have been made in the radial position sensors. Originally, ferrite reluctance sensors were selected to provide radial position sensing. During component testing, it was found that the hermetic joining of ferrite to the titanium alloy housing was difficult to achieve. Also, further testing revealed that a large change in sensor output due to magnetostriction effect (caused by launch and temperature induced stresses) could create false position readings. Alternate sensing schemes surveyed included optical and capacitive sensing. Capacitive sensing is limited by achievable bandwidth. Optical sensors were selected to replace ferrite reluctance sensors. Optical sensors were successfully fabricated and their performance was confirmed.

3. Radial Position Sensors

The sensors provide a measurement of shaft radial position; their output, after processing and amplification, actuates the magnetic bearing polepieces. The following sensor characteristics were desired: range of $50\mu m$, resolution better than $1\mu m$, high linearity and bandwidth, and low temperature sensitivity.

The sensors are built using fiber optic components. Light from an infrared LED passes through a set of fibers, is reflected by the shaft into another set of fibers, which convey it to a light sensing phototransistor. The sensed light varies with respect to shaft position. The shape

of the response curve depends on the arrangement of the illuminator and receiver fibers -- i.e., whether they are randomly intermixed, are formed into two separate circular bundles, or of any other geometry.

Given N_i illuminator fibers and N_r receiver fibers, the sensor response is the sum of the $N_i \times N_r$ illuminator-receiver pairs. A model of pair response was developed. Figure 3.1 shows elements dS_i and dS_j on illuminator and receiver fibers respectively. Given the LED/fiber output intensity characteristic I_{θ_i}, the law of radiative interchange gives the light energy coupled between these elements:

$$dP_i \propto \frac{I_{\theta_i} I_{\theta_r} dS_i dS_r}{(2y)^2+(r)^2}$$

where I_{θ_r} is the receiver fiber/phototransistor characteristic, y the target distance, and r the distance between the element normals. The element response is summed over the illuminator and receiver fibers to give the pair response. Pair responses are summed to give sensor response. The above model agrees well with experiment.

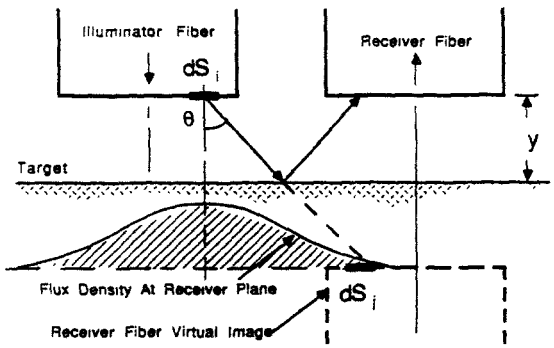

Figure 3.1. Calculation Of Fiber Pair Response

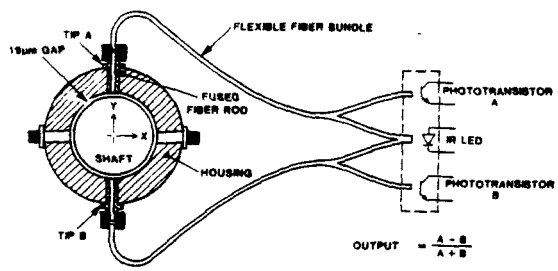

Figure 3.2. Magnetic Bearing Sensor

Figure 3.2 shows the magnetic bearing sensor. One LED serves as a common light source for an opposing pair of fiber bundles. The signals from the opposing phototransistors, A and B, are processed by analog circuitry to indicate shaft position according to

$$y = 10^*(A-B)/(A+B)$$

The above ratio is independent of common mode variations due to diode aging, phototransistor temperature, or mean shaft reflectivity changes over time. Sensor linearity was measured to be within 3% of full scale output. Electronic noise referred to displacement error is 4nm. Sensitivity is good with change in each phototransistor signal of 3% of mid-position output. Temperature coefficient referred to displacement is low at $.04\mu m/^\circ C$.

4. Counterbalance

An active counterbalance is used to attenuate the vibration of this refrigerator. The counterbalance consists of a spring-mass system with the motion of the mass being actively controlled by a linear motor. A double-acting gas spring with clearance seals was selected because of its simplicity and long life. Magnetic bearings are used to suspend the gas spring piston which functions as the countermass and the motor armature (Figure 4.1). Design concepts to achieve long life in the refrigerator were also used in the counterbalance.

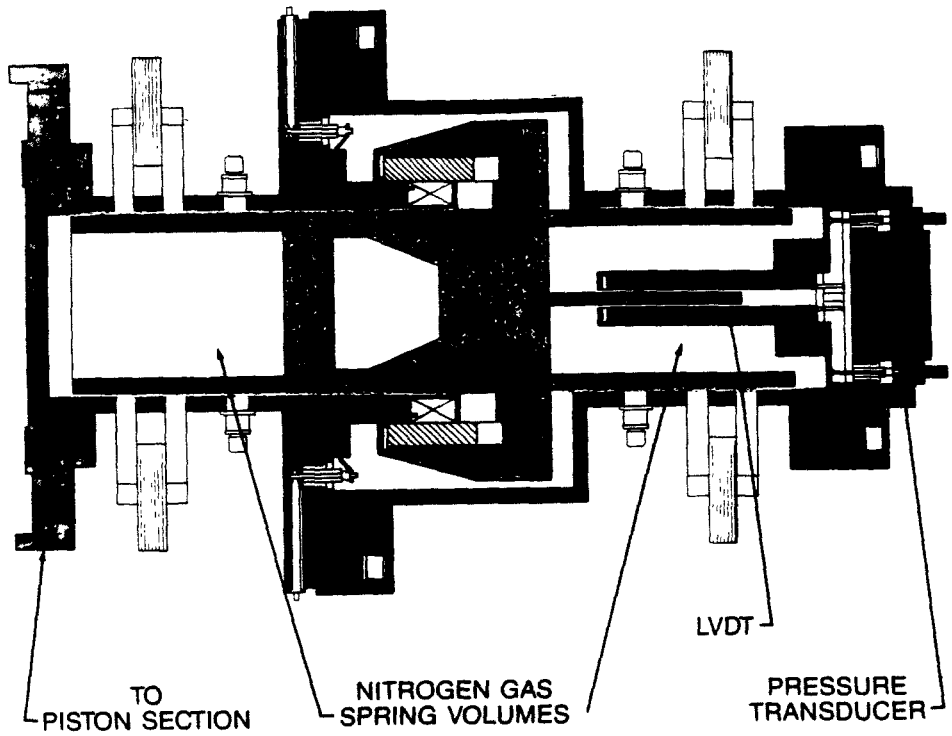

Figure 4.1. Counterbalance

Ideally the countermass should be accelerated in opposition to the sum of the accelerations of the compressor piston and the displacer. The position signals from the piston and displacer LVDTs are summed by analog circuitry to obtain the counterbalance drive signal.

One of the concerns in designing the counterbalance is the efficiency of the gas spring, as the available power is limited in most space applications. A test was conducted to evaluate the performance of the gas spring. The result showed that the double-acting gas spring with a stiffness of 40,700 N/m has a spring loss of 10 Watts. This experiment also showed that nitrogen behaved adiabatically in this spring design.

The gas spring is filled with nitrogen at a pressure of 0.46 MPa. The gas-spring piston/countermass has a diameter of 70 mm and operates with an peak amplitude of 6 mm at 18.9 Hz. Each side of the double-acting spring has a mean volume of 230 cc and a maximum to minimum volume ratio of 1.22.

5. Axial Control

The resonant nature of the system of motors and springs (gas and magnetic) ensures that the position versus time characteristic will be essentially sinusoidal. This obviates the need for a high bandwidth servomechanism to produce the desired rectilinear motion. Thus, the piston and displacer axial control system consists of a simple motor driver amplifier, a linear position transducer and a digital controller/compensator.

The controller/compensator is a microprocessor-based subsystem which compares the

measured position to preprogrammed parameters and produces a compensated (via digital PID techniques) voltage output from the driver to minimize the motion errors. The block diagram of Figure 5.1 describes the essential axial control system with the software elements highlighted in gray. The hardware implementation of the shaded areas requires three integrated circuits. Motor position is monitored via an LVDT (Linear Variable Differential Transformer) which has been incorporated within the motor housing. The LVDT returns a voltage proportional to the piston position.

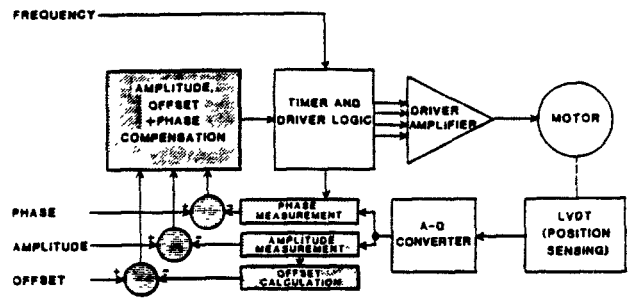

Figure 5.1. Axial Control System

The relationship of motor position response to applied motor voltage is summarized in Figure 5.2. A symmetric pair of voltage pulses are applied to the motor during each reciprocating cycle. The period between the pulses dictates the operating frequency and is, in practice, selected to drive the motor at its mechanical resonant frequency (Figure 5.2a). By increasing or decreasing the pulse width symmetrically, the amplitude of oscillation can be modified (Figure 5.2b). The disproportionate applied voltage will cause the motor to favor one direction of drive and hence change the mean position. Once the motor has reached the desired offset position, the voltage imbalance must be removed and the motor will continue to oscillate about the new mean value.

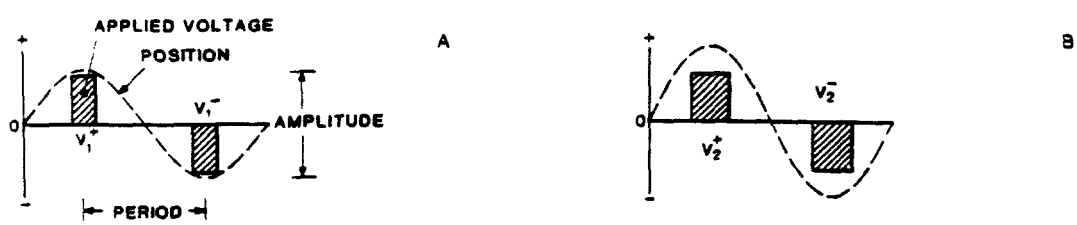

Figure 5.2. Effect Of Applied Voltage On Motor Position

Phase control is implemented by shifting the temporal relationships of each of the voltage drive waveforms relative to an independent reference signal. (Although it would be possible to control one motor relative to the other directly, the use of an independent reference permits each controller to be identical and treats mechanistic interactions as disturbances to each isolated servo control loop. Such an arrangement will permit the use of any number of motors.)

Performance testing of the axial control system was accomplished using a computer and data acquisition system which monitored the simulated position output of a model piston motor. Subsequent verification tests were performed on the first generation Engineering model. Both amplitude and offset control are excellent and will typically provide operation within 0.2% of the desired values. The accuracy of the phase control is dependent on the shaft amplitude and ranges from within 0.5 degrees (mechanical) at maximum amplitude to 1.5 degrees at 10% of

maximum.

6. System Controller

The system controller for the Philips/NASA cryocooler is a microprocessor-based system which operates the various subsystems to support cooler operation. The controller provides an orderly sequence of operation on both startup and shutdown, monitors interlocks, responds to faults and provides an interface through which the user can command or monitor operation (see Figure 6.1).

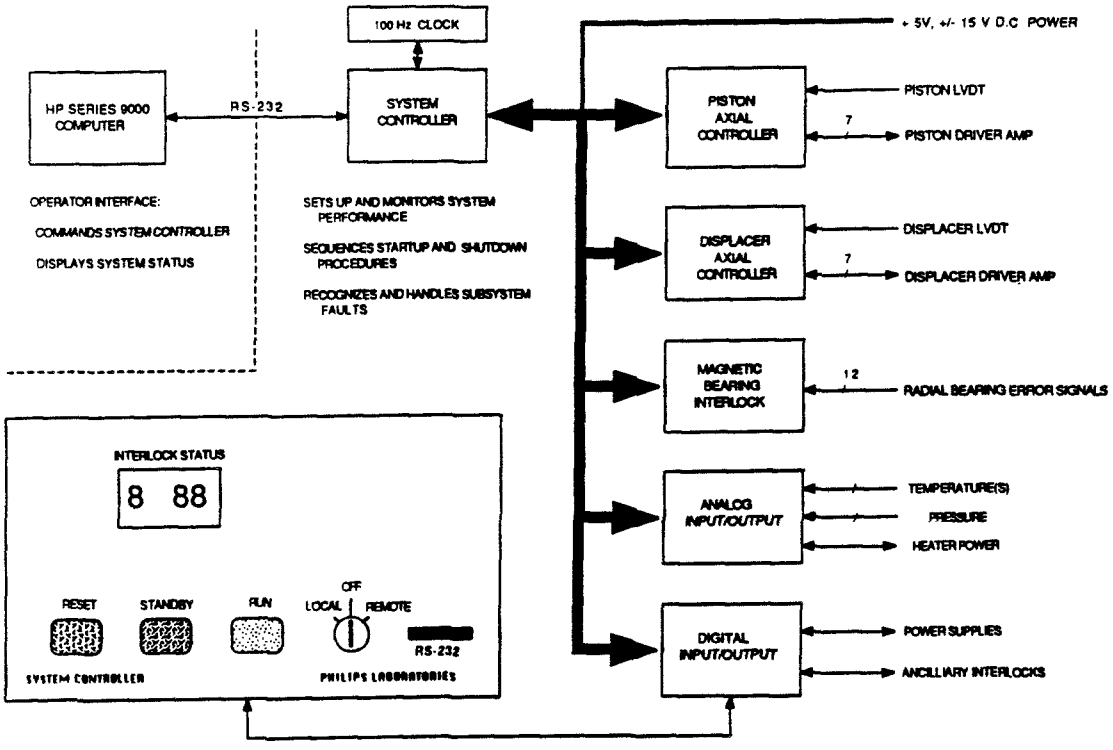

Figure 6.1. System Controller

The interface operates on two levels; a local mode, which provides simplistic control of the essential cooler functions; and a remote mode, in which a desktop computer (and software) provides an extended command set and displays detailed status information. The operation of the control system software is described below.

An initialization sequence checks the status of critical subsystems and will prevent startup if faults are detected. Error codes are presented on the front panel INTERLOCK STATUS display. If the system is ready, the front panel RESET button will light indicating that the D.C. power is on and that the magnetic bearings are active. From RESET, one may only proceed to the STANDBY mode (launch mode), in which the axial drives are held at a centered position. Cooling is initiated by going to the RUN mode. The RUN mode is started with axial drives operating at a designated nominal motion. This motion is gradually increased, in a controlled fashion, to the final operating point (maximum cooling output). Operation will continue unless the system is instructed to return to the STANDBY or RESET mode, or if it is forced to the RESET mode by the interlock system.

The interlock system is active in both the local and remote mode and utilizes prioritized recognition of system faults to provide maximum protection to the cooler mechanism. The interlock system is both hardware and software supported, depending on the response requirements of the particular subsystem.

The magnetic bearing interlock, for example, is a hardware scanning device which signals the controller processor if any of the 12 bearing error signals is out of tolerance. The high priority service routine decides if the fault is severe enough to warrant a shutdown or if operation can continue with an increased margin for error. This provides a 'fault tolerant' environment which warns of a deteriorating situation while permitting operation to continue for as long as possible.

The axial controllers (piston and displacer) are implemented with dedicated processors, which accept commands from the system controller, control motor operation and handle axial faults within a local environment. The axial controller status is monitored by the system controller. A fault condition will return the system to a RESET state.

The D.C. power system is of a redundant design, which relaxes the requirement for a high priority response time. Power supply status is monitored periodically and warnings are issued if any fault is detected while the cooler is running. A severe power fault would be handled effectively by the high level interlocks (i.e. bearing). The power supply error would then be detected during a subsequent system startup procedure.

The remaining interlocks monitor ancillary signals (temperature, pressure) which do not tend to change rapidly with time. These are tested periodically, and system response depends upon the severity of the fault.

In all cases, a system shutdown is sequenced to prevent (or minimize) damage to the mechanical components of the cooler. This is generally accomplished by disabling the axial drives to stop linear motion and then removing 28V D.C. power from the axial and radial subsystem drivers, and finally, reporting the fault to the appropriate interface.

7. Structural Analysis Of Refrigerator

The finite element program ANSYS [4] was used to calculate stresses, deflections, and natural frequencies of the main components of the refrigerator structure. Conventional beam analysis methods were also used on simplified conservative models of the above components, for verification.

Stresses and deflections in the refrigerator are caused by specified quasi-static launch loads of 7g imposed along each of three orthogonal axes. Tensile bending stresses at the ferrite radial sensor region (earlier sensor design) were of concern. The brittle ferrite material needed to be placed in a section of the housing that experienced considerable bending loads. The ultimate tensile strength of ferrite can range from 400 to 10,000 psi, depending on the material. To keep the stress below this limit, the housing was made stiffer at the ribbed section. Figure 7.1 shows a portion of the housing modeled with solid elements ("Stif45"). Fiber optic sensors eventually replaced the original ferrite reluctance sensors. The 1mm glass fiber bundle penetrates the housing, but is prestressed into compression by differential thermal expansions during fabrication. This assures its integrity.

The relative deflections between the piston and shafts and their respective housings under the launch loads are of concern in the magnetic bearing/clearance seal region. The clearance seal consists of a small gap of 20μ between the piston and housing, and relative deflections should be less than this to avoid seizure. Axisymmetric models of the piston and displacer

showed that the deflections did not pose a problem. Although the launch loads are cyclic, the natural frequencies of these components are high enough to treat the loads as static.

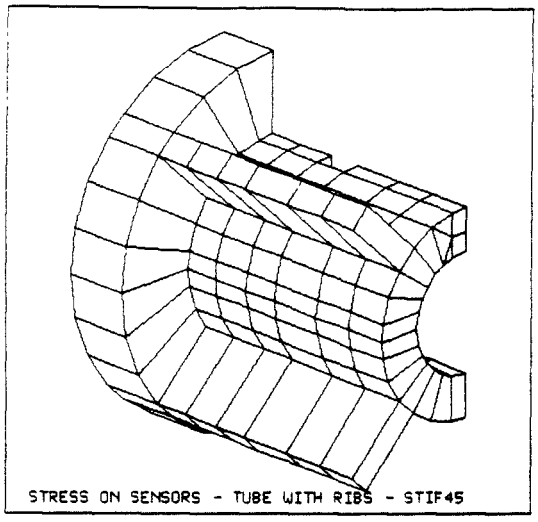

Figure 7.1. Model Of Piston Housing

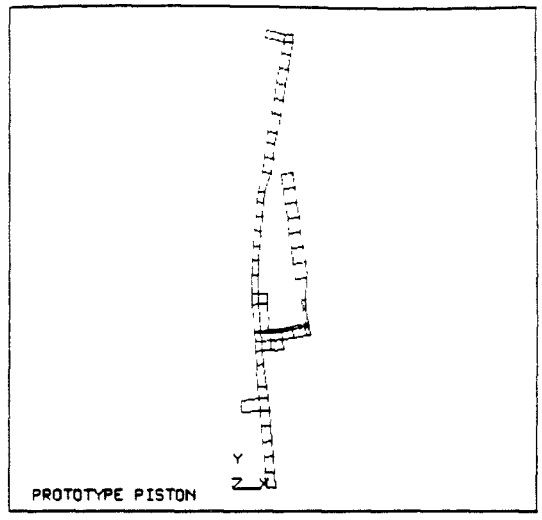

Figure 7.2. Piston Bending Resonance

The piston, displacer, and counterbalance should be designed so that their natural resonance frequencies in bending are larger than the bandwidth of the magnetic bearing control loop. If the natural frequencies are smaller, the bearing control loop could excite the piston or displacer into resonance. A large bandwidth and hence high resonance frequencies are necessary for a stiff bearing design. Several iterations were performed on the piston design in order to increase its stiffness (high resonance frequency) yet keep its weight low (to lower motor force requirements and maintain motor resonance). A model of the piston is shown in Figure 7.2, deflected to its first bending mode. Axisymmetric elements (Stif25) were used for the modeling. Experience with the cold finger natural frequency calculations showed that the finite element predictions are reasonably close to experiment.

8. Program Status

The cryocooler described above is in the final stages of assembly. Initial testing will consist of parametric testing to determine the optimum operating point and to obtain some indication of performance when system parameters such as compressor-displacer phase, compressor stroke and gas pressure are varied between narrow limits. Subsequently the cryocooler will be delivered to NASA Goddard Space Flight Center for environmental testing.

The electronic system was designed for laboratory operation and good commercial practice was observed in the construction. A flight qualified electronic package of minimum weight, maximum efficiency and high reliability must be designed and constructed in the future. However, the design of the present electronic system was guided to some extent by the anticipated demands of the future flight qualified system. Consequently, digital techniques were employed in the control of linear motors, the system controller was heavily software driven and the magnetic bearing control can in the future be reduced to four power integrated circuits to support one shaft.

Acknowledgements

The work summarized in this paper was supported by the NASA-Goddard Space Flight Center, under Contract Number NAS5-26688. The contributions of L. Bourdillon, R. Bronnes, R. Carminucci, R. Eggleston, R. Figueroa, E. Harkins, M. Hartmann, J. Hejduk, E. Lindale, P. Patt, J. Sanchez, and R. Sweet towards the design and fabrication of the refrigerator are acknowledged.

References

[1] F. Stolfi et. al., "Design and Fabrication of a Long-life Stirling Cycle Cooler for Space Application," Philips Laboratories Report No. PL-11-CR83-0307, March 1983.

[2] Patt, P., "Design And Testing Of A Co-axial Linear Magnetic Spring With Integral Linear Motor," IEEE TRANSACTIONS ON MAGNETICS, 21(5):1759-1761.

[3] Knox, L., Patt, P., Maresca, R., "Design Of A Flight Qualified Long-Life Cryocooler," PROCEEDINGS OF THE THIRD CRYOCOOLER CONFERENCE, Boulder, Colorado, 1984.

[4] Swanson Analysis systems Inc., Houston, Pennsylvania: "ANSYS Engineering Analysis System," User's Manual.

SEARCH FOR ANOMALOUSLY HIGH PRESSURE DROPS IN THE REGENERATORS OF ICE CRYOCOOLERS

John Hess
Mark Kushnir

Racah Inst. of Physics, The Hebrew University, Jerusalem 91904, Israel.
ICE Cryogenic Engineering, Ltd., P.O.Box 452, Nes-Ziona, Israel.

I. Introduction

Measurements of cooling power (QH) and coefficient of performance (COP) of two standard ICE cryocoolers were made under a variety of operating conditions. The measured results were compared with simulation results of our "SIMPLE" simulation program and an attempt was made to detect evidence of an oscillating flow (or "anomalous") contribution to pressure drops across the regenerators.

Both the measurements and the simulations have their problems. In the measurements, determination of the work integral $\oint pdV$ of the fluid has uncertainties since electric motor and compressor loss must be determined. Cooling power, especially at high heat load is fairly straight forward to measure. On the other hand for the simulation program the $\oint pdV$ work estimate is quite accurate but estimation of heat load is more difficult. Cooling power determinations are more dependable when measured while simulated COP values have less uncertainty than measured ones.

It seems to us that an oscillating flow effect is present in the regenerators as seen in the following graphs. However the results are not without some ambiguity. Our measurements may be improved and further measurements must be made before unambigious conclusions can be reached.

II. The Cryocoolers

The cryocoolers are the ICE split Stirling Cryocooler, Model MC101A, nominally rated at 0.25 W and the ICE "mini" integral Stirling Cryocooler Model MC111B, nominally rated at 100 mW. Both cryocoolers, hereafter referred to as "0.25 W" and "MINI", have MTBF's of over 1000 hours and give highly reproducible results.

III. The Simulation Program

The simulation program known as "SIMPLE" is described in references 1

and 2. It is based on the "Adiabatic Analysis" of Ref. 2 however it takes into account pressure drops, heat transfer coefficients, regenerator ineffectiveness and parasitic losses in a consistant fashion without introducing the numerical problems associated with the application to cryocoolers of "third order simulations".

IV. Presentation of the Results

Four operating parameters were varied and each graph has either the operating variable: filling pressure (bar), operating frequency (Hz), ambient temperature (C) or the cooling temperature (K) plotted on the x axis. Each graph refers to a specific cryocooler and operating variable as specified.

On each graph appear 2 groups of 3 curves each. One group has arrows pointing left and represent COP, the other group of three has arrows pointing right and represent cooling power (QH). COP is defined as QH times one period divided by the cyclic fluid work integral $\oint pdV$. Each group of three lines has a solid line representing the measured values, a dashed line representing simulation results using quasi-steady flow correlations and a dashed-dotted line representing an "anomalous" pressure drop whose rms value is 1.5 times greater than the steady flow value.

The variable FNOR (nomalized friction factor) takes the value 1.0 corresponding to steady flow correlation and value 1.5 corresponding to increased or "anomalous" pressure drop. In the following these data will be referred to simply as 1.0 and 1.5.

V. Results

We summerize in this section, according to figure number, our own conclusions from examination of the following graphs.

Fig. 1a, variable filling pressure - 0.25 W. COP favors 1.0 below 30 bar, QH approaches 1.5 above 30 bar.

Fig. 1b, variable filling pressure - MINI. COP crosses from 1.0 to 1.5 above 15 bar, QH unambigiously favors 1.5.

Fig. 2a, variable Hz - 0.25 W. COP favors 1.5 below 35 Hz and approaches 1.0 above 35 Hz, QH breaks toward 1.5 above 40 Hz.

Fig. 2b, variable Hz - MINI. COP favors 1.0, QH starts at 1.5 and approaches 1.0 above 35 Hz.

Fig 3a, variable ambient temperature - 0.25 W. COP and QH unambigiously favor 1.5

Fig. 3b, variable ambient temperature - MINI. COP favors 1.5, QH is undecided.

Fig. 4a, variable cooling temperature - 0.25 W. COP approaches 1.5 above 70 K, QH favors 1.0.

Fig. 4b, variable cooling temperature - MINI. COP crosses 1.5 at low and high temperatures and agrees with 1.0 in middle range. QH goes from 1.0 below 70 K to 1.5 above 70 K.

V. Conclusions

For more extreme (dissipative) conditions 1.5 seems to be favored however it is not certain pressure drop is the only factor operating.

The sharp break of QH toward 1.5 in Fig. 2a above 40 Hz suggests the existance of a critical time of about 12 ms (see companion paper Ref.3). As mentioned in the introduction QH measurements are more dependable than COP measurements.

REFERENCES

1. Urieli I. and Kushnir M. (1982): "The Ideal Adiabatic Cycle - A Rational Basis for Stirling Engine Analysis".Proc. 17th IECEC.

2. Urieli I. and Berchowitz D.M. (1984) "Stirling Cycle Engine Analysis". Adam Hilger Ltd, Bristol.

3. Hess J. and Kushnir M. (1988) "Alternatives to the Quasi-Steady Flow Description". These Proceedings.

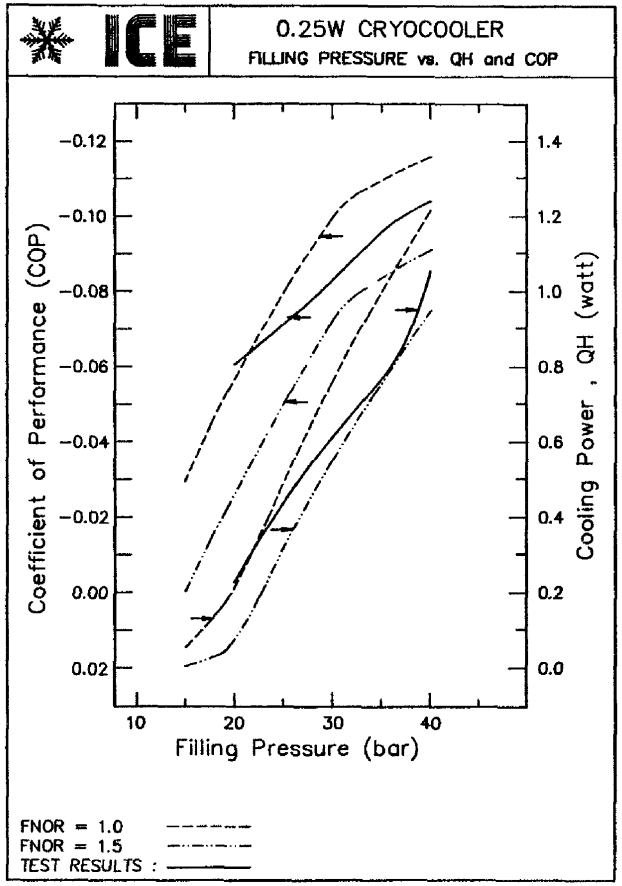

Figure 1a

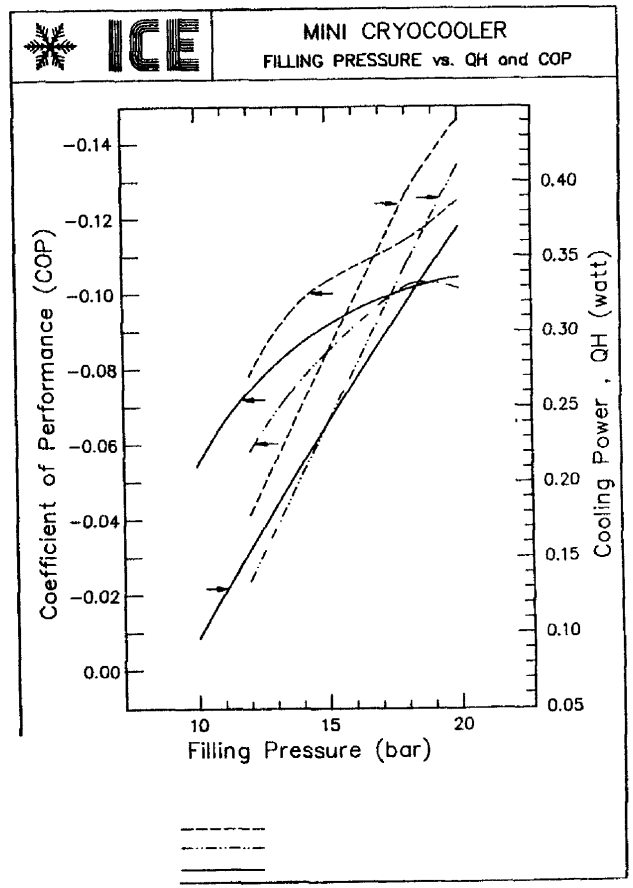

Figure 1b

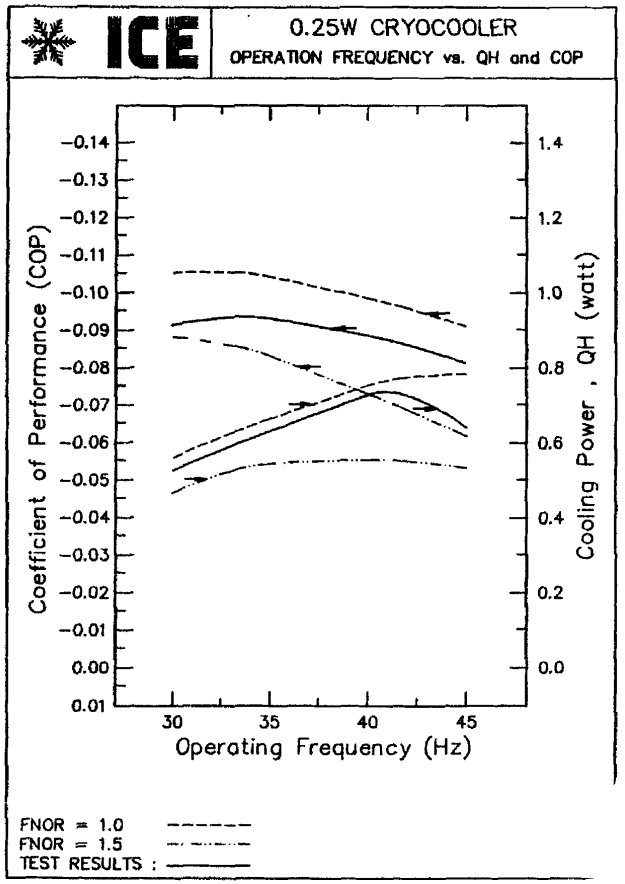

Figure 2a

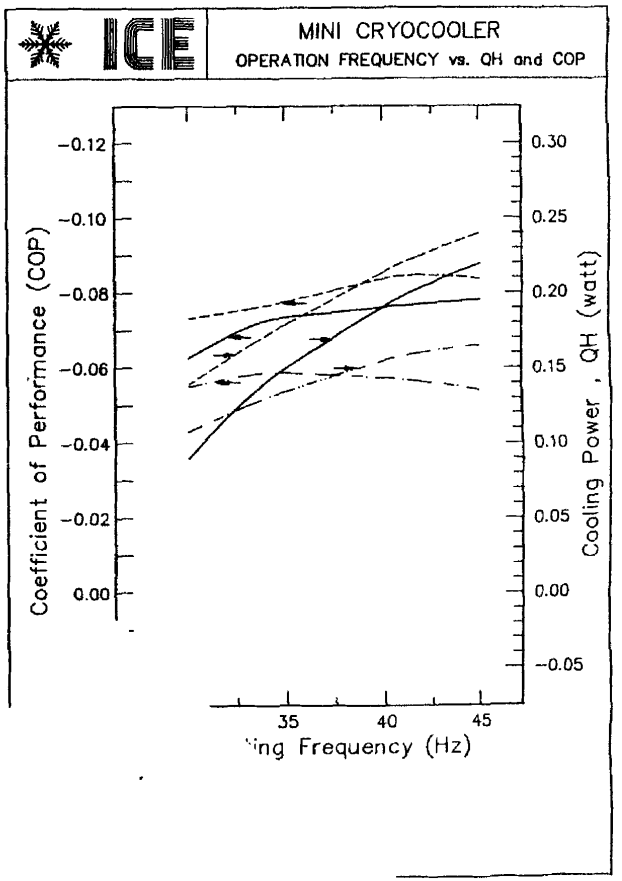

Figure 2b

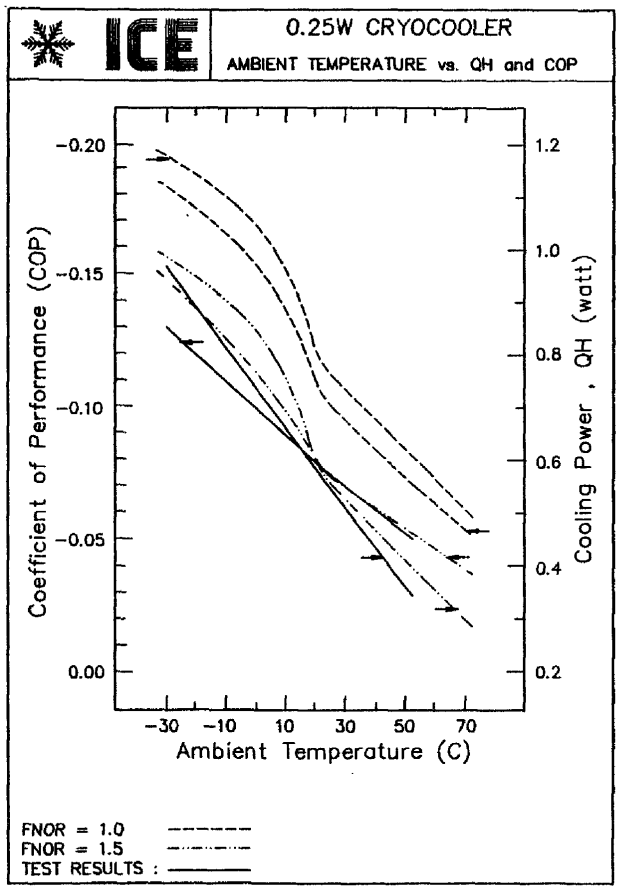

Figure 3a

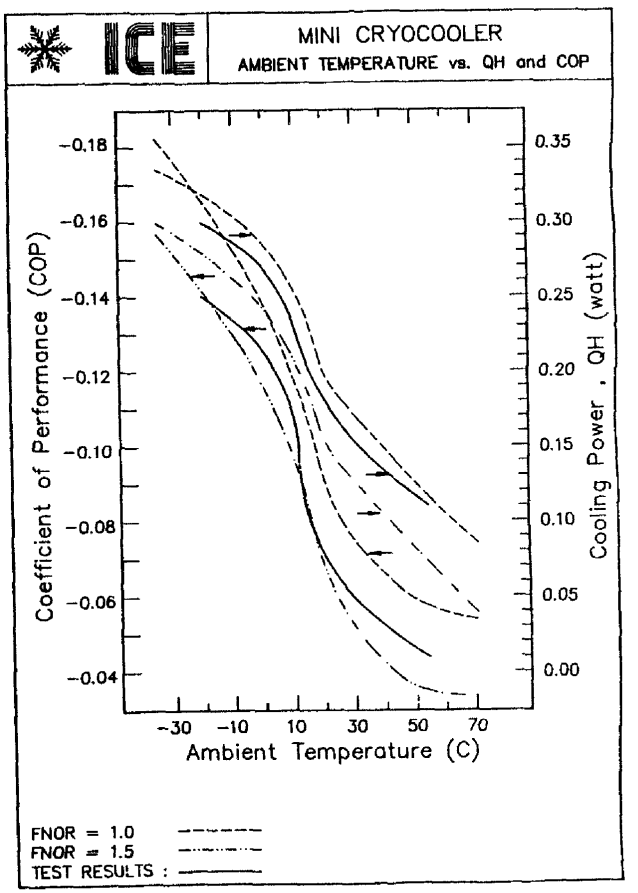

Figure 3b

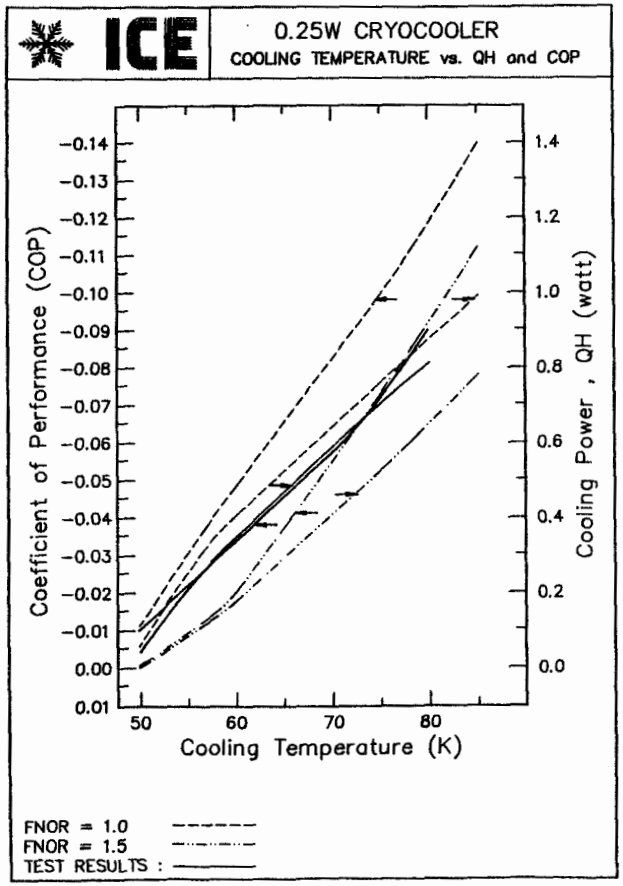

Figure 4a

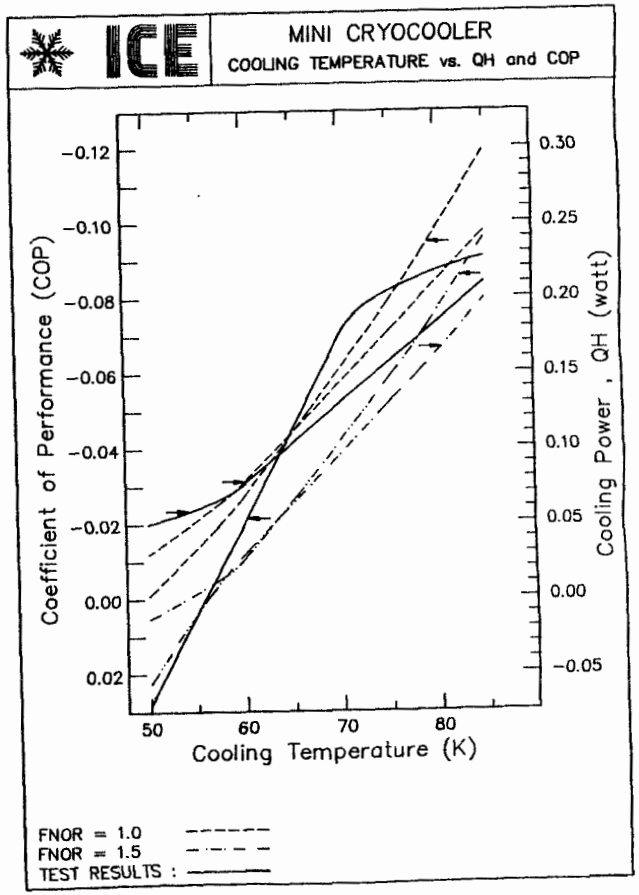

Figure 4b

DEVELOPMENT OF A MINIATURE CRYOCOOLER FOR SI(IN) - IR DETECTOR APPLICATION

Martin Bareiss
Herbert Korf

AEG Aktiengesellschaft, 7100 Heilbronn, FRG

1. Introduction

In Germany efforts for development of extrinsic indium doped silicon for application as infrared detector are underway for several years. Efforts within this scope, e.g. the subject development of a suitable cryocooler for aiding these programs are supported by the German Ministery of Defence.
As specific cooler technology is well established at AEG, this company was chosen to accomplish this mentioned cooler development program.
Here, this development will be presented in form of a short overview on objective, approach and main results of the effort. Future activities will be discussed.

2. Extrinsic Si(In) for Infrared Detectors

Silicon infrared technology is based mainly on In-doped silicon. This material is sensitive in the mid infrared range of 3-5 µm. The benefit of this material is the availability of the highly sophisticated and well established silicon semiconductor technology.
This technology provides the basis for highly complex detector matrix structures like "focal plane arrays" incorporating signal processing in form of "charge coupled devices".
As these structures can be realized in the monolithic type, costs can be kept low regardless of the mentioned complexity.
On the other hand, Si(In) - infrared detectors need to be

cooled to cryogenic temperatures which are even lower than typical values for CMT-detectors.

Fig. 1 shows this feature very clearly.

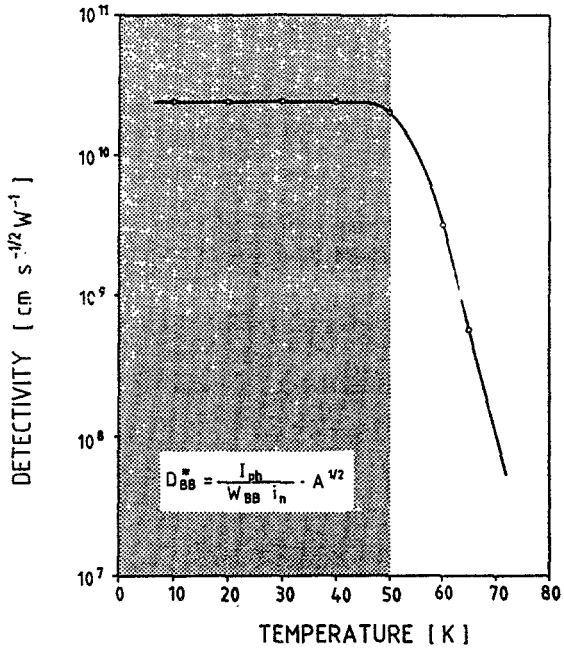

Fig. 1: Detectivity of Si(In)-IR-Detector /1/

In this figure the "Black -Body Detectivity" is plotted vs. the detector temperature.
This detector parameter is defined as

$$D^{*}_{BB} = \frac{I_{ph}}{i_n\, W_{BB}} \cdot A^{1/2}$$

Essentially this parameter represents a measure for the signal to noise ratio. I_{ph} is the signal current, W_{BB} the black body irradiance, i_n the total noise and A the detector area.
This measured curve indicates that the maximum and temperature - independent detectivity is given at temperatures below 50 K.
So, Si(In) - detectors require a cooling system, which is capable of cooling the detector temperature to values below 50 K. This means, that success of this material depends essentially on the availability of suitable coolers. This subject cooler development program was initiated to close this gap.

3. Miniature Stirling Cooler for Si(In)-Infrared Detectors

3.1 Integral Cooler

Development specification required a miniature stirling cooler with the main features based on common module philosophy. The cooler had to be designed for application in night-vision and FLIR systems. With respect to performance characteristics the following requirements were specified in the 1. phase:

Cooling Capacity at 50 K: >1 W
Input Power : <80 W
Low Vibration Output

At the time, this development was initiated, split cooler technology in general was not advanced as far as today. So, in the definition phase the integral concept was chosen to keep the technical risk low.
For benefit of efficiency the cooler was designed with a two stage expander. With respect to dimensions the coldfinger is compatible with the common module DT 594 dewar. The compressor was designed with dual opposed pistons to keep vibration low.
A brushless dc-motor is utilized as drive.
Fig. 2 shows a prototype of this cooler

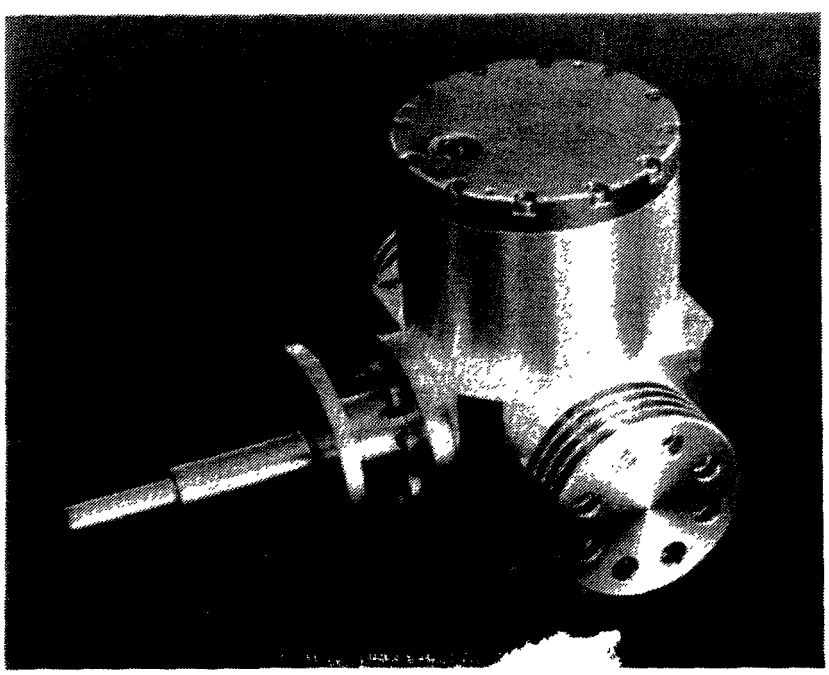

Fig. 2: Prototype of Cooler for Si(In) Application (LV 200)

A typical load curve of this prototype is presented in Fig. 3.

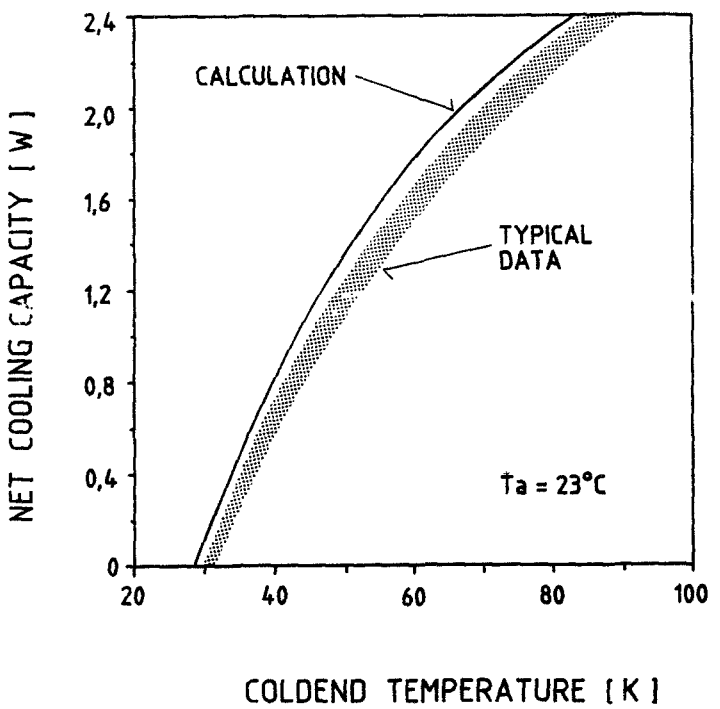

Fig. 3: Load Curve of LV 200

Net cooling capacity is plotted vs. coldend-temperature of the second stage. Typical data which fall within the dotted range, were taken at room ambient temperature. The theoretically predicted curve, which is added for comparison, agrees fairly well with the measured data. This curve was calculated with the AEG computer program, which was designed for aiding integral as well as split cooler layout.

Vibration output of this cooler could be reduced significantly compared to the HD 1033-C/UA cooler.

Prototypes of this cooler are successfully in use in mentioned Si(In)-detector technology programs.

3.2 Split Cooler (SC 200)

Development of a split stirling cooler for mentioned application was mainly initiated by the outstanding progress of split cooler technology at AEG. Both, the AEG Quarter Watt Split Cooler (SC 025) and the One Watt Split Cooler (SC 100) are produced successfully in fairly high monthly production rates and have demonstrated excellent performance and lifetime as indicated by fig. 4.

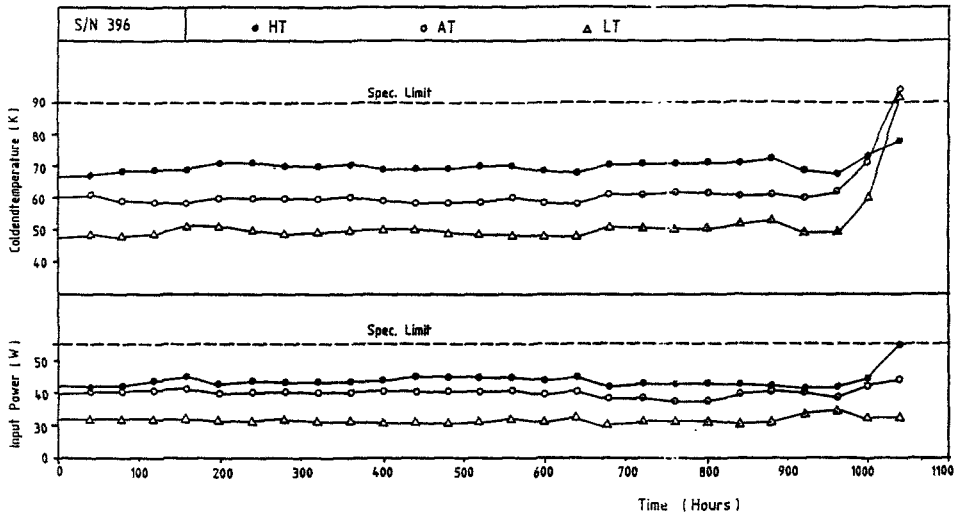

Fig. 4: SC 100 Lifetest

This figure, which shows the coldend-temperature plotted vs. operating time, represents an extract from SC 100 qualification. Within the scope of this qualification, a lifetime of MTTF 1000 h could be demonstrated for the SC 100 cooler.
So, the concept was, to start development of a split cooler for Si(In) application from the SC 100 and to utilize its proved technology as far as possible.
In a first step the compressor and displacer swept volume were increased, keeping the swept volume ratio essentially constant. Additionally, some expander parameters, e.g. regenerator matrix and pneumatic piston, were changed and the motor was replaced by a more appropriate one. As the outline configuration was kept essentially unchanged, this cooler looks similar to the AEG SC 100 cooler as indicated by the photo of Fig. 5.

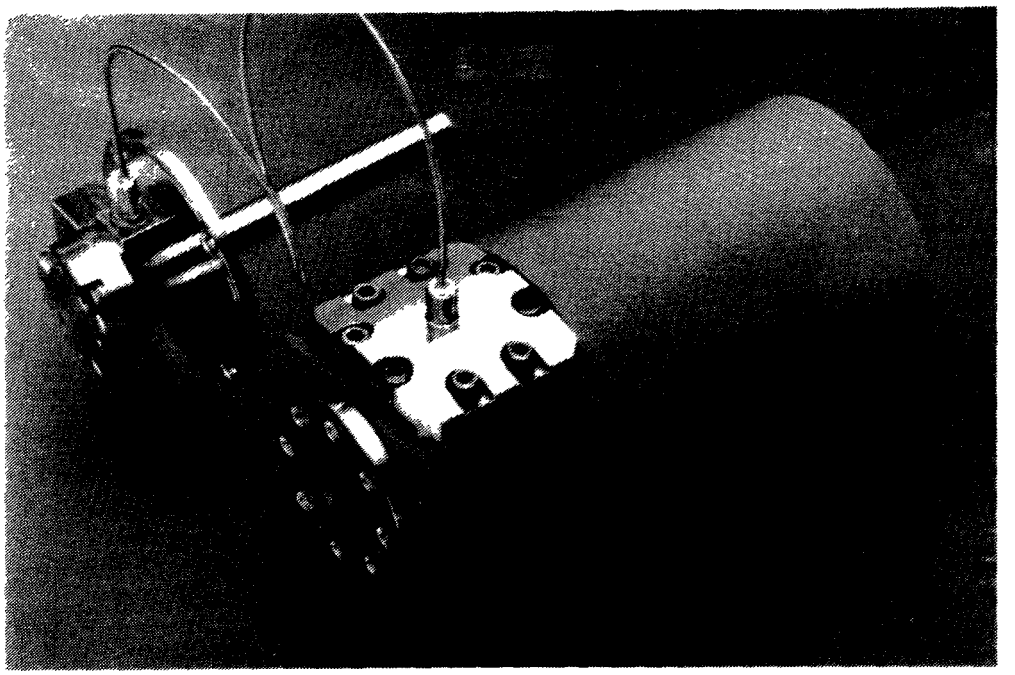

Fig. 5: Split Stirling Cooler for Si(In) Application

The performance characteristics of this single stage split cooler prototype meet the mentioned requirements as indicated by the load curve of Fig. 6.

In this graph again the cooling capacity is plotted vs. the coldend-temperature. The curve represents typical values measured on 3 prototypes at room ambient temperature. The input power was in the range of 80 W typically. This curve indicates, that the field of application for this cooler is not limited to Si(In) detector technology. In the CMT-temperature range of 80 K this cooler provides a cooling capacity of 2.2 W. Hence, this cooler can be utilized for cooling of detectors with high thermal load, e.g. detectors at high ambient temperature operation or large focal plane arrays or detectors with a high degree of signal processing implemented.

Though based on SC 100 technology, lifetime of this cooler in its current design will be lower to some extend, because some key components are subjected to higher stress. Preliminary lifetime evaluation predict a MTTF of at least 500 hours. Nevertheless, lifetests will be performed in the near future.

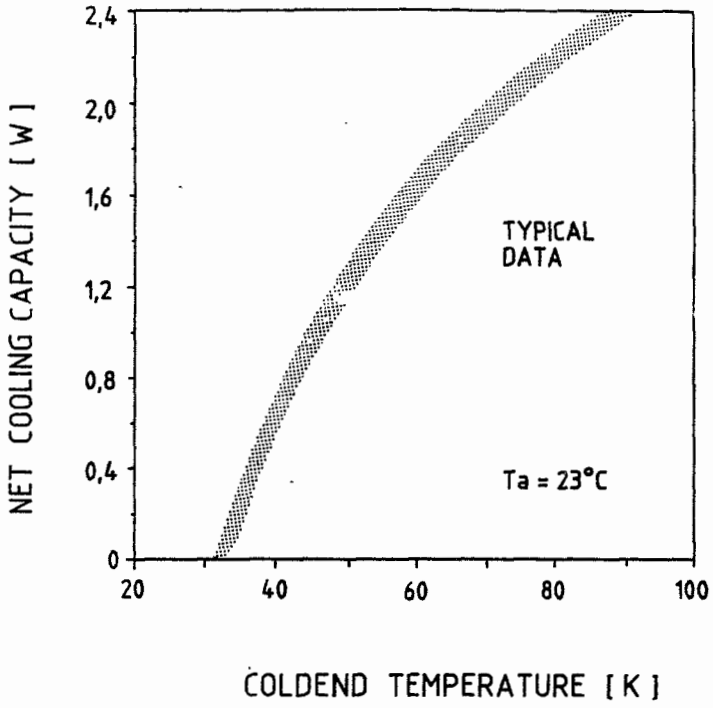

Fig. 6: Load Curve

4. Optimization and Future Development Program

In spite of the successful results of the split cooler development, there is a margin for further optimization.
On a short term, the following fields will be in the focus of the improvement effort:

a) Regenerator
   As tests and calculations indicate, the regenertor is not yet fully optimized. A test program with modified regenerator matrix (e.g. hybrid matrix) will be accomplished.

b) Compressor swept volume

c) Motor
The currently utilized motor is not operated at its optimum point.

On mid term development, implementation of demand refrigeration technology is planned.

4.1 Demand Refrigeration Control (DRC)

Development of demand refrigeration coolers is underway in a parallel program at AEG. This technology and its benefits, namely

- fast cooldown
- stabilized detector temperature
- reduced power consumption
- increased lifetime
- reduced noise and vibration

can be made available for this subject cooler development program.
Fig. 7 shows the typical characteristics of a cooler with demand refrigeration circuit.

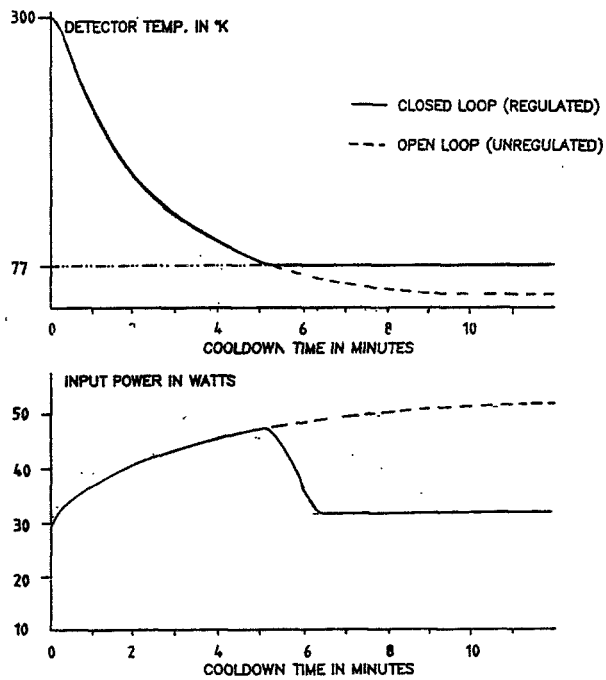

Fig. 7: Demand Refrigeration Cooler Characteristics

This figure presents typical cooldown curves with the coldend-temperature resp. the input power plotted vs. time.
When the set point for the detector temperature is reached, the input power is reduced drastically for operating the cooler in the steady state mode to keep the detector temperature constant.
Typical values for temperature stability are:

Short term:	0.2 K/s
Long term:	1.0 K/min

These data were taken using the AEG SC 100 cooler.
To transfer this technique to the SC 200 cooler, the detector temperature set point has to be reduced to the required temperature of 50 K essentially.

5. Conclusion

Extrinsic Si(In) material is an alternate material for detectors sensitive in the mid infrared.
Success of this material essentially depends on the availability of a suitable cooler. It was the objective of the outlined development to provide a cooler for these specific requirements. In addition to a specifically developed integral cooler, a split stirling cooler as spin-off from the AEG SC 100 production cooler is now available.
As the basis technology is now established, specific system options can be implemented. So, one of the main handicaps of Si(In) detector technology is eliminated.
The present development was partially supported by the German Ministery of Defence.

6. Reference

/1/ P. Nothaft, G. Kohlbacher
Degradation von Si : IN - IR - Detectoren nach Hochtemperaturprozessen
AEG Forschungsinstitut Ulm, Technischer Bericht Nr.12.040/81.

SESSION V

ADVANCED TECHNOLOGY

CHAIRPERSON: S. CASTLES
VICE CHAIRPERSON: R. RADEBAUGH

SCROLL HELIUM COMPRESSOR FOR CRYOGENIC APPLICATIONS

John E. McCullough
Arthur D. Little, Inc.
Cambridge, MA 02140-2390

Arthur D. Little, Inc. has been working on the design and development of Scroll machines since 1972.[1] These efforts have been focused on applying this technology to applications such as: air, refrigerant, and helium compressors as well as liquid and vacuum pumps. To date 23 different scroll prototypes have been developed in the power input range of 30 w. to 30 hp. Scroll refrigerant compressors for building air conditioning are now in production, under license from ADL, by The Trane Company and its three sublicensees for air conditioning products. Scroll compressors for automotive air conditioning have been in production for 4 years, under license from ADL, by the Sanden Corporation and its sublicensee. The main advantages of Scroll technology for these applications are: higher efficiency, fewer parts, lower operating noise and vibration, and better reliability.

BACKGROUND

The basic elements in a Scroll machine are two identical spiral scrolls, each fixed to (or an integral part of) a cover plate. When two Scroll plate assemblies are mated, the two Scrolls are interleaved in an eccentric fashion so that they touch and form a series of crescent shaped pockets. The two cover plates seal these pockets, thus serving roughly the same function as cylinder walls in a reciprocating compressor.

In the conventional Scroll machine, one of the Scroll plate assemblies is fixed. The other one orbits around the center point of the fixed Scroll plate assembly, and, as it moves, the pockets formed by the interleaved Scrolls follow the spiral towards the center and diminish in size. (If the device is used as an expander, the process is the reverse, i.e., the pockets move from the center to the periphery and enlarge). The moving Scroll plate assembly orbits with a fixed angular orientation; it does not rotate. It is driven by a simple short throw crank assembly incorporating a radial compliance drive feature. Figure 1 shows the typical orbiting Scroll plate and assembly configuration and Figure 2 shows the progress of the compression process.

ORBITING SCROLL OPERATION

When used as a compressor, the inlet for the Scrolls is at the periphery. The entering gas is trapped in a pocket and compressed as the pocket moves towards the center and diminishes in size. The compressed gas is exhausted through the outlet at the center of the fixed spiral. When the device operates as an expander, or Brayton cycle engine, the inlet becomes the outlet; the outlet becomes the inlet, and the moving Scroll plate orbits in the opposite direction.

The displacement of a Scroll machine is a function of the volume of the pockets formed between the Scroll pieces. The volume of the pockets, in turn, is related to the parameters

of the Scrolls, such as the outside diameter, pitch, height (i.e., axial length) and thickness. The pressure ratio is directly related to the initial and final volume of the sealed pockets. For a Scroll compressor, where the gas flows radially inward along the Scroll, a final volume is also influenced by the discharge port configuration. Precise functional relationships between the displacement, the pressure ratio, and the Scroll parameters have been completely defined. ADL has developed and is using on a regular basis computer programs that size and draw elements at any angular orbital position. Additional computer programs compute forces on the Scrolls and power input, given gas inlet and discharge pressures and operating speed.

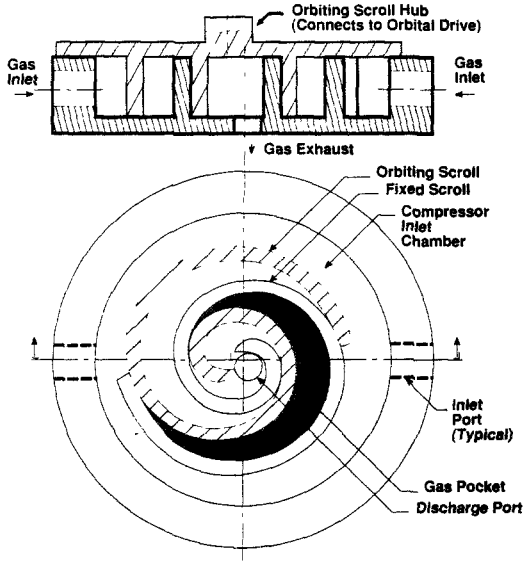

Fig. 1
Typical Scroll Compressor Configuration – Orbiting Scroll at Gas Pocket Seal-off

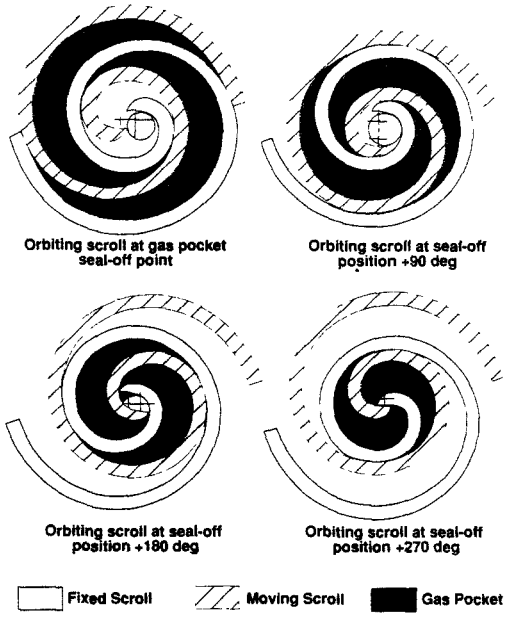

Fig. 2
Four Operating Positions of the ADL Scroll Compressor/Expander

CO-ROTATING SCROLL COMPRESSOR (CRSC)

In previous Scroll compressor developments, the orbital configuration of the machine was used with one Scroll fixed; the other orbiting, without rotation. For dry helium compression, the CRSC version of the Scroll machine is preferred because it allows higher operating speeds which facilitate the use of gas bearings and diminish the effect of gas leakage between the two Scrolls. In this version the two Scrolls rotate about their own center lines in precise angular relation but about laterally displaced parallel axes. The effect of this motion is shown in Figure 3, at 90° intervals of rotation. The same gas trapping and compression sequence occurs in the co-rotating Scrolls as in the orbiting Scrolls. In fact, the motion of one Scroll relative to the other is still orbital, even though they both rotate. The main advantage of the co-rotation is that higher operating speeds can be used since there is no centrifugal load on the Scroll drive bearings, as there is with orbital motion. Conversely, there are twice as many bearings in a CRSC (since both Scrolls are moving) and efficient bearing means is required.

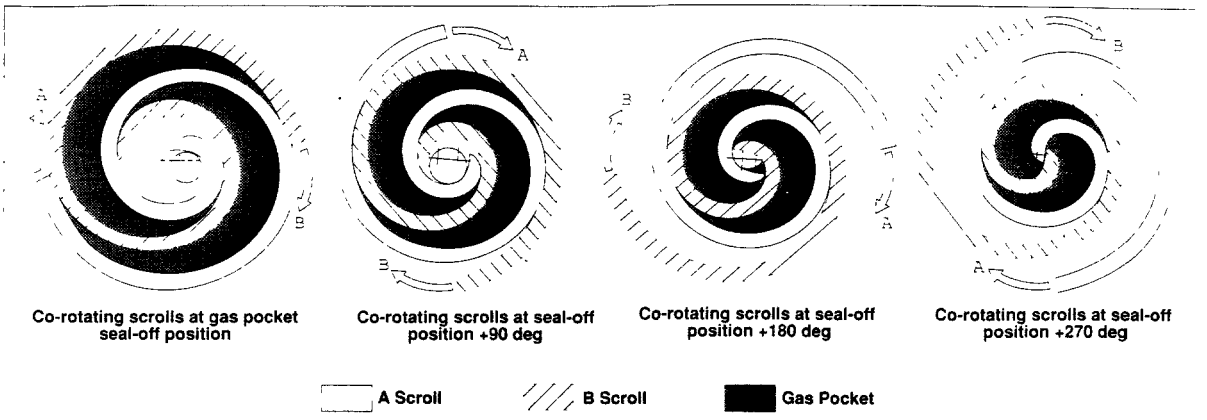

Fig. 3
Operating Sequence, Co-rotating Scroll Compressor

CRSC HELIUM COMPRESSOR

As a design example, a typical dry helium compressor requirement for a cryogenic refrigerator was selected to allow sizing a CRSC. This requirement is associated with the R^3 system currently under development at ADL; the pertinent portions of this requirement are:

- Helium flow rate = 3 - 4 lbm/hr
- Inlet pressure = 14.7 psia
- Discharge pressure = 58.8 psia

Additionally, this application requires minimum size and weight and maximum reliability in order to achieve 50,000 hrs. of operation in space, without maintenance.

Using our established Scroll design procedures, the preliminary configuration of a CRSC, suitable for meeting this requirement, was determined. The first step in this process was to establish an operating speed. The major advantage of the co-rotating version of the Scroll is that it can operate at high speeds since there is no centrifugal loading of the drive bearings, as there would be in an orbital version. In addition, the high speed reduces gas leakage within the Scrolls by minimizing physical size, which allows more accurate involute surfaces and better control of thermal and mechanical distortions during operation. High speed also minimizes overall compressor size and weight.

Based upon the results of similar studies, in the past, an operating speed of 20,000 rpm was assumed. Next, the size of the Scrolls was calculated based upon required compression ratio and flow. Once the Scroll size was established, the bearing loads were calculated using our computer design equations. Finally, gas leakage, heat transfer and compression efficiency was calculated. For comparison, the Scroll size for an operating speed of 10,000 rpm was also calculated.

A CRSC running at 20,000 rpm has relative linear dimensions of the Scrolls which are 30% smaller than for a 10,000 rpm Scroll compressor, while clearances between adjacent Scroll surfaces which control leakage, would be about the same. Also, the drive bearing forces

would be smaller; in some cases one-half as large. It was found that the 20,000 rpm Scrolls were reasonable in size with a better combination of operating clearances and loads on the supporting bearings.

As a result, it was concluded that the operating speed of 20,000 rpm would result in a CRSC which would have good size and weight characteristics, while not posing excessive development risks as a result of extremely high speed. Our previous experience with a two stage, 12,000 rpm orbiting Scroll refrigerant compressor indicated that the increase in speed to 20,000 rpm is feasible.[2]

Figure 4 shows the configuration of one of the rotating Scroll components. The Scroll has a compression volume ratio of 2.56 and is integral with a mounting disk on one end of the shaft. Behind this is a cooling fan which draws in ambient GHe and circulates it behind the Scroll disk, for cooling. The fan section is joined to the main bearing section which in turn is joined to the outboard bearing section. The shaft mounted Scroll is driven in its bearings by a rotary motor whose rotor portion is incorporated in the large main bearing area. The compressed helium exiting from the Scroll is carried through an axial passage in the shaft, to its outboard end. The outermost journal acts as a rotary seal to limit leakage of GHe, at discharge pressure, as it leaves the spinning shaft.

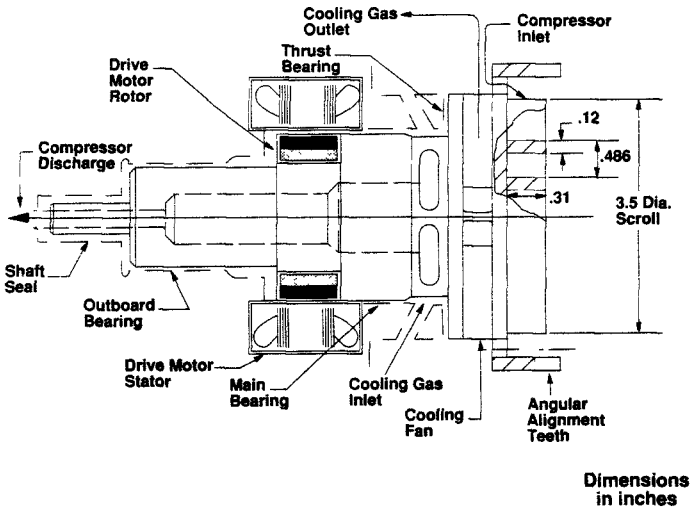

Fig. 4
Rotating Scroll Component

Surrounding the scroll periphery are a series of axially projecting teeth which serve to insure angular alignment of the two Scrolls, when they are assembled.

The two Scroll components would be mounted Scroll to Scroll as shown in Figure 5. Their axes would be laterally displaced to provide sealing between adjacent Scroll flanks located on opposite Scroll parts.

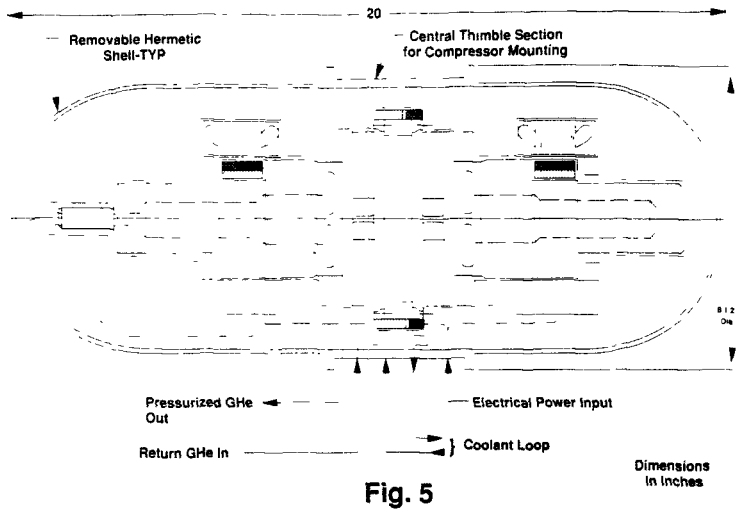

Fig. 5
CRSC Concept

In operation, both Scrolls would rotate in the same direction with their projecting teeth (around their peripheries) meshing with (but not contacting) the teeth mounted on the opposite Scroll. The meshed teeth maintain precise angular alignment between the Scrolls.

GAS COMPRESSION

GHe enters the Scrolls at their periphery and is trapped in two diametrically opposite peripheral pockets. These pockets are driven inwards during further rotation to accomplish the built in volume change (2.56) required to develop the required pressure ratio. After compression, the two pockets merge and discharge at the center of the Scrolls. Discharged gas flows down a central pipe in the support shaft of one of the Scrolls and is discharged through a rotary seal into a fixed passage in the compressor housing. This rotary seal is a helium gas bearing with clearances controlled to minimize leakage. The inlet, compression, and discharge occur continuously, without the need for valves.

DRIVE MOTORS

Synchronous motors capable of operating at 20,000 rpm would be used for driving each of the Scrolls. A permanent magnet rotor construction, similar to that used in the existing R^3 equipment, would be incorporated in the large bearing section of each Scroll component resulting in a motor air gap diameter of about 2.50 in. The construction of the rotor involves potting the magnets and rotor core in a welded stainless steel toroidal can which will seal the rotor and provide structural integrity. The rotor peripheral velocity will be about 13,090 ft/minute which is acceptable for aircraft squirrel cage induction motors.

As a result of the large size of the rotating parts and their high speed, considerable energy would be stored during operation. The drive motor would be designed so that it acts as a brake on the rotating Scrolls by functioning as an electrical generator during shutdown. If a malfunction occurred or the operator needs to shut the compressor down, the control system would bring the compressor to a stop quickly, to protect the mechanism from potential damage.

SCROLL COOLING

The Scrolls will consist of an involute wall integral with a disk which is connected to a support shaft with a cooling fan section. The cooling fan is radially bladed, integral with the support shaft, and draws in ambient helium and discharges it radially after it flows over the internal fan blades. In the process, the heat of compression absorbed by the Scrolls and transferred to the intervening disk is dissipated to the ambient helium flowing through the fan and discharged into the surrounding compressor shell. Suitable heat sink surfaces, inside the shell, which are cooled by an external coolant loop, remove the heat of compression and reject it to a fluid cooling loop.

The total heat rejected to this external loop would consist of:

- Cooling of the gas compression scrolls.
- Energy losses in the gas cooling fan.
- Drive motor losses.

SCROLL BEARINGS

The forces on the Scrolls during Ghe compression tend to separate the Scrolls axially, and laterally, and impose a tangential force in reaction to the compression work input. The forces perpendicular to the Scroll axes create an overhung load which is supported by the two-stepped bearing journals on each Scroll. The axial load is supported by an annular thrust bearing located outboard on the cooling fan, behind the Scroll section. All these bearings would be self-acting, hydrodynamic gas bearings.

The Scroll loads estimated during the sizing analysis described above were used in conjunction with an operating speed of 20,000 rpm to size the gas bearings. The bearing dimensions were determined using analytical design curves from the technical literature. Our experimental experience with the gas bearings of Arthur D. Little's R^3 have shown good agreement with these curves. The preliminary design of the thrust bearings were made using an analytical design procedure given in reference 3.

A summary of these bearing loads and the anticipated bearing clearance needed is presented in Table 1.

TABLE 1

SCROLL SUPPORT BEARINGS

BEARING	LOAD (lbs.)	CLEARANCE (Microinches)	POWER CONSUMPTION (Watts)
Axial Thrust	80	200	30
Main Journal	47	1190	43
Outboard Journal	27	770	8

LEAKAGE CONTROL

In order to achieve suitable efficiencies the Scroll compressor surfaces must be very accurate and distortions due to thermal effects or gas loading must be minimized. To establish the size of gaps which could be tolerated, an analysis of the compression process was done using an existing ADL computerized leakage estimating program for Scroll machines. To do this the details of the compression process occurring between the two co-rotating Scrolls was analyzed in great detail; the process was tracked from when the gas pocket is trapped at the scroll periphery to its discharge into the center of the Scrolls. In this analysis the thermodynamics of the compression process was estimated to predict the overall efficiencies of compression, extent of internal gas leakage, and probable heat transfer during compression.

As a result it was found that the clearances required between adjacent Scroll wall flanks would need to be about 0.00150 in. The clearance between Scroll tip and adjacent disk of the mating Scroll needs to be about 0.00075 in. or less. These clearances are quite small but can be obtained in gas bearing equipment, when proper measures are taken in design, fabrication and construction.

The Scroll components themselves can be machined very accurately. Production Scrolls for refrigerant compressors, which have been in production for many years, are machined to tolerances of $\pm$ 0.0002 in.

In order to control thermal distortion of the Scroll surfaces, during operation, the Scrolls are cooled by Ghe circulated through the fan section outboard of the Scroll disk. Preliminary calculations indicate that the Scroll metal temperature can be held below 150° F. assuming ambient helium temperatures of 70° F. In addition, the Scroll component could be made from Invar or equivalent material to minimize thermal expansion.

Since mechanical stresses in the Scrolls are modest, and the structure is quite robust, mechanical distortion can be very low.

In order to finely tune the clearance between Scrolls, it is planned to incorporate "micro-adjustment" capability in the axial and lateral bearing supports of one of the rotating Scrolls. This mechanism would be able to advance one Scroll towards the other in very fine steps, in these two directions, to minimize clearance gaps and would be actuateable during the initial setup and operational testing of the compressor.

ANGULAR PHASE CONTROL

The Scroll components of the CRSC must be accurately positioned in angular phase relative to one another, in order to achieve the desired minimum clearance between the Scroll flanks, thus minimizing gas leakage. The design alternatives for providing this precise phase control, in a machine which must meet long life requirements, are limited. In order to reach a 50,000 hr. maintenance-free life, a non-contacting means is required which has the capability to maintain precise angular positioning ($\pm$ 5 mrad) of one Scroll relative to the other, as they rotate.

In order to minimize loads on the angular phase control means, the CRSC utilizes two drive motors; one on each Scroll component. In theory, one-half the work of compression is provided by each Scroll component; therefore, motorizing each component reduces angular phase control component torque loads to zero.

There is about a 10% variation in drive torque during each revolution of the Scroll, due to detailed geometric changes in pocket size as a function of the rotation angle. However, this small torque variation acts on each Scroll simultaneously, and equally, so that no torque is exerted on the phase control component. Moreover, the high frequency of torque variation with the large moment of inertia of the Scrolls is such that the undamped amplitude of vibratory motion of each Scroll is negligible.

It is planned that the meshed teeth will operate without contact due to gas "squish film" bearing action. The faces of the meshed teeth would be precision machined to promote smooth engagement and disengagement with maximum face area to promote gas trapping during engagement.

Preliminary analyses, considering possible torque loading and angular momentum of the Scrolls indicate that meshing of the teeth should be smooth and operation highly damped; with little possibility of tooth rattle or "buzzing".

EFFICIENCY ESTIMATE

As a result of this preliminary design process, the overall efficiency of this CRSC has been estimated with power budget elements as follows:

ITEM	ESTIMATED POWER CONSUMPTION (WATTS)
Pressure reduction at inlet process	3.5
Heating of inlet charge	5.8
Gas compression power	570
Gas viscous shear	9.5
Gas bearing friction (2 Scrolls)	160
Scroll fan cooling (2 Scrolls)	60
Rotary shaft seal leakage	6
Total power required from drive motor	815
Drive motor loss (at 85% efficiency)	144
Total electrical power consumption	959

Therefore, the total overall isentrophic efficiency (compressed gas output divided by compressor shaft input) of this dry CRSC is estimated to be 71%. The overall efficiency based upon electrical power input is estimated to be 61%.

SIZE

The complete CRSC module as shown in Figure 5 would consist of the rotating Scroll components and their bearings mounted to a central bulkhead or thimble. Two hermetic

shells are attached and sealed to this thimble to enclose the compressor. All connections for electrical power, coolant flow, and helium flow are made at the thimble section which also acts as a mounting flange for the compressor. The complete compressor would be about 8.5 in. in diameter and 20 in. long (1135 $in.^3$).

A power conditioning and control electronics module would be required also, but its size should be quite small.

WEIGHT

The weight of the CRSC will probably be in the range of 25 - 45 lbs. depending upon the extent of Invar or equivalent need for thermal expansion control within the Scrolls.

COMPARISON WITH ALTERNATIVES

In order to put CRSC technology in perspective, the major advantages can be summarized as follows:

- **POSITIVE DISPLACEMENT**

  The CRSC uses positive displacement technology similar to reciprocating machines to compress helium to high pressures in one stage, efficiently.

- **SIMPLE DESIGN**

  CRSC consists of two moving parts which are geared together to accomplish gas compression without the need for valves or complicated electrical drive systems.

- **COMPACTNESS**

  The high speeds possible with CRSC allows high flow capacity with minimum size and weight.

- **HIGH EFFICIENCY**

  The use of gas-bearings to support the Scrolls results in minimum bearing friction power dissipation. The high speed allows minimum size of Scrolls with minimum internal leakage for a given gas flow.

- **LONG LIFE**

  Since the Scroll parts see no metal-to-metal contact during operation, long operating life is achievable.

As a result of these characteristics, the CRSC type of compressor should be very competitive with alternatives for special, dry gas compression such as is required for cryogenic refrigerators in the power input range up to 5 kw.

The example described above deals with a modest compression ratio requirement. For higher compression ratio applications, the CRSC would be staged, as per conventional practice.

This paper has dealt with the use of Scroll technology for dry helium compression; however, this same machine can operate as an expander by reversing the direction of rotation. The use of this type of Scroll expander for cryogenic cooling is quite intriguing in spite of the ominous requirements for leakage control, and will be the subject of future exploratory design analyses.

The CRSC concept and design details presented are the subject of a recently filed patent application by Arthur D. Little, Inc.

ACKNOWLEDGMENT

The author would like to thank Dr. Arthur A. Fowle for his assistance in carrying out the thermodynamic, fluid flow, and heat transfer analyses made in support of this CRSC preliminary design effort. The author would also like to thank John Dieckmann and David Hablanian of ADL for their contributions in the area of Scroll sizing, bearing load estimates and gas bearing calculations, respectively.

REFERENCES

1. J. E. McCullough, F. Hirschfield "The Scroll Machine" Mechanical Engineering, Vol. 101, No. 12, December 1979.

2. J. E. McCullough, "Evaluating Scroll Refrigerant Compressors for Reducing Size and Weight of Military Aircraft ECS" –S.A.E. Technical Paper #820877

3. "Design Manual for Self-Acting Plain Cylindrical Gas Journal Bearings and Thrust Bearings", Rotron Manufacturing Company, 1963.

USE OF AN ELECTRIC FIELD GRADIENT INSTEAD OF GRAVITY TO OBTAIN A SUITABLE ^{3}HE-RICH/^{4}HE-RICH INTERFACE IN THE MIXING CHAMBER OF A DILUTION REFRIGERATOR

U.E. Israelsson
D.Petrac
H.W. Jackson
D.M. Strayer

Jet Propulsion Laboratory
California Institute of Technology
Pasadena, California 91109

ABSTRACT

A major obstacle to be overcome before a dilution refrigerator can be operated in space is that a conventional unit relies in a fundamental way on gravity to physically separate the ^{3}He-rich phase from the ^{3}He-poor phase in the mixing chamber. Experimental and theoretical work performed at the Jet Propulsion Laboratory show the feasibility of controlling the interface between the two phases using an appropriate electric field gradient instead of gravity. A single cycle dilution refrigerator incorporating this feature is presently being constructed. The refrigerator is designed to cool only if an electric field is applied, and to test any influence the applied electric field has on the cooling power. Other key features include a radially symmetric design and the possibility of altering the relative position of the still and the mixing chamber to allow operation in a horizontal mode.

1. INTRODUCTION

NASA's primary interest for developing refrigeration well into the subkelvin temperature range stems from the significant reduction in noise equivalent power (NEP) of long wavelength infrared bolometers and X-ray detectors obtained as the temperature is lowered. Planned future astronomical space missions that benefit from subkelvin temperatures to cool some of their detectors are: the Space Infrared Telescope Facility (SIRTF), the Advanced X-Ray Astrophysics Facility (AXAF), the Large Deployable Reflector (LDR), and it's predecessor the Submillimeter Telescope. Subkelvin temperatures in a microgravity environment can also be used to investigate phenomena that are perturbed by gravity effects in ground-based laboratories, such as studies of the tricritical point and of emulsions in ^{3}He/^{4}He-mixtures.

In addition, the ultimate stability of Superconducting Cavity Stabilized Oscillators (SCSO's) is improved when cooled to subkelvin temperatures. Development work at JPL indicates that the cooled SCSO can outperform currently used hydrogen maser clocks. A number of scientific and engineering applications exist for this potentially ultrastable frequency standard. Such a frequency standard can be used as the timing device in a global positioning system with unprecedented resolution. Precise clocks are also a necessary in performing tests of the general

theory of relativity, satellite ranging, navigation, and other applications..

To produce temperatures below 0.3 K continuously, a $^3He/^4He$ dilution refrigerator must be used. Cooling is obtained in a mixing chamber where ^3He atoms from a concentrated ^3He-rich phase are continuously mixed (or evaporated) into a dilute ^4He-rich phase. An osmotic force that moves the ^3He-atoms across the interface is produced by evaporating ^3He-atoms in a still at higher temperatures. The still and the dilute phase in the mixing chamber are connected by a capillary tube.

There are three interfaces in the earth-based dilution refrigerator where gravity plays an important role: the liquid/vapor interface in the still, the liquid/vapor interface in the condenser where the evaporated ^3He is recondensed, and the dilute/concentrated interface in the mixing chamber. All these interfaces must be controlled by means other than gravity to allow a dilution refrigerator to function in space.

2. ADAPTATIONS FOR SPACE OPERATIONS

Two methods have been proposed for controlling liquid/vapor interfaces of helium in space: passive capillary confinement in metal sponges[1] and active liquid confinement into a region of high electric field[2,3]. The pore size d, or applied electric field E, necessary to confine a liquid sample of height h against an adverse acceleration a, are given by:

$$d = \frac{4\sigma}{\rho h a} \qquad \text{(capillary confinement)}$$

and

$$E^2 = \frac{2\rho h a}{\epsilon_o(\epsilon-1)} \qquad \text{(electric field confinement)}$$

where ϵ_o is the permittivity of vacuum, σ is the surface tension, ρ is the density, and ϵ is the dielectric constant of the helium fluid. To compare the effectiveness of the two confinement techniques, we form the product of these two equations.

$$E^2 d = \frac{8\sigma}{\epsilon_o(\epsilon-1)} = C(T)$$

The surface tension and the dielectric constant have rather weak dependence on temperature in the pure liquids at low temperatures. Below 1 K the proportionality constant is $3.4 \cdot 10^9$ V^2/m for ^3He and $7.2 \cdot 10^9$ V^2/m for ^4He. These numbers imply that electric field confinement of ^3He using 10^6 V/m is equally as effective to confine a volume of liquid against an adverse acceleration as a sponge with 3.4 mm pore size, and a field of 10^7 V/m matches a sponge with 34 micron pore size. It seems possible to design liquid/vapor phase separators with both methods, but

there may be difficulties testing the electric field separator on ground due to arcing problems when trying to hold off the full gravitational field. To counteract a 1-g acceleration of a 1cm column of liquid ^{3}He, a field of $6.6 \cdot 10^6$ V/m is required. So large a field often leads to arcing through the vapor in contact with the electrodes. However, to counteract an acceleration of 10^{-3}g, a field of only $2.1 \cdot 10^5$ V/m is required which can be accomplished with a few hundred volts across an electrode separation of 1mm.

To control the dilute/concentrated liquid/liquid interface in the mixing chamber of the dilution refrigerator in a low-g environment, we have recently shown that a suitably designed electric field gradient may be used[3,4]. Figure 1 shows actual measurement observed visually in our laboratory using a v-shaped electrode geometry. The dilute ^{4}He-rich phase (grey), has a larger dielectric constant than the concentrated ^{3}He-rich (white) phase and is therefore forced into the high field region as the applied voltage across the electrodes is increased. The plate separation at the narrow end is about 0.75 mm, and the slope of the lower electrode is 0.1. Our measurements agree well with our theoretical calculation based on the two-fluid model which yields an equation for the interface line between the two phases as a function of applied voltage V.

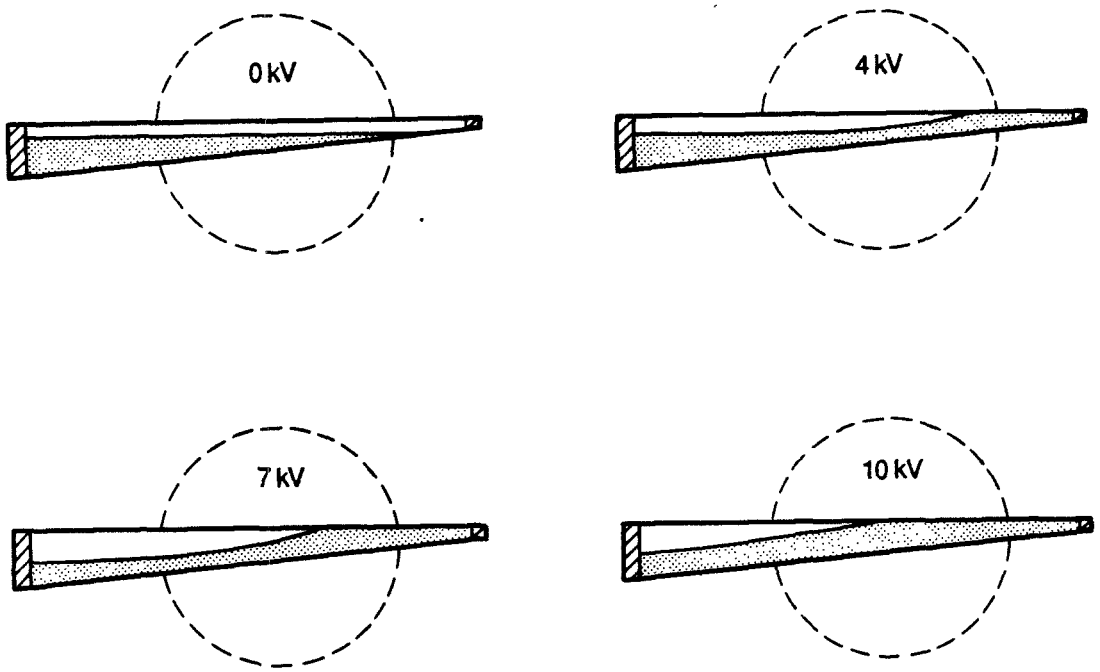

Figure 1. ^{3}He-rich/^{4}He-rich interface line control using an applied voltage across v-shaped electrodes. As the voltage is increased the dilute phase is preferentially moved into the high field region. The dashed circle indicate the visual access into the cell.

$$z(x) = 0.5V^2\epsilon_o \frac{\epsilon_d-\epsilon_c}{g(\rho_d-\rho_c)} \left[\frac{1}{z_b^2(x)} - \frac{1}{z_{bo}^2}\right]$$

Here z and x are the vertical and horizontal coordinates respectively, z_{bo} is the cell width where the interface line touches the upper electrode, and g is the acceleration due to gravity. Subscripts d and c refer to the dilute and concentrated phase respectively.

These initial experiments have shown the feasibility of the electric field approach for mixing chamber interface control and also have furnished us with valuable design parameters. The remainder of this paper will discuss the design and construction of a single cycle dilution refrigerator which requires an electric field generated force in the mixing chamber to overcome an adversely oriented gravitational force for its operation.

We should also mention that capillary retention has recently been proposed as a possible alternative to provide an interface in the mixing chamber[4].

3. SINGLE CYCLE DILUTION REFRIGERATOR WITH ELECTROSTATIC MIXING CHAMBER

As a first step towards designing and constructing an engineering model of a low gravity dilution refrigerator we are building a single cycle refrigerator. We thus eliminate complications associated with returning the ^{3}He into the mixing chamber, such as heat exchangers and ^{3}He recondensation. Furthermore, we focus on low gravity aspects of the mixing chamber only, so our first design utilizes gravity to control the liquid/vapor interface in the still chamber.

3.1. General Features

The dilution refrigerator is of a compact design fitting inside a 10 cm outer diameter vacuum can which is immersed in liquid Helium at 4.2 K. A schematic representation is shown in figure 2. The high temperature stage is a 1 K pot formed by bending a 0.64 cm outer diameter copper tube in a circle and brazing the ends together. The 1 K pot can hold 5 cc of liquid, and is pumped by a mechanical pump at room temperature through a 1.27 cm diameter pumping line inside the cryostat. Continuous filling of the 1 K pot is accomplished through a high impedance capillary from the main bath at 4.2 K. The 1 K pot is used to condense liquids for the still and ^{3}He pot and for thermal anchoring of instrumentation wires.

The still chamber is formed in the same toroidal shape as the 1 K pot to enable the mixing chamber to fit radially inside the still. The liquid in the still is pumped by a charcoal sorption pump at 4.2 K. When the dilution refrigerator is started, the still chamber will be about half full (3 cc). As the ^{3}He rich phase in the mixing chamber is depleted, dilute phase from the still will replace it to maintain the mixing chamber full and thereby avoid arcing problems. Connection between the still and mixing chamber is via a capillary of 0.5 mm inside diameter.

The mixing chamber contains about 3 cc of liquid. To precool it to

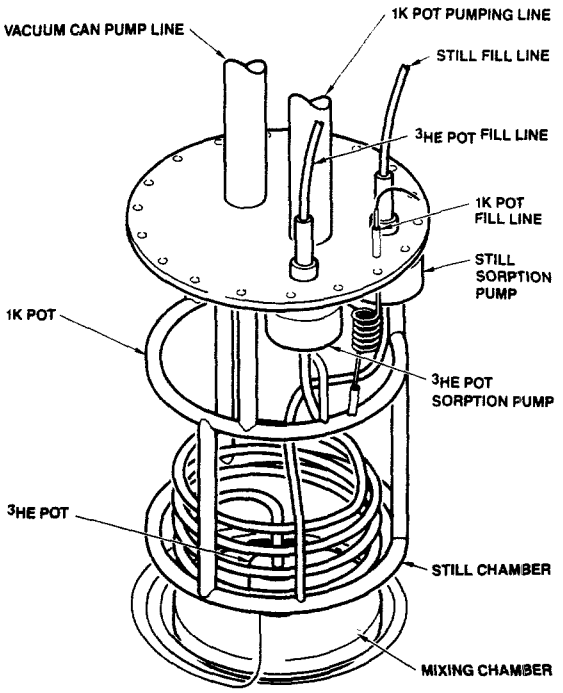

Figure 2. Schematic diagram of the single cycle dilution refrigerator. It is of compact radial design and fits inside a 11 cm diameter helium dewar.

0.3 K before the dilution process is started a small attached ^{3}He pot is used. The vapor pressure of the liquid in the ^{3}He pot is reduced by a charcoal sorption pump in the same manner as the still pump. The 1.5 cc of liquid in the ^{3}He pot provides sufficient cooling to reduce the mixing chamber temperature to 0.3 K and the still temperature to 0.6 K, thereby producing phase separation in the mixing chamber and diluting the still ^{3}He content to about 5%.

To illustrate the general operation of our refrigerator a complete cycle will be described. The mixture of about 35% molar ^{3}He concentration and the pure ^{3}He for the ^{3}He pot are initially adsorbed in the charcoal pumps at 4.2 K. Heaters are used to raise the temperature of the sorption pumps temporarily to about 20 K, thereby desorbing the gases. Condensation of the gases occurs where the connecting pump tubes are thermally anchored to the 1 K pot, and the cold liquid works its way through the pumping tubes and into the chambers using the heat pipe effect. Once the mixing chamber cools below 1.2 K, the heater for the ^{3}He sorption pump is turned off and the pump cools in a few minutes to 4.2 K, thereby starting cooling of the ^{3}He pot. When the mixing chamber has cooled to 0.3 K and the ^{3}He pot is empty, the heater on the still sorption pump is turned off to start the still pumping action. The mixing chamber will now start to cool below 0.3 K only if an electric field gradient is applied. The relative orientation of the mixing chamber and the still also influence the dilution cooling and will be described in the next subsection. Once the concentrated phase in the mixing chamber has been depleted, the charcoal pumps must be recycled to initiate a new cooling cycle.

3.2 THE MIXING CHAMBER-STILL SYSTEM

The key feature of our single cycle dilution refrigerator is that we will be able to test the cooling capabilities of the mixing chamber under unfavorable gravity conditions. Figure 3 shows the design. The capillary from the toroidally shaped still enters the mixing chamber right at the center from above where the electric field created by the

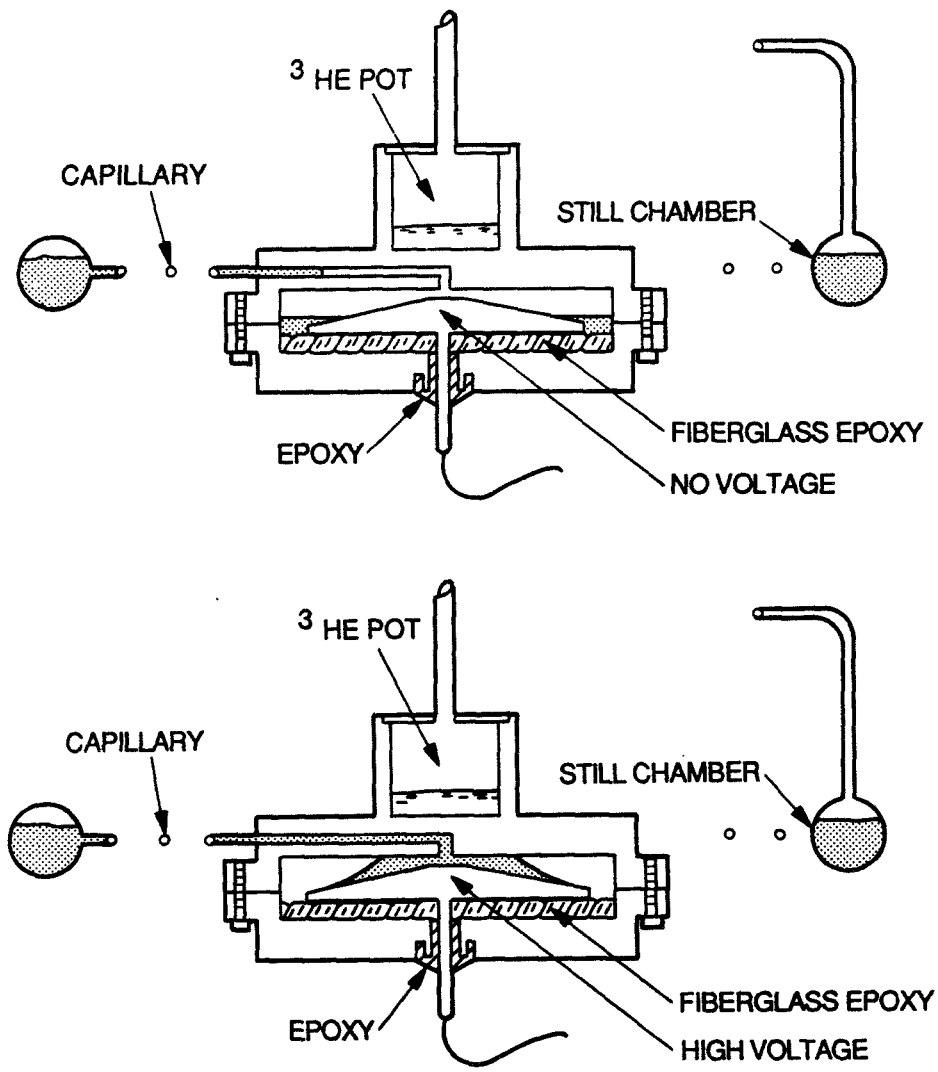

Figure 3. Details of the still/mixing chamber system in our dilution refrigerator. When the electrode voltage is turned off (upper figure) the outlet capillary from the mixing chamber to the still is covered with ^{3}He-rich phase (white) and dilution cooling will not take place. When the voltage is turned on (lower figure) the dilute phase (grey) moves into the high voltage region thereby covering the outlet capillary. Cooling will now commence.

cone shaped electrode is strongest. The inlet to the capillary is thus covered with dilute phase only when the voltage is applied. If the still is pumped without having the voltage on, the dilution refrigerator will simply act as a ^{3}He refrigerator, while if the voltage is turned on the inlet capillary will be covered with dilute phase and the dilution process will commence. An additional feature of the design is that the relative height of the still and mixing chamber can be easily changed (this must be done at room temperature), thus in essence controlling the applied gravity. The mixing chamber is made out of OFHC Copper, and instrumented with a heater for cooling power measurements, a GRT for temperature measurements, and a small coaxial capacitor to measure the position of the ^{3}He-rich/^{4}He-rich boundary interface. The high voltage electrode is insulated from the copper by a fiberglass-epoxy plate and the high voltage is fed into the mixing chamber through an insulated sealed epoxy feedthrough. To reduce radiation from the surrounding vacuum can wall at 4.2 K, the mixing chamber is enclosed by a copper radiation shield held at the same temperature as the still.

4. PRESENT STATUS

The single cycle refrigerator has been fabricated, assembled, and wired. Preliminary testing is underway.

5. Acknowledgements

The research described in this publication was carried out by the Jet Propulsion Laboratory, California Institute of Technology under contract NAS-7-918 with the National Aeronautics and Space Administration.

6. References

1. R.M. Ostermeier, I.G. Nolt, and J.V. Radostitz, Cryogenics **18**, 59 (1978)
2. H.W. Jackson, Cryogenics **22**, 59 (1982)
3. U.E. Israelsson, H.W. Jackson, and D. Petrac, Cryogenics **28**, 120 (1988)
4. P.R. Roach, these Conference Proceedings.

THERMAL EFFICIENCY OF A ZERO-G DILUTION REFRIGERATOR

PAT R. ROACH

NASA AMES RESEARCH CENTER
MOFFETT FIELD, CA 94035

ABSTRACT

In the process of developing a 0.1 K ^{3}He-^{4}He dilution refrigerator to operate at zero-g for space applications, a careful analysis of the thermal efficiency of the proposed refrigerator has been carried out. The dilution refrigerator being considered is a recent innovation that uses gas adsorption onto charcoal for all pumping operations. Although this makes the refrigerator most suitable for single-cycle operation, modifications to allow continuous operation are presented. In the single-cycle mode, reasonable assumptions about the operation of the charcoal pumps and of the refrigerator suggest that it should be possible to have a cooling power of 2.5 μW at 0.1 K for a run time of greater than 17 hours, recycle times of 3 hours and an average power rejected to 2.0 K of less than 4 mW. By suitable modifications to allow continuous operation it is possible to take advantage of some of the unused cooling power of the circulating He-3 gas, and a similar analysis shows that the same operation at 0.1 K should be possible with only about 1 mW of heat rejected to 2.0 K.

INTRODUCTION

Many types of infrared astronomy benefit greatly if the infrared detectors are cooled to very low temperatures. Temperatures from 4 K down to 0.3 K are readily achieved by pumping on baths of liquid He-4 or the rare isotope, He-3. In order to cool to temperatures below 0.3 K it is necessary to use techniques beyond simply pumping on such a bath. The most common technique that has been used for the last 20 years is the use of a He-3-He-4 dilution refrigerator. Such refrigerators are normally very large, very complex pieces of equipment that would hardly be suitable for remote applications in space.

However, a different type of dilution refrigerator has recently become available[1]. This refrigerator is very compact and much simpler and more reliable to operate than the previous type. The design of this refrigerator makes it very well-suited to space applications if it can be made to operate in zero gravity.

The commercially available compact refrigerator is based on a single-cycle operating mode where a small fraction of the duty cycle must be devoted to recycling the system. It is believed that this refrigerator can not only be modified to operate in zero G, it can also be modified to operate continuously so that the recycle time can be eliminated.

WHAT IS A DILUTION REFRIGERATOR?

Basically, a dilution refrigerator is a system that passes the rare isotope He-3 into and through a stationary portion of liquid He-4, producing cooling at the phase boundary where the two isotopes mix:

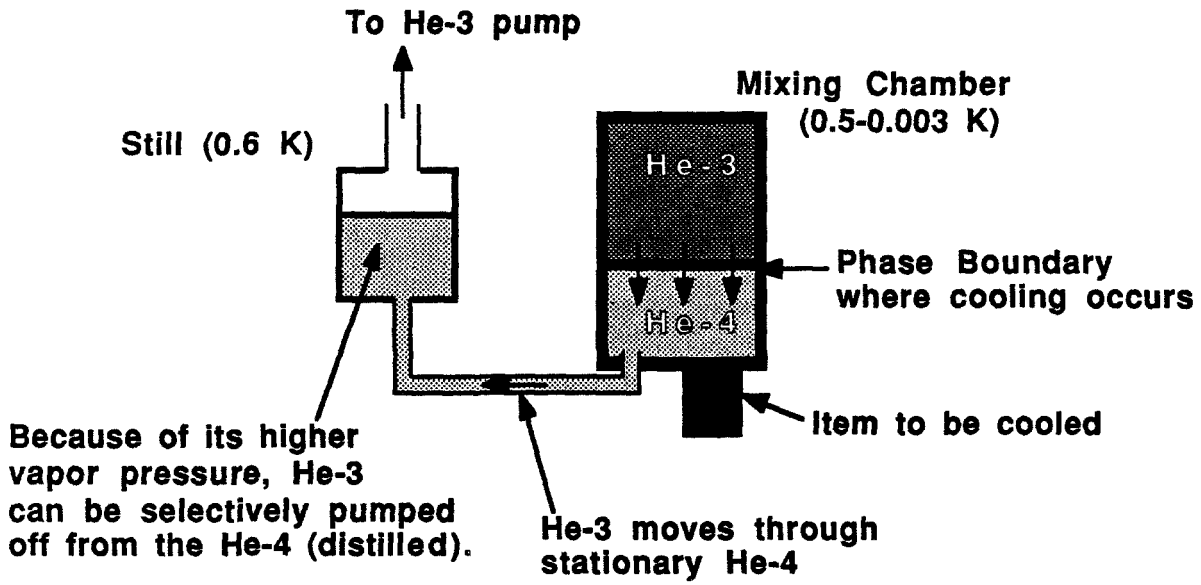

Fig. 1. Basic elements of a dilution refrigerator.

The cooling process can be thought of as 'evaporative' cooling: the He-3 'evaporates' into the background of He-4. The reason this process is important is that some unique properties of He-3 and He-4 allow this cooling to take place down to temperatures below 0.01 K. The main reason that the technique has been so popular, however, has been the fact that it can be operated in a continuous mode. By returning the He-3 that has been pumped off back to the mixing chamber, a continuously-operating refrigerator can be created that is invaluable for very-long-term experiments or experiments where very large amounts of heat must be removed.

An important feature of a dilution refrigerator is that the cooling power is proportional to the He-3 circulation rate and to the square of the temperature. In practice, the machines can vary from small systems with little cooling

power and limited low-temperature capabilities to enormous machines with huge cooling powers and the ability to cool below 0.003 K. Until recently, all such machines had elaborate and bulky gas-handling systems and large external pumps. In addition, they required considerable expertise to run and even then it was very difficult to keep them running routinely without frequent problems. The compact dilution refrigerator that has recently become available changes all this[2]. Its design uses gas-adsorption onto charcoal at low temperatures to provide the He pumping. This leads to a self-contained refrigerator with no external gas handling system:

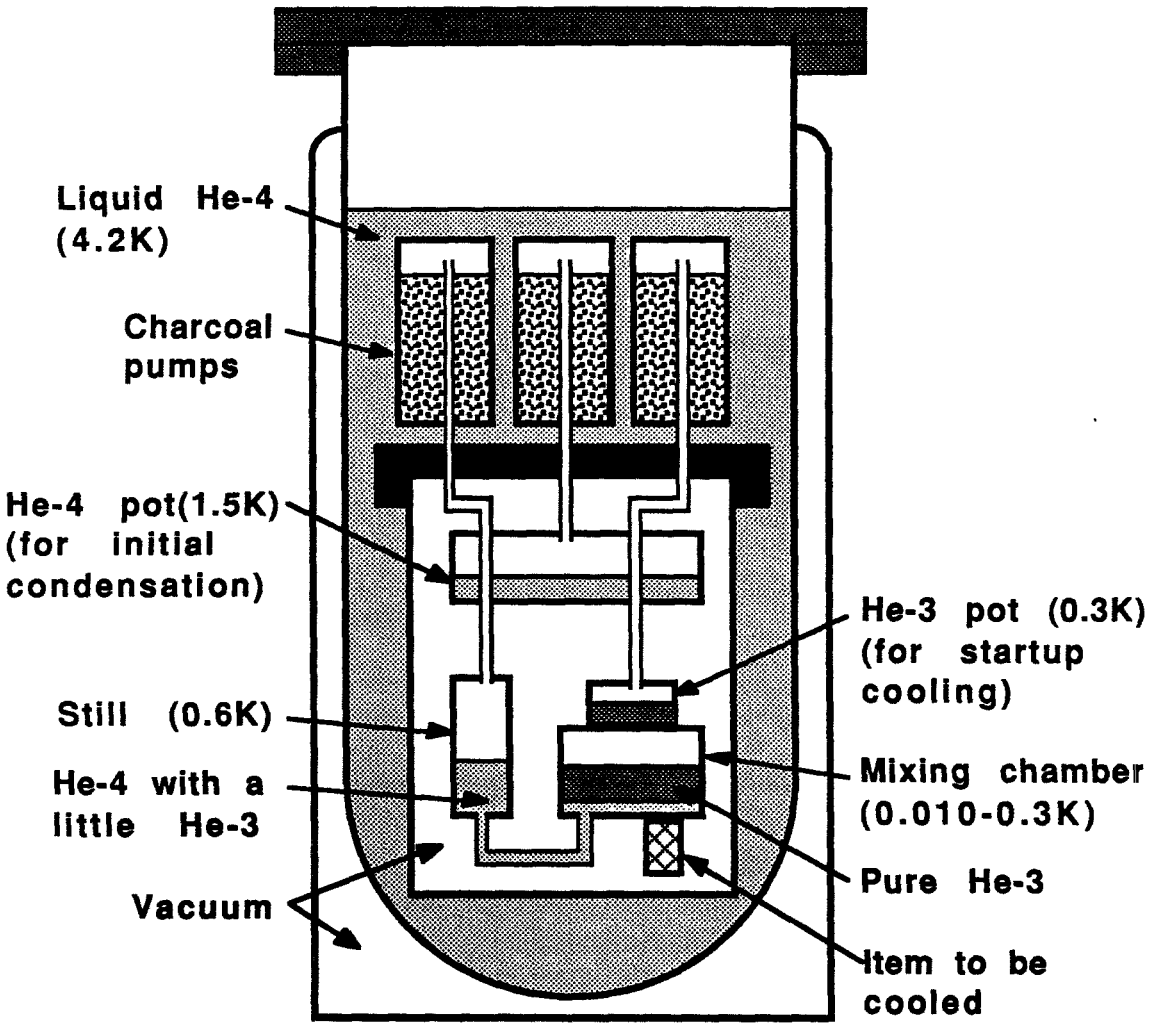

Fig. 2. Schematic of commercial compact dilution refrigerator.

This particular version is a single-cycle refrigerator; the system must be recycled when the charcoal pumps get full. In order to start up a single-cycle

refrigerator it is necessary to provide a He-4 pot for condensing the operating mixture of He-3 and He-4. In addition, it is necessary to have a He-3 pot attached to the mixing chamber to provide precooling to 0.3 K so that the dilution process can be efficiently started.

All pumping and recycling operations are controlled by heaters. There are no moving parts in the refrigerator. During operation none of the helium leaves the low-temperature region. These factors lead to very reliable performance and the option of completely automating all aspects of its operation so that no operator expertise is required.

MODIFICATION OF REFRIGERATOR FOR ZERO-G

In the configuration above, the force of gravity is used to keep the various liquids in their chambers and to keep the lighter He-3 floating on top of the He-4 in the mixing chamber. For operation in zero-g, another mechanism is needed to control the location of the liquids. It is proposed to use capillary confinement in porous metal sinter in order to do this. For a liquid chamber being pumped on, this would be done as follows:

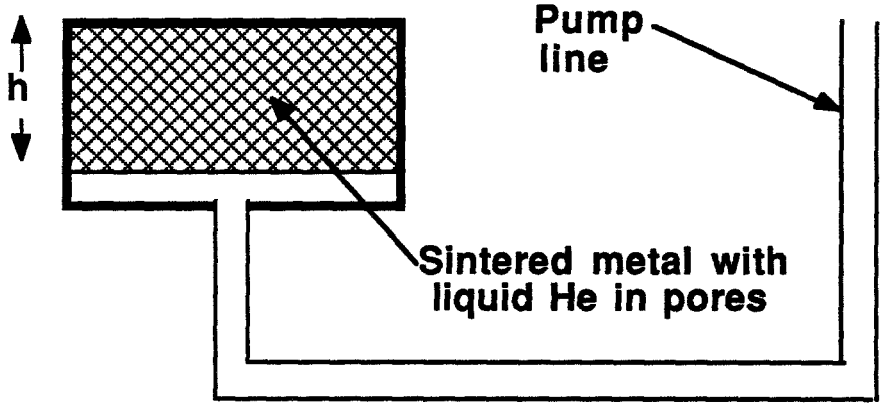

Fig. 3. Capillary confinement using sintered metal.

This technique causes the liquid to be retained in its chamber under the influence of adverse accelerations and also exposes a substantial liquid surface for pumping. If the pores of the sinter are of diameter, d, and the height of the liquid column is h, then the surface tension forces will cause the liquid to be retained in the pores as long as

$$d\,h < \frac{4\sigma}{\rho a}$$

where σ is the surface tension of the helium, ρ is its density and a is the acceleration.

The way the sinter would be installed in the compact dilution refrigerator

is as follows:

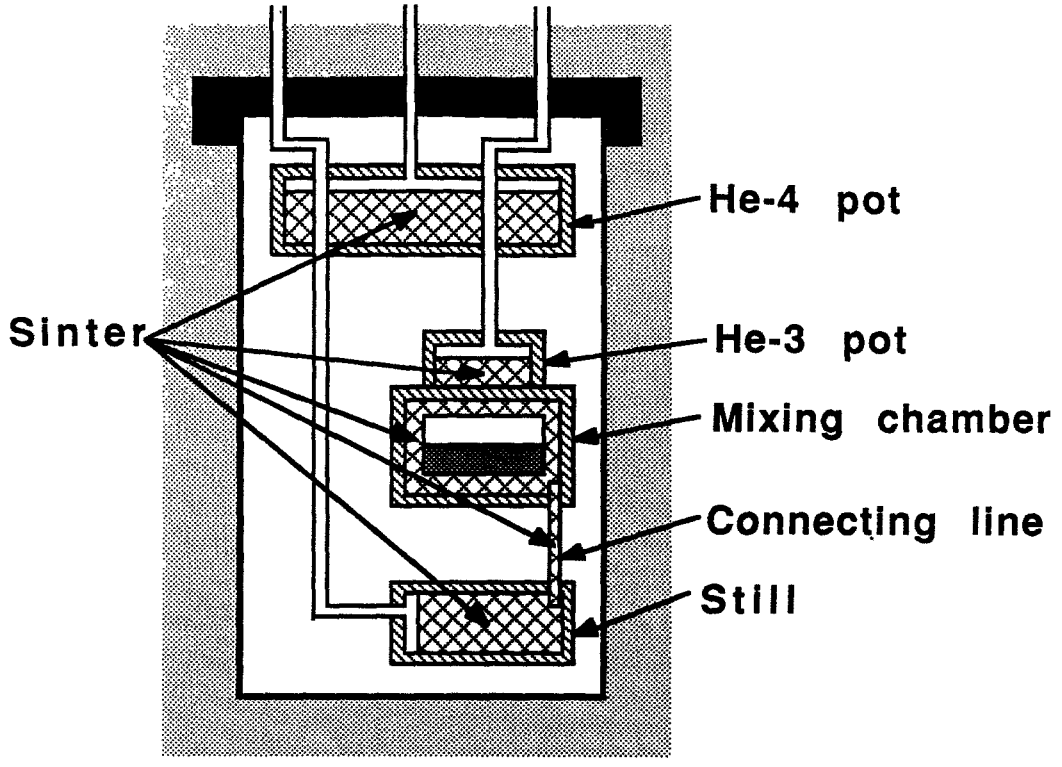

Fig. 4. Sinter installation in compact refrigerator.

All the chambers that normally have liquid in them will have porous sinter in them. For this modification the still is placed below the mixing chamber in order to facilitate the installation of sinter into the connecting line. The mixing chamber will have sinter only lining the walls. The cavity in the center will hold the He-3, and the sinter will contain the He-4. The small surface tension between the phases will prevent bulk He-3 from entering the sinter and leaving the mixing chamber.

EFFICIENCY OF REFRIGERATOR REJECTING HEAT AT 2.0 K

The main function of the He-4 pot is to condense in the mixture of He-3 and He-4 at 1.5 K; it turns out that satisfactory condensation of the mixture can also be obtained without the He-4 pot if a heat sink at 2.0 K is available. Since this is the temperature of superfluid He used for many cryogenic systems in space, it is reasonable to assume that such a heat sink temperature is available for space applications of the dilution refrigerator. This has the considerable advantage of allowing one to eliminate the He-4 pot and the

inefficiencies associated with condensing its He-4.

The heat rejected to the 2.0 K heat sink (the 2.0 K bath in Fig. 5) can be divided into two main parts: that occurring when the pumps are pumping their respective liquids, and that occurring when these liquids are being condensed into their chambers:

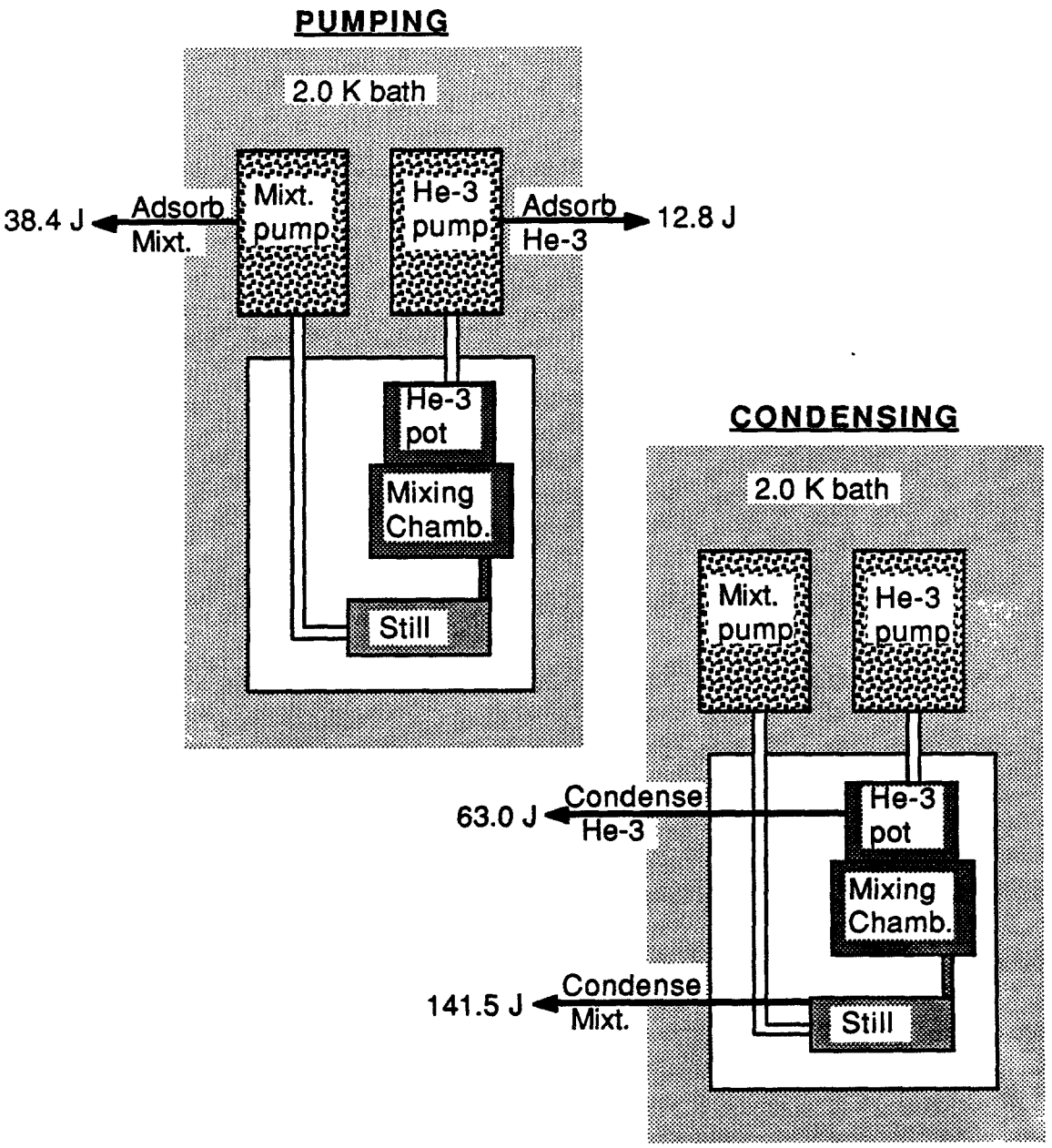

Fig. 5. Heat rejected to 2.0 K bath (heat sink).

The assumptions for the numbers in Fig. 5 are that the pumps are degassed at 25 K and that no helium remains in them at this temperature; that the He-3 pot contains 0.24 moles of He-3 and that the mixture system contains 0.28 moles of He-3 and 0.26 moles of He-4. These amounts are calculated to be sufficient to cool the system to 0.1 K and to run at this temperature for 17 hours at a He-3 circulation rate of 3×10^{-6} moles/sec. The cooling power at this circulation rate is 2.5 μW.

The numbers above can be summarized as follows:

Table 1. Performance of single-cycle compact dilution refrigerator.

Heat rejected during pumping	51.2 J
Heat rejected during condensation	204.5 J
Total heat rejected	255.7 J
Operating time at 0.1 K	17 hours
Cooling power at 0.1 K	2.5 μW
Recycle time	3 hours
Total cycle time	20 hours
Average power rejected	3.6 mW

CAN PERFORMANCE BE EXTENDED TO LOWER TEMPERATURES?

Because the He-3 is flowing in the small pores of the sinter, there will be some viscous heating in the mixing chamber and connecting line that will use up some of the cooling available. This effect is not important at 0.1 K but becomes increasingly serious at lower temperatures. Since the cooling power of the refrigerator without sinter is $\dot{Q}_o = P_o c T^2$, where P_o is a proportionality constant and c is the He-3 circulation rate, then the net cooling power of the refrigerator with sinter is $\dot{Q}_o - \dot{Q}_v$ where $\dot{Q}_v$ is the viscous heating in the sinter. If this net cooling power is divided by cT^2, the departures of the resulting quantity from P_o represent the effect of the viscous heating in the sinter. The regions where this quantity goes to zero are the effective limits of operation with the chosen sinter.

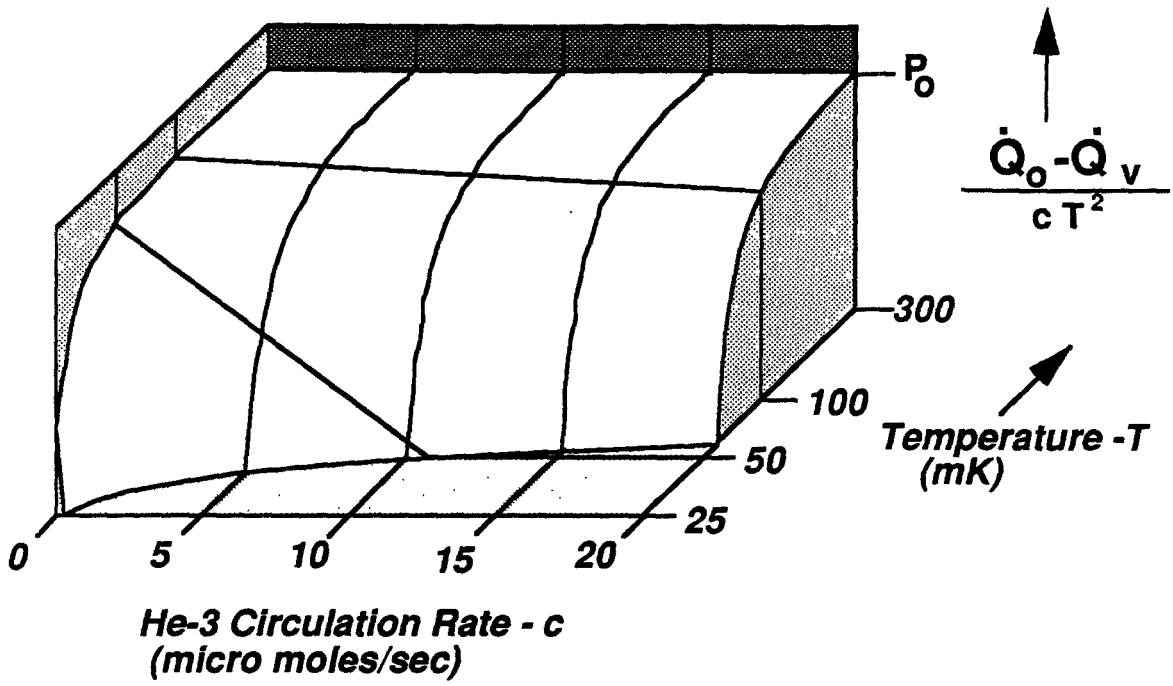

Fig. 6. Performance limits of refrigerator with sinter.

It can be seen that the performance at 100 mK is not much affected by the sinter but that the cooling power drops off sharply near 50 mK. It should be pointed out that the sinter used for the above evaluation has quite small pores so that it will be effective in 1 G for testing on the ground. For actual space applications accelerations much less than this are normally encountered. The sinter for these applications could be much coarser, in which case the viscous heating problem encountered above would be much less serious and much lower temperatures could then be achieved.

FURTHER IMPROVEMENTS

Analysis of the performance of the single-cycle refrigerator shows that there is still substantial cooling power contained in the He-3 that leaves the mixing chamber. This cooling power can be put to very good use if the refrigerator is converted to continuous operation. The He-3 that would then need to be returned to the refrigerator can be cooled and condensed by the He-3 leaving the mixing chamber. Another advantage of continuous operation is that the He-4 of the mixture and the He-3 of the He-3 pot would no longer have to be repeatedly condensed in; the He-4 would remain in the refrigerator during continuous operation and the He-3 pot would not be used

after the initial startup. Several modifications would have to be made for continuous operation:

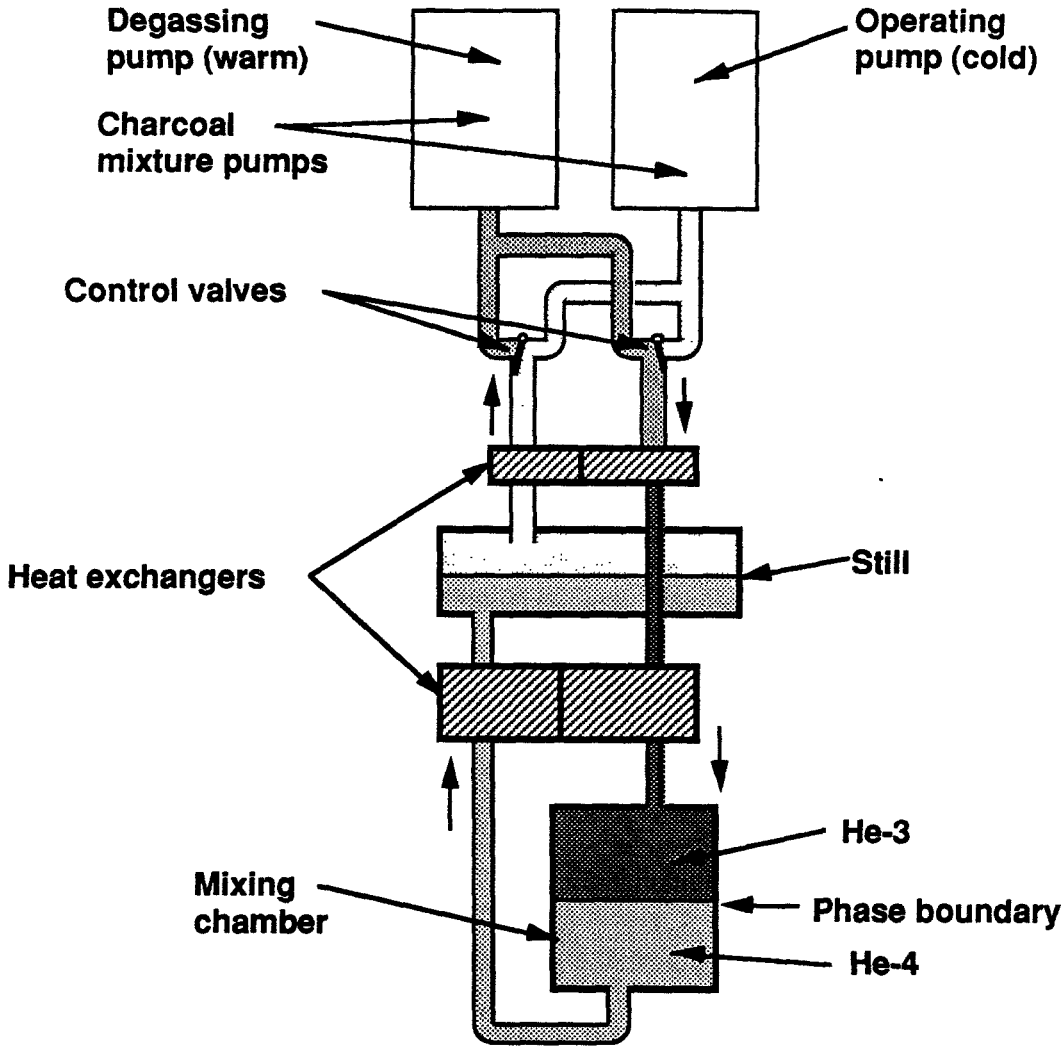

Fig. 7. Continuously-operating compact dilution refrigerator.

An additional charcoal pump must be added; one pump is being warmed and is putting He-3 into the system while the second pump is cold and pumping on the still. When the second pump gets full, the roles are reversed. Low-temperature control valves must be added to direct the flow of He-3 between the two pumps. Special heat exchangers must be added between the incoming and outgoing He-3 in order to take maximum advantage of the cooling power of the pumped-off He-3. When this is done one can achieve very good thermal efficiency:

Table 2. Performance of continuous compact dilution refrigerator.

Heat rejected - each half cycle	73.5 J
Operating time for each pump	26 hours
Cooling power at 0.1 K	2.5 μW
Recycle time	none
Average power rejected	0.8 mW

Although this refrigerator uses the same amount of He-3 as in the previous calculation, it lasts for 26 hours on each half cycle instead of 17 hours as before because none of the He-3 has to be used to cool the system from 0.3 to 0.1 K as in the single-cycle system; once the continuous system is at 0.1 K the He-3 is used just to maintain that temperature. The result is that the power rejected now is more that 4 times lower than for single-cycle operation.

SUMMARY

The main points about the compact dilution refrigerator are as follows:

1. A commercial dilution refrigerator is available which is highly appropriate for space applications--it is compact and reliable and it operates under computer control.
2. Modification of this refrigerator for zero-g operation is feasible; the use of sintered metal in all liquid chambers is capable of properly constraining the liquid in the presence of adverse accelerations.
3. The performance obtainable from the modified refrigerator is attractive from the viewpoint of cooling power, running time and heat rejected to the heat sink.
4. Modification for continuous operation is possible; this would greatly improve thermal efficiency and eliminate recycle time. Continuous cooling might be particularly useful for physics experiments in space.

Initial testing of a compact dilution refrigerator is currently underway and modifications to install sinter in the liquid chambers are about to begin. Tests will be conducted to verify the performance and thermal efficiency of the refrigerator with the sinter. If the testing is successful, a very different refrigerator for ultra-low-temperature space applications will be available.

REFERENCES

1. Model 302000; RMC-Cryosystems, 1802 W. Grant Road, Suite 122, Tucson, AZ 85745
2. P. R. Roach and K. E. Gray, *Advances in Cryogenic Engineering*. 33, 707 (1988)

Performance of the Philips Usfa Stirling cycle cooler.

R.J. de Putter
Philips Usfa B.V., Postbus 218, 5600 MD Eindhoven, The Netherlands

INTRODUCTION.

Philips Usfa BV makes a range of small cryogenic coolers for cooling the sensors of thermal imaging systems. These coolers operate around 80 K and have cooling capacities of 0.25 W, 0.5 W and 1.0 W. The diameters of the "cold fingers" are respectively 5, 7 and 10mm.
The standard compressor used at present has a diameter of 71mm and a length of 145mm, and we are currently developing two new compressors : one for the 0.25 W and 0.5 W cold fingers and one for the 1.0 W cold finger. The 1.0 W compressor has a diameter of 55mm and a length of 122mm. The compressor for the 0.25 W and 0.5 W cold fingers is 44mm in diameter and 142mm long. These coolers have an MTBF of 3500 hours and need no routine maintenance.

During the last few years a lot of experience has been gained with various cooler-Dewar combinations, one of the most widely used being the 0.5 W type UA 7041 cooler combined with the R185 Dewar. The R185 Dewar is a TICM class II Dewar containing Sprite detectors and produced by Philips Components, Mullard division. This paper reports on the measured performance of the UA 7041 cooler with this Dewar. It also includes data measured during tests on other coolers in the range, together with some early results obtained with prototypes of the new compressor.

The paper is arranged as follows :
- basic technical principles of the cooler.
- typical cooling capacity of the UA 7041.
- typical cooling demand of the R185 Dewar.
- performance of the UA 7041 - R185 combination.
- typical cooling capacity of the UA 7043.
- performance of the UA 7043 - R175 combination.
- typical cooling capacity of the UA 7040.
- results of lifetime testing.
- new developments.
- summary.

Basic technical principles of the cooler.

The principles of our cooler are based on the well-known Stirling cycle, using a free piston and free displacer (Figure 1).

The piston, driven by a linear motor, creates a pressure wave while the displacer moves in such a way that expansion takes place mainly at the top of the cold finger and compression takes place in the space between the piston and the displacer. The mass of the piston/coil assembly, in combination with the mechanical spring and the gas forces ("gas spring"), gives a mass-spring system which is tuned to the drive frequency of 50 Hz. Movement of the displacer is caused by the pressure drop across it, which also has a frequency of 50 Hz. Because the driving forces on both the piston and the displacer act in the direction of movement the side loads are extremely low. This is the main reason for the very long operational lifetime achieved with this type of cooler.
The compressors which are currently under development employ two pistons to cancel out vibration, but the same linear motor technology is retained.

Typical cooling capacity of the UA 7041.

The curves in Figures 2 and 3 are plotted from measurements made on two UA 7041 coolers (serial numbers 0300 and 0303), taken from normal production. UA 7041 coolers are equipped with a specially developed thermal interface (figure 4) which gives an optimal match with the R185 Dewar. The cold production of the UA 7041 is always measured on top of this thermal interface (without thermal interface it is even higher).
At input powers around 50 W it can be seen from Figures 2 and 3 that the increase of cold production by increasing the cold tip temperature is about 20 mW/K.

Typical cooling demand of the R185 Dewar.

The R185 Dewar used in these experiments had a heat loss of 100 mW at T_{amb} = 25°C. This was measured by examining how liquid nitrogen (77K) evaporated in the Dewar. It was assumed that the maximum heat loss in an eight-element Sprite detector during normal use in TICM II systems is 100 mW ; this is with an electrical field on the detector of 3V/mm. Hence the total cooling demand of the R185 with detectors biased is equal to 200 mW at T_{amb} = 25°C.
At T_{amb} = 70°C the heat loss of the Dewar is about 140 mW and therefore the total cooling demand of the R185 at T_{amb} = 70°C is equal to 240 mW.
According to Figure 2 we expect an input power in the order of 18 W to cool the R185 at 25°C and with detectors biased at 80 K. According to Figure 3 we expect an input power in the order of 32 W to cool the R185 at 70°C and with detectors biased at 80 K. The measured results are given in the next paragraph.

Performance of the UA 7041 - R185 combination.

The performance of the cooler-Dewar combination is shown in Table 1. The cooldown time was measured with the detectors unbiased and an input power of 55 W. The performance at 80 K and 95 K was measured with a heat dissipation of 100 mW in the Sprite detectors.

Table 1 : Performance of the UA 7041 - R185 combination with biased detectors except during cooldown.

	$T_{detector}$ = 80 K		$T_{detector}$ = 95 K	
T_{amb} (°C)	Q_{inp} (W)	Cooldown time (minutes)	Q_{inp} (W)	cooldown time (minutes)
-40	15	2' 07"	11	1' 41"
25	16	2' 05"	11	1' 42"
50	22	2' 32"	14	2' 03"
70	29	3' 12"	18	2' 36"

The table shows that the cooldown time to 95 K is significantly shorter than the cooldown time to 80 K. It also shows that operating Sprite detectors at 95 K instead of 80 K gives a significant reduction in input power, especially at T_{amb} = 70°C. The UA 7041 is tuned in such a way that the compressor is exactly in resonance when the "gas spring" is at 70°C.
At -40°C the inner pressure in the cooler is much lower than at +25°C and 70°C, and therefore at -40°C the compressor is a little out of resonance. That is the reason why the performance of the UA 7041 - R185 combination at -40°C is not much better than at 25°C.
When the cold production of the UA 7041 (figures 2 and 3) at Q_{inp} = 50 Watts is compared with the cold demand of the R185, it becomes clear that the UA 7041/00 has enough overcapacity to accommodate some long-term degradation of the Dewar and cooler.

Typical cooling capacity of the UA 7043.

The curves in figure 5 are plotted from measurements made on two UA 7043 1 Watt coolers (serial numbers 1528 and 1530), taken from normal production.
The cold production is measured on top of the cold finger and not on top of the thermal interface.

A thermal interface, soldered on top of the cold finger, is optional with the UA 7043. The use of a loose fuzz button is also possible ; however this is less efficient from the point of view of cold conduction.
With a thermal mass of 850 Joules the UA 7043 has a typical cooldown time to 80 K of 4 minutes at T_{amb} = 15°C.
At T_{amb} = 70°C the cooldown time equals 6 minutes.

Performance of the UA 7043 - R175 combination.

The 1 Watt cooler (type UA 7043) can be combined with a USCM Dewar containing 120 or 180 detector elements. A Dewar compatible with the USCM Dewar (i.e. the R175 supplied by Mullard) was used for testing. The R175 has a heat loss of 320 mW at T_{amb} = 25°C. The performance of this combination is shown in Table 2.
The cooldown time was measured with the detectors unbiased and an input power of 55 W. The performance at 80 K and 95 K was measured with a heat dissipation of 100 mW in the detectors.
In this test set up the UA 7043 was supplied with a thermal interface, soldered on top of the cold finger.

Table 2 : Performance of the UA 7043 - R175 combination with a dissipation of 100 mW in the detectors.

	$T_{detector}$ = 80 K		$T_{detector}$ = 95 K	
T_{amb} (°C)	Q_{inp} (W)	cooldown time (minutes)	Q_{inp} (W)	cooldown time (minutes)
15	24	6' 20"	19	5' 10"
55	39	8' 50"	23	6' 55"
70	46	10' 50"	28	7' 40"

The typical cooling capacity of the UA 7043 is 1.6 W at 80 K and T_{amb} = 15°C. At 50 K and T_{amb} = 15°C it is possible to reach 0.5 W of cold production with 75 W of input power. Some detectors work at 50 K ; the combination of UA 7043 cooler and R175 Dewar can meet this requirement.

Typical cooling capacity of the UA 7040.

The curves in figure 6 are plotted from measurements made on two UA 7040 0.25 Watt coolers (serial numbers 1104 and 1105), taken from normal production. The cold production is measured on top of the cold finger.

The cold fingers in the UA 7040 and UA 7043 conform to USCM dimensions, but the existing standard compressor (71mm diameter does not.

Results of lifetime testing.

In a recent life test, four 1 W UA 7043 coolers were run for 20 hours a day at ambient temperatures which alternated between -32°C and +52°C. The coolers were run at full input power, and cessation of specified performance was the failure criterion.

Results : cooler 0361 failed after 2480 hours
cooler 0362 was stopped after 5150 hours
cooler 0393 failed after 4057 hours
cooler 0394 failed after 4287 hours

These results give an MTBF of 3993 hours.

In the present life test six 0.5 W UA 7041 coolers are being run for 20 hours a day at ambient temperatures which alternate between -40°C and +70°C, with one extra cooldown during the remaining four hours. These coolers are not running with full input power, but with input powers which give sufficient cooling capacity to cool the detectors of a R185 Dewar to 80 K. Hence the input power is also alternating because the required cold production is 150 mW at T_{amb} = -40°C and 250 mW at T_{amb} = 70°C ; these cold production demands are based on the worst-case conditions of the R185 Dewar. The failure criterion is a input power of 55 W or, in other words, if a cooler needs more than 55 W to cool the detectors of the R185 to 80 K, the cooler is taken out of the test and analysed.

Results (excluding the standard 200 hours burn-in during production) :
cooler 1339 : failed after 2525 hours
cooler 1355 : still running after 2890 hours
cooler 1357 : failed after 1408 hours
cooler 1362 : still running after 2625 hours
cooler 1504 : still running after 1351 hours
cooler 1515 : still running after 591 hours

The early failure of coolers 1339 and 1357 was due to expansion problems at T_{amb} = 70°C ; when these coolers were taken off test, both were working well at 23°C and -40°C with no significant degradation. A corrective action was introduced in the production line and coolers 1504 and 1515 were then put on test.
This life test is being witnessed by TNO, a Dutch government laboratory comparable to NVEOL in Washington.

In addition, five 0.5 W UA 7041 coolers are currently being run continuously for 24 hours a day at an input power of 40 W and a constant T_{amb} of 23°C. The running time to date for each cooler is shown below. All five coolers are stil running.

Cooler 1258 : ..... 6591 hours
Cooler 1259 : ..... 6776 hours
Cooler 1260 : ..... 6744 hours
Cooler 1263 : ..... 6766 hours
Cooler 1264 : ..... 6756 hours

On the basis of these tests Philips is able to guarantee the specified MTBF of 3500 hours. No routine maintenance is needed.
When a cooler fails it must be either repaired or discarded.

New developments.

In comparison with the existing standard compressor used with all three types of cold finger, the new compressors mentioned in the introduction will have the following advantages :

- full USCM compatibility
- very low vibration (opposed pistons)
- internal EMI shielding
- very low static magnetic field outside the compressor
- 10 V (50Hz) running voltage
- low noise level
- optional DC/AC converter supplied with compressor

The cryogenic performance will be the same as that of the existing coolers described in this paper. Some early results are given in Table 3.

Table 3 : Results from the first 1 Watt prototypes (Serial Nos. 0001 and 0002)

T_{amb} °C	Q_{inp} (W)	Vin (V)	Q_o at 80 K (W)
-40	50	9.9	1.96
25	55	11.7	1.67
70	60	12.4	1.11

Vibration level of compressor : peak force is 1.1 N

Summary.

- Philips coolerrange : 0.25 W, 0.50 W and 1.0 W
- half Watt cooler Dewar combination : cooldown of 2 minutes and Q_{inp} at 80 K : 16 W.
- one Watt cooler Dewar combination : cooldown of 6 minutes and Q_{inp} at 80 K : 24 W.
- results life tests : MTBF $\geqslant$ 3500 hours
- new USCM compressors under development

August 1988

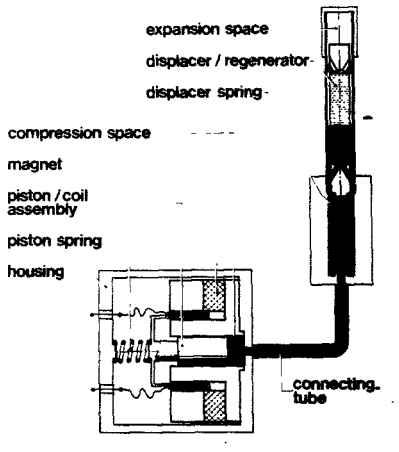

Fig.1: Diagrammatic cross section of the split Stirling cooler with linear motor.

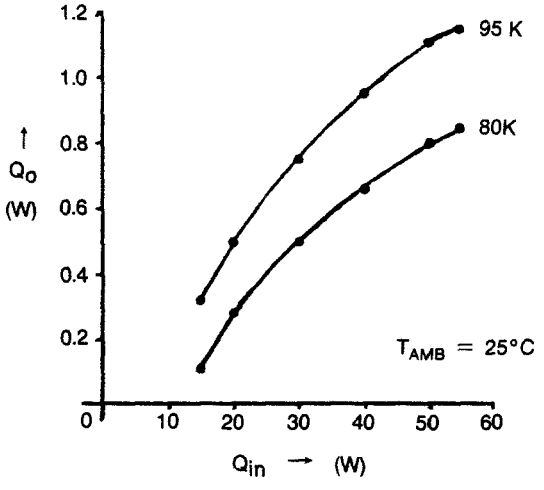

Fig.2: Cold production of the UA 7041 at two different cold tip temperatures at T_{amb} = 25°C.

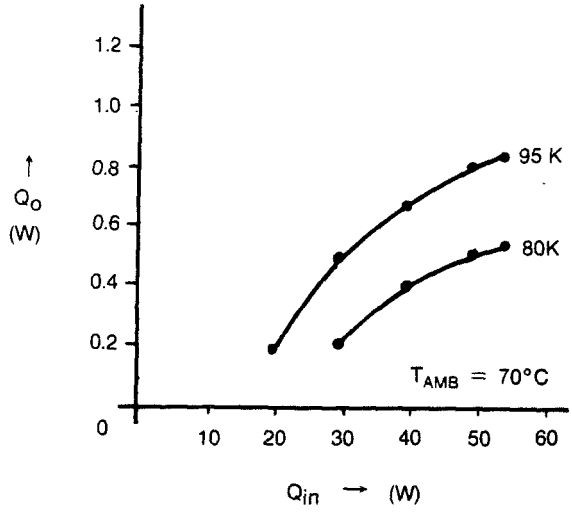

Fig.3: Cold production of the UA 7041 at two different cold tip temperatures at T_{amb} = 70°C.

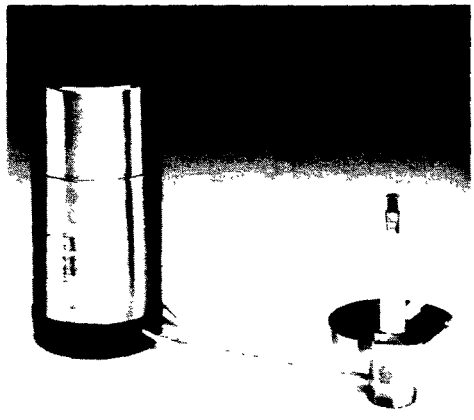

Fig.4: The UA 7041 cooler with the standard thermal interface.

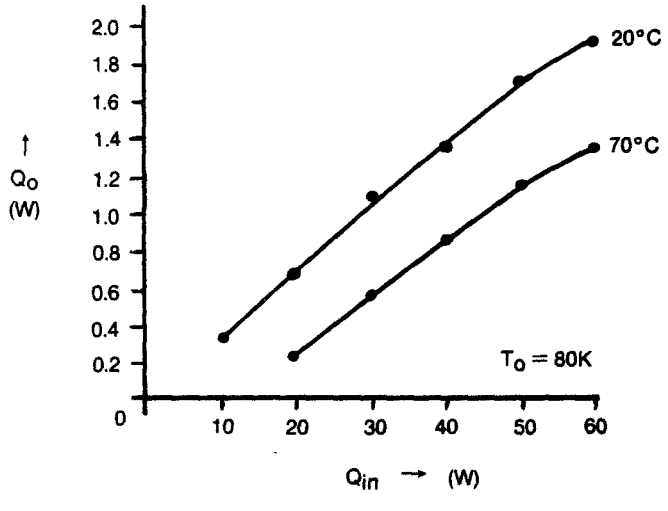

Fig.5: Cold production at 80 K of the UA 7043 at two different ambient temperatures.

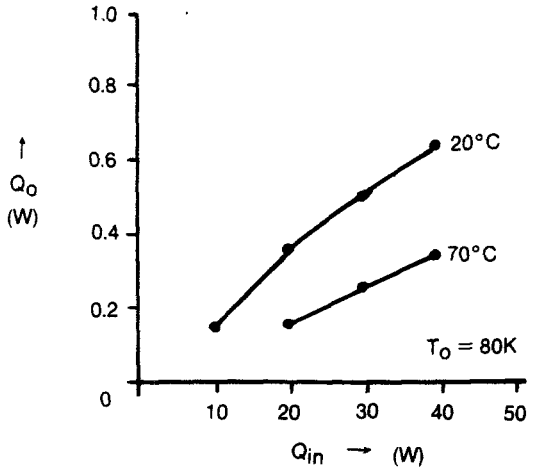

Fig.6: Cold production at 80 K of the UA 7040 at two different ambient temperatures.

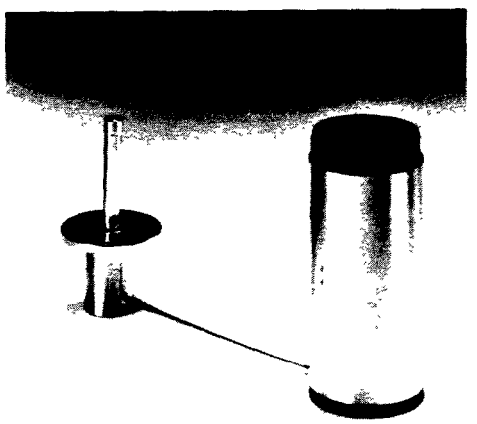

Fig.7: The dual opposed piston compressor with a diameter of 55 mm and a length of 122 mm combined with the 1 Watt cold finger.

MULTI-STAGE CRYOCOOLER PERFORMANCE AND STAGE EFFICIENCY PREDICTIONS

Christina L Cain

Flight Dynamics Laboratory, Wright-Patterson AFB OH 45433

A method to estimate the required input power of multi-stage cryocoolers has been developed, and a FORTRAN program has been written to predict cooler input power. The input power is calculated given the required ambient temperature, stage temperatures and loads, and stage efficiencies. The program can be used in early system design and tradeoff studies to compare various types of multi-stage cryocoolers including hybrid machines.

In order to reasonably predict the required input power, the coolers' stage efficiencies must be known. A FORTRAN program to predict stage efficiencies given input power, ambient temperature, and stage temperatures and loads has been developed. Estimated stage efficiencies for existing cryocoolers are presented.

1. Introduction

For preliminary system design and integration studies, the input power of a staged cooler may need to be calculated at many design points. A method to easily estimate input power as a function of operating conditions would be very useful -- such a method is available if cooler stage efficiencies are known. Many cooler efficiencies have been compiled by Strobridge [1]; however, the efficiencies presented are system efficiencies shown as a function of cooling capacity at the coldest temperature. Also, once a cooler is designed, the manufacturer often develops a complex design and prediction tool to either size cooler components to optimize a design or to predict operating conditions from a cooler design. Typically these tools require a lot of knowledge to operate, and are not generally available. It is therefore desirable to estimate stage efficiencies for any cooler given its operating conditions. The stage efficiencies could then be used for system studies of similar coolers (including hybrids).

2. Approach

Two related problems will be considered. The ultimate objective is to estimate cooler input power with a small amount of computation. First an equation is given to predict input power as a function of the number of stages, the required temperature and cooling capacity at each stage, the ambient heat reject temperature and the stage efficiency of each stage. Clearly, in order for the predicted input power to be accurate, stage efficiencies must be known. Consequently, a method to estimate stage efficiencies of coolers given operating conditions is presented.

3. Nomenclature

n	Number of stages
Q_i	Useful cooling provided by the i^{th} stage
Q_{G_i}	Gross cooling provided by the i^{th} stage
Q_{R_i}	Heat rejected by the i^{th} stage
T_i	Absolute temperature of cooling at the i^{th} stage Note: T_0 = system reject temperature
W	System input power
W_i	Input power required for the i^{th} stage
η_i	Stage efficiency of the i^{th} stage
τ_i	Temperature ratio for i^{th} stage (T_{i-1}/T_i)
ϕ_i	$\tau_i - 1$

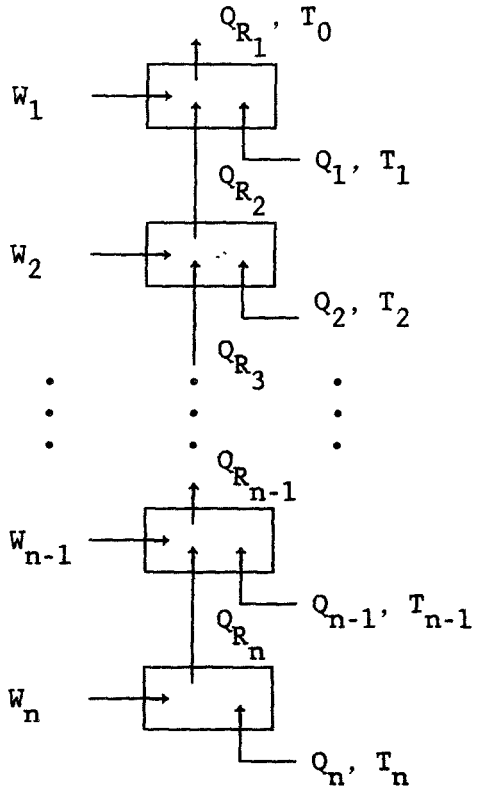

Figure 1. System Representing a Multi-Stage Cooler

4. Discussion

Consider the system shown in figure 1. The following stage conditions result from applying energy balances to various portions of the system. The gross cooling provided by individual stages follows:

$$Q_{G_n} = Q_n$$

$$Q_{G_i} = Q_i + Q_{R_{i+1}} \quad ; \quad 1 \le i \le n-1$$

The required input power for each stage is given by the following equation:

$$W_i = Q_{G_i} \phi_i / \eta_i$$

The heat rejected from each stage follows:

$$Q_{R_i} = W_i + Q_{G_i} = Q_{G_i} [1 + \phi_i / \eta_i]$$

The required system input power follows:

$$W = \sum_{i=1}^{n} W_i = Q_{R_1} - \sum_{i=1}^{n} Q_i \tag{1}$$

Expanding equation (1) while recognizing that

$$Q_{R_i} = [Q_i + Q_{R_{i+1}}][1 + \phi_i / \eta_i]$$
$$= \sum_{j=i}^{n} Q_j \prod_{k=i}^{j} [1 + \phi_k / \eta_k]$$

results in the following expression for system input power:

$$W = \left(\sum_{i=1}^{n} Q_i \prod_{j=1}^{i} [1 + \phi_j / \eta_j] \right) - \left(\sum_{i=1}^{n} Q_i \right) \tag{2}$$

It is convenient to expand equation (2) in terms of combinations of efficiencies and coefficients that are functions of stage temperatures and loads.

$$\text{Let } a[m:s(1),s(2),\ldots,s(m)] = \left(\prod_{i=1}^{m} \phi_{s(i)} \right) \left(\sum_{i=s(m)}^{n} Q_i \right)$$

where: $1 \le s(1) < s(2) < \ldots < s(m) \le n$
$1 \le m \le n$

Next, find system input power by considering all $\sum_{m=1}^{n} \binom{n}{m}$ combinations of stage efficiencies:

$$W = \sum_{m=1}^{n} \sum_{s(1)=1}^{n-m+1} \sum_{s(2)=s(1)+1}^{n-m+2} \cdots \sum_{s(m)=s(m-1)+1}^{n} a[m:s(1),\ldots,s(m)] \Big/ \prod_{i=1}^{m} \eta_{s(i)} = P(n) \tag{3}$$

In equation (3) P(n) is the system input power calculated using temperatures, loads, and efficiencies; and W is the actual system input power. The object is to find the set of stage efficiencies which cause P(n) = W (or P(n)/W = 1). Define f_k as follows:

$$f_k = [P_k(n)/W_k - 1] \prod_{i=1}^{n} \eta_i$$

This is a measure of the error between the input power calculated using the efficiencies and the actual input power. A set of efficiencies that makes $f_k = 0$ describes the k^{th} operating point. A single set of stage efficiencies that will satisfy many operating points is desired. F is defined as the sum of the square of the errors of all the operating points considered.

$$F = \sum_{k=1}^{j} (f_k)^2 \quad \text{where: j is the number of operating conditions} \quad (4)$$

The best set of stage efficiencies which satisfy j operating conditions is found by minimizing F. Note, if there is only one stage, the best efficiency that describes the system can be calculated directly by setting $dF/d\eta_1$ to zero and solving for η_1:

$$\eta_1 = (1/j) \sum_{k=1}^{j} a[1:1]_k / W_k$$

Arranging equation (3) in terms of the coefficients a[m:s(1),...,s(m)] allows the coefficients to be evaluated once for each data point, then equation (4) can be evaluated for many combinations of stage efficiencies without recalculating the coefficients. Equation (3) is also very useful if the optimization technique requires derivatives of F with respect to efficiency.

5. Search Method

Since equation (4) has many local minima, a direct search method is employed to find the best set of stage efficiencies which describe the system. An increasingly fine grid is used to compare the values of F calculated using different combinations of efficiencies. The mesh size starts by considering a range of all combinations of efficiencies with intervals of .1 (the user can choose the minimum and maximum efficiencies to be considered for each stage). At the end of each iteration, the combinations of efficiencies with the smallest values of F are used to choose ranges of efficiency combinations which are evaluated with a finer mesh. The smallest mesh size considered is .001.

Before applying the search method to actual coolers, a check was performed to see if it would predict the best set of stage efficiencies. A set of operating conditions (n, ϕ_1 ... ϕ_n, Q_1 ... Q_n) and a set of

CASE	# of Stages	Stage (i)	T_0 (K)	τ_i	Q_i (W)	W* (W)	η_i	F
1	1	1	300	3.75	50.	343.75	.40	0.E0
2	2	1	300	3.75	50.		.40	
		2		2.00	10.	637.50	.35	0.E0
3	3	1	300	3.75	50.		.40	
		2		2.00	10.		.35	
		3		2.00	5.	1290.625	.30	.49E-31
4	4	1	300	3.75	50.		.40	
		2		2.00	10.		.35	
		3		2.00	5.		.30	
		4		4.00	1.	3000.75	.25	0.E0

* Calculate using eq (2) and $\eta_1 = .40$, $\eta_2 = .35$, $\eta_3 = .30$, $\eta_4 = .25$

Table 1. Individual cases used to check search method.

CASE	Stage (i)	T_0 (K)	τ_i	Q_i (W)	W* (W)	η_i	W Calc (W)
1	1	320	4.00	50.		.350	
	2		4.00	10.		.233	
	3		2.00	5.	5534.41	.206	5629.2
2	1	300	3.90	40.			
	2		3.50	20.			
	3		2.44	3.	5253.98		5098.5
3	1	310	3.78	60.			
	2		4.55	20.			
	3		2.00	1.	4364.97		4215.7
4	1	298	3.73	40.			
	2		2.67	10.			
	3		2.73	.5	1277.71		1353.4

* Case 1: $\eta_1 = .34$, $\eta_2 = .25$, $\eta_3 = .20$
Case 2: $\eta_1 = .33$, $\eta_2 = .25$, $\eta_3 = .19$
Case 3: $\eta_1 = .35$, $\eta_2 = .23$, $\eta_3 = .18$
Case 4: $\eta_1 = .33$, $\eta_2 = .27$, $\eta_3 = .22$

Table 2. System of four cases used to check search method.

efficiencies (η_1 ... η_n) were arbitrarily chosen. Equation (2) was used to calculate input power using the chosen set of operating conditions and efficiencies. Next F was minimized using the set of operating conditions and input powers. Table 1 shows that the set of stage efficiencies predicted by equation (4) are the efficiencies that were expected. Next a check was done to see if one set of appropriate efficiencies will be predicted for a set of operating conditions with different efficiencies. Again arbitrary operating conditions and efficiencies were chosen and the corresponding system input powers were calculated. Table 2 shows the four operating conditions used to predict the best set of efficiencies. If the entire possible range of efficiencies is considered ($0 \leq \eta_i \leq 1$) the best set of efficiencies predicted by minimizing F follows: $\eta_1 = .625$, $\eta_2 = .122$, $\eta_3 = .236$. This solution does not fall within the ranges of efficiencies predicted for each individual operating condition. Although this set of efficiencies causes the error of the four cases to be small, it will give unrealistic estimates of the change in input power with change in operating conditions. To improve the estimate of input power for operating conditions near the four points used to estimate the stage efficiencies, the range of efficiencies considered during the optimization must be restricted so the solution falls within the range of efficiencies defined by the individual cases. When the efficiencies considered during the optimization are restricted as follows $.33 \leq \eta_1 \leq .35$, $.23 \leq \eta_2 \leq .27$, $.18 \leq \eta_3 \leq .22$, the following set of efficiencies optimizes equation (4): $\eta_1 = .350$, $\eta_2 = .233$, $\eta_3 = .206$ (input power predicted by this set of efficiencies is listed in Table 2 in the column labeled W Calc).

In order to insure that the change in input power with operating conditions is realistic, the search method was modified slightly. When a set of efficiencies is to be found for many cases, first the optimum set of efficiencies is found for each case. These efficiencies are then used to restrict the range of efficiencies considered during the search.

6. Results

The code to estimate stage efficiencies was applied to published performance predictions on coolers using the Reverse Brayton cycle (Rotary Reciprocating Refrigerator -- Arthur D. Little [2]), and the Vuilleumier (VM) cycle (High Capacity Spacecraft cooler -- Hughes [3]). Once stage efficiencies were found, the input power calculated using the efficiencies was compared to the actual input power [% Error = $(W_{calc}/W_{actual} - 1) \times 100$].

Rotary-Reciprocating Refrigerator (R^3)

Predictions of input power were provided for one, two, and three stage coolers for a number of loads and temperatures -- the heat rejection temperature was 328 K in every case. The single stage results are not presented in detail; however, $\eta_1 = .146$ predicts input powers within 15% of those presented in reference [2] (figure 7) for loads of 10 W to 40 W at temperatures from 100 K to 30 K.

The two-stage performance curves are presented in ref [2] (figure 8). The best set of stage efficiencies found for each set of operating

W (W)	τ_1	τ_2	Q_1 (W)	Q_2 (W)	η_1	η_2	% Error
900	4.75	6.90	22.	1	.155	.452	- 1.5
800			18.				- 1.3
700			15.				- 2.4
600			10.				- .7
500			6.				.5
1000	4.26	3.85	37.5		.150	.383	.6
900			32.5				- .3
800			28.				- .1
600			18.				- 3.0
500			14.				- 1.0
400			10.				2.1
1000	3.86	2.83	44.		.151	.243	.2
900			38.				- 1.3
800			33.				- .7
700			29.				2.6
600			22.5				- .8
500			17.5				.1
400			12.				- .9
300			7.				.6
900	3.53	2.33	42.5		.144	.215	- 2.4
800			38.				- .2
700			33.				1.6
600			27.				.9
400			16.				3.2
300			4.				- 3.4
800	3.25	2.02	42.		.142	.154	- 2.0
700			36.				- 1.4
600			30.				- .5
400			18.				2.4
300			11.				.1
200			4.5				- .6
800	2.69	1.63	50.		.124	.122	- 3.8
700			44.				- 1.7
600			37.				- 1.2
500			31.				2.2
400			24.				3.9
300			16.				2.2
200			8.				- 1.2
700	2.31	1.42	50.		.105	.090	- .1
600			41.				- 2.2
500			34.				- .1
400			27.				3.0
300			18.				- .0
200			10.				.1

Table 3. Results for two-stage R^3 (T_0 = 328 K)

conditions are presented in Table 3. The input power calculated using these efficiencies is within 4% of the input power presented in ref [2] (figure 8).

Three-stage performance curves are presented in reference [2] (figure 9). The best set of stage efficiencies found for each curve is presented in Table 4. Again, the input power calculated using these sets of stage efficiencies is within 4% of the input power shown on the performance curves.

High Capacity Spacecraft Cooler

Off design performance for this cooler is presented in figures 1,2, and 3 of reference [3]. The program used to prepare the graphs (figs 1,2,3 Ref [3]) was used to generate the operating parameters used to determine the stage efficiencies presented in Table 5. The third stage load and temperature varied within each group. Consequently, the average set of efficiencies was found for each group. then the first and second stage efficiencies were fixed at the average values and the third stage efficiency was found as the third stage load and temperature changed.

τ_1 *	τ_2	τ_3	Q_1 ** Range(W)	η_1	η_2	η_3	% Error Range
4.05	3.24	2.50	13 : 50	.296	.341	.441	- .7 : .6
3.69	2.54	1.75	15 : 50	.255	.345	.381	-2.3 : 3.2
3.38	2.20	1.47	15 : 38	.270	.273	.221	-2.4 : 1.7
3.15	1.93	1.35	15 : 33	.277	.221	.161	-2.1 : 1.3
2.93	1.72	1.30	16 : 38	.309	.159	.108	-1.8 : 2.0
2.50	1.51	1.16	32 : 50	.275	.126	.057	-3.3 : 3.8
2.17	1.36	1.11	18 : 46	.279	.086	.030	-3.0 : 1.3

*
** $T_0 = 328$ K
$Q_2 = .4Q_1$, $Q_3 = 1$ W

Table 4. Average stage efficiencies for three-stage R^3

7. Summary

A method to determine stage efficiencies of multi-stage coolers has been presented. Using this method, the efficiencies can be determined knowing only the operating conditions (input power, and heat reject temperature; and each stage cooling capacity and temperature). Since there are many sets of efficiencies which will make f_k very small, some judgment must be used to get results that will provide accurate input power predictions for large changes in system parameters. Using this method, stage efficiencies can be estimated without having access to detailed design information. Once stage efficiencies are known, system trades can be preformed easily.

W (W)	τ_1^*	τ_2	τ_3	Q_1 (W)	Q_2 (W)	Q_3 (W)	η_1	η_2	η_3	% Err
1934	4.96	3.00	2.77	6.17	5.28	.071	.356	.205	.014	.00
1934	5.00	3.05	2.63	5.41	4.84	.205	.358	.205	.037	.03
1932	5.00	3.05	2.55	5.66	4.92	.309	.357	.204	.055	-.03
1930	5.04	3.02	2.47	5.43	5.06	.398	.357	.204	.069	.03
1928	5.04	3.02	2.40	5.65	5.14	.482	.358	.204	.081	.03
1926	5.04	3.02	2.27	6.07	5.29	.627	.356	.205	.100	.01
1926	5.08	3.07	2.10	5.40	4.92	.747	.356	.204	.106	-.01
1924	5.08	3.07	2.00	5.76	5.07	.847	.358	.204	.112	.03
1923	5.08	3.07	1.95	5.92	5.14	.892	.357	.205	.114	.02
1914	4.89	2.47	3.21	12.32	10.13	.122	.394	.231	.022	.02
1912	4.89	2.47	3.12	12.58	10.18	.238	.395	.230	.042	-.05
1910	4.92	2.45	3.03	12.36	10.28	.338	.395	.232	.057	.00
1909	4.92	2.50	2.89	12.17	9.91	.448	.395	.231	.073	.00
1907	4.92	2.50	2.81	12.39	9.97	.532	.395	.230	.085	.04
1905	4.92	2.50	2.74	12.59	10.02	.610	.395	.230	.095	.03
1904	4.96	2.48	2.67	12.33	10.12	.676	.394	.232	.101	.04
1901	5.00	2.46	2.54	12.24	10.27	.796	.394	.230	.114	-.02
1900	4.96	2.53	2.37	12.61	9.92	.918	.394	.232	.121	-.03
1896	4.81	1.99	3.83	18.63	15.13	.069	.393	.189	.018	.00
1894	4.85	1.97	3.72	18.42	15.17	.179	.394	.189	.045	-.04
1892	4.89	1.96	3.62	18.21	15.22	.278	.393	.189	.068	.00
1890	4.89	1.96	3.53	18.43	15.24	.373	.394	.189	.089	-.04
1888	4.89	1.96	3.44	18.64	15.27	.460	.394	.187	.110	-.03
1885	4.92	1.97	3.22	18.28	15.06	.627	.393	.188	.143	.02
1883	4.92	1.97	3.14	18.28	15.09	.696	.394	.187	.156	.02
1882	4.92	1.97	3.07	18.64	15.12	.760	.393	.189	.165	-.04
1879	4.96	1.95	2.93	18.52	18.20	.869	.394	.189	.177	.01
1879	4.78	1.58	4.36	24.57	19.75	.088	.361	.144	.034	-.02
1878	4.81	1.56	4.25	24.35	19.76	.182	.360	.145	.066	-.01
1875	4.81	1.56	4.15	24.56	19.77	.272	.360	.144	.099	.03
1874	4.85	1.56	4.05	24.31	19.78	.351	.361	.144	.121	.00
1871	4.89	1.54	3.86	24.24	19.80	.497	.361	.144	.161	.03
1869	4.89	1.54	3.78	24.42	19.81	.566	.361	.144	.181	.00
1867	4.95	1.53	3.62	24.30	19.83	.684	.361	.144	.205	.01
1864	4.92	1.53	3.47	24.61	19.86	.796	.360	.145	.230	-.01
1862	4.96	1.52	3.33	24.45	19.89	.889	.361	.144	.242	.01
1863	4.78	1.21	4.83	30.52	24.75	.090	.236	.145	.038	.04
1862	4.81	1.20	4.72	30.27	24.73	.160	.235	.145	.064	-.10
1858	4.81	1.20	4.53	30.59	24.72	.305	.236	.145	.117	.01
1856	4.85	1.18	4.39	30.62	24.85	.398	.236	.145	.128	.02
1856	4.89	1.17	4.31	30.33	24.83	.447	.236	.145	.132	.03
1853	4.89	1.17	4.15	30.60	24.83	.552	.235	.144	.165	-.06
1851	4.92	1.16	3.93	30.55	24.81	.684	.236	.144	.179	-.01
1850	4.96	1.15	3.80	30.34	24.79	.760	.235	.144	.183	-.04
1849	5.00	1.14	3.61	30.22	24.77	.865	.235	.145	.183	-.05

Table 5. Stage efficiencies for High Capacity Cooler (T_0 = 320 K)

Sets of efficiencies were found for the two-stage Reverse Brayton cycle; and three-stage Vuilleumier, and Reverse Brayton cycles. These sets of stage efficiencies predict input powers within 4% of the input powers presented in published performance curves [2,3].

Although the individual stage efficiencies presented in Tables 3, 4 and 5 seem high, the entire system efficiency predicted by the stage efficiencies is consistent with the system efficiencies presented by Strobridge [1]. For example consider the fourth entry in Table 5 (η_1=.357, η_2=.204, η_3=.069). In this case system efficiency (defined as W_{carnot}/W_{actual}) is .056.

8. Recommendations

The method should be used to quantify existing coolers -- once the coolers are quantified, trade studies can be performed easily.

The method to determine the best set of stage efficiencies can be improved by considering both the change in input power with respect to the operating conditions, and the input power itself. The change in equation (2) with the change in ϕ_1 ... ϕ_n, and Q_1 ... Q_n should be derived. In addition to finding a set of stage efficiencies which satisfies equation (4), the set of stage efficiencies should also force the observed change in input power to equal the calculated change in input power.

9. References

1. Walker, G. Cryocoolers Part 1: Fundamentals, Plenum Press, New York, 1983, pp 20-36.

2. Harris, R. E. and R. W. Breckenridge, Jr., "Rotary-Reciprocating Refrigerator Performance Spectrum", AFFDL-TR-73-149 Closed Cycle Cryogenic Cooler Technology Applications, Proceedings of the Cryogenic Cooler Conference, USAF Academy, CO, 16-17 October 1973, p395.

3. White, R. "Program for Predicting V-M Off-Design Performance", AFFDL-TR-73-149 Closed Cycle Cryogenic Cooler Technology Applications, Proceedings of the Cryogenic Cooler Conference, USAF Academy, CO, 16-17 October 1973, p163.

SESSION VI

SYSTEMS INTEGRATION

CHAIRPERSON: B. BENEDICT
VICE CHAIRPERSON: M. SUPERCYNSKI

CLOSED LOOP TEMPERATURE CONTROL FOR IR SYSTEM APPLICATIONS

W.J.GULLY

G.M.HUGHES ELECTRONICS, TORRANCE, CA 90505

In many circumstances precise control of the cold end of a cryocooler offers advantages to the user. We at Hughes have been adding such closed loop temperature control using pulse width modulation to our miniature cryocoolers. This paper will discuss the method and its consequences.

Key words:cryogenic cooler;feedback;temperature control; electromagnetic interference.

Introduction

The Thermal Products product line of Hughes manufactures a variety of cryogenic coolers in high volume primarily for tactical IR sensor cooling applications. These are principally single stage Stirling coolers of 0.25 to 2.5 watt cooling capacity at 80K. They are used to cool detector dewars containing arrays of infrared sensitive semiconductor elements. We are interested in temperature control because it allows the optimization of the detector radiometric performance in the system. In addition, temperature control eliminates the excess refrigeration usually generated in order to meet the cooldown requirements imposed by the system designers.

Our approach was to include the control circuitry within the present volume of our coolers to simplify retrofit of existing systems. We chose a pulse width modulation scheme as opposed to linear regulation for control because it resulted in a power savings as well. With PWM the motor is disconnected during part of the dutycycle which reduces the average input current and results in a lower rotational speed of the compressor. In temperature control we arrange it so the compressor slows when it cools below the desired control point to a rate sufficient only to maintain that temperature. An illustration of a cooldown to the temperature control point and the resulting cutback in power for one of our one watt capacity rotary coolers is shown in the Figure 1.

The implementation of temperature control has many side benefits. It reduces heat rejection to the system as well as power draw from the system supply. Similarly, acoustic noise, vibration levels, and low frequency electrical noise decrease. Indications are that cryocooler life also increases because of the decreased linear travel of bearings and seals. The main disadvantage in our sensitive IR application is that attention has to be paid to the suppression of EMI.

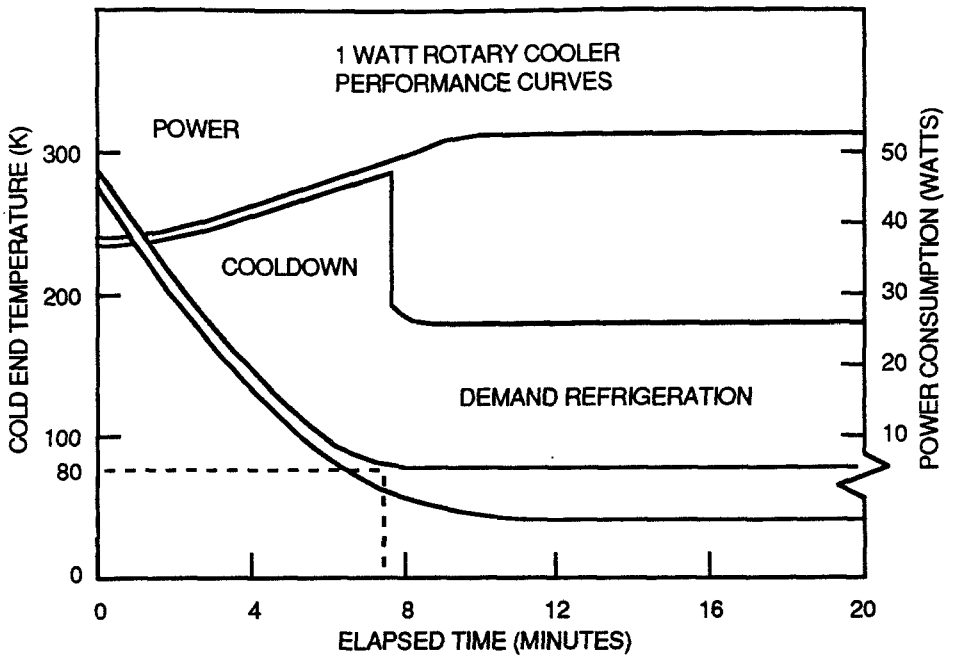

Figure 1. Temperature and power evolution for a one watt capacity rotary cooler with and without temperature control.

Implementation

Since the circuit had to fit within the cooler it had was designed with a minimum number of components and built as a hybrid circuit (where unencapsulated parts are used and the circuit is encapsulated as a whole to minimize size). In this case the hermetic hybrid package could be omitted because the contamination requirements for the circuit [1] are already provided by the cryocooler environment.

The circuit consists of three primary parts:analog control section, motor driver section, and input power filter. These are shown schematically in Figure 2. We begin with the analog section, which provides the closed loop temperature control for the cooler. It consists of a diode temperature sensor on the cold end of the expander, a voltage reference for a setpoint, and a sense amplifier for comparing them. The use of a diode as a temperature transducer has been extensively investigated.[2] We have used both 1N914 silicon diodes and the BE junctions of 2N2222 NPN silicon transistors because they are already provided on the arrays of commercial detector dewars. They have slopes of approximately 2 mv/K and an output of about a volt at 80K. Since there is an interface between the array and the expander coldfinger, as shown in Figure 2, the sensor is not in direct contact with the cooler but is in contact with the object to be cooled.

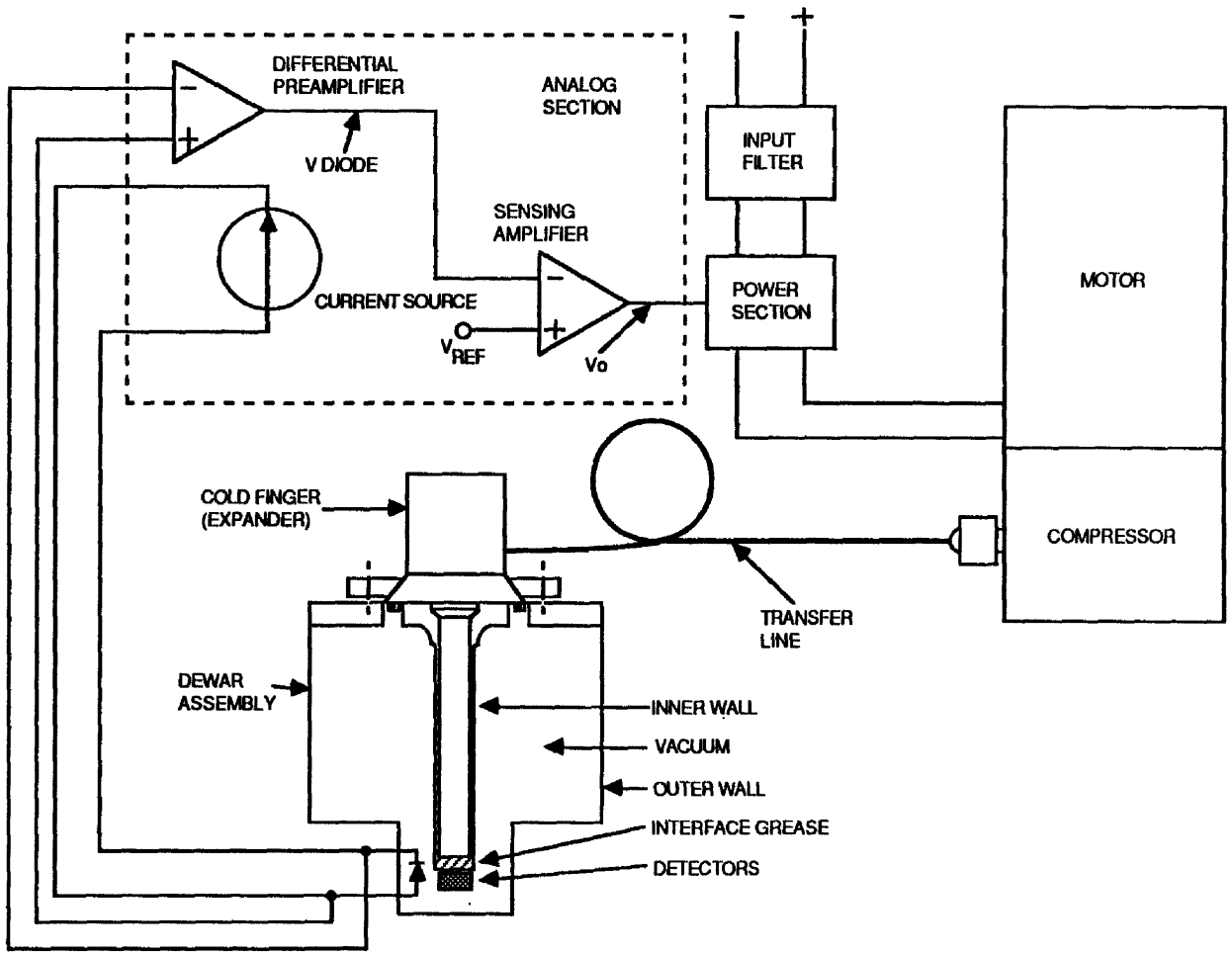

Figure 2. A schematic of the cryocooler control loop.

The diode voltage is buffered by a differential amplifier with unity gain. A sense amplifier with a gain of about 250 compares the diode output with a setpoint derived from a temperature stable reference voltage source. Because of the high gain, and because the output can swing only about two volts between maximum and minimum speed "stops", the sense amplifier is in a linear region for only a very small range of diode voltages. The output of the sense amplifier provides the duty cycle control level of the pulse width modulator.

The compressor is driven by a typical brushless DC motor. Six transistors in three totems with a delta or wye motor connected across their taps are fired in a commutation sequence determined by Hall effect position sensors. To implement demand control, the relatively slow commutation signals are combined with the high frequency pulse width modulator output to produce the total control signal. The PWM turns the current on and off hundreds of times in each commutation state. The fraction of time that the current is on is determined by the width of the pulse, which is in turn determined by the output level of the analog section. The greater the average current the higher the rotational speed of the compressor and the greater the refrigeration.

We will now turn to the last major section, the input power filter. Since the input current has to be completely interrupted to achieve efficient power control, it suffers a serious modulation that is an unacceptable noise source for the infrared systems. The input current flow can be smoothed by adding an LC filter between the input and the motor. These have been thoroughly investigated for DC to DC converters.[3] Since the volume of the filter is inversely proportional to its resonance frequency, and the switching frequency has to be much higher than the resonance for effective filtering, it is desirable to make the switching frequency as high as possible. In our circuits the switching frequency has to be above 50Khz because of the limited volume available for the electronics.

Temperature control

The degree of temperature control is primarily determined by two factors, the "gain" of the loop and the shift of the setpoint with ambient temperature. These can be deduced from the cooler control curves illustrated in Figure 3. The gain of the loop is the numerical factor by which the control loop divides the usual response of the cooler to a stimulus because it can counteract the response by adjusting the input power. We can estimate the open loop gain by considering the response to a substitute control signal applied to the analog circuit input. If we decrease the input voltage by 4 millivolts while idling at minimum speed in control at 80K (1.063 V at 23C in Figure 3) we would completely turn on the power.

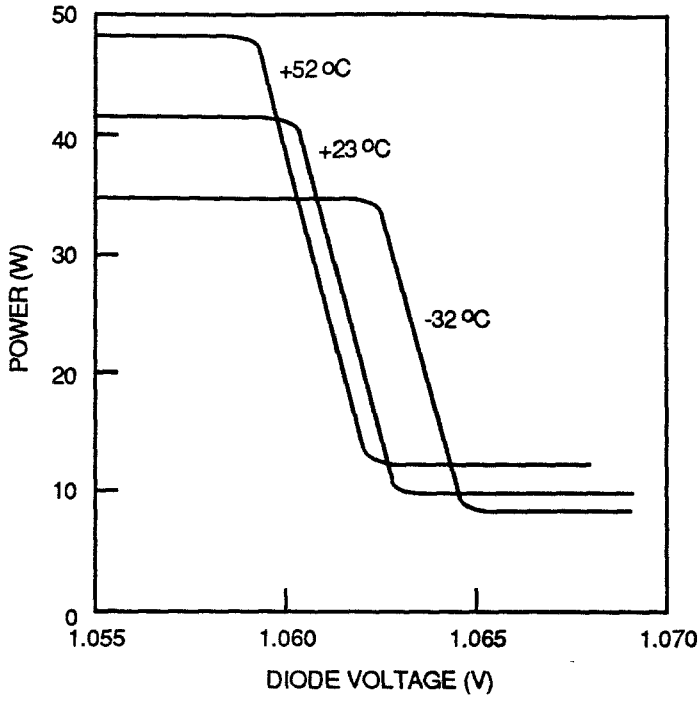

Figure 3. Input power versus diode control voltage at several ambient temperatures.

This would correspond to the full power case illustrated in Figure 1, where the cold end is approximately 40K colder in temperature. The delta T is equivalent to an 80 millivolt rise in voltage on the sensor, a twentyfold return on the stimulus. The open loop gain is therefore about twenty.

The shift in setpoint is also shown in Figure 3, where the control curves are given for a range of input temperatures. The shifts are traceable to a combination of temperature dependence of the reference voltage source and input offsets of the sense amplifier.

The plot can be used to understand the shift in the diode temperature with a change of ambient temperature from low to high illustrated in Figure 4. The cooler needs more power to maintain 80K on the cold end when the compressor and dewar assembly are at a high ambient temperature, so the diode must warm slightly to generate the necessary control signal to produce that power. In addition, the setpoint voltage shifts and causes the cooler to control the thermometer around a temperature that is not 80K. The total shift is a combination of both effects.

One can make a similar argument for the cooler response as it approaches the end of its useful life. As it ages, the bottom temperature increases and the refrigeration drops off because of lost gas, higher levels of internally generated

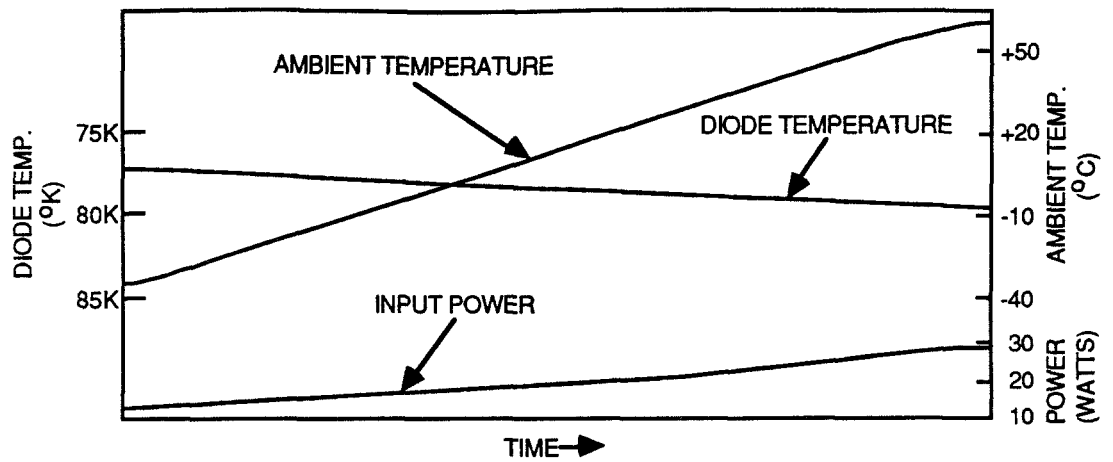

Figure 4. Temperature control during ambient temperature change.

contaminants, increased drag, or other factors. In closed loop control the effect one would have had in open loop is divided by the gain, resulting in the necessary increase in power with no appreciable change in diode voltage to provide the needed control.

Time response

Another aspect of interest is the response time of the feedback loop. In cryocoolers the response is unusually slow because the expander cools at a rate determined by the cold end heat capacity divided by the refrigeration rate, which is on the order of the cooldown time. In addition, the extended interface between the coldfinger and sensor results in a complex delay to this basic lag.

A manifestation of the slow response is illustrated in Figure 5, a measurement of the small step response of the cooler in closed loop to a change in the setpoint. The step was introduced by adding a small voltage to the diode voltage at the input to the circuit. This eventually caused the circuit to slow down until the sum of the diode signal and the perturbation returned to the original control value. The slow response illustrated in Figure 5 insures that there will be no short time noise in the detector due to the control of the cooler. However, a disadvantage of the slow and distributed response is the accompanying phase delay of finite frequency perturbations to the loop. If the phase delay of the perturbation exceeds half a cycle in addition to the inversion for negative feedback before the gain of the circuit is less

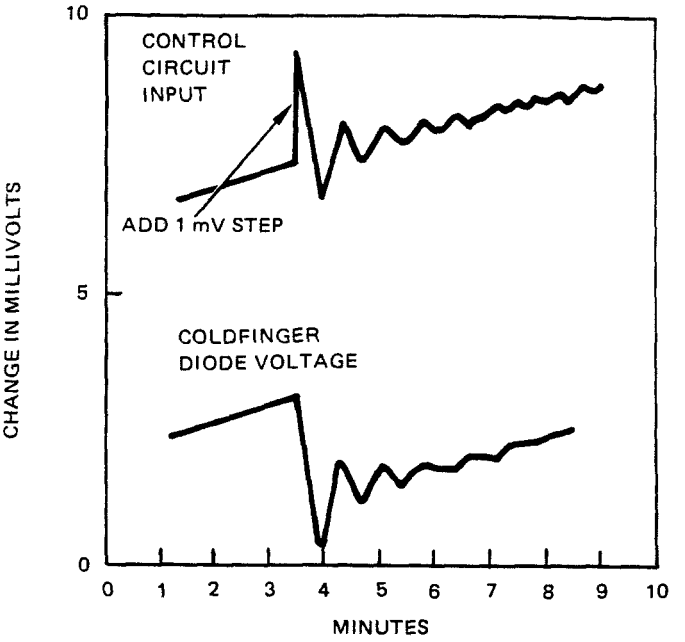

Figure 5. Step response to a non-saturating offset.

than one, the perturbation feeds back on itself and the circuit will oscillate about the control temperature. During our breadboard phase this instability was observed for our cooler in a detector dewar for gains an order of magnitude larger than we currently use, which shows that there is a limit to the gain and tightness of temperature control as we have implemented the loop. The damped oscillations in Figure 5 indicate that at present the circuit has a phase margin at unity gain of about an eighth of a cycle. This control behavior is quite adequate for our present applications.

The damped oscillation is characteristic of a two timeconstant response. Dynamic signal averager results indicate that this is approximately correct, but that the true behavior is more complex because of the distributed thermal response of the cold end of the system.

Electromagnetic Interference

One potential problem in providing temperature control for cryocoolers is the resulting EMI. Two avenues will be discussed, the input current and temperature sensor lines.

The current variations are measured with a current probe around either of the power leads between the power supply and the filter. The result is shown for a rotary cooler in Figure 6. There are low frequency modulations related to the

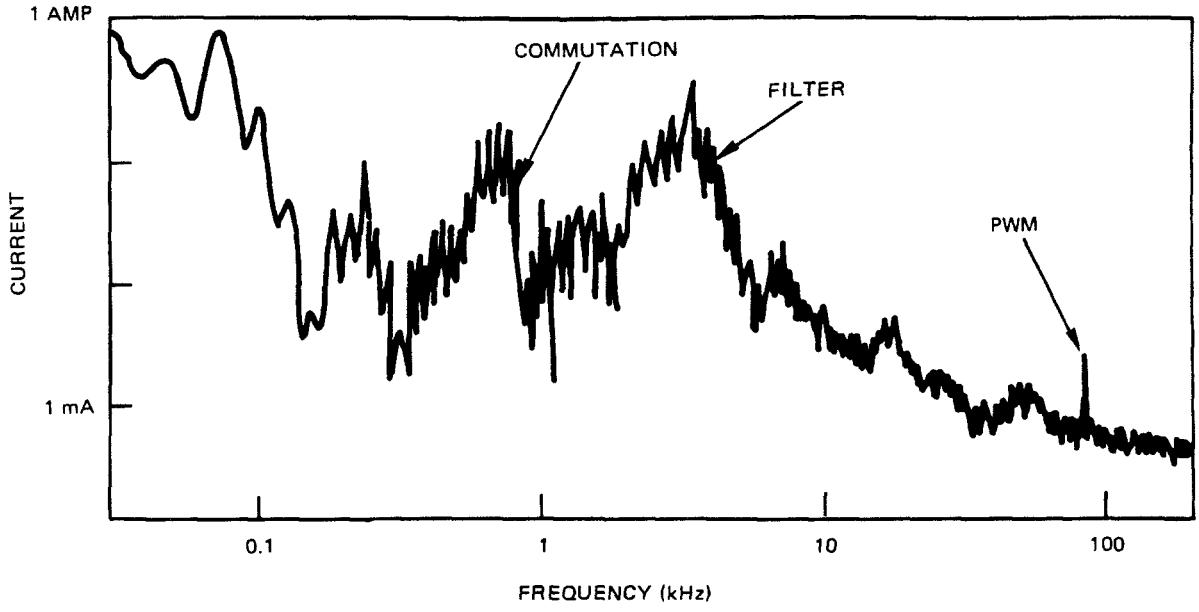

Figure 6. Current spectrum for a one watt rotary cooler.

operation of the coolers that have nothing to do with temperature control. The input power filter does nothing to affect these and the levels are the same as if temperature control were absent. At slightly higher frequencies one finds currents due to the "ringing" of the input filter, which is driven by discontinuities in the motor current. At higher frequencies yet we find the residual current ripple due to the pulse width modulation that the input filter was added to suppress. This has been attenuated by several orders of magnitude by the filter. Not shown is a smaller broadband response in the megahertz range due to transients associated with the leading and falling edges of the PWM pulses. These can be eliminated if necessary with transient absorbing filters.

The temperature sensor is a conduit for EMI into the IR system because it is typically located in close proximity to the sensitive cold electronics, and the resulting capacitive coupling between them provides a path for high frequency signals. The source of the noise can be understood by the following model: In a typical system, both the cooler power supply and the detector dewar electronics are in some way tied to the system ground plane. When power flows to the cooler from the supply some of it tries to capacitively return to the supply through the detector and the groundplane. An example of the noise that can occur is provided in Figure 7, which shows the diode signal relative to the cooler case. The diode signal carries vestiges of the switching transients that

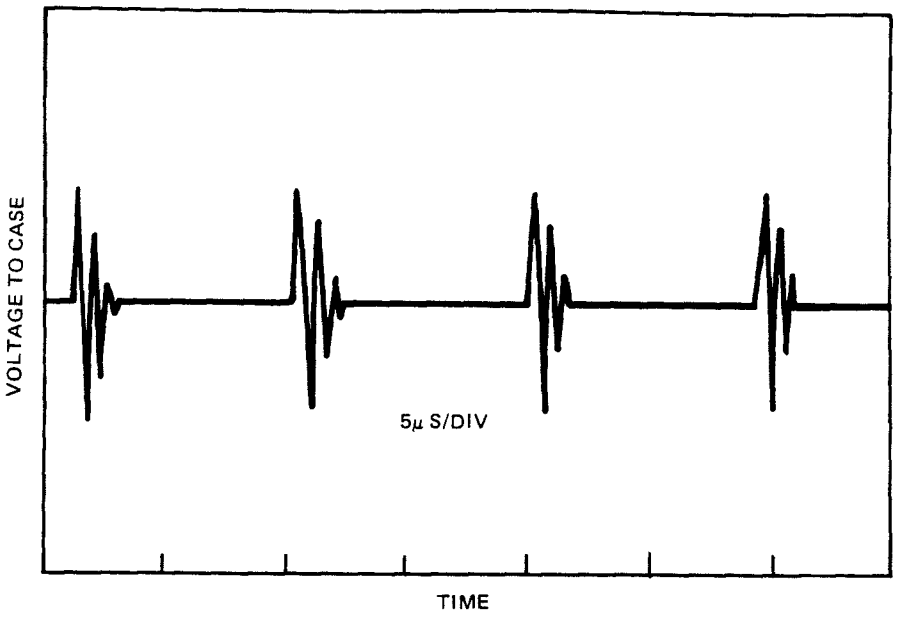

Figure 7. EMI on the temperature sense leads.

delineate the edges of the pulse width modulation discussed above. To minimize these transients it is necessary to reduce their initial size by careful circuit design. The circuit common must be as close to the case ground as possible to make sure that the minimum signal occurs across the capacitance to the detector. The diode leads have to be filtered relative to the case at the input to the differential amplifier and the case has to be tightly connected to the system ground. These steps have been sufficient for noise free temperature control in a variety of IR systems.

The coupling discussed assumes the simplest scenario in which the cooler is directly connected to a typical commercial detector dewar, which has the diode centrally located near the sensitive IR detector elements. In some systems the problem has been circumvented by adding a buffer circuit between the cooler and the diode to provide filtering as well as scaling and offsetting. If the detector design were not fixed, the problem could be eliminated by minimizing the capacitance between the sensor and its leads and the sensitive area to be cooled.

SUMMARY

The addition of temperature control by means of pulse width modulation has been implemented within the volume of our miniature cryocoolers. Control of the temperature to within a

few degrees of the setpoint over a variety of conditions has been achieved, accompanied by decreases in power and heat rejection. In our application the implementation requires internal filtering and a good electrical ground for the compressor case to eliminate EMI.

Special thanks to Dave Giguere, Stan Spencer, Gene Wilcox, Dave Goldenberg, George Altemose, and Tom Goodman for their contributions to this work.

References:

1. "Considerations in the Hermetic Packaging of Hybrid Microcircuits", M. Byrnes, J. Carter, J. Sergent, and D. King, Solid State Technology, 1 August, pp 183-186.
2. "Precision Silicon Transistor Thermometer" A. Ohte, M. Yamasata, and K. Akiyama, TEMPERATURE (Instr. Soc. of America), Vol.5, part 2 (1982), p1197, and Loc.Cit.
3. "Switching and Linear Power Supply, Power Converter Design", by A. I. Pressman, Hayden Book Co. (1975)

VIBRATION SPECTRA OF A G-M CRYOCOOLER WITH VARIOUS POWER SUPPLIES.

Moses Minta
Jim Stolz

Varian Associates, Santa Clara, California, 95054

Introduction:

Gifford-McMahon cryocoolers are predominantly used as high vacuum pumps in the semiconductor processing industry. In this application, the cold head is normally bolted to a processing equipment housing which is invariably of substantial mass. Consequently the input vibration from the cold head is attenuated. Also low frequency vibrations causing rigid-body motions do not affect wafer handling. Recent advances in semiconductor processing equipment design have evolved into lighter, more compact systems with small footprints. Also refined designs of control mechanisms for handling wafers at the various processing stations in the equipment have made the systems more susceptible to vibrations from the cryocooler.

Further, in high vacuum applications, there are still a few applications such as scanning electron microscopy where G-M cryocoolers have not been used, even though they are the preferred vacuum source based on reliability and cost considerations. The level of the inherent vibration associated with the cryocooler precludes its use in these applications.

Recent developments in SQUIDS and high critical temperature superconductivity open up the potential for other extensive applications of two-stage G-M type cryocoolers in the sensor cooling industry. The reliability record makes them an attractive industrial cooler. However, the use of these cryocoolers invariably requires close-coupling and therefore vibration caused by the cooler becomes a potential limitation to its use.

These issues have raised the need to investigate the vibration characteristics of the G-M cryocoler. The objective of the work reported here was to determine the lowest level of vibration attainable with G-M cold heads without substantial redesign or any sacrifice in the traditional reliability of the G-M cooler. The use of D-C motors was not considered an option.

This report summarizes results of laboratory measurements designed to identify the mechanisms for generating the cryocooler vibrations; quantify the contribution of each mechanism to the overall level of cold head vibration; determine the dominant source(s) of vibration and evaluate simple options for eliminating or reducing the vibration due to these sources.

Procedure:

The sequence of laboratory measurements adopted was intended to provide information on the effect of the following possible sources of vibration: expander drive motor; expander drive mechanism - the interaction between the cam and scotch yoke, scotch yoke and bushing; the process gas intake and exhaust; and the mechanical valves.

The effect of the drive motor alone on the 10 K station was first investigated by attaching the motor to the expander drive housing. Subsequently, the cold head was built-up by sequentially adding the cam, the valves, the scotch-yoke and the displacer: measuring the vibration level at each step.

Measurements were also made with no gas flow to the expander (but with the expander drive motor running), during the cold head cooldown period, and after complete cooldown.

The effect of mechanical tolerances was investigated by testing several combinations of cams and scotch-yokes of known dimensions. The vibration levels of several drive motors were also measured. In addition to the standard single-phase ac synchronous motor conventionally used for G-M cryocoolers, a three-phase synchronous motor was tested. Further, a SCOTT-T power supply was tested with the single phase motor.

All the laboratory measurements were made using two general purpose low impedance piezoelectric accelerometers: the first was chosen for its high sensitivity and electrical ground isolation; the second was chosen for its low frequency response characteristics. The signal from the transducer was processed using a charge amplifier and then fed to a spectrum analyzer. The laboratory measurements were made with the accelerometer attached to the second stage heat station of the cold head.

Discussion of results:

The following is a qualitative summary of results extracted from the vibration spectra. The vibration spectra shown in the figures are voltage analogs of the acceleration. The Tables include displacement data calculated from the acceleration data by double integration of the acceleration.

(a) Free body measurements:

Figure 1 shows a typical vibration spectra for the single phase ac synchronous motor with characteristic peaks at 120 Hz and 240 Hz. The SCOTT-T power supply reduces the amplitude of the 120 Hz vibration component but otherwise maintains the general shape of the spectra. The three-phase power supply configuration shows an overall vibration amplitude reduction (Fig.2). The peak vibration also occurs at a higher frequency. The vibration reduction

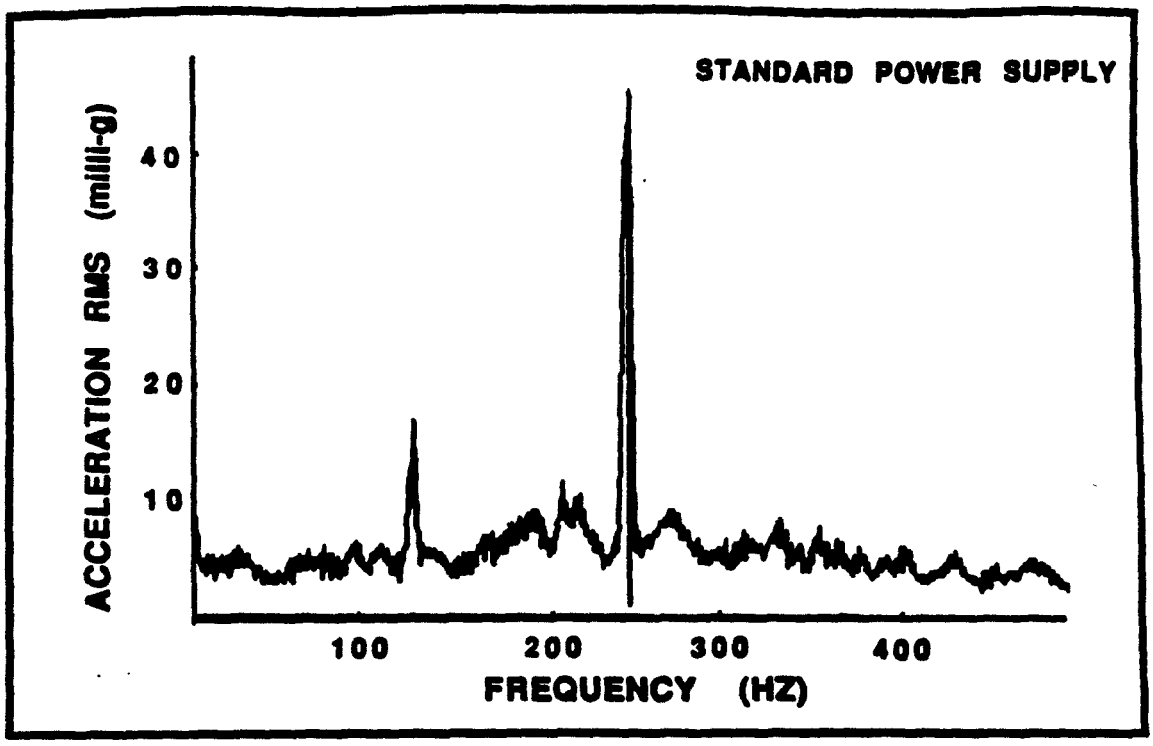

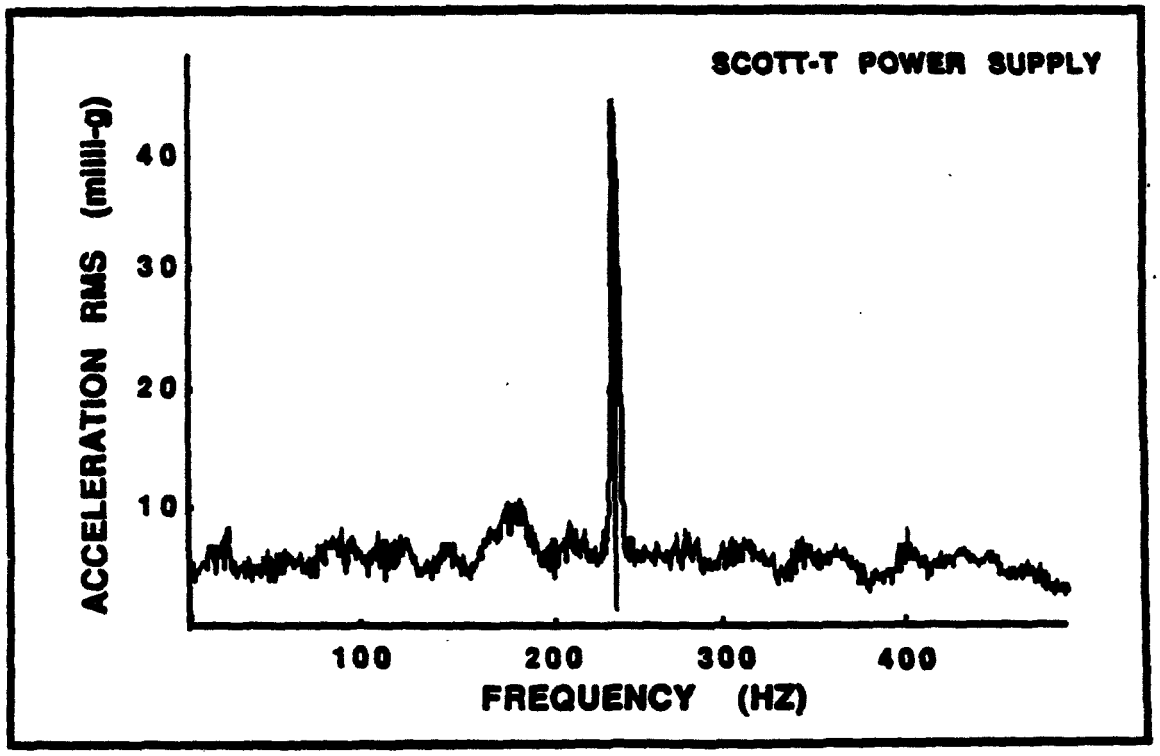

FIG. 1 VIBRATION SPECTRA OF COLD HEAD ON TEST STAND

levels at the lowest frequency obtained with the three-phase motor configuration varied from a minimum of 2 to over 10. Sample data is tabulated on Table 1. The combined effect of the amplitude reduction and the shift of the peak amplitude to a higher frequency results in a much higher vibration signal attenuation at the system level as discussed presently.

TABLE 1: VIBRATION AMPLITUDE-FREE BODY MEASUREMENT AT 10K STATION.

POWER SUPPLY	FREQUENCY (Hz)	ACCELERATION (mg)	DISPLACEMENT (micro-in)
STANDARD P/S	120	18.2	35.0
	240	48.9	23.5
SCOTT-T P/S	120	7.5	14.4
	240	43.4	20.9
3-PHASE P/S	160	12.7	13.7
	240	8.4	4.0

Free-body-measurements also indicate that the dominant source of vibration at the level being considered is the expander drive motor. While the motor itself produces a low level of vibration, the loading condition dramatically increases the vibration level. Figure 2 shows a five-fold increase in the vibration amplitude at 160 Hz. The mechanical components of the expander drive unit affect the overall vibration level by contributing to the load on the drive motor. Similarly, the effect of gas flow and the mechanical valves on the vibration level is not significant at the amplitude levels measured.

(b) system level measurements:

In order to investigate the dynamic characteristics of the cold head, measurements were made on two semiconductor processing equipments each of which integrated a cold head to provide its high vacuum requirement. Both systems depend on gravity to hold the wafers in place for processing.

On the first system (an in-line coater), slight modifications are made to the processing stations to accomodate changes in wafer size. These changes affect the resonant frequencies of the wafer handling tables resulting in vibration severe enough to upset the delicate wafer balance. Typically with the conventional power supply, the vibration level was high enough in 20% of the machines for the wafers to fall off the handling tables.

Initial vibration meaurements identified a resonance effect at 120 Hz as the source of the problem (Fig 3). Stabilizing the phase of the power input and thereby minimizing the 120 Hz

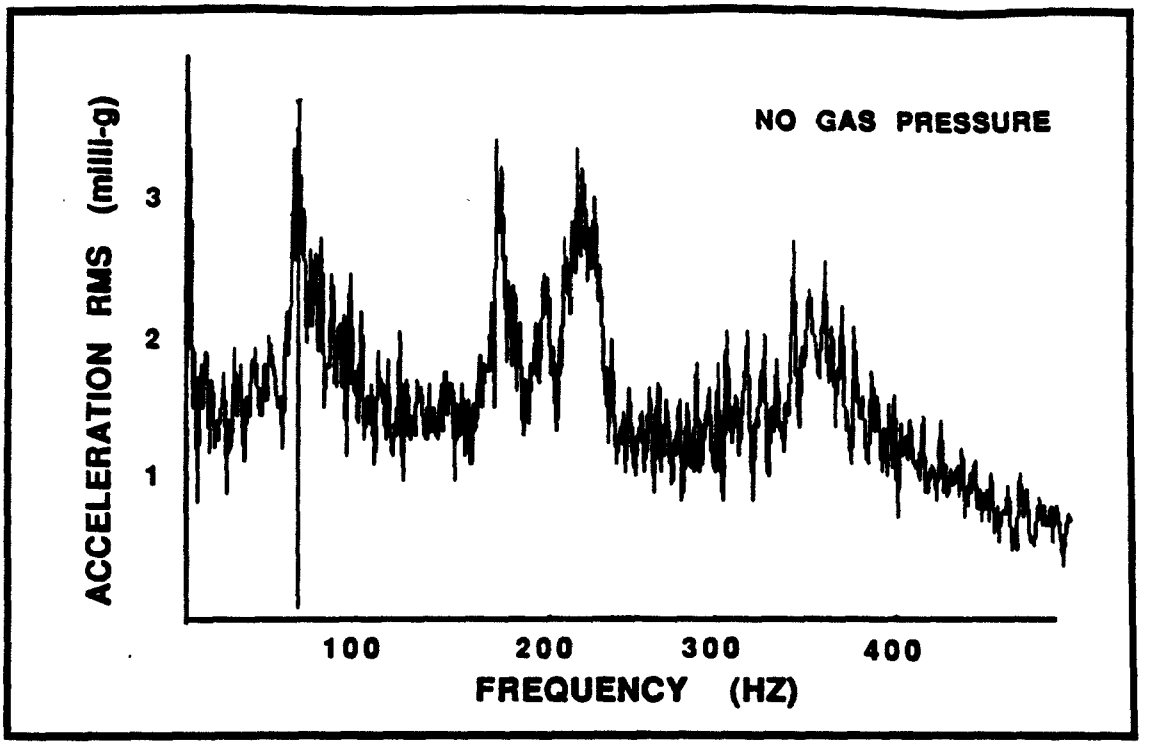

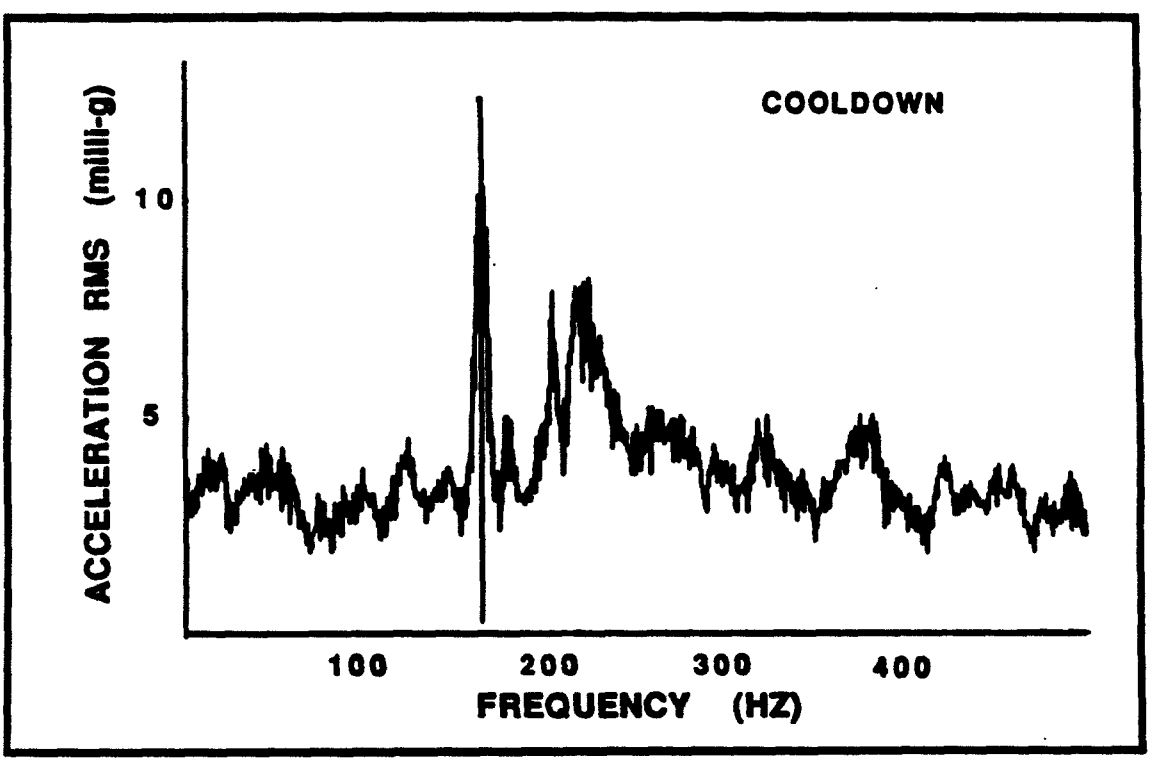

FIG. 2 VIBRATION SPECTRA FOR THREE-PHASE MOTOR

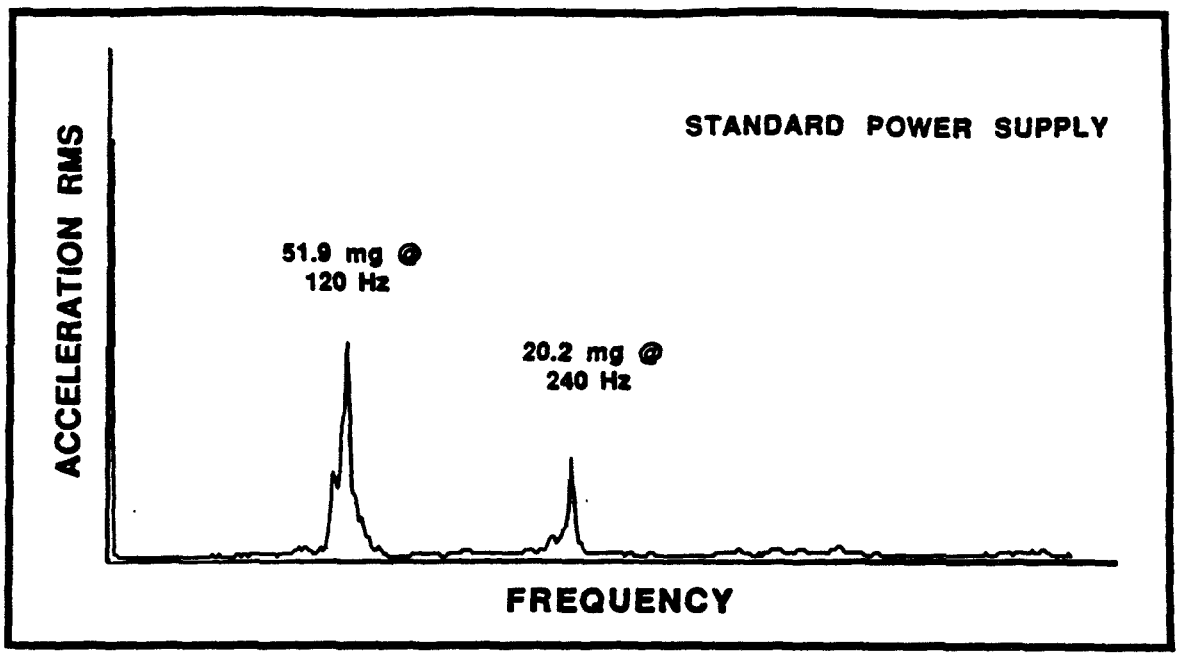

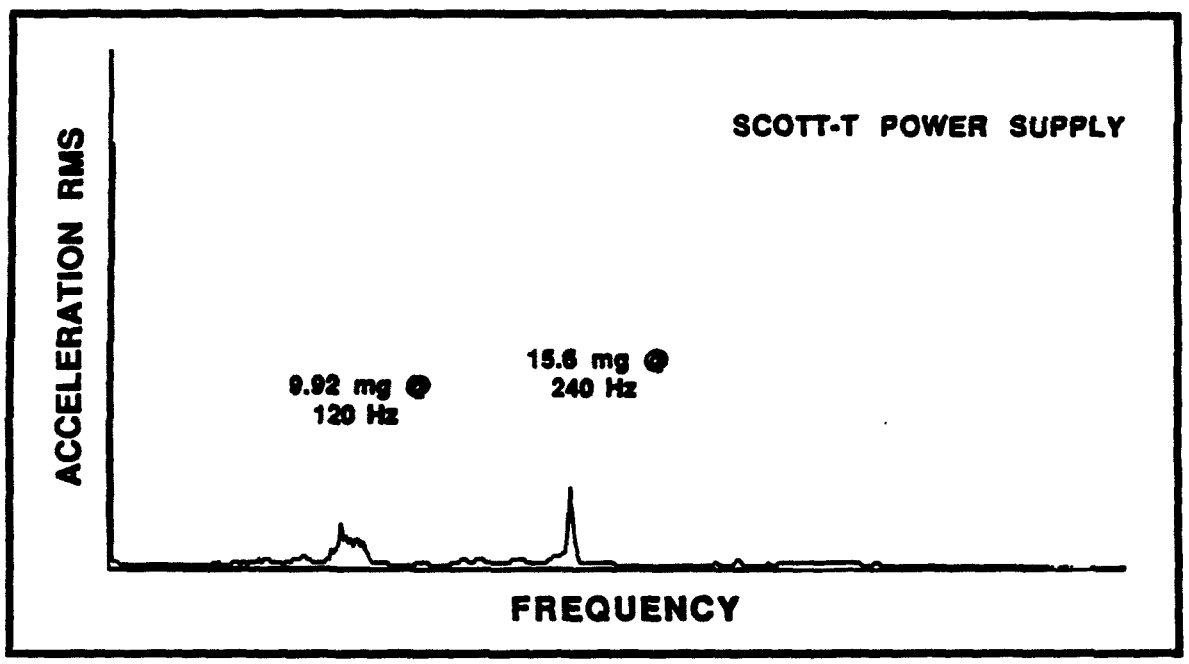

FIG. 3 VIBRATION SPECTRA OF WAFER PROCESSING EQUIPMENT AT ENTRY LOCK POSITION

vibration level reduced the vibration amplitude from 100 to 19 micro-inches (Table 2) and effectively eliminated the wafer "walk" problem.

TABLE 2: VIBRATION AMPLITUDES AT THE ENTRY LOCK POSITION OF A WAFER PROCESSING EQUIPMENT (IN-LINE COATER).

POWER SUPPLY	FREQUENCY (Hz)	ACCELERATION (mg)	DISPLACEMENT (micro-in)
STANDARD	120	51.9	99.8
	240	20.2	9.7
OPTIMIZED*	120	19.0	36.5
R-C VALUES	240	16.0	7.7
SCOTT-T	120	9.9	19.0
	240	15.6	7.5

* Optimizing for vibration performance sacrifices torque.

The second system was a prototype sputtering machine designed with constraints aimed at low particulate generation and increased

TABLE 3: VIBRATION AMPLITUDE OF A WAFER PROCESSING EQUIPMENT - SPUTTERING SYSTEM.

POWER SUPPLY	FREQUENCY (Hz)	ACCELERATION (mg)	DISPLACEMENT (micro-in)
* STANDARD P/S			
(a) 50	100	20	55.4
	200	52	36.0
(b) 60	120	32	61.6
	240	26	12.5
* SCOTT-T P/S			
(a) 50 Hz	100	4	11.0
	200	52	35.8
(b) 60	120	8	15.4
	240	26	12.1
* 3-PHASE P/S	120	4	7.7
	175	5	4.5
(60 Hz)	200	8	5.5

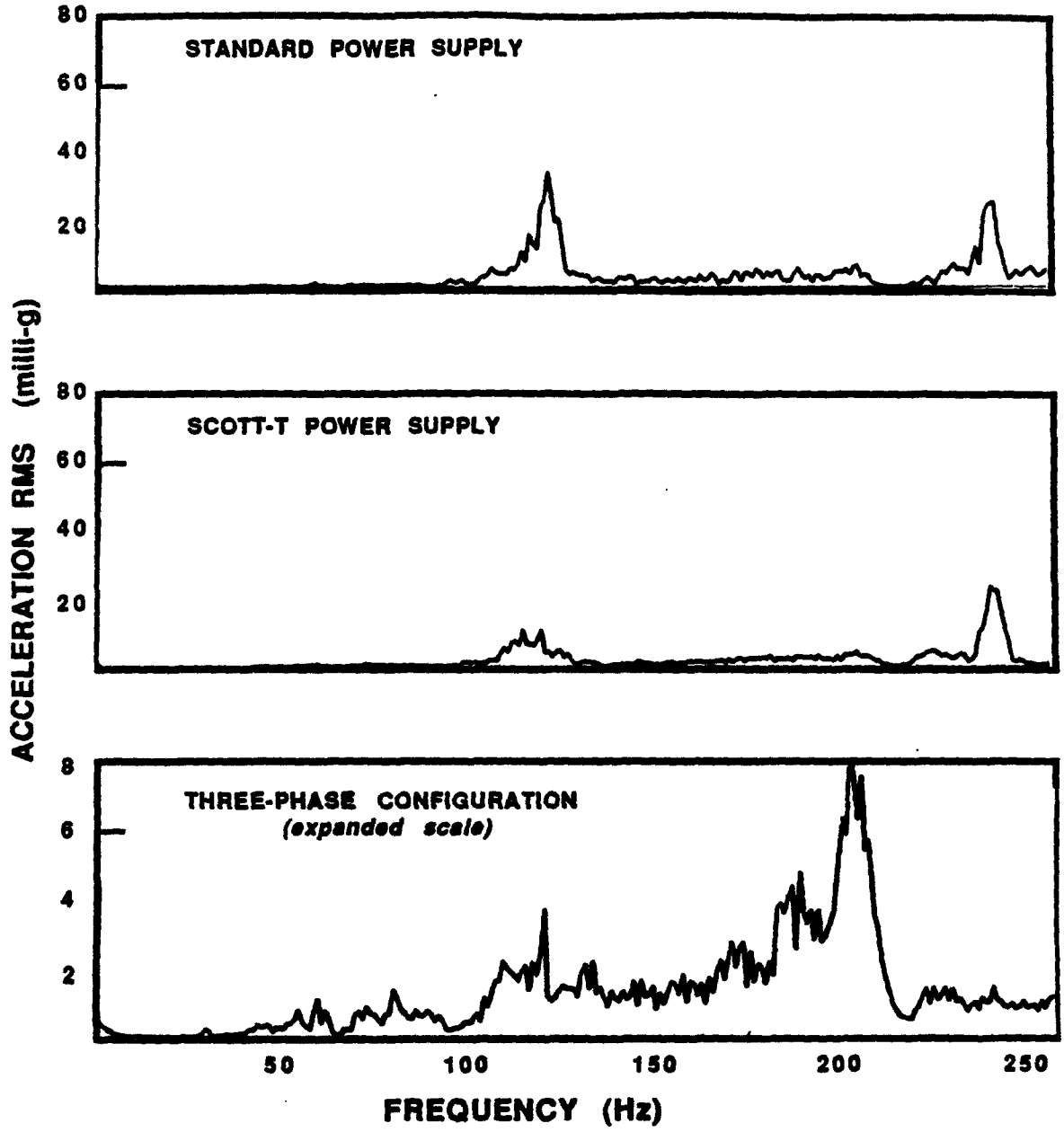

FIG. 4. VIBRATION SPECTRA OF COLD HEAD ATTACHED TO WAFER PROCESSING EQUIPMENT

wafer throughput. Simultaneously, the equipment footprint was reduced to take up less clean room area. Consequently, the level of vibration from the standard power supply, even with the stabilized phase configuration, could not be tolerated (Table 3). The initial thrust was to develop a vibration isolation interface to address the vibration problem. Vibration measurements on the system revealed that:

- The low frequency vibration due to the displacer reciprocation (1.2 Hz) was not the problem: it caused a rigid body motion effect on the total system.
- The problem frequency was at about 120 Hz although any significant input vibration between 100 and 120 Hz induced severe vibration of the wafer.

The use of the three-phase motor configuration effectively resolved the problem by mismatching the system natural frequency and the forcing frequency from the motor (Fig. 4). Shifting the peak signal frequency to a higher value causes signal attenuation assuming the typical transmissibility curve for a single-degree-of-freedom system.

(c) Expander drive motor effect

The motor used for the product is a standard 72 rpm ac synchronous motor. This motor requires a two phase power input with a 90 degree phase shift. Typically, an R-C phase shift network is used to produce an approximate 90 degree phase shift. This phase difference changes with motor load (because the phase impedance of the second winding varies with motor load). This results in motor torque modulation and hence motor vibration. Another source of motor vibration results from changes in torque as the rotor poles move relative to the stator poles. The force between the rotor and stator poles is maximum when the poles are close to alignment and decreases as the poles move away from each other. A given rotor pole moves from one stator pole to the next in one cycle of the 60 Hz ac line. During this cycle, the motor torque goes through two cycles of variation because the motor torque is the sum of the torque from each of the two phases. Consequently the resulting motor torque modulation due to pole motion causes vibration at 120 Hz and its harmonics.

In order to stabilize the two phases, a SCOTT-T arrangement which converts three phase input power to a two phase drive is used. The resulting 90 degree phase shift is independent of motor loading or pole motion effects. The 120 Hz vibration source is therefore significantly attenuated. However, vibration signals at other frequencies are not affected.

By contrast, the three-phase motor has three windings instead of two and its poles are closer together. The windings are also driven by three stable phases accurately spaced 120 degrees apart. The motor torque obtained from summing the torque from the three phases is therefore less modulated. Consequently the vibration signature of the three-phase motor is significantly different:

the vibration peaks are low in amplitude and the highest peak occurs at a higher frequency.

Conclusion:

The focus of this work has been to reduce the intrinsic vibration associated with the G-M cold head to an "irreducible minimum" and thereby facilitate its use in a wider range of applications, without the need for a vibration isolation interface. For such applications, a three-phase motor chosen with a liberal capacity margin will offer a low overall vibration level. Further, in cases of known problem frequencies, efforts to mismatch the system problem frequency and the peak vibration frequencies (ie the exciting force frequencies) of various motors can result in overall system simplicity while eliminating the vibration problem.

Acknowledgement:

We acknowledge the help of Carlos Silva in obtaining the data and Johan de Rijke for his input.

SYSTEM DESIGN OF A CRYOGENIC THERMAL BUS

William Burt
TRW Space & Technology Group
Redondo Beach, CA 90278

David Hustvedt
UCLA
Los Angeles, CA 90034

ABSTRACT

A well-recognized technology issue for some space applications is the availability and suitability of cryocoolers. A less-documented issue is the extent to which the system used to connect the cryocooler with the cooled instrument affects the required cooling capacity and operating temperature of the cryocooler. The connecting system is a thermal bus having four thermal functions: transport, switching, storage, and interfacial contact. The elements of the bus can be modeled to evaluate the impact of various bus configurations on cryocooler performance and to investigate strategies for optimizing system performance. This paper describes an analytical approach for evaluating thermal bus/cryocooler interactions: thermal bus option trees are developed and systematically applied to a hypothetical system in which redundant multitemperature cryocoolers are to be connected to loads at 10K and 80K. Results show the effect of bus element performance and bus configuration (e.g., length) on system thermodynamic efficiency.

INTRODUCTION

The heat transfer system between the cooler sink and a cryogenic heat source is a cryogenic thermal bus. Although the thermal issues involved are generally straightforward, the technology choices and sensitivities are not necessarily obvious. This is particularly true for redundant, distant, high load, or very low temperature space cooler applications. A recognized problem area is performance degradation that can occur when multiple buses are tied together at one end as is the case with redundant coolers.[1] A systems study of the interaction of components can identify critical areas, optima, if any, and provide a broader understanding of synergistic effects. The benefit of such study for space applications would be a better understanding of the effect of system design parameters on cryocooler performance requirements.

Previous work on the topic of the cryogenic thermal bus has been limited. Historically, systems have been simple enough so that the overall performance had little effect on cryocooler requirements. The integration issues have been typically addressed in the context of well-defined point designs on a case by case basis using measured data for switching and interface hardware.[2,3,4] The present work seeks to provide a conceptual framework for assessing the thermal bus technology issues.

THE GENERIC THERMAL BUS

The low temperature thermal bus consists of elements with four distinct functions--transport, switching, storage, and interface (Figure 1). Every thermal bus requires at least the functions of transport and interface with the basic requirement that its conductance be sufficiently high to prevent very low temperature operation of the cooler. At temperatures below 20K thermal bus resistance can dramatically increase cooler power requirements. The hardware elements for the cryogenic bus can be defined by means of functional analysis trees shown in Figures 2 and 3 which provide a comprehensive menu of possible bus hardware elements. Some of the elements may already have been demonstrated: cryogenic heat pipes, for example. Others, such as fully rotating joints for space application of helium gas transfer have not. The performance of various basic bus elements have been cataloged based on conductance at 10K in Figures 5 through 7. Such figures are only representative since various processing techniques and material properties strongly influence the thermal performance. Nonetheless some general conclusions can be drawn when comparing these figures against cooler penalty of Figure 4.

In Figure 4, the cooler-to-load allowable conductance is plotted as a function of incremental increase in cooler input power for various cooling loads. For each cooling load the conductance must be above a well defined value in order that little penalty is paid. If the conductance is too low the load can never be cooled. From an entropy point of view this additional power is just the lost work in the system and is proportional to the entropy generation rate of the thermal resistance given by,[5]

$$\dot{S}_{gen} = \frac{Q_L^2}{T_L\,(UT_L - Q_L)} \qquad (1)$$

where Q_L is the load in watts, T_L is the load temperature, and U is the conductance of the bus.

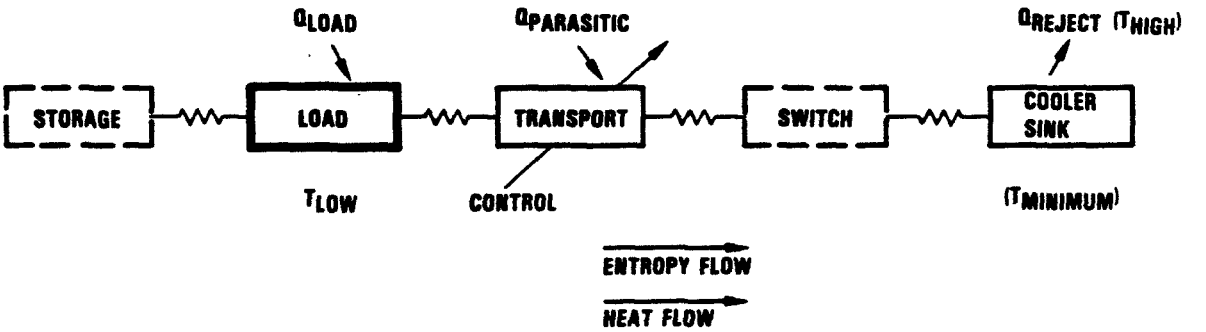

Figure 1. Conceptual Cryogenic Thermal Bus

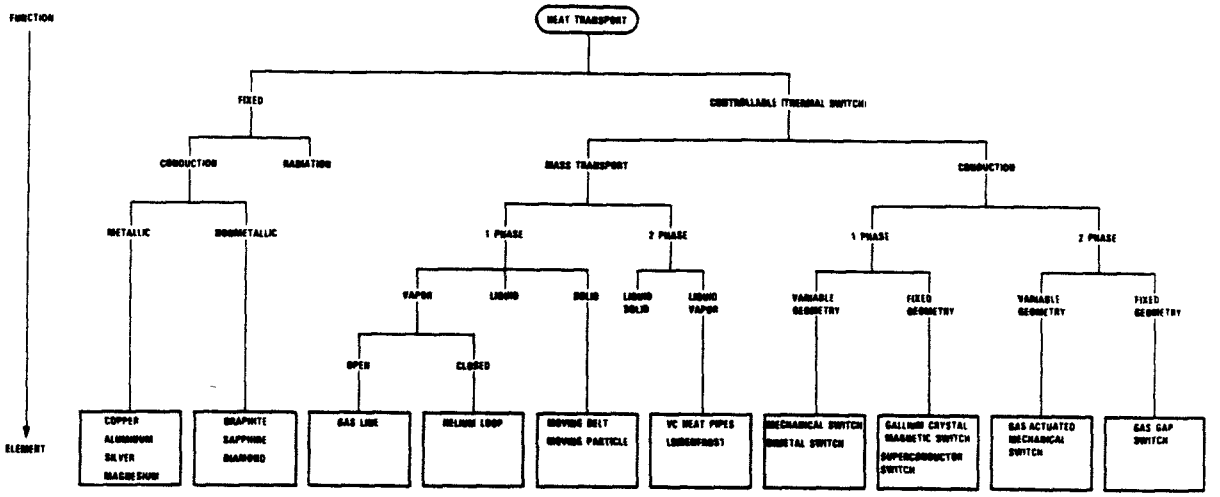

Figure 2. Heat Transport Option Tree

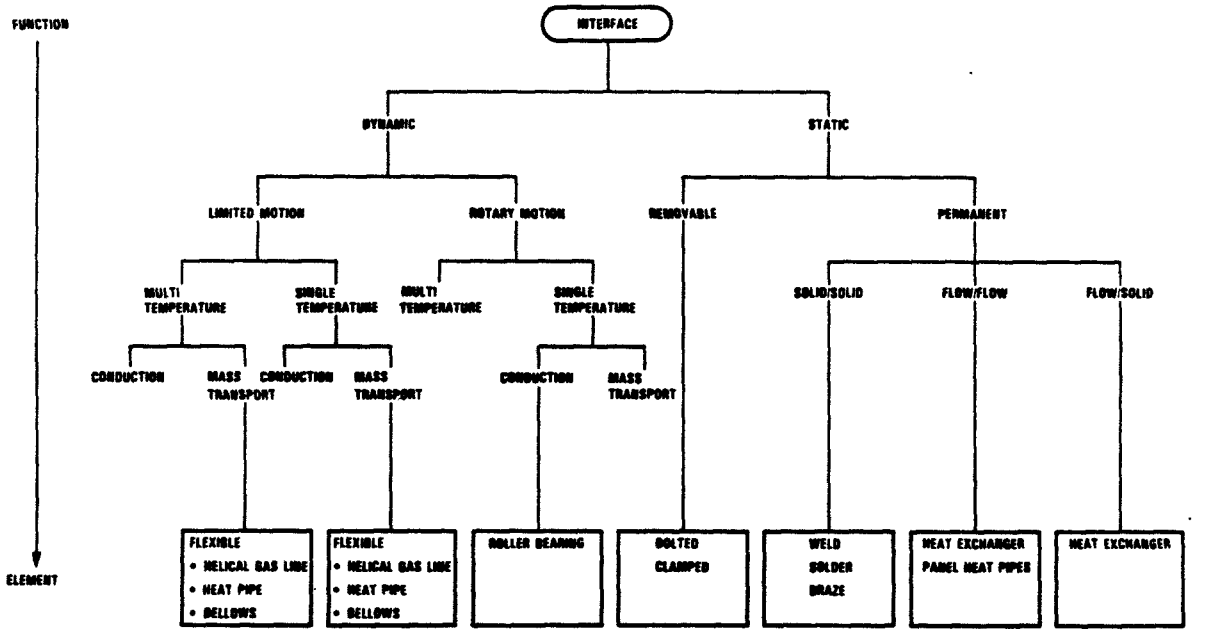

Figure 3. Thermal Interface Option Tree

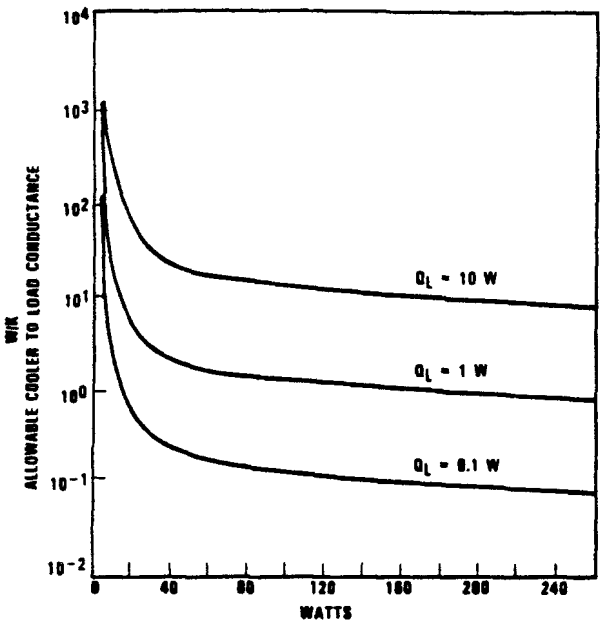

Figure 4. Additional Power Required by a 10K Cooler Operating at 2% of Carnot Efficiency Due to Thermal Bus Resistance (Rejection Temperature 290K)

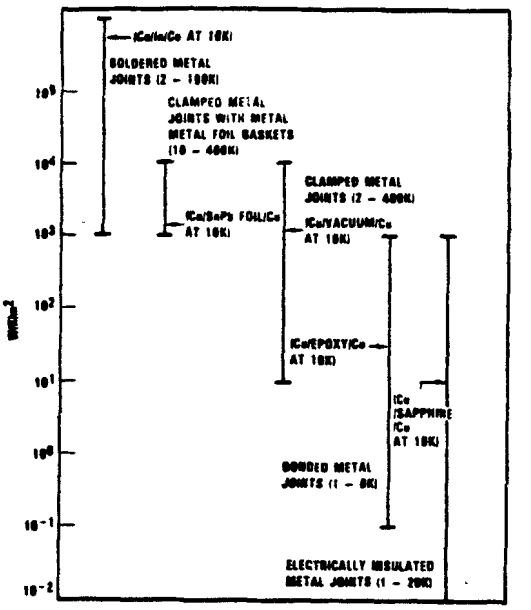

Figure 5. Relative Thermal Conductance per Unit Area for Various Interface Types (Reported Ranges)

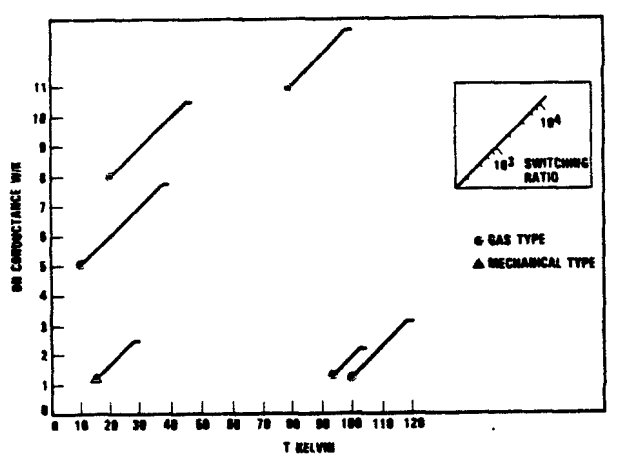

Figure 6. Relative Performance of Extrinsic Thermal Switch Technologies

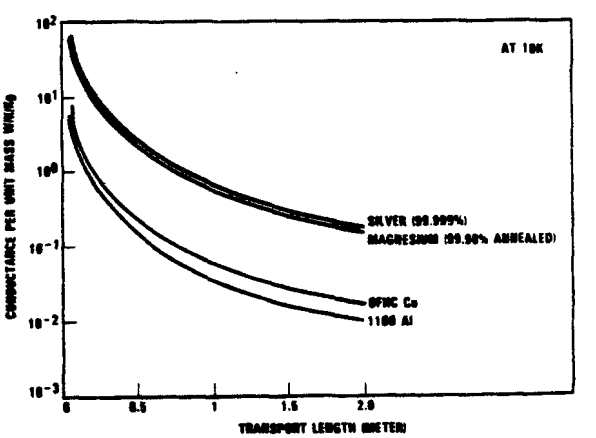

Figure 7. Relative Conductance versus Length for Solid Transport Elements

Interestingly enough, this is the same conductance regime for thermal bus elements of practical availability and readily demonstrates regions of high power penalty avoidance. In Figure 5 the relative thermal interface conductance is shown. For common bolted contacts the conductance spans the range between 10^1 and 10^4 W/K/m^2 and is as strongly dependent on surface roughness and processing technique as it is on applied force after the initial compression. So for example a Cu/Cu contact with 10^4 W/K allows for about 10 joints of this type in a 10W bus before cooler power increases sharply. Several poor joints within the standard range would have a dramatic degrading effect. As an aside, the surface area has been neglected in this example in accordnce with evidence[3] that thermal contact resistance depends not on apparent surface area but on interfacial point contact which is proportional to the applied force.

Figure 6 shows that for various thermal switching technologies the "on" conductance falls in the power sensitive asymptotic portion of the curve for the 1-watt load at 10K indicating the need for care in application. Hustvedt[6] has shows that gas gap switch optima can be found for systems by trading switch size against increasing switching ratio, decreasing resistance, and increasing parasitics.

Figure 7 compares the conductance of various solid transport elements on a normalized mass basis assuming that the 10K load is connected to a sink not significantly lower than 10K. It is apparent that on a fixed weight basis that cooler power can increase significantly for lengths beyond 20-30 cm (not including parasitic effects) for copper and aluminum. Since the mass of a solid transport system would increase as the square of the transport length, heat pipes or forced flow gas transport systems therefore find application for longer lengths.

Analysis Approach

Three approaches can be used to analyze a thermal bus. One is the detailed nodal approach which requires good system definition as a prerequisite. The approach calculates subsystem performance by numerically evaluating each of the components within a specific set of boundary conditions by using a thermal program such as SINDA. If properly applied, this method provides the best accuracy but only limited insight. Sensitivities and optima are difficult to identify unless a large number of cases are computed. Another approach is the lumped parametric nodal approach. In this approach the thermal system is constructed using scalable data collected on similar components in the regime of interest. The information is combined analytically or numerically to calculate thermal performance. This approach is relatively realistic and more efficient than the detailed nodal approach but does not provide much insight into system interactions. The last approach uses a closed form approximate solution which provides the least realism but offers perhaps the best chance of providing physical insight by dealing with an entire range of interacting phenomena at once. This approach is most useful in preliminary system studies and is used in the following example.

Analysis of a Hypothetical Thermal Bus

A simple yet realistic cryocooler system that illustrates the impact of the bus thermal design is a multicooler system using circulating helium gas as the heat transfer medium. Such a system is shown schematically in Figure 8. An active cooler removes heat from a device at temperature T_L. Idle standby coolers increase overall system reliability but increase the cooling load on the active cooler with heat conducted from the environment through the helium plumbing. An additional heat load on the active cooler is due to heat from the environment leaking through the insulation of the active helium system. For a first-order closed form model it is convenient to assume that material properties are constant and that fluids obey simple property relations such as the ideal gas law. In many cases such assumptions do not change the qualitative nature of the solution and permit insights into the significance of system parameters.

Subsystem models. In this case there are only two significant subsystem models: the active helium gas transport loop and the inactive, or standby, loops. For simplicity other important subsystems such as heat exchangers, couplings, and insulation are not modeled.

Active system. The thermodynamic model of the active helium subsystem is shown in Figure 9. At the cryocooler, helium from a cryocooler enters the transport system at pressure and temperature P_i and T_i and is returned at a lower pressure P_o and higher temperature T_o. For simplicity the gas temperature at the inlet of the return line is assumed to be the load temperature T_2. The temperature difference δ across the cooled device is assumed to be fixed by external (e.g., electro-optical) considerations. If the parasitic heat flux through the insulation is q, the inlet and outlet gas temperatures can be solved for directly:

$$T_o = \frac{\dot{q}PL\delta}{Q_L + \Sigma Q_p} + T_L, \qquad T_i = T_L - \delta\left[\frac{qPL\delta}{Q_L + \Sigma Q_p} + 1\right] \tag{2}$$

where P is the outer perimeter of the tubing.

The pressure drop ΔP in the gas lines can be calculated using ordinary equations for turbulent flow, but recast as a function of tube diameter, D, length, L, and mass flow rate, $\dot{m}$, viscosity, μ, and density ρ.

$$\Delta p = 0.284 \frac{\mu^{0.2}}{\rho} \frac{\dot{m}^{1.8} L}{D^{4.8}} \frac{\text{dyne}}{\text{cm}^2} \tag{3}$$

Standby systems. The standby helium piping can be viewed as a fin with a cooled base (the cooled device) and a tip temperature equal to the temperature of the environment. Using classical solutions for fixed properties, the heat transferred to the base of the fin is:

$$\Sigma Q_p = (n-1)\sqrt{h\,P\,k_{eff}\,A}\,(T_H - T_L) \tag{4}$$

Parameter	Low Temperature	High Temperature	Definition
Q_L	1 W	10 W	Device heat output
T_L	10 K	80 K	Load temperature
T_H	300 K	300 K	Environment/sink Temperature
q	4.00E-5 W/cm^2	2.75E-5 W/cm^2	Insulation heat flux
p_i	21400 dyne/cm^2	21400 dyne/cm^2	Inlet gas pressure
k_i	5.00E-7 W/(cm·K)	5.00E-7 W/(cm·K)	Insulation conductivity
k_w	0.110 W/(cm·K)	0.124 W/(cm·K)	Pipe wall conductivity
k_f	0.052 W/(cm·K)	0.002 W/(cm·K)	Gas conductivity
t/D	0.020	0.020	Pipe wall thickness to diameter ratio
w/D	2	2	Insulation to diameter ratio
k_{eff}	0.054 W/(cm·K)	0.007 W/(cm·K)	
n	3	3	Number of cryocoolers
R	2.85 J/(g·K)	2.08 J/(g·K)	Gas constant
c	5.90 J/(g·K)	5.16 J/(g·K)	Gas specific heat
visc	2.42E-5 g/cm sec	8.37E-5 g/cm sec	Gas viscosity
ρ	1.64E-2 g/cm^3	1.91E-3 g/cm^3	Gas density

Table 1. Example Input Design Parameters

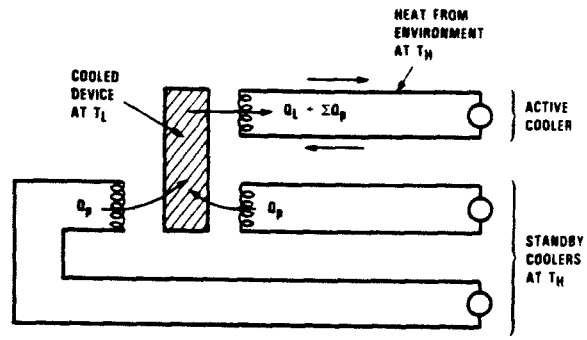

Figure 8. Schematic Diagram of a Simple (Unshielded) Multi-cooler System

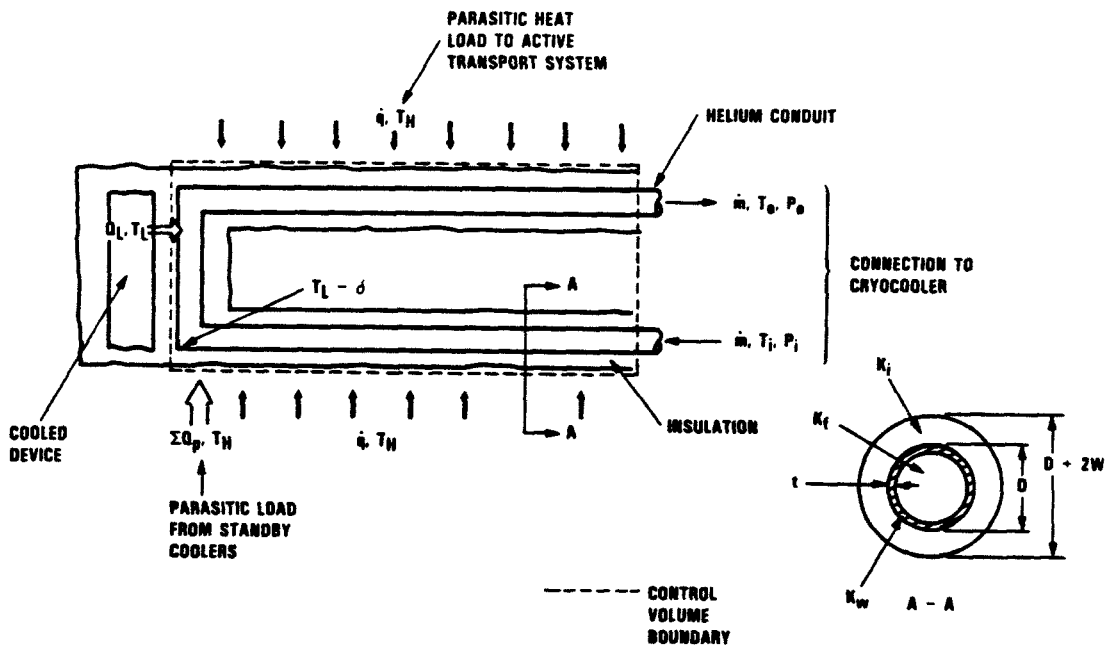

Figure 9. Thermodynamic Model of a Simple Cooler System

where h is the insulation radial heat transfer coefficient, n is the number of coolers, A is the surface area in terms of the inner diameter D, and

$$k_{eff} = k_f + 2(k_w - k_f)(t/\delta) - 4(k_w - k_f)(t/\delta)^2 \qquad (5)$$

The effective conductivity of the gas transport lines is a weighted average of the conductivities of the helium gas and the tubing wall based on the total cross section of the tubing.

The "fin" heat transfer coefficient can be derived using conduction for cylindrical shells as

$$h = \frac{2k_i}{\ln(1 + 2\ W/D)\ D} \tag{6}$$

This implies that

$$\Sigma Q_p = 2\pi\ (n-1)\ D \sqrt{\frac{k_i k_{eff}}{\ln\left(1 + \frac{2W}{D}\right)}}\ (T_H - T_L) \tag{7}$$

The particular fin model is an accurate assumption as long as the tubing is long enough and small enough so that parasitic heating predominates. This is the case for all tubing diameters considered with lengths above two meters and for the smaller tubing diameters in the one meter case.

System model. In this case it is useful to model the overall entropy generation of the system. This approach allows the effects of parasitic heat transfer and gas pressure drop to be considered on a common basis. From the Guy-Stodola theorem, the lost work is proportional to the entropy generated. The system with the minimum entropy generation will require the minimum input energy for refrigeration. The entropy generation rate[5], assuming the ideal gas law, is:

$$\dot{S}_{gen} = -\frac{Q_L}{T_L} - \frac{\Sigma Q_p}{T_H} - \frac{2\dot{q}PL}{T_H} + \dot{m}c\ \ln\frac{T_o}{T_i} + \dot{m}R\ \ln\left(\frac{P_i}{P_i - \Delta P}\right) \tag{8}$$

Substituting equations for temperatures, pressures, and parasitic heat load developed in the subsystem models gives an expression for the entropy generation rate as a function of system design parameters (tubing diameter, length, etc.)

Since $\dot{m} = \frac{Q_L + \Sigma Q_p}{c\delta}$,

$$\dot{S}_{gen} = -\frac{Q_L}{T_L} - \frac{\Sigma Q_p}{T_H} - \frac{2\dot{q}\pi DL}{T_H} + \frac{Q_L + \Sigma Q_p}{\delta}\ \ln\left[\frac{\dot{q}\pi DL\delta + T_L(Q_L + \Sigma Q_p)}{(Q_L + \Sigma Q_p)T_L - \delta\pi D\dot{q}L - \delta(Q_L + \Sigma Q_p)}\right]$$

$$- \frac{(Q_L + \Sigma Q_p)\ R}{\delta c}\ \ln\left(1 - \frac{\Delta P}{P_i}\right) \tag{9}$$

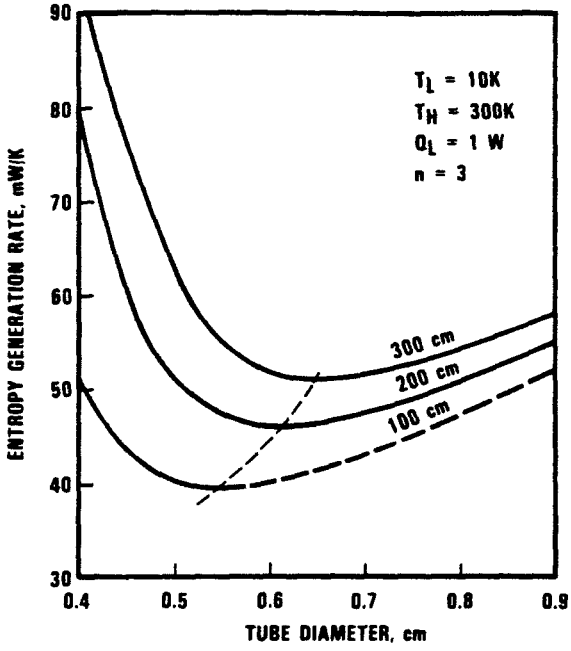

Figure 10. Entropy Generation in a 10K Crycooler

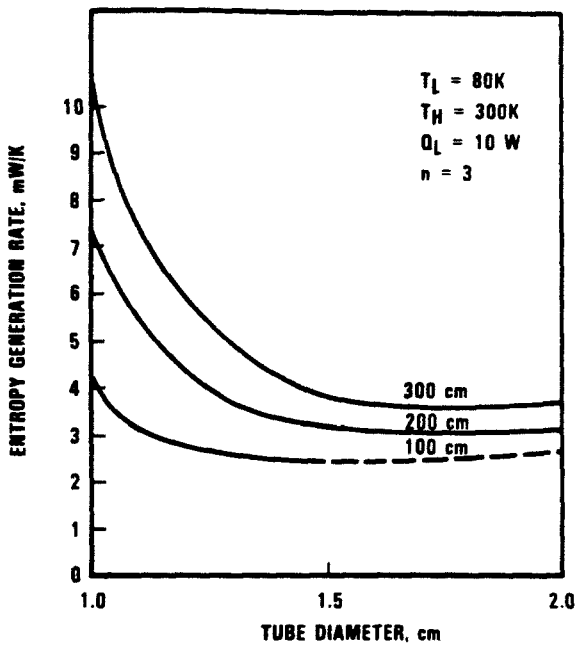

Figure 11. Entropy Generation in a 80K Cryocooler

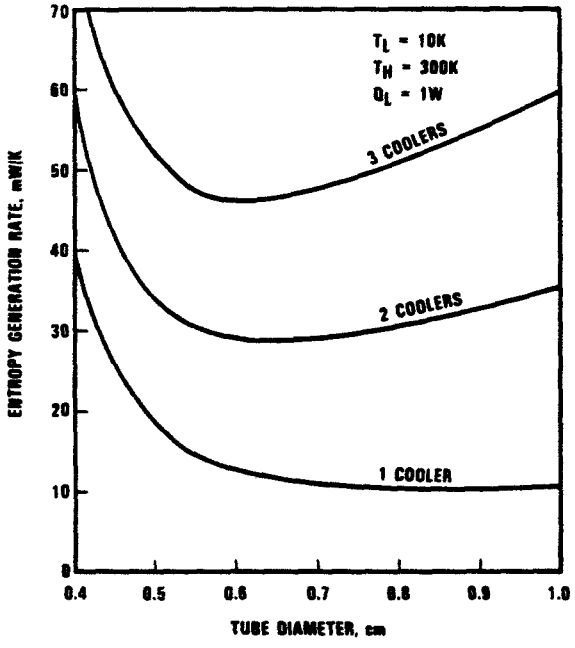

Figure 12. Entropy Generation Rate in a 10K Cooler System Is Strongly Dependent on the Number of Redundant Coolers

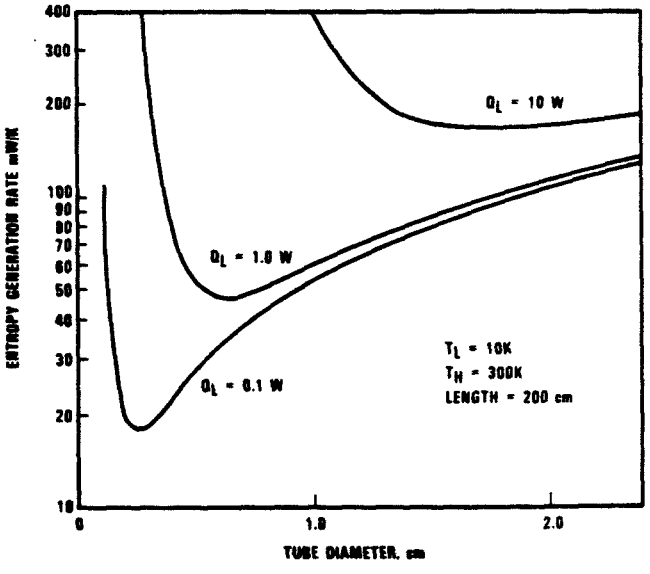

Figure 13. Sensitivity of Entropy Generation Rate to Load for a Single Cooler

Results. The system model was used to investigate 10K and 80K cooling systems. The input design parameters are summarized in Table 1. Figures 10 and 11 show the entropy generation rates for the two different systems as a function of tubing diameter for various tubing lengths. The entropy generation rate initially decreases with diameter because the pressure drop decreases with diameter. However, as the diameter increases, the parasitic heat transfer also increases and ultimately overwhelms the benefits of decreased pressure drop. Thus, there is an optimum tubing diameter that minimizes overall entropy generation and, consequently, minimizes input power requirements. As might be expected, the low temperature system is much more sensitive to parasitic heat loads (and therefore tubing diameter) than the high temperature system. Figure 12 shows the effect of varying the number of coolers on the low temperature system. Increasing the number of coolers increases the minimum entropy generation rate and also increases the sensitivity of the system to variations in design parameters. The price of increased system reliability (through redundant coolers) is decreased system efficiency. Figure 13 shows the effect of varying the system cooling load. Increasing the cooling load increases the minimum entropy generation rate but decreases the sensitivity of the system to variations in mechanical design parameters.

Conclusions

Functional analysis trees can identify bus elements and modeling or empirical data can characterize the indiviual elements but integrative system models are necessary to optimize system performance. In particular, conductance of the cryogenic thermal bus can affect cooler power input by appearing as a significant additional effective heat load. Entropy generation is a way to approach the optimization process while taking into account various and disparate system effects including pressure, mass flow, parasitic loads, and thermal resistance. The entropy generation approach could be developed beyond the closed form approach to form a finite element model that can take into account the real physical properties of gases and metals over the applicable temperature range.

REFERENCES

1. A. L. Johnson, "Spacecraftborne long life cryogenic refrigeration status and trends," Cryogenics, 7:339 (1983).
2. A. M. Lehtinen, "Cryocooler Subsystem Integration," AFWAL-TR-87-3054, (1987), (Limited Distribution).
3. S. W. Van Sciver, M. J. Nilles, J. Pfotenhauer, "Thermal and electrical contact conductance between metals at low temperatures," Proceedings of the [Berlin] Space Cryogenics Workshop, 37 (1984).
4. C. K. Chan, "Gas Adsorption/Absorption Heat Switch," NASA-CR-181327, NTIS (1987).
5. A. Bejan, Entropy Generation through Heat and Fluid Flow, Wiley, New York (1982).
6. D. C. Hustvedt, "Systems considerations for cryogenic thermal switch development," Advances in Cryogenic Engineering, R. W. Fast (ed), Vol 31:915, Plenum Press (1986).

INTEGRATED COOLER/DEWAR STRUCTURES FOR DETECTOR ARRAY COOLING IN INFRARED SYSTEMS

Mark Kushnir
ICE Cryogenic Engineering Ltd.
Nes Ziona, Israel

Charles S. Naiman
International Cryogenic Enterprises Inc.
Brookville, New York

Abstract

The trend in infrared systems is toward larger detector arrays, requiring more power and weight for their proper cooling. This is in conflict with a simultaneous trend toward miniaturization--which demands lower power and weight. Based on the development of high reliability Stirling cryocoolers, ICE has redesigned the dewar and cryocooler, "integrating" them directly with the detector array.

In the newly designed structures, thermal savings are achieved in two ways: (a) the outside wall of the cold head now serves as the inside wall of the dewar; and (b) the detector array is mounted directly on the cold head. With this design approach, for example, a Common Module, 250 milliwatt, Stirling Cryocooler can be replaced by a 100 milliwatt package. Use of a low vibration Integral Stirling is mandatory.

Additional power and weight savings, along with increased MTBF, are realized through the use of closed cycle temperature control (demand refrigeration). Results on power, weight, and cooler performance will be presented.

1. Introduction and Background

International Cryogenic Enterprises (ICE) Inc., and its wholly owned subsidiary, ICE Ltd., have introduced a Stirling Cycle mini-cooler product line, encompassing various innovations to improve MTBF, efficiency, manufacturability, and maintainability. These products are used to cool IR detectors used in Thermal Imaging systems. Clearance seal technology is used exclusively, eliminating the deleterious effects of plastic dynamic seals.

Included in this product line is a high reliability 150 mW Integral Stirling Minicooler, the MC111B. It serves as the heart of an "integrated" approach for redesigning the dewar and detector assembly. The savings in thermal losses drastically reduce power and weight needed for cooling the system. All Thermal Imaging systems benefit. However, greatest advantages are seen for systems that need to be kept

small, such as hand-held units, missiles, and RPV's. In the next two sections we present the rationale behind our design approach. We then discuss data generated with some early prototypes, of value to system designers.

2. Comparison of the "Integrated" vs. the "Common Module" Structure

Because of the military's poor experience with the reliability of cryocoolers, it was originally necessary to develop a packaging technique that allowed for rapid removal of the cryocooler with minimal disturbance to the IR detectors and the dewar used to house them. Thus the "Common Module" dewar was created. It has a standardized inner wall with a precision bore. In that way the cold head of the cryocooler of multiple manufacturers can be inserted and removed without breaking into the dewar and detector assembly portion of the system. We can appreciate where savings in thermal cooling can be achieved by studying the schematic diagram of the Common Module dewar/cryocooler assembly shown in Figure 1. (A sapphire window is shown for a 3 - 5 micron application.)

Table 1 lists the typical thermal losses associated with the cooling provided by a "0.25 Watt" cryocooler. There are two major thermal losses from this construction where, potentially, savings can be achieved. One is in the region of the "thermal coupler," which is where heat is "coupled" out of the dewar/detector region to the cold head. This is realized in the form of either a spring loaded contact mechanism, a bellows mechanism, or a "fuzz-button", composed of steel wool and thermal grease. Integration losses for the coupler typically are about 100 mW for the standard 0.25 Watt Common Module assembly. The second opportunity for savings is the dewar losses. These include about 50 mW conduction losses for the inner bore of the Common Module dewar.

One eliminates these two major regions of thermal loss by using an "integrated" construction, as can be seen schematically in the left hand side of Figure 2. If one mounts the infrared detector array directly on the cold head, and places the detector cold head assembly under and inside the envelope of the dewar, one now has achieved a savings of about 150 mW in thermal losses, as shown in Table 2. Not having an inner bore of the dewar to cool saves about 50 mW of conduction losses. We refer to this configuration as an Integrated Cooler Dewar Detector Assembly or ICD^{2}A. (There will still be some losses in the mounting interface between the detector and the cold head. Also the wires, as shown on the left hand side of Figure 2, will have slightly greater losses because they are shorter.)

The Common Module dewar, because of its tightly specified inner bore, is an expensive part, a source of leaks with low manufacturing yield. In the process of changing to the ICD^{2}A configuration, we have also decreased the cost of construction of the total assembly.

We have reduced the overall cooling power required by about 60 to 70%. Because of this, the cryocooler needed will be considerably reduced in its overall size and weight. Basic to this ICD^{2}A approach is the use of a cryocooler with enough reliability to begin the assembly procedure. Assuming that, the simpler and more rugged dewar will increase the reliability of the total assembly.

3. Choice of Cryocooler Type

There are two major categories of Stirling minicoolers in use in the cooling of IR detectors. These are the "Integral" and "Split" types. In the Integral Stirling, the compressor and the expander are attached to the same crankshaft. In the Split Stirling there is a gas transfer line connecting the compressor to the expander/displacer cold head, but which is now a free piston. One reason the Split Stirling design was introduced was in order to reduce the effects of microphonics. This is because, in the Integral Stirling construction, by sharing the same crankshaft, microphonics generated by the compressor are transmitted to the tip of the cold head where the infrared detector array sits. Such vibration can be unacceptable from the standpoint of an IR thermal imager depending on the resolution required. The "Split" Stirling transfer line volume, which lowers its efficiency, "buffers" the expander/displacer section from excessive vibrations of the compressor. However, it also introduces a "free-piston", whose dynamics must be properly "phased" with respect to the compressor with an appropriate linear damping mechanism, and it does still show some microphonics.

In the "integrated" approach, we are mounting the infrared detector directly on the end of the cold head. We need to worry about the Split Stirling's free piston, which cannot be guaranteed not to hit the end of the cold tip. With the Integral Stirling we know that the total distance traveled by the piston in the cold head is controlled by the crankshaft and can be guaranteed not to actually hit the detector. From the standpoint of reliability and efficiency, the Integral Stirling is definitely preferable to the Split Stirling construction.

Thus, if we can develop an Integral Stirling minicooler that has truly low microphonics in its compressor, then the Integral is the preferred type to use for an ICD^{2}A structure. The next section discusses the characteristics of the ICE MC111B minicooler which operates in the nominal 150 mW cooling power region. We then will discuss some of the vibration and acoustic properties.

4. ICE MC111B Minicooler--Operating Characteristics

Table 3 presents the preliminary specifications of this cryocooler. Figure 3 shows a photograph of this unit. A prototype of the minicooler has been integrated into an ICD^{2}A unit as is shown in Figure 4. Its construction is with a simulated detector array,

composed of a 1 kOhm resistor as a thermal load, and a thermister type N2222A to measure temperature. Figure 5 shows the configuration control drawing of the ICD^{2}A. We report in this publication the results of ongoing measurements, both on the MC111B cryocooler with a "static" (sealed) dewar and other experiments with a "dynamic" dewar (where a metal dewar is attached to a pump to maintain the appropriate vacuum).

Figure 6 shows the typical input power vs. ambient temperature necessary to cool a thermal load of 50 mW and where we maintain the cold tip temperature in the 77 to 80 K range. It will be seen that at 23 C, this input power is under 6 W input power. In Table 4, we see the input power vs. ambient temperature for two extremes of temperature. Here we have allowed the cold tip temperature to vary. We see that even at the +75 C ambient region we can maintain a 71 K cold tip temperature with an input power of less than 10 Watts.

We have operated these cryocoolers at various input voltages, and made measurements on cooldown times and power input as is shown in Tables 5 and 6. As expected, one can speed up the cooldown time by running the cryocooler "harder." In looking at the power requirements for higher total heat loads, we see in Tables 7 through 10 the results of operating the same cryocoolers with heat loads of 95 mW and 145 mW, as opposed to 50 mW.

We have also developed for our line of minicoolers a Closed Cycle Temperature Control (CCTC) circuit, and have applied it to the ICD^{2}A package. The use of CCTC (sometimes referred to as "Demand Refrigeration") is now widely recognized as having extensive advantages for operating such cryocoolers. This includes: (a) positive control of the detector array temperature, to some specified range; (b) lower average input power, yielding greater efficiency; (c) lower acoustic noise, because the system is run at a lower duty cycle; and (d) potentially improved MTBF, for the same reason. In Table 11 we show operating characteristics for an ICD^{2}A set up with CCTC and a static dewar, with a heat load of about 20 mW. We see from Table 11 that, at ambient, one achieves an 85 K cold tip temperature (a requirement of one of our systems users) with an input power of under 5 Watts. Even at the higher ambient of 52 C, the input power stays under 6.5 Watts.

5. Higher Temperature Operation

Use of the MC111B minicooler for infrared detector cooling is not just limited to the 77 K region and ICD^{2}A structures. In Table 12 we show some of the spectral regions for various popular infrared detector materials and their operating temperature ranges. Other ranges of interest are not just the 60 - 80 K region, but also 100 - 120 K and 150 - 200 K.

For example, Indium Antimonide (InSb) for some detector suppliers, wants to be operated at 65 K so that it can be impervious to temperature variations. For various applications it can be operated in the photoconductive or photovoltaic mode, and without too much loss of detectivity (D*) in the 100 - 120 K range.

Indium doped extrinsic Si can operate with good D*, but one must remain below 50 K. Mercury Cadmium Telluride (MCT or HCT), when used for detection in the 3 to 5 micron region, and shorter wavelengths, can be operated at higher temperatures of 150 - 200K.

Where possible, the MCT utilized at 190 - 200 K is operated with multistage thermoelectric cooling. Similarly, lead selenide operates in this higher temperature region. However, in many cases the thermal loading becomes excessive. Then even with multistage thermoelectric coolers the system goes unstable because of thermal runaway, and/or liquid coolants must be used to pump the heat away from the thermo-electric module. This requires a mechanical pump, thus losing the advantage of "no moving parts" for thermoelectrics. In any event, lowering the detector temperature to the 140 - 160 K region greatly enhances the system's Signal to Noise Ratio.

The MC111B, particularly as part of an ICD^{2}A structure, can provide an alternate and highly acceptable solution. Figure 7 shows the input power typical for a 50 mW heat load with the cold tip in the 55 K to 70 K range. Figure 8 extends this range to the 95 K region for the cold tip,showing the lowering of input power needed to achieve the same cooling of 50 mW. In Figure 9, which covers the 110 K to 150 K range for the cold tip, we see how the input power drops to about 3 W for a 140 K cold tip temperature. All this data is measured without the benefit of Closed Cycle Temperature Control (CCTC). We can expect further lowering of input power, perhaps as much as 15 to 20%, with the use of such Demand Refrigeration circuitry.

6. Self-Induced Vibrations

As mentioned earlier, a central issue associated with the use of an Integral Stirling cryocooler for an ICD^{2}A structure is microphonics. The MC111B has been designed specifically to minimize vibrations and acoustic noise.

Using a calibrated optical microscope, measurements were performed on the transverse vibration in the detector plane. It was found that the maximum transverse vibration of the cold finger was less than 4 microns peak-to-peak ($\pm$ 2 microns), within the accuracy of the microscope. Since the typical size of a detector is 25 to 30 microns, we can see where this vibration represents a small fraction of the optical "footprint" on the detector.

Additionally we have also carried out preliminary experiments on the self-induced vibration of the MC111B cryocooler using a simple

"optical lever." Two measurements were made. In the first, the cryocooler was attached to a plate whose mass had a moment of inertia of 1.5 oz-in-sec^2. This simulated the moment of inertia of a particular gimballed FLIR system of interest. As shown in Figure 10, a laser beam was reflected off the front of the detector array region of the ICD^{2}A to a distance 10 meters away and the spot size at the "target" was measured both with the cooler on and the cooler off.

The laser beam spot diameter before the motor was turned on was 20 mm, and after it was turned on, 21 mm. This is within the experimental error of the setup. The self-induced vibration had been damped out by the "simulated" system's inertial mass, and therefore not "measurable."

The experiment was then repeated by suspending the cryocooler by a string, without the additional inertia mass simulating the system. In this case, the beam displacement due to turn-on of the cryocooler, was an additional 15 mm at a distance of 10 meters. This corresponds to a total peak to peak angular beam spread of 0.75 milliradians, due to the self-induced vibration of the ICD^{2}A. That particular ICD^{2}A package has a measured moment of inertia of 0.0693 oz-in-sec^2. Thus, for a system such as described above, whose moment of inertia is approximately 22 times that of the ICD^{2}A, the self-induced vibration corresponds to $\pm$ 17 microradians. Effectively, for that gimballed system, the degradation due to the self-induced vibration becomes $[(100^2 + 17^2)/(100^2)]^{+1/2}$, or less than 1.5%. This is considered "highly acceptable" by the systems manufacturer.

7. Acoustic Noise

The acoustic noise of the MC111B was measured in the following manner. The unit was acoustically isolated from the examination table by a rubber cushion, and the background noise was measured to be 37 dB. At a distance of 1 meter, the acoustic noise, with the MC111B operating was found to be 50 dB. At 5 meters it corresponds to 39.5 dB, taking the background noise into account. This measurement was carried out with a B and K type 2225 dB meter.

8. Second Generation and Focal Plane Arrays, & Larger ICD^{2}A's

During the last few years it has been recognized that considerable advantage can be achieved by using a larger number of detectors, each with a much smaller size. As the size of the total array grows, particularly for non-scanning large area Focal Plane arrays, the average cooling power needed also grows. The ICD^{2}A configuration for such arrays is a major asset. Second generation and Focal Plane Arrays incorporate the integrated circuits in the dewar to amplify, buffer and time multiplex the signals generated. Fortunately, multiplexing allows one to increase the number of detectors but decreases the number of leads. This keeps load losses low. Also, the major other issue associated with an ICD^{2}A, that of outgassing of the

dewar, is not onerously increased by the number of leads. For example, compare first and second generation MCT Detector arrays. In the first generation where one has 180 elements, typically the number of leads is 220. In the second generation, even though one goes to a 480 element linear array, only 30 leads are used to extract the signals.

The lower number of wires is also completely compatible with less outgassing from the dewar. Of course this is common to both the ICD^{2}A structure and the Common Module dewar structure. We have also made measurements and estimated what would be the ingassing effect into the dewar through our cold head. We have found that this will be less than 10^{-12} Torr, which corresponds to a life for the dewar, from this source of leakage, of approximately ten years.

We can also consider future growth and requirements in the field. As we have seen, detector arrays requiring 20 to 30 mW of cooling in the Common Module dewar configuration typically need a 0.25 W cryocooler. This can be satisfied by a 100 mW ICD^{2}A. For larger detector array's requiring cooling in the 50 to 100 mW range, the "Common Module" standard requirement is for a cooling power of between 0.5 to 1 W. An ICD^{2}A structure lowers this to a 200 to 400 mW load. We have already operated our MC111B at cooling levels up to 0.4 W. We feel confident that the inherently balanced structure created in our MC111B leads to solving higher average power requirements for FPA's.

9. Acknowledgments

We wish to thank Prof. N. Ben-Yosef of the Hebrew University, and E. Manor, for assistance in the transverse vibration and acoustic noise measurements. We also acknowledge the assistance of members of the staff at the Electro Optical Division of Kollmorgen Inc., who carried out the first self-induced vibration experiments.

Table 1. 0.25 Watt Common Module Heat Load Distribution

Detector Load	=	0.03 W - 0.05 W
Dewar Losses*	=	0.10 W
Integration Losses	=	0.10 W
		0.25 W

Dewar Losses* = $Q_{conduction} + Q_{radiation} + Q_{wires}$

$Q_{conduction}$	=	0.050 W
$Q_{radiation}$	=	0.015 W
Q_{wires}	=	0.035 W
Total	=	0.100 W

Table 2. Heat Load Distribution. Common Module *vs.* Integrated Cooler Dewar Detector Assembly (ICD^2A)

	0.25 W Common Module	Integrated Cryocooler with Directly Mounted Detector
Detector Load	0.030 to 0.050 W	0.030 to 0.050 W
Dewar Losses		
-- Conduction	0.050	none
-- Wires	0.035	0.050
-- Radiation	0.015	0.015
Integration Losses	0.100	none
TOTAL	0.230 to 0.250 W	0.095 to 0.115 W

Table 3. Preliminary Specification of 0.15 Watt MC111B Integral Stirling Cryocooler

Cooling capacity at 80 K	0.15 W
Typical Input Power	< 8.0 W
Cooldown time from 300 K to 80 K	< 4.5 Min
MTBF	> 2000 Hr
Ambient Temperature Operating Limits	-40 to +71 C
Input Power with Closed Cycle Temperature Control at 80 K	< 5.0 W
Weight without dewar	< 0.45 Kg
External Cooling	Heat Sink

Table 4. ICD^2A--Input Power *vs.* Ambient Temperature (2 extremes)

Ambient Temperature (C)	Input Power (W)	Cold Tip Temperature (K)
+ 75	9.17	71
- 37	7.56	45

Notes: (a) "Static" Dewar Total Heat Load = 92 mW of which 50 mW is "Load"
(b) Voltage is kept Constant and Cold Tip Temperature is Free to Vary

Table 5. Performance of MC111B P/N 000014/Input 12 V DC

Date: 3 July 1988

Parameters	Results
23 C Test:	
A. Cooldown Time to 100 K	5 Min 38 Sec
B. Cooldown Time to 85 K	7 Min 26 Sec
C. Cooldown Time to 77 K	8 Min 29 Sec
D. Power Input with Cold Tip at 58 K	7.14 Watts
52 C Test:	
A. Cooldown Time to 100 K	7 Min 18 Sec
B. Cooldown Time to 85 K	10 Min 01 Sec
C. Cooldown Time to 77 K	12 Min 06 Sec
D. Power Input with Cold Tip at 70 K	6.96 Watts
-20 C Test:	
A. Cooldown Time to 100 K	3 Min 24 Sec
B. Cooldown Time to 85 K	4 Min 28 Sec
C. Cooldown Time to 77 K	5 Min 00 Sec
D. Power Input with Cold Tip at 48 K	6.96 Watts
23 C Test:	
A. Cooldown Time to 100 K	5 Min 37 Sec
B. Cooldown Time to 85 K	7 Min 18 Sec
C. Cooldown Time to 77 K	8 Min 18 Sec
D. Power Input with Cold Tip at 58 K	7.14 Watts

Note: "Static" Dewar Total Heat Load = 92 mW of which 50 mW is "Load"

Table 6. Performance of MC111B P/N 000014/Input 14.27 V DC

Date: 30 June 1988

Parameters	Results
23 C Test:	
A. Cooldown Time to 100 K	3 Min 48 Sec
B. Cooldown Time to 85 K	4 Min 58 Sec
C. Cooldown Time to 77 K	5 Min 32 Sec
D. Power Input with Cold Tip at 51 K	9.49 Watts
52 C Test:	
A. Cooldown Time to 100 K	4 Min 39 Sec
B. Cooldown Time to 85 K	6 Min 05 Sec
C. Cooldown Time to 77 K	6 Min 52 Sec
D. Power Input with Cold Tip at 56 K	9.63 Watts
-20 C Test:	
A. Cooldown Time to 100 K	2 Min 33 Sec
B. Cooldown Time to 85 K	3 Min 18 Sec
C. Cooldown Time to 77 K	3 Min 39 Sec
D. Power Input with Cold Tip at 50 K	9.56 Watts
23 C Test:	
A. Cooldown Time to 100 K	3 Min 40 Sec
B. Cooldown Time to 85 K	4 Min 47 Sec
C. Cooldown Time to 77 K	5 Min 19 Sec
D. Power Input with Cold Tip at 51 K	9.49 Watts

Note: "Static" Dewar Total Heat Load = 92 mW of which 50 mW is "Load"

Table 7. Performance of MC111B P/N 000012

Set Up: Dynamic dewar with no temperature controller used
Dewar vacuum at start of test: 5×10^{-4} Torr (5×10^{-3} Torr Min.)
Dewar boil off rate LN_2 25 SCC 95 mW
Additional Heat Load 0 mW
Total Heat Load 95 mW

Parameters		Results
23 C Test:		
A.	Cooldown Time to 85 K	7 Min 40 Sec
B.	Cold Tip Temperature @ 14 V min	69 K
C.	Power input	8.9 Watts
52 C Test:		
A.	Cooldown Time to 85 K	11 Min 37 Sec
B.	Cold Tip Temperature @ 14 V min	81 K
C.	Power input	9.0 Watts
-20 C Test:		
A.	Cooldown Time to 85 K	5 Min 14 Sec
B.	Cold Tip Temperature @ 14 V min	54 K
C.	Power input	8.5 Watts

Table 8. Performance of MC111B P/N 000012

Set Up: Dynamic dewar with no temperature controller used
Dewar vacuum at start of test: 5×10^{-4} Torr (5×10^{-3} Torr Min.)
Dewar boil off rate LN_2 25 SCC 95 mW
Additional Heat Load 50 mW
Total Heat Load 145 mW

Parameters		Results
23 C Test:		
A.	Cooldown Time to 85 K	10 Min 33 Sec
B.	Cold Tip Temperature @ 14 V min	73 K
C.	Power input	8.8 Watts
52 C Test:		
A.	Cooldown Time to 85 K	13 Min 00 Sec
B.	Cold Tip Temperature @ 14 V min	87 K
C.	Power input	8.9 Watts
-20 C Test:		
A.	Cooldown Time to 85 K	6 Min 44 Sec
B.	Cold Tip Temperature @ 14 V min	56 K
C.	Power input	8.5 Watts

Table 9. Performance of MC111B P/N 000014

Set Up: Dynamic dewar with no temperature controller used
Dewar vacuum at start of test: 5×10^{-4} Torr (5×10^{-3} Torr Min.)
Dewar boil off rate LN_2 25 SCC 95 mW
Additional Heat Load 0 mW
Total Heat Load 95 mW

Parameters	Results
23 C Test:	
A. Cooldown Time to 85 K	8 Min 06 Sec
B. Cold Tip Temperature @ 14 V min	65 K
C. Power input	9.1 Watts
52 C Test:	
A. Cooldown Time to 85 K	12 Min 15 Sec
B. Cold Tip Temperature @ 14 V min	79 K
C. Power input	9.1 Watts
-20 C Test:	
A. Cooldown Time to 85 K	5 Min 34 Sec
B. Cold Tip Temperature @ 14 V min	47 K
C. Power input	8.6 Watts

Table 10. Performance of MC111B P/N 000014

Set Up: Dynamic dewar with no temperature controller used
Dewar vacuum at start of test: 5×10^{-4} Torr (5×10^{-3} Torr Min.)
Dewar boil off rate LN_2 25 SCC 95 mW
Additional Heat Load 50 mW
Total Heat Load 145 mW

Parameters	Results
23 C Test:	
A. Cooldown Time to 85 K	9 Min 45 Sec
B. Cold Tip Temperature @ 14 V min	76 K
C. Power input	8.8 Watts
52 C Test:	
A. Cooldown Time to 85 K	11 Min 43 Sec
B. Cold Tip Temperature @ 14 V min	88 K
C. Power input	8.9 Watts
-20 C Test:	
A. Cooldown Time to 85 K	6 Min 36 Sec
B. Cold Tip Temperature @ 14 V min	61 K
C. Power input	8.4 Watts

Table 11. Performance of MC111B P/N 000014A ICD^{2}A with Closed Cycle Temperature Control

Set Up: Static dewar with temperature controller (CCTC)
Dewar boil off rate LN_2 5 SCC, 19 mW--Total Heat Load

Parameters	Results
23 C Test:	
A. Cooldown Time to 85 K	4 Min 59 Sec
B. Min. Cold Tip temperature (*)	51 K
C. Power input @ 85 K	4.9 Watts
52 C Test:	
A. Cooldown Time to 85 K	6 Min 37 Sec
B. Min. Cold Tip temperature (*)	57 K
C. Power input @ 85 K	6.3 Watts
-20 C Test:	
A. Cooldown Time to 85 K	3 Min 23 Sec
B. Min. Cold Tip temperature (*)	50 K
C. Power input @ 85 K	3.7 Watts

(*) Measured without temperature controller

Table 12. Operating Regions of Popular Modern IR Detectors

Material	Spectral Range (Microns)	Operating Temperature (K)
PbSe	2 - 5	160 - 200
InSb	3 - 5	60 - 80; and 100 - 120
Pt:Silicide	1 - 2.5; 3 - 5	77
HgCdTl (MCT)	1 - 2.5	150 - 200
	3 - 5	70 - 80; and 100 - 180
	8 - 12	80 and 40
Si(In)	3 - 5	40 - 50

Figure 1 COMMON MODULE

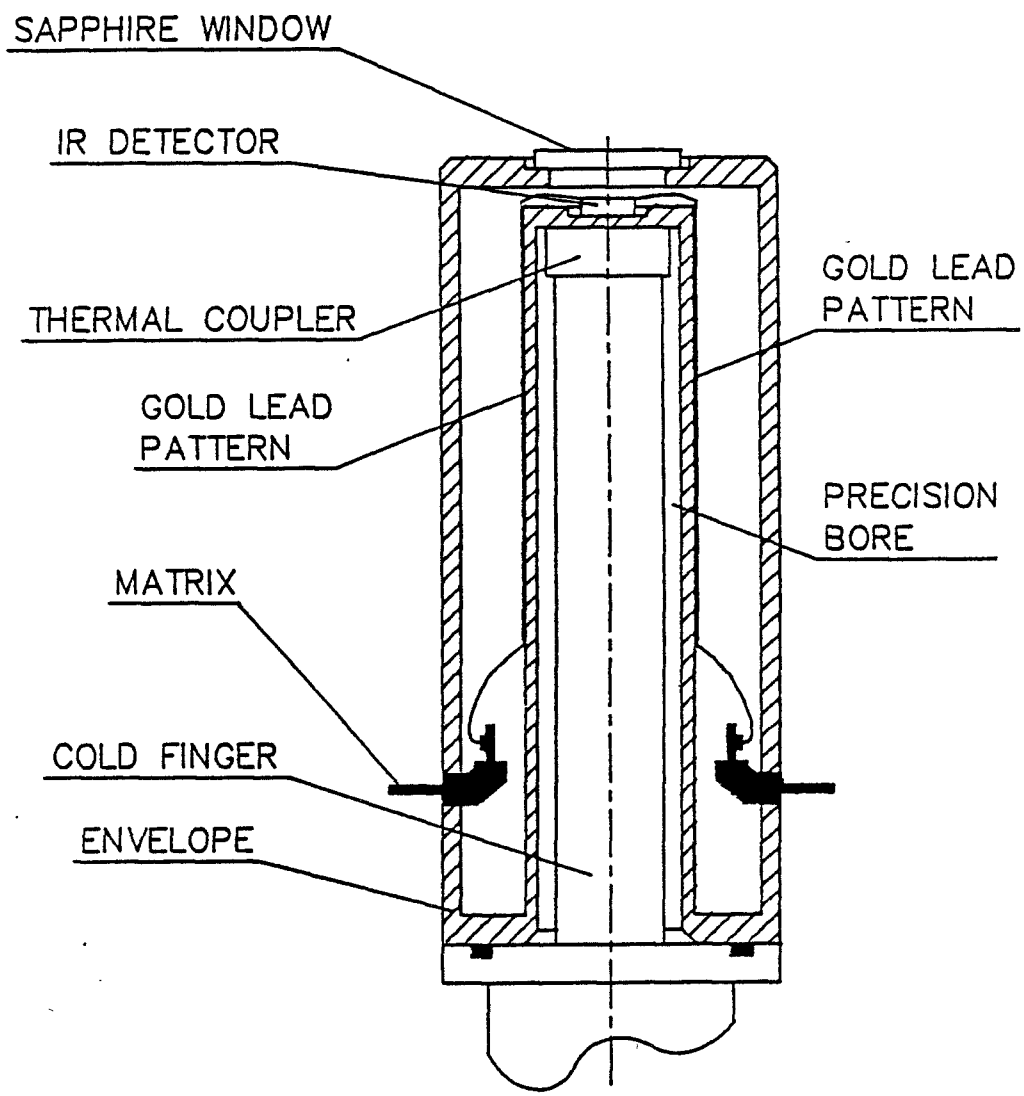

ICE

Figure 2 CRYOCOOLER / DEWAR / DETECTOR STRUCTURES

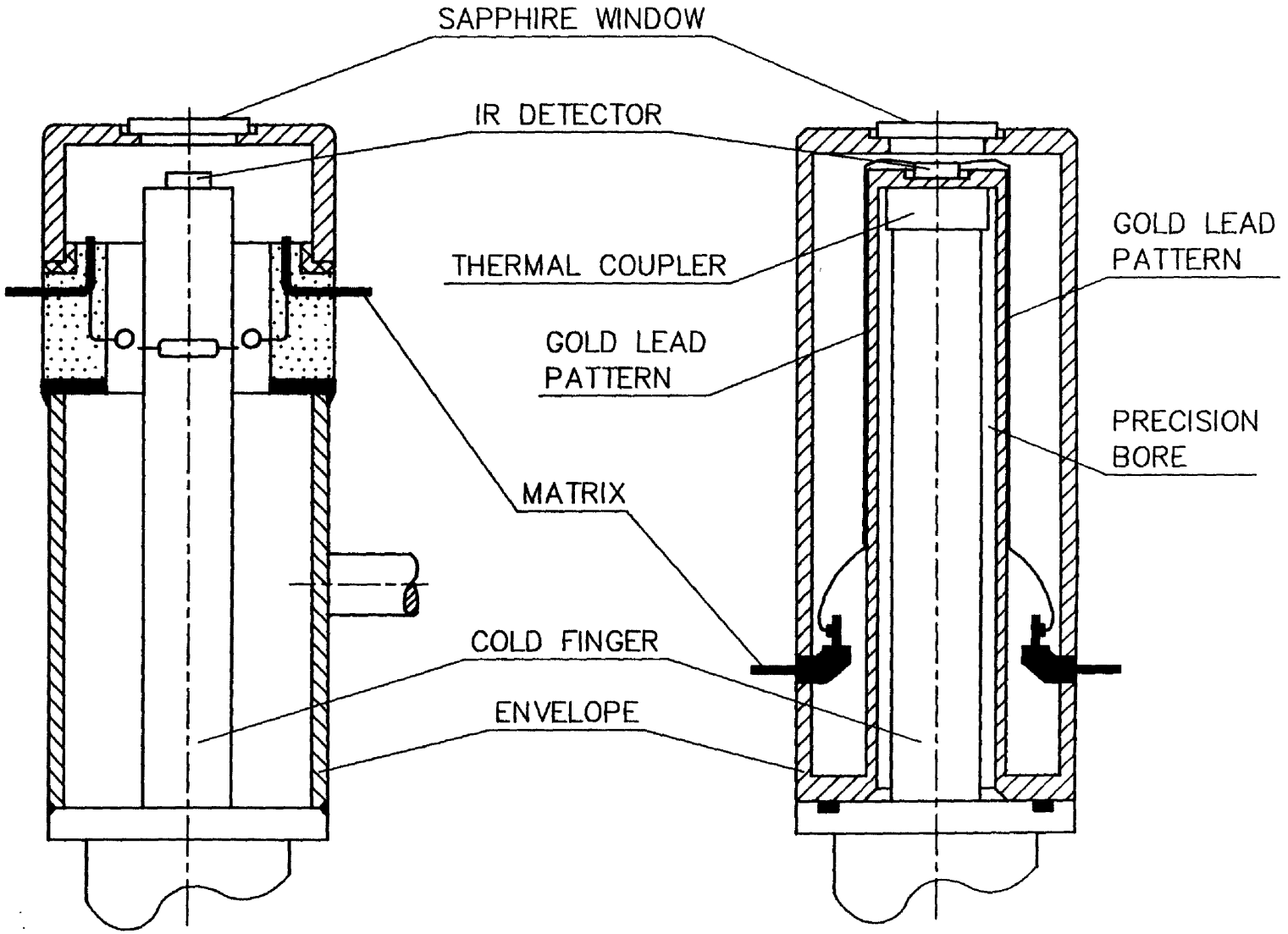

271

FR 100 171

Fig. 3 MC111B--0.15 W Integral Stirling Minicooler

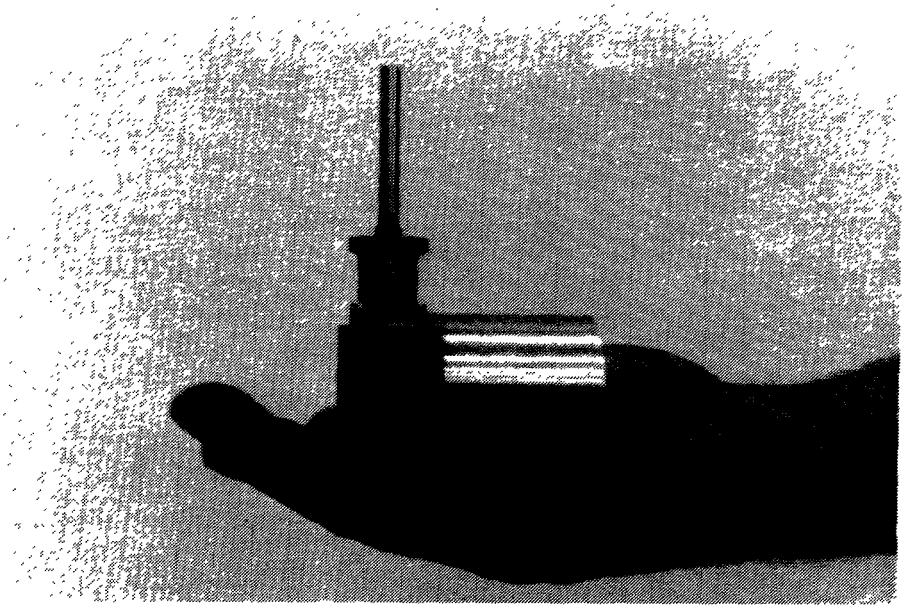

FR 000 061

Fig 4 ICD ^{2}A

INTEGRATED COOLER DEWAR DETECTOR ASSEMBLY

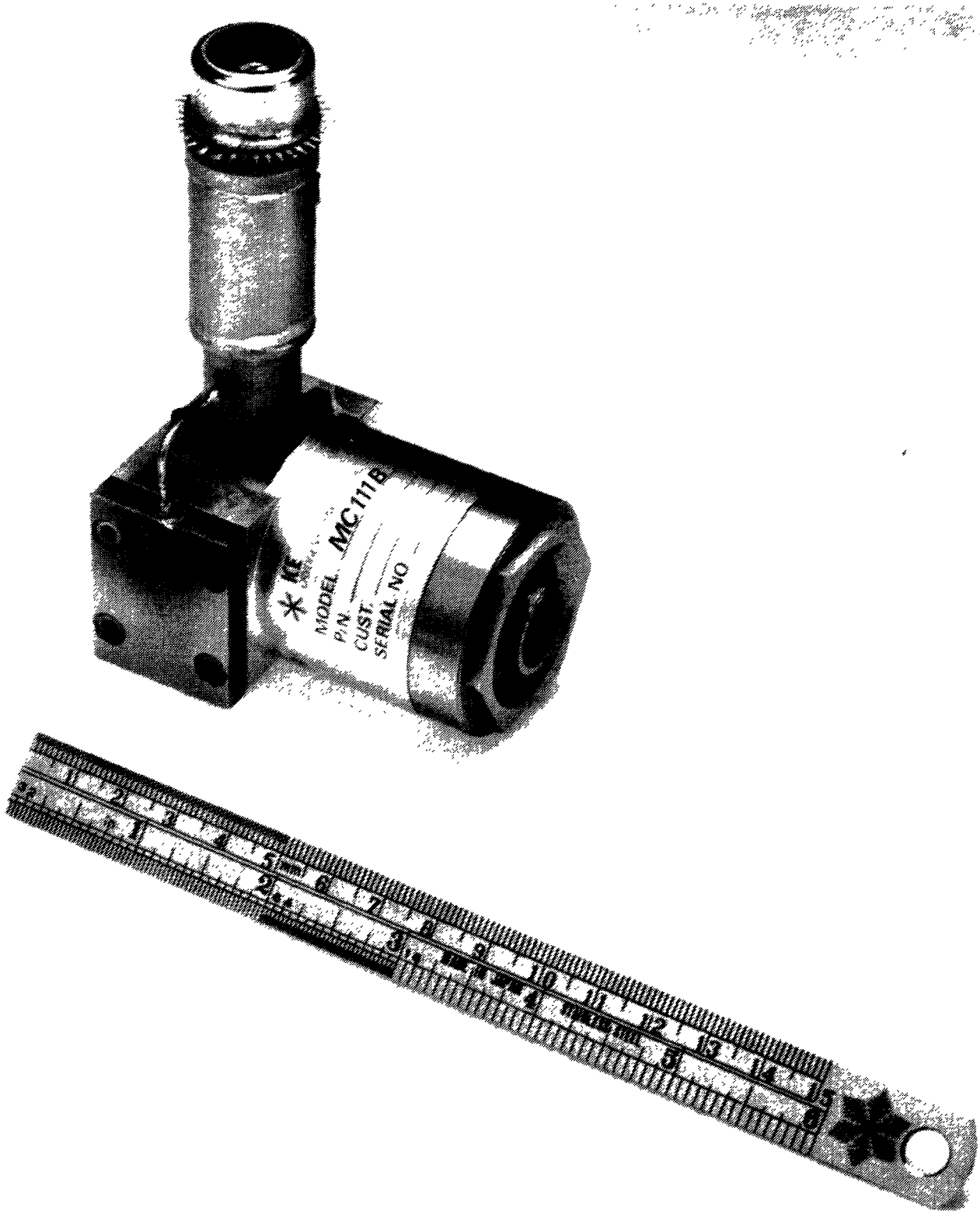

Figure 5 CONFIGURATION CONTROL DWG. OF ICD²A

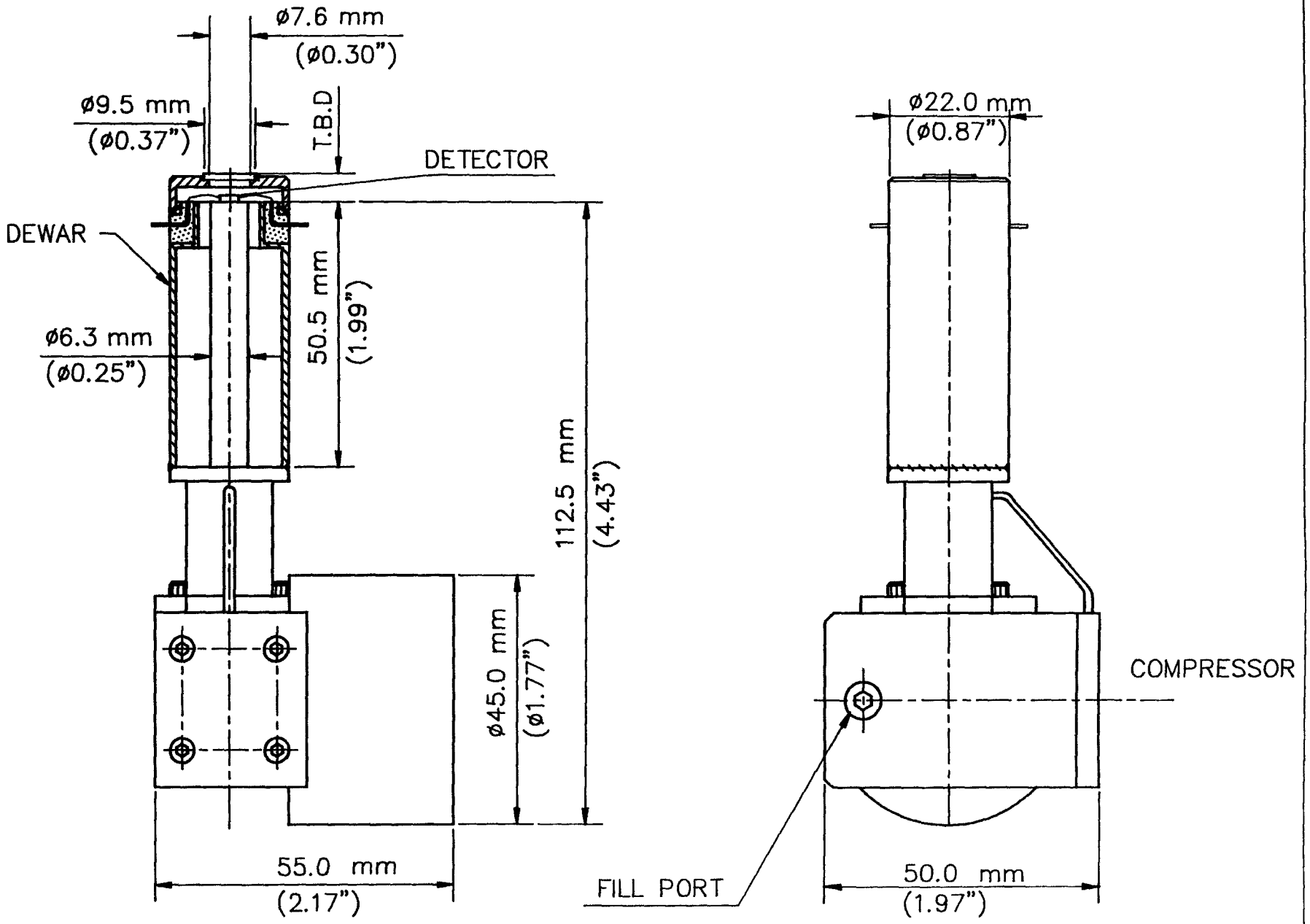

Figure 6

MC111B MINICRYOCOOLER

INPUT POWER VS AMBIENT TEMPERATURE

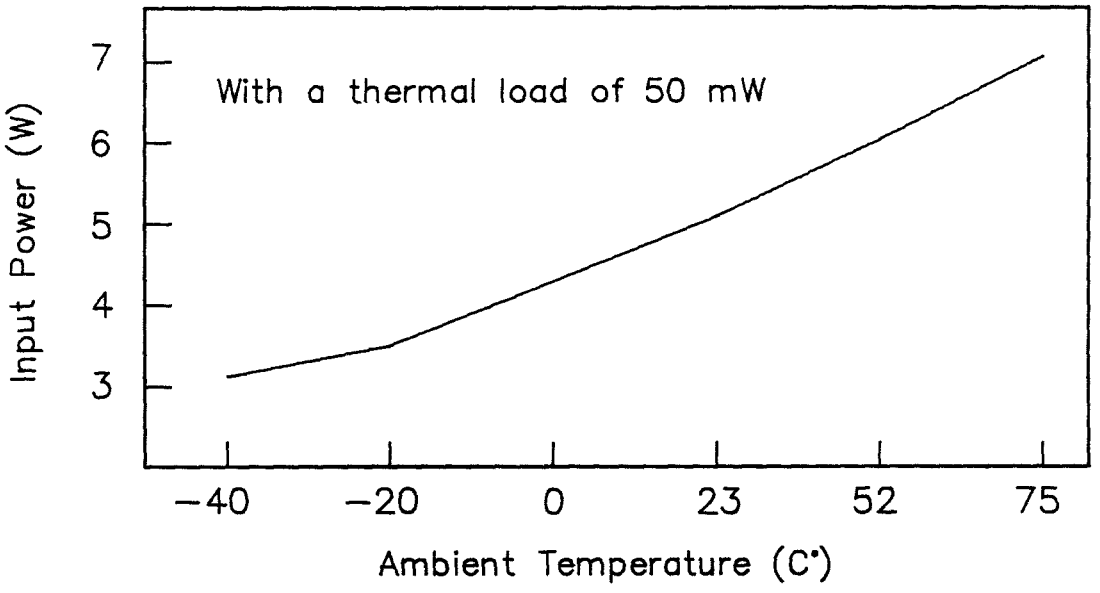

Note: Cold Tip Temperature held constant at 78 +/- 1 K

Fig 7 MC111B MINICRYOCOOLER

COOLING TEMPERATURE vs. INPUT POWER

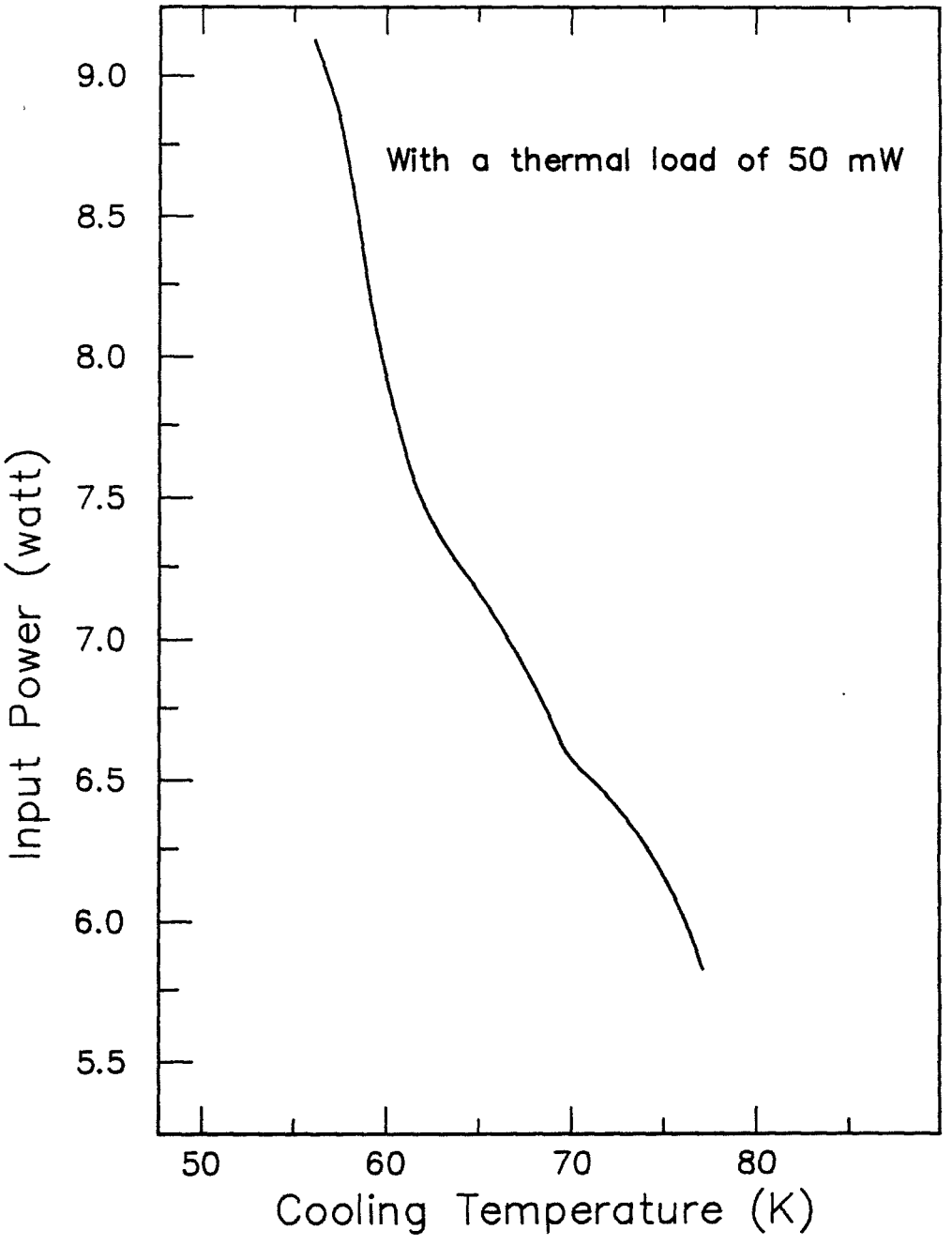

FR 100 328

Fig 8 MC111B MINICRYOCOOLER

COOLING TEMPERATURE vs. INPUT POWER

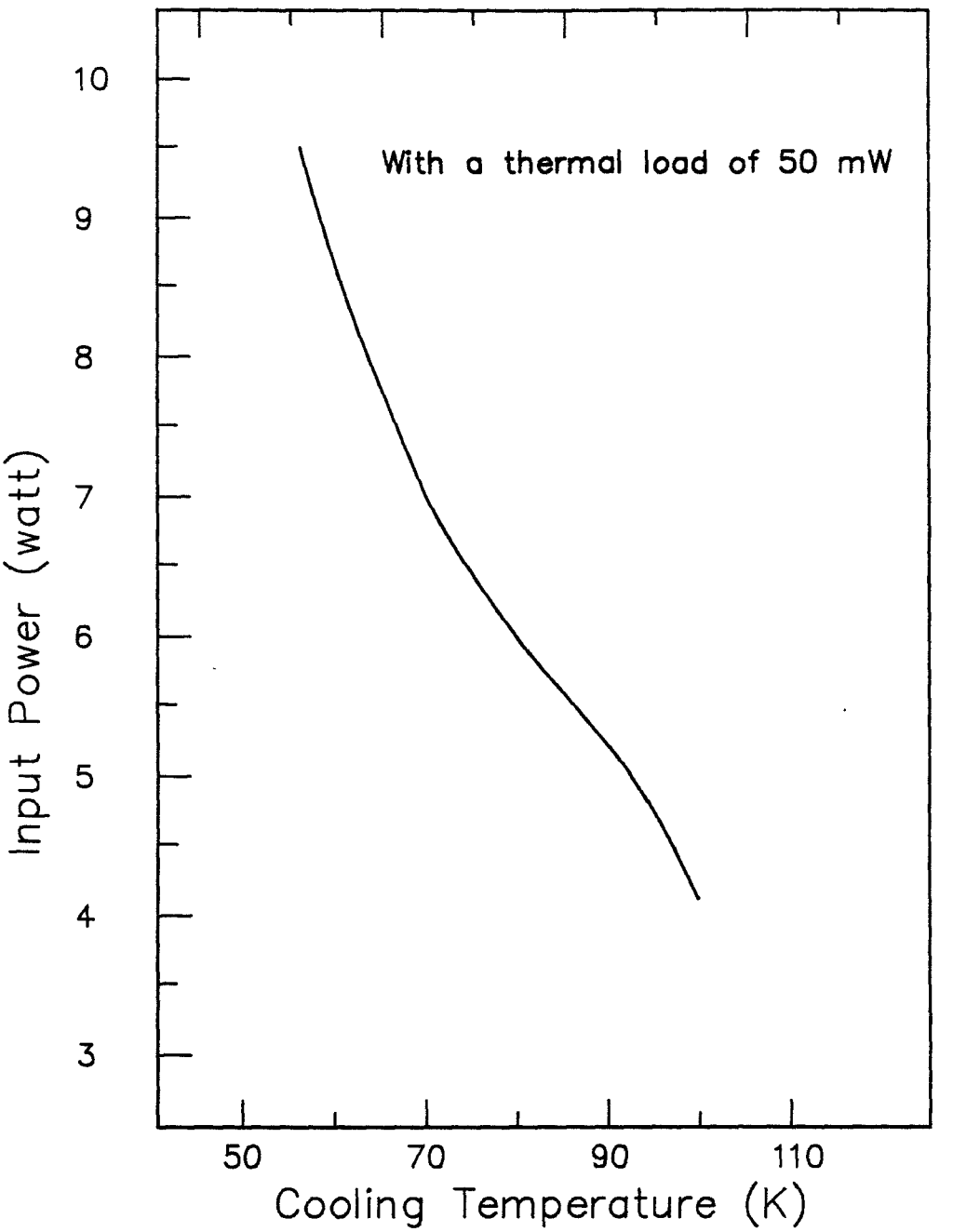

fr 100 329

Fig 9 MC111B MINICRYOCOOLER

COOLING TEMPERATURE vs. INPUT POWER

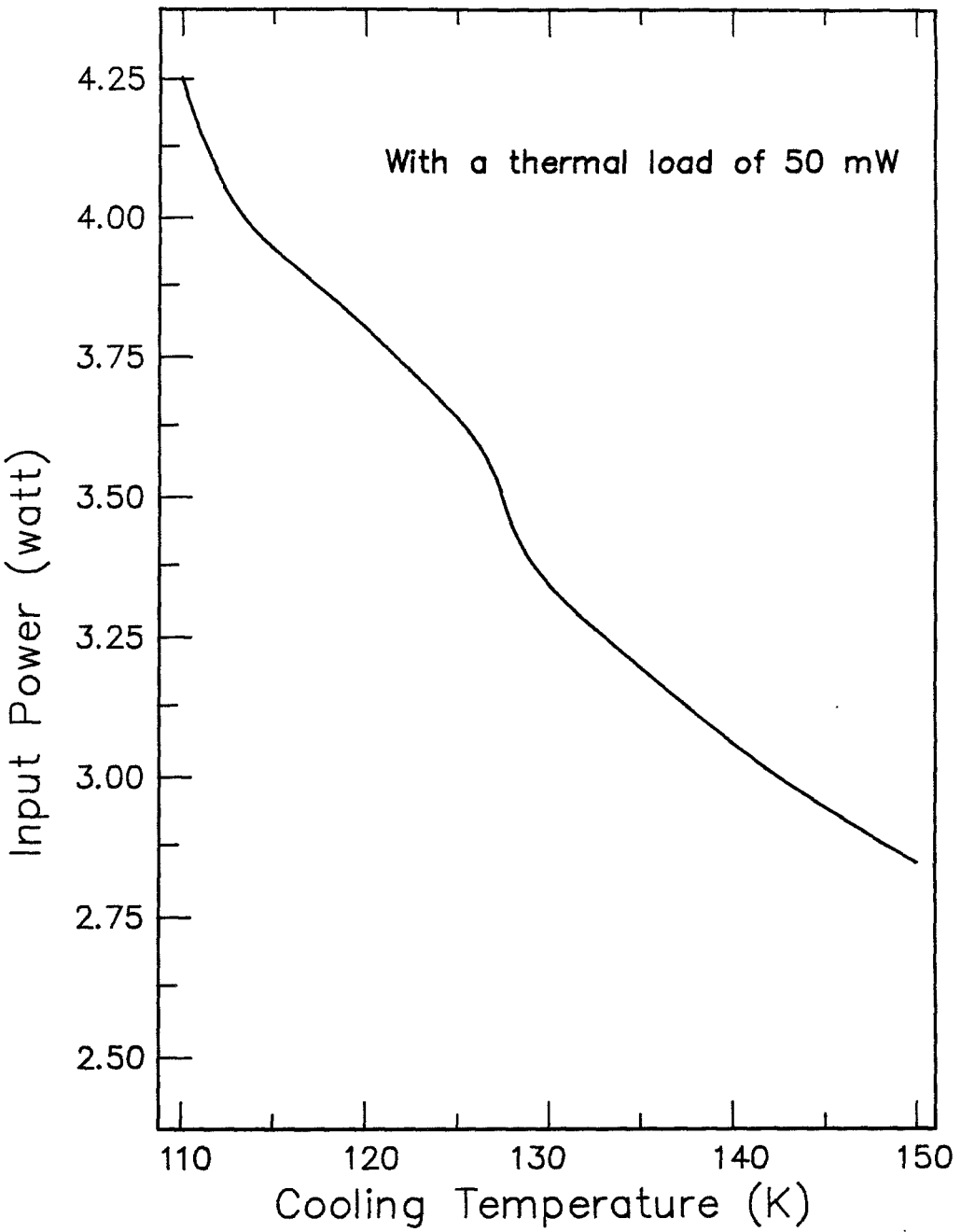

FR 100 330

Figure 10 SETUP OF SELF-INDUCED VIBRATION TEST

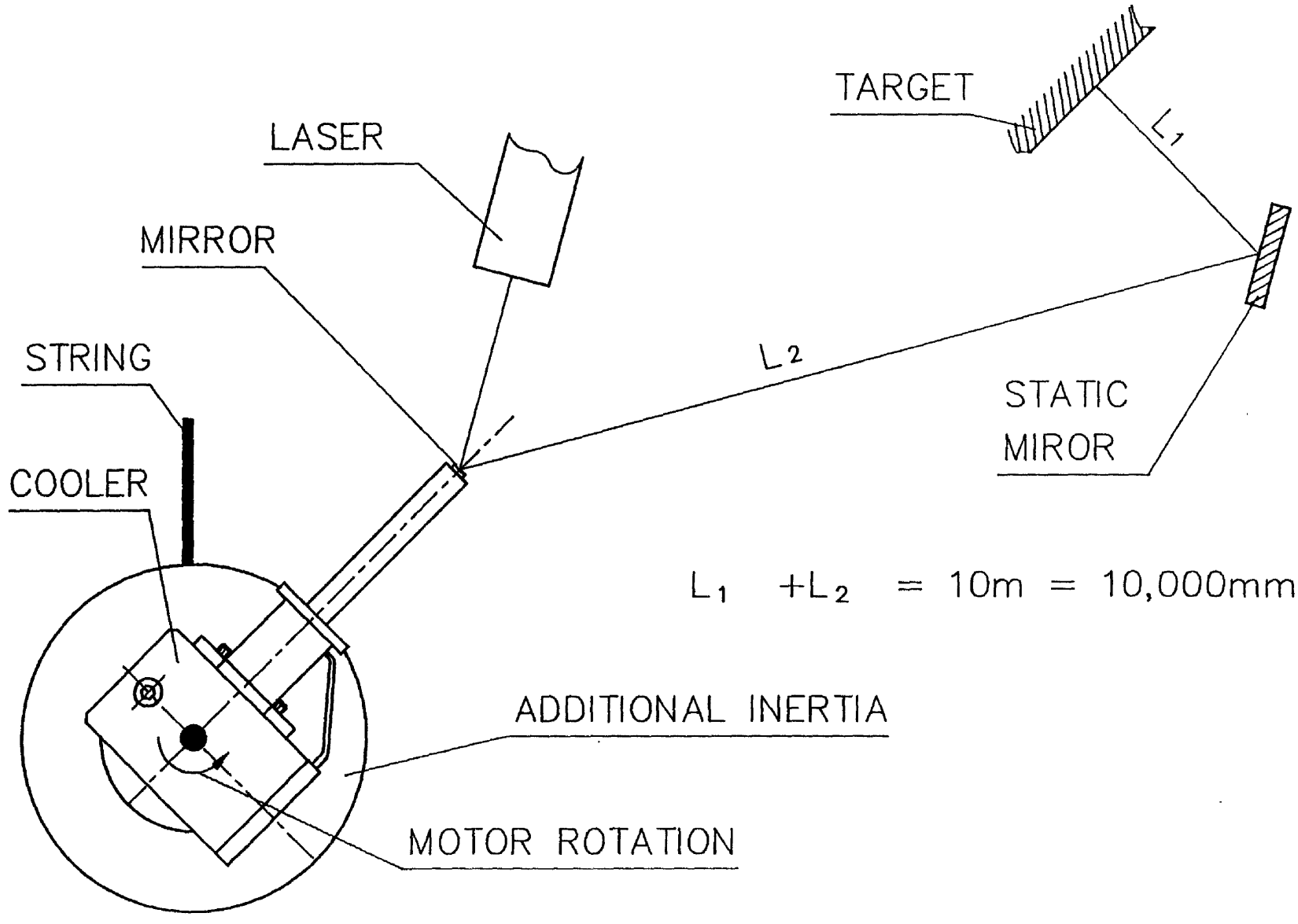

FR 100 174

SESSION VII

HYBRID COOLERS

CHAIRPERSON: W. LITTLE
VICE CHAIRPERSON: S. RUSSO

SAFETY CONSIDERATIONS IN OPERATING DIP TUBE ACCESS 10K AND 3K CLOSED-CYCLE CRYOCOOLERS

Calvin Winter
Andrzej Swiecicki

Quantum Technology Corp.
6237 - 148 Street, Surrey, B.C., CANADA V3S 3C3

ABSTRACT

The use of a helium gas filled, positive pressure, dip tube access well, coupled to a closed-cycle cryocooler, has the advantage of allowing quick and easy access to the cold space. A detector or sample can be cooled simply by lowering it into the cold helium. This allows samples or detectors to be changed in minutes without breaking any vacuum seals. Thermal stratification of liquid helium at the bottom of the well allows continuous positive pressure operation at temperatures well below the boiling point of helium. Temperature fluctuations due to the cryocooler cycle are geatly dampened due to the large heat capacity of helium. The helium bath also allows large instantaneous heat loads. Substantially lower temperatures may be reached by vacuum pumping on the liquid helium bath. A safety interlock system has been designed to prevent drawing air or water into the dip tube access well.

Results from several years of safe operation of the QUANTUMCOOLER (TM) closed-cycle cryocoolers is presented.

INTRODUCTION

Dip tube access experimental crycoolers combine the advantages of using a liquid helium dip dewar with closed-cycle refrigeration. The dip tube well is filled with helium gas at above atmospheric pressure. A sample or experimental apparatus to be cooled is lowered into the dip tube well and is cooled by convection in the cold helium gas. Gravitational stratification of the helium gas maintains the colder (and denser) helium gas at the bottom. In equilibrium there are no convection currents. Due to the low thermal conductivity of helium gas, little heat is carried down the dip tube in the quiescent state. A dip tube access, liquid helium temperature cryocooler is shown schematically in Figure 1.

We have built a number of these QUANTUMCOOLER (TM) dip tube access systems coupled to both 10K and 3K closed-cycle cryocoolers. These systems are used for a variety of experiments including Hall effect measurements (narrow tail version), optical fluorescence measurements with the sample immersed in liquid helium (optical access version), variable temperature

magnetic susceptibility measurements, germanium bolometer cooling, and sample and detector cooling. In all cases the vacuum dewar space is permanently sealed. This allows continuous operation of the closed-cycle cryocooler while the items to be cooled are being inserted, changed or removed. This ease of operation and the speed with which samples can be changed are major advantages of the dip tube access system.

Helium gas in the 3K system is also at above atmospheric pressure. In this case thermal stratification in the liquid helium at the bottom of the dip tube access well allows the sample to be immersed in liquid at a temperature below the boiling point. Naturally, higher up, at the liquid to gas interface, the liquid helium is warmer and is at the boiling point corresponding to the pressure of the gas.

FIGURE 1

CROSS-SECTIONAL SCHEMATIC OF A LIQUID HELIUM TEMPERATURE QUANTUMCOOLER (TM) SHOWING THE HELIUM FILLED DIP TUBE ACCESS WELL

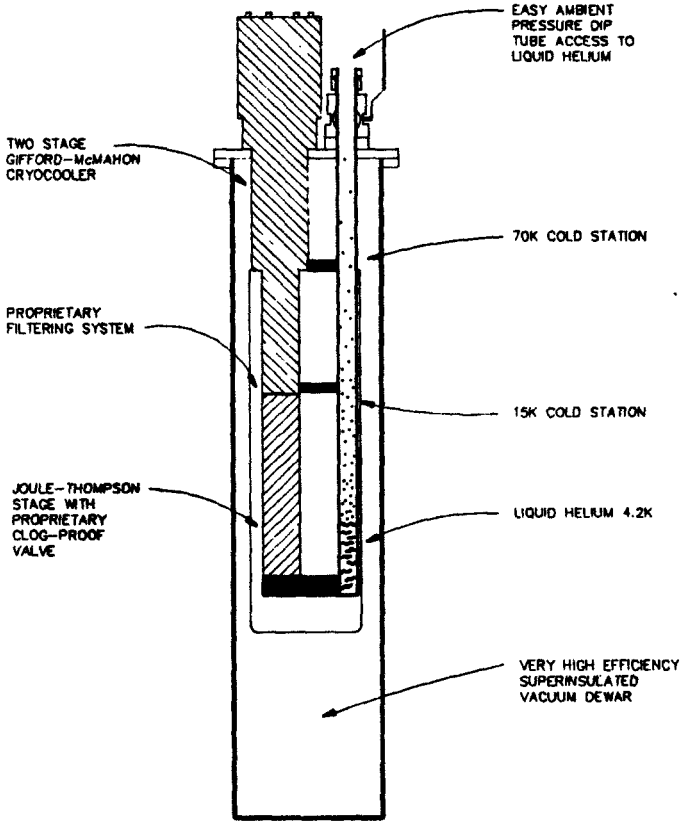

SAFETY CONSIDERATIONS

Due to the extremely dense state of gas in a cryogenic system, precautions must always be taken to allow the gas to safely vent during warm-up. The catastrophic consequences to the vacuum vessel and the surroundings when liquid helium is allowed to warm but the vent line is plugged are well known. The hazard comes from inadvertent plugging of the vent line. Naturally, it is essential to have a tested relief valve before any manually operated valves to prevent accidental manual closing of the vent line.

An additional hazard may be caused by the condensation of air in the venting system. This hazard is present in all liquid helium cryostats which are vented to the atmosphere. For example, if a large diameter vent tube is left open at the top, an inherently unstable helium-air interface exists. The helium gas at the bottom of the interface is very nearly at room temperature. The room temperature air above it is approximately seven times denser. Convection will occur allowing helium gas to escape upwards and air to be drawn downwards into the cryostat. The air freezes in the cold and may eventually form a gas tight plug in the neck of the cryostat. This plug is very dangerous because the warming of the cold gas and/or liquid below the plug may generate pressures sufficient to rupture the vessel before dislodging the plug.

Recent studies of the formation of frozen air plugs in a liquid helium cryostat show that if two vent lines are open at slightly different heights then rapid convection flow occurs. Frozen air formation may be extremely rapid, two to 20 cubic centimeters per minute through a duct of one square centimeter cross-section (1).

In the case of dip tube access closed-cycle cryocooler systems the possibility of air contamination is increased. Unlike a liquid helium cryostat in which there is always some helium gas flow outwards which tends to keep the air out, in the closed-cycle cryocooler systems (if helium gas is not supplied) air will be inhaled, condensed and frozen by the cooling action.

SAFETY INTERLOCK SYSTEM

The safety interlock system used on the QUANTUMCOOLER (TM) dip tube access cryocoolers was designed to meet the following criteria:

i) to maintain above atmospheric pressure in the dip tube space,
ii) to provide a safety pressure relief vent for the dip tube well,
iii) to provide a safety pressure relief vent for the vacuum dewar,
iv) to allow sample holder tubes to be inserted or removed without introducing air into the helium, and
v) to automatically switch off the closed-cycle cryocooler in the event that a helium gas over-pressure is not maintained.

Different configurations of the safety interlock system are used for the 10K and 3K cryocooler systems. For simplicity the 10K system is shown in Figure 2.

FIGURE 2

SCHEMATIC OF 10K QUANTUMCOOLER (TM) DIP TUBE ACCESS SYSTEM
SHOWING SAFETY INTERLOCK FEATURES

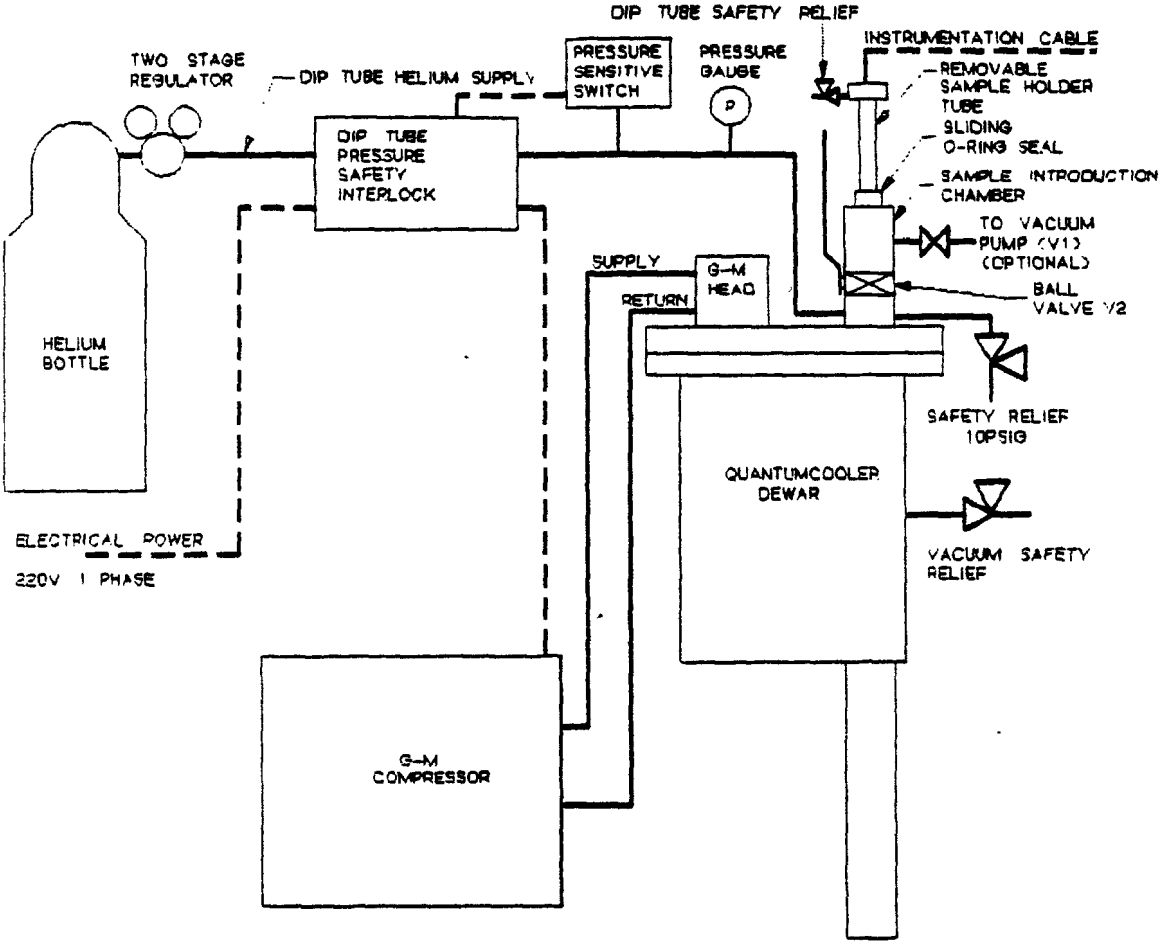

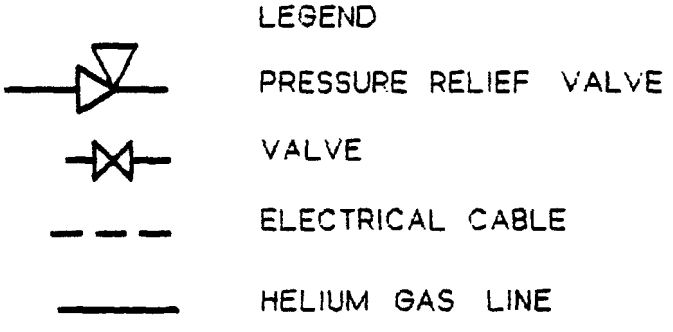

The vacuum dewar is of a permanently sealed, super-insulated construction. Cooling is provided by a closed-cycle Gifford-McMahon (G-M) compressor and cold head. A totally independent helium gas supply is used to pressurize the dip tube well. Low pressure helium at 1.4 bar absolute (6 psig) flows through the safety interlock to the dip tube well. The top of the dip tube port is provided with a close-off ball valve "V2", a vent valve "V1" and a sliding O-ring seal to allow sample tubes up to 22 millimeters (7/8 inch) diameter to be inserted.

The safety interlock system has a safety relief valve vent set at 1.7 bar absolute (10 psig). It also has a digital or analog display of the dip tube well pressure. A pressure sensitive switch set to trip at 1.15 bar absolute (2 psig) on the helium line is connected to an interlock which will automatically switch off the power to the cryocooler if an over-pressure is not maintained.

INSERTING THE SAMPLE

The process of inserting the sample holder tube is straightforward. With the ball valve closed the sample holder tube is lowered into the sample introduction chamber and the O-ring seal is tightened. To remove air the vent valve "V1" is opened allowing the sample and removable sample holder tube to be evacuated. The valve "V1" is closed and the ball valve "V2" is opened allowing the sample to be lowered into the positive pressure helium dip tube well. For systems in which small amounts of air contamination do not present a problem a vacuum pump is not required. The removable sample tube is simply purged by momentairly opening the dip tube safety relief prior to insertion.

The O-ring provides a good sliding seal against the polished stainless steel sample holder tube as it is lowered. The sample is lowered slowly to allow the majority of its heat to be removed by the first cooling station of the cryocooler. The process of cooling a sample from room temperature takes only a few minutes. In operation the sample temperature can be regulated either by changing its height or by means of an electronic temperature controller. The controller is connected to a heater and temperature sensor located on the bottom of the sample holder tube by means of the instrumentation cable shown.

REMOVING THE SAMPLE

To remove the sample, the sliding O-ring seal is loosened and the sample holder tube is raised. Once the sample is above the ball valve, the ball valve "V2" is closed and the sample holder tube may be totally withdrawn. Due to the fact that the lower part of the sample holder tube is very cold, increased friction is encountered as it is removed because the sliding O-ring freezes to the wall of the tube. After a few seconds the ambient heat warms the thin sample holder tube wall and allows it to be raised a few centimeters before it sticks again. Nevertheless, the sample can be removed in about two minutes without opening the dip tube space to atmosphere.

For systems where minor contamination of the helium gas in the dip tube well is not a concern, it is possible to remove the sample holder tube very quickly by totally unscrewing the sliding O-ring seal and pulling the sample holder tube out in one movement then quickly closing the ball valve. The sliding O-ring seal may be recovered from the sample holder tube a few minutes later, after it has warmed to ambient temperature. This manoeuvre causes the pressure in the dip tube access well to fall to atmospheric pressure and therefore trips the pressure sensitive switch. To prevent nuisance shutdowns of the cryocooler system, the safety interlock system is equipped with a short interval timer which allows the cryocooler to continue operating during this manoeuvre. The safety interlock will nevertheless switch the cryocooler off if the ball valve is inadvertently left open too long. The safety interlock box also has a manually operated timer and solenoid valve to allow the dip tube helium supply to be switched off during this manoeuvre.

OPERATING EXPERIENCE

The closed-cycle dip tube access cryocooler systems are very easy to use and operate very reliably. A technical description of one 3K system is given in reference (2).

The 10K systems operate with an external supply of helium gas for the dip tube well. In continuous operation no helium gas is consumed. Samples can be inserted and removed with the cryocooler in continuous operation. However, the initial cooldown of the cryocooler requires that helium gas be supplied to the dip tube well and that gas is lost on warmup. The consumption of gas is negligible. A single cooldown/warmup cycle of the cryocooler consumes approximatey 7 standard liters (0.2 SCF) of gas. If, for example, the cryocooler is cooled and warmed once per week for one year, the total consumption of gas is only 3% of one standard helium gas cylinder.

The 3K systems require a more substantial quantity of helium gas during cooldown as a volume of up to two liters of liquid helium may be produced. One standard gas cylinder is sufficient for 6 cooldowns. For this reason an optional closed-cycle helium gas recovery system and storage tank is available for the liquid helium temperature systems. With the recovery compressor and tank, the consumption of helium is limited to losses on inserting and removing sample holder tubes. These losses are very small and only require that the recovery tank be topped up annually.

In implementing the dip tube access and safety interlock system some difficulties were encountered with the components we tested initially. The pressure sensitive switch, safety relief valve and helium gas supply regulator must all operate within very narrow, non-overlapping bands of pressure. If the regulator "creeps" at zero flow, the helium pressure will rise and gas will be lost through the relief valve. Additional problems are related to hysteresis in the pressure sensitive switch and safety relief valve. After testing several alternatives, we found that components with a large pressure sensitive area (large diameter) had the

least hysteresis. The initial difficulties were resolved by using good quality, large diameter components.

No accidents have occurred in our experience. On one occasion when the safety interlock was intentionally bypassed, a sufficient quantity of frozen air accumulated to prevent lowering the sample holder tube. A special jig was used to uneventfully remove the frozen plug on this occasion. The jig consists of a length of copper tube attached with a flexible rubber hose to a helium supply bottle. It is used by setting a moderate flow rate of room temperature helium through the tube and then lowering the copper tube into the dip tube well and slowly melting the plug from the top down. This allows the frozen plug to be removed without warming the liquid helium underneath.

CONCLUSIONS

After several years of experience building and operating dip tube access, closed-cycle cryocooler systems, we have found that they offer the ease and speed of use of conventional helium cryostats and the convenience of closed-cycle cooling. Our systems are designed with particular attention to safety and are fully protected against accidental plugging of the helium gas vent line. No accidents have occurred.

The four safety components of our systems are: (1) safety relief over-pressure vent valve on the dip tube well; (2) display of the pressure of the dip tube well; (3) electrical pressure sensitive switch connected to an interlock which will automatically switch off the cryocooler in the event that an over-pressure of helium gas is not maintained in the dip tube well; and (4) safety relief over-pressure vent valve on the vacuum space. It is recommended that, as a minimum safety requirement, all builders of such systems incorporate the above four safety features.

ACKNOWLEDGMENTS

We are grateful for assistance and advice from Prof. Suso Gygax and Ken Myrtle. Financial support from the Science Council of British Columbia and the National Research Council, Canada, is gratefully acknowledged.

REFERENCES

(1) Schnapper, C. - "Condensation of Air in the Venting System of a Liquid Helium Cryostat" to be published by Butterworth Scientific Ltd., U.K. in the Proceedings of the Twelfth International Cryogenic Engineering Conference (ICEC 12), 1988 July 12-15, Southampton, U.K.

(2) Winter, C. and Gygax, S. - "Closed-Cycle Liquid Helium Dip Cryocooler" published in the proceedings of the 4th International Cryocooler Conference (Cryocooler-4), 1986 September 25-26, Easton, Maryland, U.S.A.

EXERGY ANALYSIS OF A CRYOGENIC HYBRID REFRIGERATOR

John E. Ahern
EXTECH
P.O.Box 1323, Glendora, CA 91740

I INTRODUCTION

The exergy method is a realistic and effective means of determining the distribution of the irreversible losses associated with the entropy production in an energy related system. These irreversible losses are a significant cause of the low efficiencies and high power requirements for cryogenic systems. The recognition of this problem led to the use of staged systems by early users of exergy (Trepp,ref 1) and the irreversible production of entropy (Ball, ref 2). These papers showed the benefit of second law thermodynamic analysis of cryogenic systems although they did not examine the detailed system losses which is required for a system performance improvement analysis. A book and paper by the author (refs. 3,4) and a book by Brodyanskii and Semenov (ref. 5) used the exergy method to examine the second law characteristics of cryogenic systems, but there has been little else published on the engineering applications of the second law analysis for cryogenic systems despite the need for improved efficiency and lower power requirements for many applications. This is especially true for complex systems with multiple components and fluid circuits.

This paper discusses the application of the exergy method to cryocooler systems. The technique of using the exergy method is presented using 1 and 3 stage examples.

II EXERGY ANALYSIS

A. FUNDAMENTALS

A recent discussion of the exergy method (ref.6) concluded that it is now fully developed for use in the analysis of real engineering systems. The exergy method is based on the second law of thermodynamics and has developed in two distinct paths. One path has restricted its focus on only thermal aspects of energy conversion and maintains strict adherence to the classical thermodynamic principles. One feature of classical second-law thermodynamics is that a reversible process is an equality defined by $dS = dQ/T$ and capable of direct analysis. On the other hand, any process where dS is greater than dQ/T is an inequality and not capable of direct definition and calculation. The other development

path, involving applied engineering, has extended the basic thermodynamic principles to include all types of energy losses as compatable equalities. This is done by equating the irreversible losses in a process to values of the irreversible production of entropy in the process. This applied engineering approach of the second law of thermodynamics is most useful for performance analysis of real energy-related systems, while the classical second law principles limit the quantitative analysis to ideal, reversible processes and systems. The modifications made to the classical second law of thermodynamics in developing the applied engineering concept of exergy were accomplished with full technical justification since they are logical extensions of the basic principles.

One clear basis for the integration of all types of energy into a single, simple analytical method is the use of a common factor...the irreversible production of entropy as developed by Tolman and Fine at Caltech (ref. 7). They developed equations for the irreversible production of entropy in heat flow, fluid flow, electrical flow and thermoelectric circuits. The integration of the irreversible production of entropy concept with the zero-exergy reference state of the basic exergy method provides a simple, quantitative analytical approach to evaluating complex energy-related engineering systems. The second law of thermodynamics can be expressed by equation 1 which equates the increase of entropy in a system. The first term on the right is the entropy change from mass transfer, the second term is that due to heat transfer and the final term is that from irreversible effects. This entropy production equation is converted to the basic exergy equation by relating the entropy changes to a reference state.

$$\Delta S = \sum_M S_M + \sum_N \frac{Q_N}{T_N} + \Delta S_{IRR} \qquad [1]$$

$$EH = \sum_M [H_M - T_0 S_M] + \sum_N \frac{T_N - T_0}{T_N} Q_N - T_0 \Delta S_{IRR} \qquad [2]$$

MASS TRANSFER TO EXTERIOR — HEAT TRANSFER TO EXTERIOR — INTERNAL IRREVERSIBILITY

H=ENTHALPY S=ENTROPY Q=HEAT FLOW EX=EXERGY
SUBSCRIPT 0 INDICATES REFERENCE CONDITION

The ability to equate the losses throughout an energy intensive system is of particular importance for cryogenic systems where the irreversible losses can have a very

significant impact on system efficiency as the refrigeration load temperature is reduced toward absolute zero.

The value of the Carnot specific work for a single stage increases rapidly with lower cryogenic load temperatures. The point that is generally missed in the application of the second law is that each and every irreversible loss in the system is multiplied by the specific work factor associated with its temperature to determine its impact on the input work. In other words, each irreversible loss at a given temperature is equivalent to a cooling load of the same magnitude at that temperature. This is the primary reason for the very low (<10%) overall efficiencies associated with cryogenic systems. These irreversible losses are caused by heat that is transferrred and pressure that is reduced without producing useful work. The losses also include those involving no-work mass transfer between temperature and pressure zones within the system as well as between the system and its surroundings. Mechanical and viscous flow losses are also involved.

The irreversible losses in a system can be determined by calculating the irreversible production of entropy for each process in the system or between the system components and the surrounding environment. The values of the irreversible production of entropy which are determined in an entropy balance of a system (equation 1) are useful in establishing the relative magnitudes of the irreversible losses in the system. However, these entropy change values can not be directly compared to the input and output work of the system which is desirable for a full unnderstanding of the system performance characteristics. For example, a reduction in entropy production by improving a component performance can not directly show the impact on the input power and the efficiency.

The irreversible losses in the system are converted into work terms in the exergy method of analysis (equation 2). The exergy method determines the total exergy (or available work) at each station in a system between the processes so that the total exergy change in a process or component is provided. All of the exergy change in a process or component must be accounted for by the useful input or output work and the individual dissipative losses from friction,heat leaks,mass leakage,etc. A general exergy equation comprised of most common dissipative losses in energy systems is given in equation 3. The terms on the right side of this equation would be selected for the particular conditions at the station being evaluated. In most cases only two or three terms would apply. In any case, the calculation of the exergy and exergy loss values in a system are not major tasks once the first law heat balance data are available.

It should be pointed out that the exergy analysis does not replace the conventional first law heat balance of a system or the performance and design analysis required in the design

GENERAL EXERGY EQUATION

$$\text{EXERGY} = (I - I_o) - T_o (S - S_o) + \frac{P_o}{J}(V - V_o) +$$

INTERNAL ENERGY — ENTROPY — P/U WORK

$$+ \frac{U^2}{2gJ} + (Z - Z) \frac{g}{g_o J} + \sum (m_o - m_o) N_o +$$

KINETIC ENERGY — GRAVITY — CHEMICAL

$$+ e_i A_i F_i \sigma (3T^4 - T_o^4 - 4T_o T^3) + \ldots\ldots \qquad [3]$$

RADIATION — SUBSCRIPT O REFERS TO THE REFERENCE CONDITION

and development of components. It is an additional tool for the system analyst to use in the search for the best system to meet the application requirements.

The results of an exergy analysis can be best displayed in tables that show the magnitude, location and cause of each significant irreversible loss in the system and by schematic diagrams that show the magnitude and location of the exergy more graphically. In some reports the exergy analysis results are shown by flow lines where the line width depicts the magnitude of the exergy flow. This display becomes cumbersome and confusing for complex systems and has little advantage over diagrams showing only the component and process losses since it is the magnitude and location of the exergy losses that are important in system performance evaluation.

B. METHODOLOGY

The procedure for performing an exergy analysis of a system is described in the flow chart in Fig. 1. The first step is to collect and tabulate the data available at each station in the system from the first law heat balance which is the conventional method of system performance analysis. The first law heat balance results usually include the pressure, temperature, enthalpy and mass flow of the fluid streams throughout the system. The additional information required to perform an exergy analysis is the entropy value at each station and these same properties for the surrounding medium. Entropy values are tabulated for most cryogenic working fluids in handbooks and other publications (ref. 8).

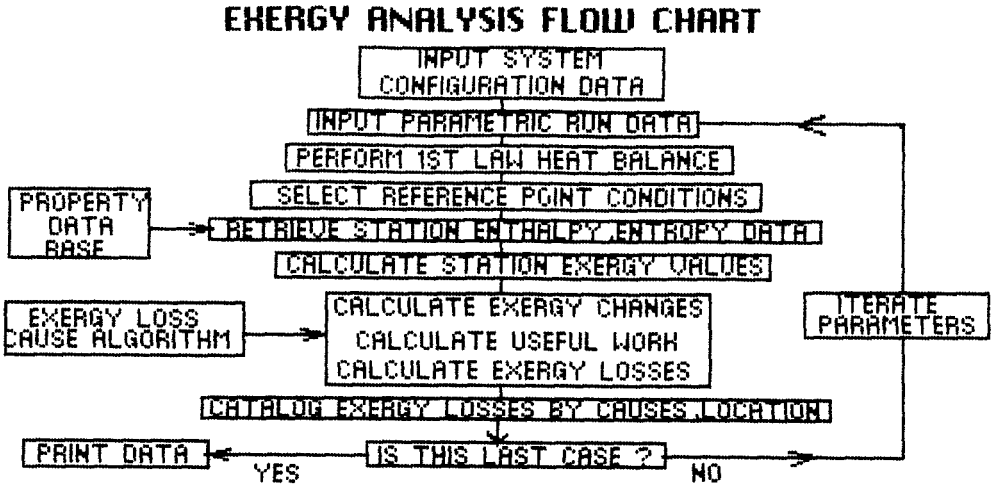

FIGURE 1

To illustrate the procedure used in an exergy analysis a simple example is taken for which the schematic is shown in Fig. 2 and the operating conditions of pressure, temperature, enthalpy and entropy for each station are given in Table 1. The first three columns contain data that would be available from a first law heat balance. The entropy values in the fourth column are determined from tables or charts using the pressure and temperature values. To complete this table of station properties the values of exergy are calculated and entered into the fifth column.

A primary feature of the exergy method is that the work available at the different stations in the system are referenced to a single " dead state" condition in which the exergy value is taken as zero. For terrestrial systems this zero exergy state is usually taken as the ambient temperature and pressure. This reference state is a tool to simplify the second law analysis. Since the difference in exergy values between stations in the system is the major factor in the analysis, the specific value of the reference state condition is not critical. In spacecraft cryogenic systems this reference condition should ideally be the deep space heat sink where the exergy losses in the heat rejecting radiator are included (ref. 9). However, for cryocooler exergy analysis it is more convenient and justified to use the heat rejection radiator temperature conditions.

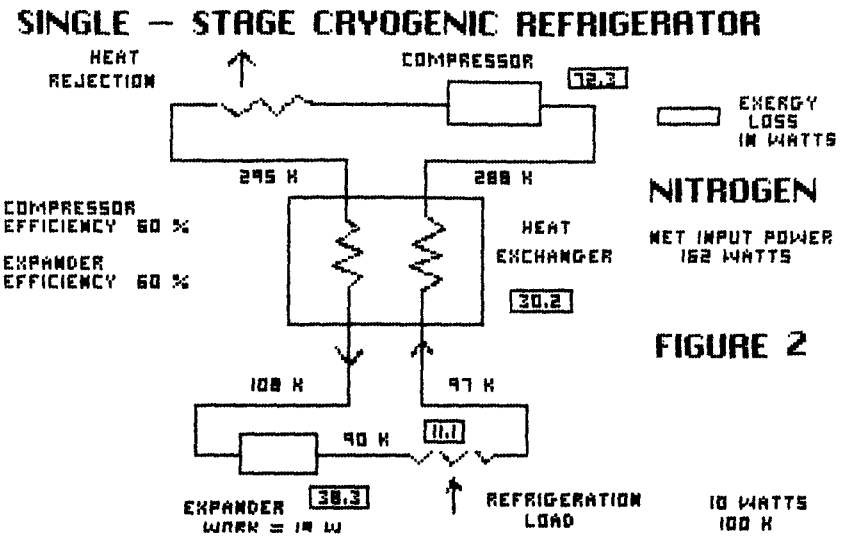

The basic equation for calculating the exergy at a station i in this system where a simple working fluid (nitrogen gas) is used is

$$EH_i = M\left[\left[h_i - h_o\right] - T_o\left[s_i - s_o\right]\right] \qquad (4)$$

where the subscript 0 refers to the reference state. The derivation of this equation from fundamentals is given in reference 3. The values of exergy for the conditions in Table 1 are calculated using equation (4) and are shown in the last column in the table. All values are rounded off for clarity.

Table 2 shows the total exergy change between the stations in the system and the separate work and exergy loss values. The columns on the right tabulate the irreversible exergy losses. The exergy losses entered into the columns at the right part of Table 2 are calculated from the irreversible production of entropy caused by the individual losses. The types of exergy losses and the number of these columns will vary as a function of the complexity, size and degree of sophistication of the system and the analytical goals.

The exergy changes in the compressor are divided into the input work and the total exergy loss from friction, fluid turbulence and bearings. This exergy loss generally is not further separated into individual losses in a system analysis but would be in a component design analysis. The heat exchanger exergy change is 100% losswhere no work is entered or removed from the component. The total heat exchanger exergy loss is comprised of those due to temperature difference between the fluid streams and the viscous pressure drop in the fluid streams. The exergy change in a Joule-Thomson expander

is a complete loss since the process is isenthalpic and no work is produced while entropy is produced. The magnitude of the exergy loss in a J-T expansion is a strong function of the temperature at which the expansion occurs. Precooling the working fluid to lower temperatures will reduce the J-T actual exergy loss but this is partly compensated by the additional work introduced at the higher temperature level to perform the precooling.

Table 1 PROPERTIES TABLE

STATION	PRESSURE ATM	TEMPERATURE DEG K	ENTHALPY J/GM	ENTROPY J/GM K	EXERGY J/GM
A	5	295	456.1	3.923	140.8
B	5	107.6	254.6	2.844	257.6
C	2	90.3	240.5	2.940	215.3
D	2	97	247.9	3.018	199.7
E	2	288	449.4	4.173	60.5
REF	1	295	456.9	4.403	0

Table 2 EXERGY LOSS TABLE

STATION OR COMPONENT	EXERGY	EXERGY CHANGE	WORK	EXERGY LLOSSES MECHANICAL	HEAT TRANSFER	TOTAL
A	190.2					
HEX		157.8			15.1	15.1
B	348					
EXPANDER		57.2	-18.9	38.3		38.3
C	290.8					
LOAD		21 2	10		11.2	11.2
D	267.7					
HEX		188			15.1	15.1
E	81.7					
COMPRESSOR		108.5	89.6	72.3		72.3
A	190.2					
					TOTAL LOSSES	152.0

NET INPUT POPOWER = TLOSSES (152) + LOAD ((10) = 162 WATTS

III CRYOGENIC COMPONENT ANALYSIS

The individual losses in the system mechanical components, i.e. bearing loss, windage loss, shuttle loss, heat loss, mass leakage loss, and miscellaneous frictional losses are analyzed during the component design phase. The inclusion of these individual irreversible losses in a system analysis will depend on the desired degree of sophistication of the system analysis. Typical overall component efficiencies were used for the mechanical components in the examples in this paper.

The exergy analysis of the heat exchanger is a different situation since the idividual performance features of heat exchangers (heat transfer, pressure drop, longitudinal conduction) can be readily calculated using empirically derived data and the exergy losses can be specifically defined. Second law exergy analyses of heat exchangers that have been reported in the literature (ref. 10) point out the need to balance the pressure drop exergy losses with the heat transfer exergy losses for optimum heat exchanger performance. However, the minimum exergy loss in a heat exchanger component may not be the best for minimum system exergy loss because of the interacting effects of a component operating conditions on other components in the system. The sensitivity of a systems overall exergetic efficiency to the pressure drop/temperature difference ratio of a heat exchanger has not been adequately examined, but this could be a particularly important factor in cryogenic systems with expanders since both temperature difference and pressure drop effects are so significant.

Component optimization for minimum exergy loss (maximum performance) must be performed within the overall system requirements as dictated by the system criteria. Depending on the application, these system criteria can involve the total system power, cost, reliability, weight or volume or combinations of them.

IV CRYOGENIC SYSTEMS ANALYSIS

The 3 stage system analyzed in this paper is shown in Fig. 3 and is generally based on the performance parameters of the hybrid refrigerator described by Matsubara (ref. 11). A Brayton cycle replaces the Stirling cycle for the upper two stages since the Brayton cycle is more amenable to demonstrating the exergy method. The temperatures and operating conditions are given in Fig. 3 for this system. A station property table, similar to Table 1, for this system is too large for this paper as is the case also for the exergy loss table, Table 2. The system characteristics including the individual component exergy losses are shown in the system schematic, Fig. 4. This schematic shows the distribution of the component exergy losses and clearly indicates the components that are dominant in causing the high specific work requirements for system operation.

A summary of the work characteristics in this system is given in Table 3. The sum of all the work and exergy losses in the system, excluding the compressor, provides the base work load of the compressor. This load plus the compressor loss is then the input power to the compressor.

FIGURE 3 3 STAGE CRYOCOOLER DATA

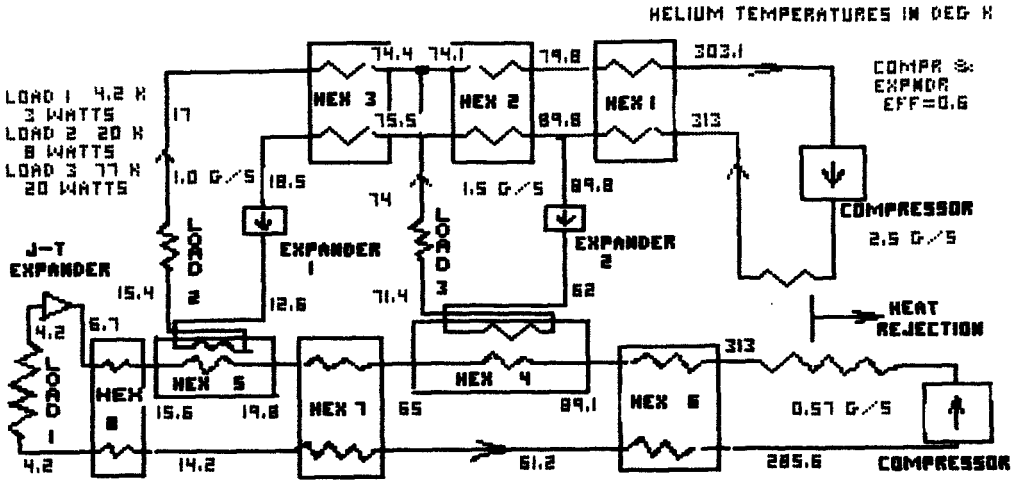

FIGURE 4 CRYOCOOLER EXERGY LOSS SCHEMATIC

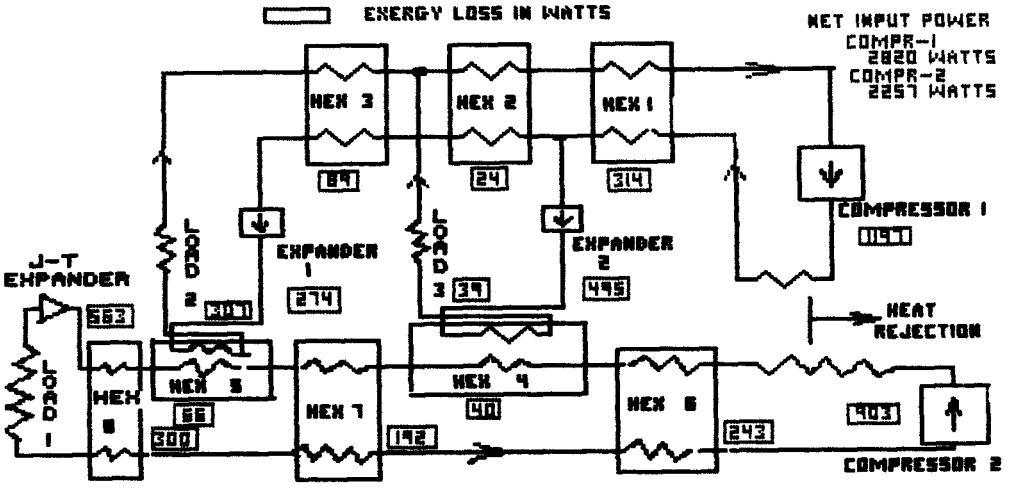

tABLE 3 EXERGY ANALYSIS SUMMARY

BRAYTON CYCLE	EX LOSS	WORK
HEX-1	314	
HEX-2	24	
HEX-3	89	
HEX-4	20	
HEX-5	33	
LOAD-2	307	8
LOAD-3	39	20
EXP-1	274	-29
EXP-2	495	-144
COMPR-1	1197	1796

J-T CYCLE	EX LOSS	WORK
HEX-4	20	
HEX-5	33	
HEX-6	243	
HEX-7	192	
HEX-8	300	
J-T	563	3
COMPR-2	903	1354

INPUT POWER	
COMPR-1	
1796/.6=2993	
EXPANDERS	-173
	2820
COMPR-2	
1354/.6=2257	

V SUMMARY

The exergy method of analysis is a tool that can provide the systems engineer with a view of the real losses throughout the system based on the first and second law of thermodynamics modified for real engineering systems. It allows losses due to the irreversible production of entropy to be directly and simply calculated with little effort beyond the first law heat balance.

The exergy method is fully developed for application to systems analysis. Its application is most suitable to complex systems involving multiple components and circuits since it tracks the degradation of the available work throughout the system. This information is important for optimal design and operation of complex systems.

REFERENCES

1. Trepp, C."Refrigeration Systems for Temperatures Below 25K With Turboexpanders", Advances in Cryo. Engrg.,Plenum,NY,1961.

2. Ball, W."Freon Cascade Refrigerator for Liquid Air Plant Precooler", Advances in Cryo. Engrg.,Plenum,NY,1960.

3. Ahern, J. The Exergy Method of Energy Systems Analysis, Wiley-Interscience, John Wiley & Sons, NY, 1980.

4. Ahern J.,"Applications of the Second Law of Thermodynamics to Cryogenics-A Review", Energy,Vol. 5,Pergamon Press, 1980.

5. Brodyanskii, V. & Semenov, A., Thermodynamic Fundamentals of Cryogenic Engineering, Energiya, Moscow, 1980 (in Russian).

6. Brodyanskii, V.M., "The Exergy Method and the Prospects of its Growth", Teploenergetica, No. 2, 1988 (in Russian).

7. Tolman,R. & Fine,P., "On the Irreversible Production of Entropy", Rev. Mod. Phys., 10,1,1948.

8. Thermodynamic Properties of Refrigerants,ASHRAE,1969

9. Petela,R., "Exergy of Heat Radiation",ASME J.Heat Transfer, May, 1964.

10. Bejan, A., "A Second Look at the Second Law",Mech. Engr., May 1988.

11. Matsubara, Y.,"Recent Cryocooler Progress in Japan", 3rd Cryocooler Conf., Sept. 1984.

SESSION VIII

STIRLING REFRIGERATORS II

CHAIRPERSON: Y. ISHISHIZAKI
VICE CHAIRPERSON: T. NAST

ALTERNATIVES TO THE QUASI-STEADY FLOW DESCRIPTION

John Hess
Mark Kushnir

Racah Inst. of Physics, The Hebrew University, Jerusalem 91904, Israel.
ICE Cryogenic Engineering, Ltd., P.O.Box 452, Nes-Ziona, Israel.

I. Introduction

In a recent review paper by Seume and Simon[1] evidence is summarized for the existence of oscillating flow effects in tubes, porous materials and corresponding Stirling engine heat exchangers/regenerators. Since Cryocoolers use helium gas usually far removed from the critical temperature of 5.26 K the perfect gas law holds for the cryocooler working fluid. Thus engine results should apply to cryocoolers. There are differences in the values of kinetic viscosity and kinetic Reynolds number between engines and cryocoolers due to different operating parameters. These differences do not however alter the conclusion that in cryocooler regenerators instabilities or large bounded fluctuations are ruled out according to normal criteria.

Still Seume and Simon quote experimental results by Kim [2,3] which show that in regenerators steady-flow friction factors are exceeded by as much as 20%. More recently much larger increases in oscillatory friction factors are reported by the Argonne Reversing Flow Test Facility (RFTF) group[4,5]. Values of oscillatory friction factors 4 to 6 times larger than corresponding steady flow values are reported.

Since the operating conditions in regenerators are far removed from those which might be expected to give rise to instability or large bounded flow fluctuations, there seems to be a dilemma about what actually takes place in Stirling machine regenerators under oscillatory flow conditions. In a previous paper, (Seume and Simon (1986))[6] conclude that the use of quasi-steady correlations in Stirling machine heat exchanger/regenerator design is probably incorrect.

II. Unrestricted formulation of one dimensional Oscillating Flow Model

List of Greek Letter Notations

ν kinetic viscosiy of helium gas working Fluid in m^2/s
ρ density of helium gas in kgm/m^3

ω angular frequency in radians/s

η reduced unitless channel variable corresponding to coordinate variable y perpendicular to flow direction x. If width of channel is "a" then η =y/a

α Wormesley number. If "a" is channel width then $a = \alpha\sqrt{\frac{\nu}{\omega}}$

δ thickness of boundary layer for a thin plate see, section III

A very useful initial approach to the problem of oscillating flow using a one dimensional model has been given by Gedeon[7]. Seume and Simon[1] point out that in its original configuration the one dimensional model gives incorrect phase shifts of pressure drop and wall shear stress with respect to a section averaged effective mass flow velocity. We would like to point out that with a more general complex vector formulation, such as can be used in AC circuit theory, these restrictions can be removed.

Capital G in the equation numbers refers to equation numbers of ref. 7.

The one dimensional model of Gedeon (1986)[7] starts with the momentum equation

$$U_{yy} - U_t \frac{1}{\nu} = \frac{1}{\nu\rho} P_x \qquad \text{(G1)}$$

Subscripts refer to partial differentiation and P_x is a constant pressure gradient. Referring to a characteristic length "a" the dimensionless variable η = y/a is introduced and it is assumed that the real velocity U(x,y,t) takes the form

$$U = U_0 \text{Real}(f(\eta)e^{i\omega t}) \qquad \text{(G3)}$$

One restriction which will immediately be removed is to require P_x and U to both be real, which automatically puts them in phase. Another restriction which will be removed further on is to relax the total supression of the convective term $\vec{V}\cdot\nabla\vec{V}$ of the momentum equation. A

term of the form $\vec{a} \otimes \vec{U}$ (the product of two complex vectors, where the constant vector $\vec{a}$ represents a constant velocity gradient down the flow channel (Oseen approximation)) can be used to introduce a much needed additional length into the model.

To remove the phase restriction imposed by real velocity and real pressure gradient we let U of G3 (Gedeon equation 3) be represented by a complex vector $\vec{U}$. Geometrically $\vec{U}$ may be considered as a two dimensional cartesion vector in an x-y coordinate system with coordinates given by the pair (U_1, U_2) along the unit vectors $\vec{i}$ and $\vec{j}$. (i.e. $U = U_1\vec{i} + U_2\vec{j}$). $\otimes$ will represent complex vector multiplication. For example for the $\vec{a} \otimes \vec{U}$ term referred to above, the cartesian representation of the product is:

$$a \otimes U = (a_1, a_2) \otimes (U_1, U_2) = (a_1U_1 - a_2U_2, a_1U_2 + a_2U_1)$$

The above product could also be expressed in polar representation. The time dependent factor $e^{i\omega t} = (\cos\omega t, \sin\omega t)$, which occurs in all the $\vec{U}$ and $\vec{P}_x$ vectors of the generalized (G1) or (G24), divides out of all the terms of the linear equation leaving a combination of static vectors which retain fixed amplitudes and phases. The section averaged velocity $\langle U \rangle$ (G19) and acceleration $\langle U_t \rangle$ are then represented by static vectors $\vec{U}$ and $\omega\vec{j} \otimes \vec{U}$. With these remarks (G24) takes the compact form:

$$\frac{-\vec{P}_x}{\omega\rho} = \vec{U} \otimes \left(\vec{J} + \frac{2}{\alpha^2}\vec{S}\right) \qquad (1)$$

where α^2 is the squared Wormersley number. $\vec{P}_x$ and $\vec{S}$ correspond to the similar quantities of (G24). A justification for introducing new notation is that we now have two equations instead of one. In component form (1) gives

$$\frac{-P_x}{\omega\rho} = \frac{2}{\alpha^2}S_1U_1 - \left(1 + \frac{2}{\alpha^2}S_2\right)U_2 \qquad (2)$$

$$0 = \left(1 + \frac{2}{\alpha^2}S_2\right)U_1 + \frac{2}{\alpha^2}S_1U_2 \qquad (3)$$

The complex vector $\vec{P}_x$ is taken as the real vector $(p_x, 0)$ and (2) corresponds exactly to (G24) if (G20) is written as

$$\langle U_t \rangle = -\omega U_o \mathrm{Imag}(\langle f \rangle e^{i\omega t})$$

(3) is the complex completion of (G24). $\vec{S}$ represents the complex oscillating-flow shear stress as in ref. 7

Contrary to the remark made in ref. 7, the steady-flow limit is not obtained simply from the limit $\alpha \to 0$. What is required is for $\vec{U}$ to be in phase with $\vec{P}_x$ so that $S_2 = -\alpha^2/2$. This may be seen from (1), (2) and (3) by inspection.

While in ref. 7 S is taken as complex there is no provision for a phase shift between mean velocity and applied pressure. The actual situation existing in cryocooler regenerators is that even at high frequencies the total pressure drop is essentially due to the frictional component of $\vec{S}$ [4,5] which is in phase with $\vec{U}$ but not necessarily with $\vec{P}_x$ as required in a one component theory. For regenerators then it is more convenient to take $\vec{U}$ as a phase reference and make it real and let $\vec{P}_x$ be an arbitrary complex vector.

According to ref. 4,5, S must be parallel to U so $S = s_o U$, where s_o is a scalor quantity with units s/m. Eqn. 1 then takes the form:

$$\frac{\vec{P}_x}{\omega \rho} = \vec{U} \otimes \left(\vec{\mathcal{I}} + \frac{2 s_o}{\alpha^2} \vec{U} \right) \qquad (4)$$

It is seen to be convenient, as has been done, to take $\vec{U}$ as a real vector and let $\vec{P}_x$ be rotated at some angle relative to $\vec{U}$. In cryocoolers representative values are

$\alpha^2 \cong 0.01$ and $|\vec{U}| \cong 1.0$ m/s so for significant phase shift to be observed $s_o < 0.1$ s/m where the units of s_o are one over velocity.

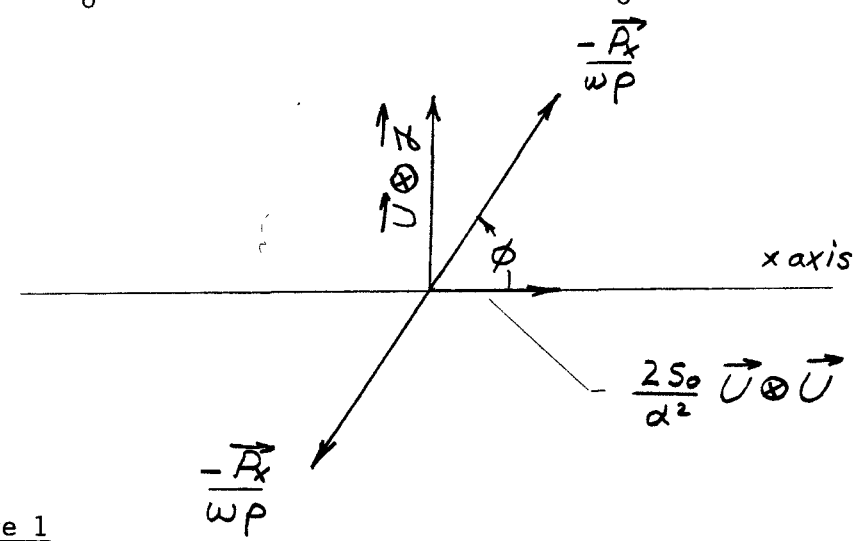

Figure 1

From figure 1 the angle between $\vec{U}$ and $-\vec{P}_x$ is determined from the expression (the common factor $\vec{U}$ divides out of the quotient):

$$\tan\emptyset = \alpha^2/(2s_o|\vec{U}|) \qquad (5)$$

Since reactive pressure drops through the regenerator are themselves relatively small $\emptyset$ may be largely detemined by the pressure drops in the heater and cooler which makes the rigid expression of eqn. 5 difficult to apply. To remove the constraint upon $\tan\emptyset$, an additional term, $\vec{b} \otimes \vec{U}$ (Oseen term), can be added to eqn. 4. Since $\vec{b}$ is a vector meant to be rotated (see Fig. 2) it is convenient to write $\vec{b}$ in the form $\vec{b} = b\,F(\emptyset)$ where b is the absolute value of $|\vec{b}|$ and $\vec{F}(\emptyset)$ is a unit vector pointing in the direction of $\vec{b}$. Because $\vec{F}(\emptyset)$ also represents a complex number, the product $\vec{F}(\theta) \otimes \vec{U}$ results in the vector $\vec{U}$ simply rotated by θ from its original direction. In cartesian representation $\vec{F}(\theta) = (\cos\theta, \sin\theta)$ and the complex product $(\cos\theta, \sin\theta) \otimes \vec{U}$ can be expanded to look like a rotation matrix acting upon $\vec{U}$.

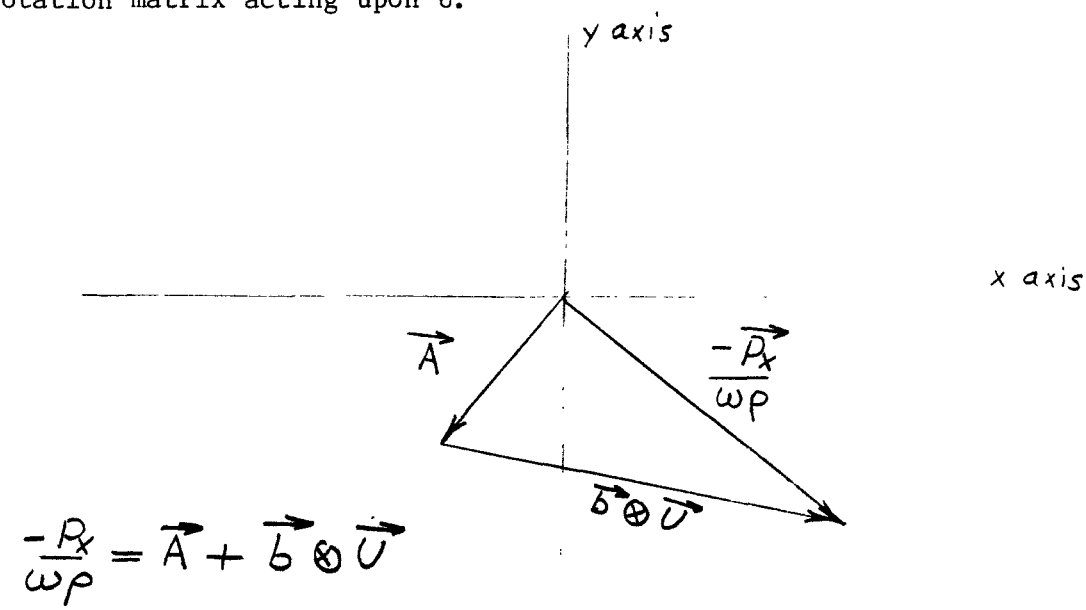

Figure 2

From Fig.2 it can be seen that for the angle between pressure gradient and mean velocity to be completely free it is required that

$$|\vec{U}|b > |\vec{A}| \text{ where } \vec{A} = \vec{U} \otimes \vec{j} + \frac{2s_o}{\alpha^2}\vec{U} \otimes \vec{U}$$

Finally, if (2) and (3) are solved for U_1 and U_2 in terms of S_1 and S_2 then two "Ohms law" type relations are obtained similar to the Ohms Law and the capacitor law used to derive the differential equation of say a series RC circuit. For the hydrodynamic case the differential equation is put into vector form and the resulting linear equations yield hydrodynamic

"Ohms laws" which correspond to V = IR and the capacitor law for AC circuits. For the AC circuit case the "Ohms laws" are first be put into vector form and then used to write down the differential equation. In both cases vector forms are a common or connecting link.

III. Hydrodynamics not Applicable to Regenerators

According to Jefferies[8] the theoretical justification for the boundary layer theory of Prandtl is that for distances large compared with $l = 2\sqrt{\nu t}$ from a vorticity source the vortex intensity is negligibly small (t is a characteristic time). This follows from the exponential solution of the Helmholtz equation which describes the diffusive motion of vortices in a viscous medium. If a value of t is determined from some characteristic length and velocity relating to a particular hydrodynamics problem then the vortex diffusion length is determined and gives the width of a boundary layer. For instance for a thin flat plate one defines the boundary layer thickness $\delta = \sqrt{x\nu/V_\infty}$ by taking $t = x/V_\infty$ where x is the distance along the plate and V_∞ a steady velocity far from the plate. The equation and solution of Blasius for the thin plate problem then follows from the substitution $\eta = y/\delta$ into the Prandtl boundary layer equations. y is the perpendicular distance from the plate. The validity of this type of solution in aerodynamics is known. In Schlieren photographs of supersonic flow in a wind tunnel the $\sqrt{x}$ dependence of δ is directly observable.

For steady flow in a closed channel at high Reynolds number one also speaks of a thin boundary layer of thickness δ. After passing from the channel wall through the boundary layer one enters into a central region of uniform velocity flow called "plug flow" in which there is negligible transverse velocity gradient.

Mathematically a thin laminar boundary layer may be described as a limiting vortex sheet which supplies a discontinuity in the flow velocity U at the channel surface. This is necessary for satisfying the rigorous U = 0 boundary value at the channel surface. The physical picture is that of vortices being constantly created or nucleated within the thin vortex sheet thus replacing vortices which are being constantly expelled by diffusion (described by the Helmholtz equation) into the uniform core where their intensity exponentially decreases.

If the flow is near a critical Reynolds number the vortices can diffuse out of the boundary layer with intensity sufficient to nucleate large bounded fluctuations or turbulance in the core flow. Above the critical Reynolds number the vortices diffuse out of the boundary layer with intensity sufficient to nucleate large flow fluctuations (turbulence).

The laminar boundary layer also plays a role in the description of

thermal advection for oscillating flow in a closed channel[9]. This can be the cause of a very efficient form of heat transport which in principle could produce large conduction losses in regenerators. In a cryocooler context the effect is most simply described as a type of "shuttle-loss" across the thin boundary layer. While the original mathematical formulation of this type of effect for the case of mass diffusion[10] made no committment to a thin boundary layer, cases of actual applications of the theory and experimental verifications[9] have all considered the boundary layer to be thin. It is often stated in the literature, probably correctly, that the effect is to be associated with thin boundary layers. In this case as pointed out in the next section the oscillating flow thermal advection effect has no relevance to oscillating flow in cryocooler regenerators. In a recent paper Siegel (1987)[11] has calculated the oscillating flow heat advection using a Darcy Law description of the regenerator flow. His formulas indicate again that the effect is negligible in regenerators of reasonable thermal effectiveness.

IV. Hydrodynamics applicable to Regenerators

If the regenerator of a crycooler operating between 300 K and 75 K is divided into two parts then a representative kinematic viscosity for the helium gas in the hotter half is 3.0×10^{-6} m^2/s and for the colder half is 1.5×10^{-6} m^2/s. For a 12 ms half period this then gives a vortex diffusion length ($l = 2\sqrt{\nu t}$) of $l_H = 0.40$ mm for the hot part and $l_K = 0.30$ mm for the cold part. A representative hydrodynamic diameter is about 0.05 mm. Thus in one half period vortices created in the regenerator space can fill up a cell in about 15% of the half period. Thus for about 85% of the half period the flow in a cell is fully developed in the sense that vortices completely penetrate the volume. This roughly means that for about 85% of the time the quasi-steady flow picture should be applicable and for about 15% of the time it is not since the vortex distribution has not reached a steady state.

The non-steady vortex distribution can hardly be considered as a form of hydrodynamic instability. However as flow accelerates in the "non-steady" portion of the cycle extra energy is required to create the vortex distribution characterizing the steady state which fills up an entire cell. Also counter rotating vortices remaining from the previous half cycle will absorb additional energy at this stage when interacting with the newly created vortices.

There may also be a steady non-perturbed vortex distribution in the neighborhood of a wire of mesh, similar to a wake. Oscillating flow enhances this effect as shown in Fig. 3 since flow occurring in two directions can produce "wakes" on both sides of an obstruction.

Both the above mentioned effects can result in pressure drops larger than that of the corresponding steady flow.

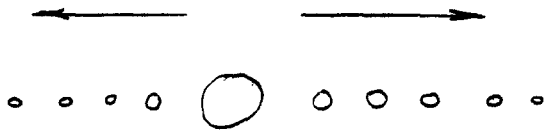

Figur 3. Wakes near an Obstruction. Arrows indicate the flow direction.

V. An experimental suggestion

It would seem that detailed calculation requires the authority of more experimental information. We wish to suggest the possibility of using the absorbtion of ultrasonic waves as a probe of the porous fluid filled regenerator structure. The ultrasonic absorbtion method is used in a variety of fluid filled consolidated or unconsolidated systems to determine elastic modulae or acoustic wave velocities[12]. It is possible that acoustic measurements on oscillating flows could produce real time information on the vortex distributions suggested in the previous section.

Acknowledgement

The authors would like to thank Shlomo Alexander, William Glaberson and Itamar Procaccia for helpful discussions and also Paul Roach and Joerg Seume for providing us with their reports and papers, in time for this paper.

REFERENCES

1. Seume, J.R. and Simon, T.W.(1987): "Flow Oscillation Effects in Tubes and Porous Material: Unresolved Issues". Proc. ASME Winter Annual Meeting, Boston, MA, December 1987, HTD-vol 93, pp 55-62.

2. Kim, J.C. (1970): "An Analytical and Experimental Study of Heat Transfer and Flow Friction Characteristics for Perdiocally Reversing Flow through the Porous Matrix of Thermal Regenerators". Ph.D Thesis, Mech. Eng. Dept., Purdue University.

3. Kim, J.C. (1973): "An Analytical and Experimental Study of Flow-

Friction Characteristics for Periodically Reversing Flow." ASME-paper 73-WA/FE-13.

4. Roach, P.D. (1986) "Reversing Flow Test Facility Technical Report". March 1986, ANL-CT-86-1 (Argonne National Laboratory Report)

5. Krazinski J.L., Holtz R.E., Uherka K.L., and Lottes,P.A.(1986): "An Analysis of Pressure Drops under Reversing Flow Conditions". Proc. 21st IECEC (1986), paper No. 869116, Washington: Am. Chem. Soc

6. Seume J.R., and Simon T.W.(1986): "Oscillating Flow in Stirling Engine Heat Exchangers". Proc. 21st IECEC, pp.533-538. Washington: Am. Chem. Soc.

7. Gedeon, David (1986): "Mean-Parameter Modeling of Oscillating Flow." ASME Journal of Heat Trans., vol. 108, pp. 513-518, August.

8. Jefferies, Harold (1930). "The Wake in Fluid Flow Past a Solid", Proc. Roy. Soc. A128, 376-393 (1930).

9. Kurzweg, U.H. and Ling de Zhao (1984) "Heat Transfer by high-frequency Oscillations: A new Hydrodynamic Technique for achieving large Effective Thermal Conductivities". Phys. Fluids 27 pp2624 (1984).

10. Watson, E.J., "Diffusion in Oscillatory Pipe Flow". J. Fluid Mech. 133, 233 (1983).

11. Siegel, R., "Effect of Flow Oscillations on Axial Energy Transport in a Porous Material. Trans of the ASME 109, 242 (1987).

12. Johnson, David Linton and Plona, Thomas J., "Acoustic slow waves and the Consolidated Transition" J. Acoust. Soc. Am. 72, 556 (1982).

TRANSFER LINE HEATING IN STIRLING REFRIGERATORS

Mark Hanes
Larry Sobel

Hughes Aircraft Company
Electron Dynamics Division
Thermal Products
Torrance, California 90509

ABSTRACT

The development of a high-power Stirling cycle refrigerator has revealed interesting phenomena associated with large volume transfer lines. A long, nearly adiabatic transfer line volume between the compressor heat exchanger and the regenerator can lead to thermal runaway in the gas temperature at the inlet to the regenerator. The problem is shown to follow from placement of the warm heat exchanger too far from the regenerator. Inadequate heat transfer area in the transfer line causes gas temperatures to increase dramatically in very short periods of time. A computer model is developed to account for the adiabatic transfer line and is used to compute fluid trajectories within the transfer line. Experimental results are presented with various configurations of heat exchangers and regenerator, and with transfer lines of various diameters.

INTRODUCTION

Until recently, Stirling cycle refrigerators were used primarily for low power, cryogenic applications. The development of a high-power Stirling refrigerator operating near room temperature uncovered problems which were not apparent on the cryogenic machines. One concern was how different locations in the system of the regenerator, heat exchangers, and transfer line would affect the performance. Since the performance of a Stirling machine is dependent on having small amounts of system dead volume, the size and location of the transfer line should have an affect on performance.

Tests were performed to determine the effects of having long transfer lines in the system. The transfer line was placed in various locations relative to the heat exchangers and regenerator. When the transfer line was located between the regenerator and the hot heat exchanger, the results were unexpected. These results are discussed in the remainder of the paper.

DISCUSSION

Test Setup

The refrigerator operates at 20 Hz with a charge of 550 psig helium. The swept volume of each piston is 21.2 cc and the piston motion is phased at 90 degrees. The dead volume of each heat exchanger core is 12 cc. The heat exchangers are helium to water, shell and tube type. The transfer line is 0.5 inch O.D. tubing with a total length of 28 inches and a volume of 67 cc. There is approximately 10 cc of remaining dead volume in the system. These volumes are shown schematically in Figure 1. This configuration results in an actual pressure ratio of 1.46, compared to a predicted isothermal value of 1.30.

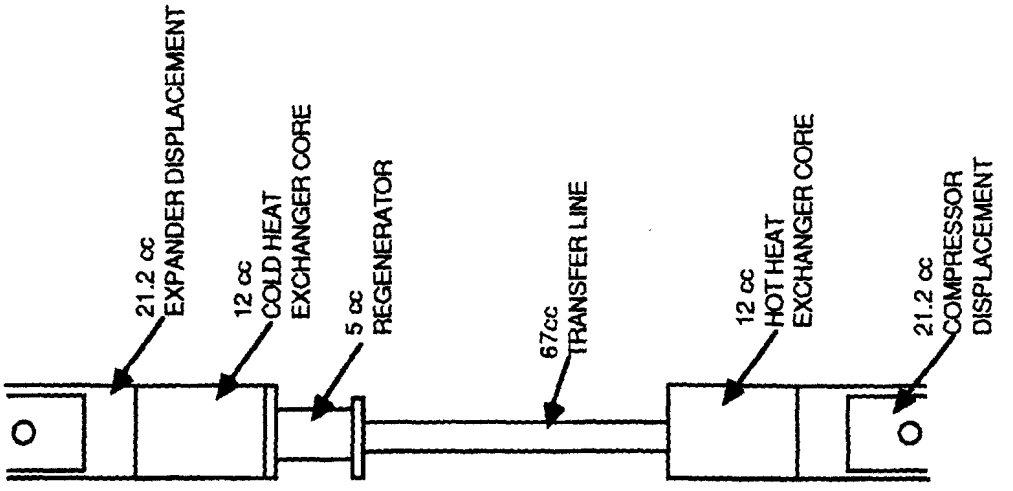

Figure 1 System volumes.

Initially, the transfer line was placed between one of the heat exchangers and its corresponding cylinder, so that gas enters and exhausts the regenerator directly into the heat exchangers as shown in Figure 2. The results of this configuration were as expected. The refrigeration was decreased because of the increased dead volume associated with the long transfer line. However, when the same length transfer line was moved between the regenerator and the heat rejection heat exchanger, as shown in Figure 3, the results were quite different. The transfer line temperature increased dramatically, and the refrigeration decreased further.

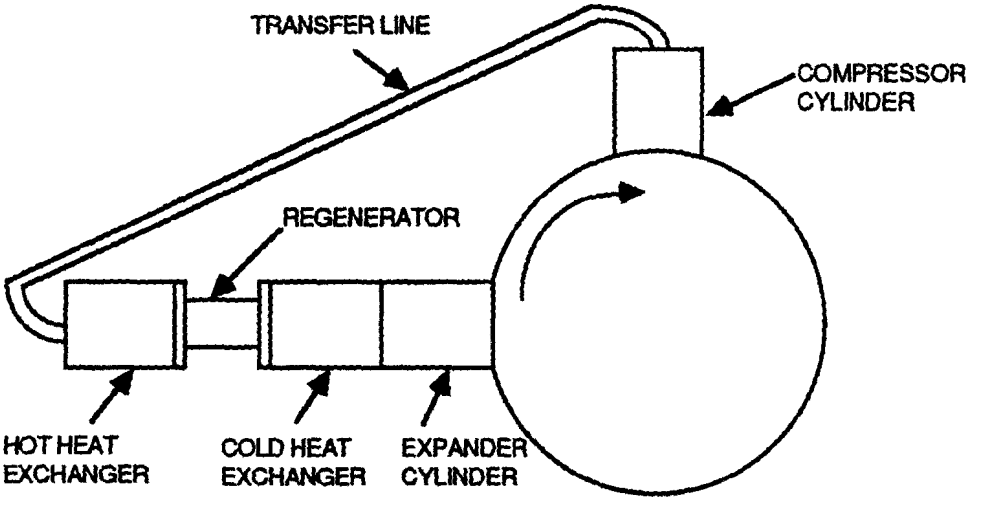

Figure 2 First configuration

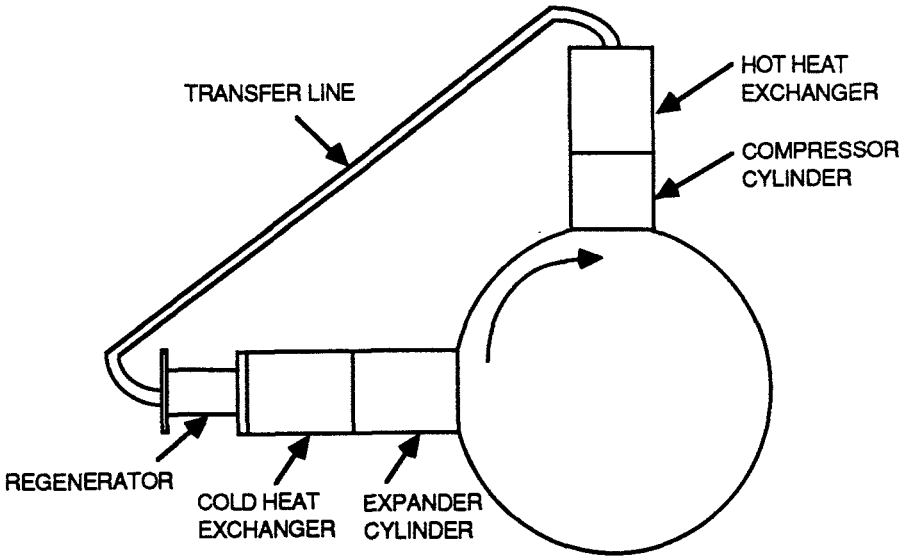

Figure 3 Second configuration.

With the refrigerator configured with the transfer line between the regenerator and the hot heat exchanger, as shown in Figure 3, tests were performed to determine the amount of heat rejected at the transfer line and in each heat exchanger during the transient phase when the refrigerator was first turned on. The heat transfer at the heat exchangers was determined by measuring the water flow rate and the temperature difference of the inlet and outlet. The heat rejected in the transfer line during the transient phase was determined by measuring the rate of temperature rise, and knowing the mass and specific heat of the various components.

Experimental Results

When the setup in Figure 3 was initially tested, the transfer line temperature did not reach a steady state before its temperature was too high to continue the test (>400°F). This temperature was attained in less than two minutes of operation. A water evaporating jacket was placed around the outside of the transfer line, which limited the transfer line temperature to 268°F. The hot side of the regenerator was not actively cooled, and its temperature reached 318°F at steady state.

Compilation of the temperature increase data taken from thermocouples placed along the transfer line and regenerator flange showed that the greatest amount of heat was rejected from the gas along a portion of the transfer line closest to the regenerator. This length corresponds roughly to the distance traversed by fluid exhausting the regenerator, which is determined by the piston swept volume. The total heat absorbed thermally by the structure and tubing was approximately 300 watts in this region. The cold heat exchanger provided a near constant 110 watts of refrigeration while the hot heat exchanger rejected 124 watts and the input power quickly steadied out to 283 watts. The heat balance was 393 watts into the system and 424 watts out of the system, a difference of 6.4 percent. The temperature profile of the system at steady state as a function of the system volume to displaced volume ratio is shown in Figure 4. Again, the large temperature gradient at the outlet of the regenerator indicates that most of the heat is being rejected in this region. It

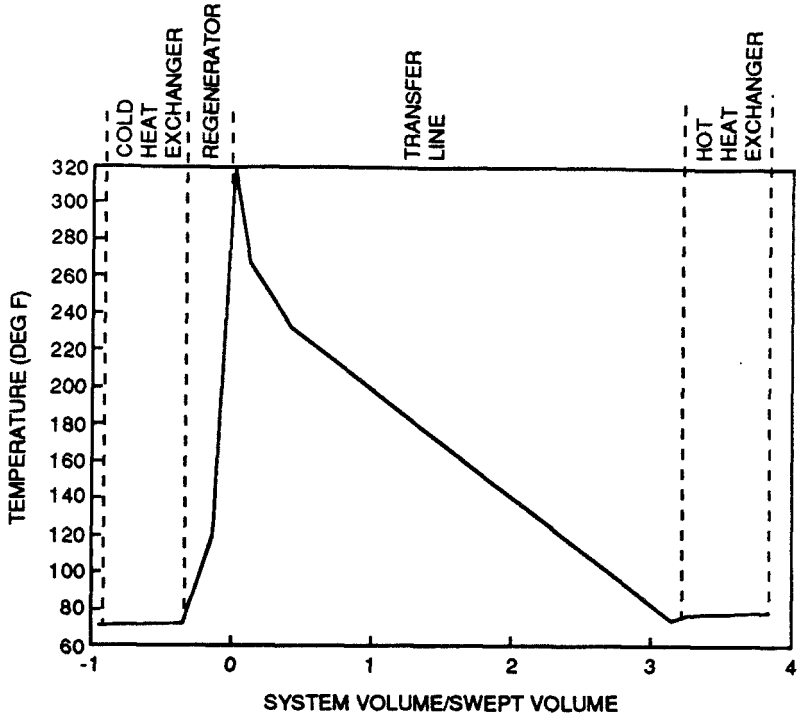

Figure 4 Steady state system temperature gradient.

was not possible to calculate an energy balance at steady state, because it was not possible to measure the rate of evaporization in the water jacket.

For comparison, when the system is operated with the same length transfer line located between either the hot or cold heat exchanger and the corresponding cylinder, as shown in Figure 2, the refrigeration is 230 watts, the heat rejected, 345 watts, and the input power, 144 watts, which are very acceptable results.

Since all volumes in each setup are equal, the reason for this difference in performance must be due to the location of the transfer line. When both heat exchangers are located next to the regenerator, the gas which passes through the regenerator will have an opportunity to give up its heat during compression to the water in the nearly isothermal heat exchanger. When the volume of the transfer line between the regenerator and the heat exchanger is large, gas which passes through the regenerator will not be displaced enough to enter the heat exchanger. Since the transfer line initially has a very poor heat transfer coefficient on the outside, this results in its temperature rising rapidly. As the temperature difference across the regenerator increases, the refrigeration decreases and the input power increases. Most of the heat rejected at the hot heat exchanger is from the adiabatic compression which occurs in the cylinder, followed by gas shuttling heat down the transfer line and conduction in the transfer line wall.

There is also a small amount of refrigeration present at the exit of the hot exchanger into the transfer line. This effect is most noticeable immediately after starting the refrigerator, before it is overwhelmed by the heat transfer down the transfer line by conduction and shuttle effects. This phenomenon will be discussed further in the next section.

Computer Simulation

A computer program was written using a lumped parameter model of the Stirling refrigerator to supplement the closed-form Schmidt analysis. Timewise integration of a set of differential equations makes it a simple matter to track fluid trajectories, and to track pressure drops and mass flows everywhere in the system. Fluid trajectories in the transfer line were calculated using Equation 1:

$$\frac{dx}{dt} = \frac{\dot{m}_{in}}{\rho A_{in}} - \frac{dp}{dt}\,\frac{x}{\rho RT} \qquad \text{Eq. 1}$$

where

dx = change in distance traversed in transfer line

dt = change in time

$\dot{m}_{in}$ = mass flow rate into transfer line

A_{in} = transfer line cross-sectional area

dp = change in pressure

x = distance traversed into transfer line

R = gas constant

T = temperature (assumed constant in transfer line)

ρ = gas density at x.

The temperature in this case is assumed to be the average bulk fluid temperature in the transfer line. The trajectories of fluid particles with paths beginning at several locations along the transfer line are shown in Figure 5. The particle trajectories are shown plotted with system pressure as the ordinate. In all cases, the trajectories are traversed in the clockwise direction. The first trajectory is for a particle originating near the outlet of the warm heat exchanger (0.05 on the normalized displacement). The second trajectory is for a particle originating 2/10 of the way down the transfer line, and the final trajectory begins at 7/10 of the way down the transfer line, and the fluid particle travels up to the inlet of regenerator. As expected, the distance each fluid particle travels is roughly equal to the displaced compression or expansion volume divided by the area of the transfer line. (The compression volume is 21 cc, while the transfer line volume is 67 cc.) Now, if we define a phase to be the relationship in degrees between the maximum system pressure and the maximum displacement of a fluid particle in each of the three transfer line regions shown, it is clear that the phasing between each trajectory and the system pressure wave varies as you move down the transfer line. In the first trajectory, the maximum system pressure

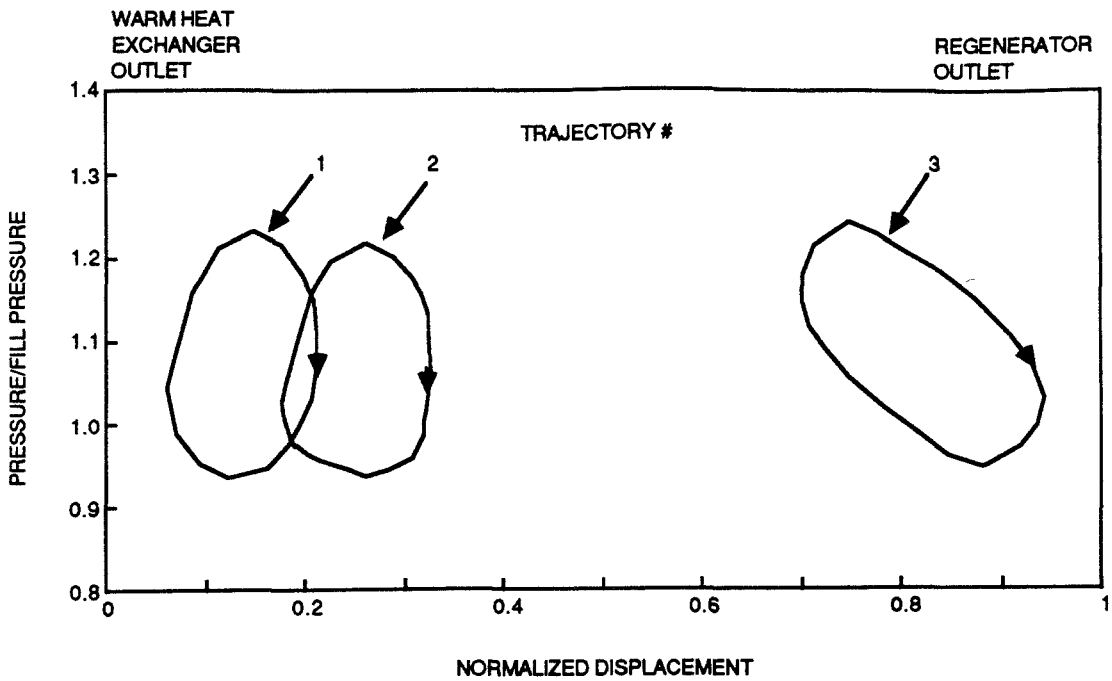

Figure 5 Particle displaced volume vs. pressure.

leads the maximum particle displacement by roughly 75 degrees. In the second trajectory, the lead is now 90 degrees. And at the regenerator end of the transfer line, the pressure now leads the displacement by 120 degrees. The areas enclosed within these trajectories are all equal, however, since the transfer line is assumed to be adiabatic and lossless. Since the phase of the trajectories necessarily changes along the length of the transfer line, the distance each fluid particle travels also changes. Roughly, one compressor displaced volume into the transfer line (curve 2 in Figure 5) the fluid trajectory is 90 degrees out of phase and the particle trajectory is the shortest.

The most significant result of these simulations is the confirmation that the hot fluid leaving the regenerator does not reach the warm-side heat exchanger. Since there is very little heat transfer area on the outside of the transfer line, the average temperature of the fluid in this region rises significantly before steady state is reached and performance suffers accordingly. (In the experiment described previously, with evaporative heat transfer on the outside of the transfer line, the average gas temperature at the regenerator outlet reached 318°F at steady state). The consequence of having such large volume separating the regenerator and the heat exchanger is that the warm heat exchanger is largely ineffective. One can imagine the trajectory of a wall of fluid which starts at the outlet of the warm side of the regenerator as representing a piston. This imaginary piston moves from the regenerator outlet back into the transfer line, a distance representing a volumetric displacement of the order of the compressor swept volume. The poor area-to-volume ratio within the transfer line, and the small surface area on the outside of the transfer line make this compression space nearly adiabatic with disastrous consequences on performance of the refrigerator.

Reducing the diameter of the transfer line, while keeping the length of line constant in order to shuttle more gas from the regenerator outlet to the warm heat exchanger,

increased the effectiveness of the warm heat exchanger but with a significant penalty. The increased pressure drop in the smaller diameter transfer line and the increased frictional heating far outpaced the performance increases resulting from higher pressure ratios and increased heat exchange in the compressor heat exchanger. It is interesting to note that pressure drop and frictional heating in the transfer line goes up dramatically with decreasing transfer line diameter. Since the pressure drop goes like $V^2 * l/d$ and the gas velocity in the transfer line goes inversely with d^2, if the friction factor is constant (flow is highly turbulent on average) the losses go like d^{-5}, in the laminar range, the losses would go like d^{-4}. Even in this refrigerator where transfer line losses are relatively insignificant, at 1/2 the diameter of the present transfer line, the effect of the small diameter clearly degrades overall system performance.

The fluid trajectories shown in Figure 5 also help explain another phenomenon that is characteristic of a Stirling refrigerator with a long transfer line separating the hot-side heat exchanger and the regenerator. As soon as the system is turned on, a very noticeable refrigeration effect takes place along a stretch of the transfer line on the outlet of the warm heat exchanger. Having a long transfer line has essentially created two inefficient refrigerators out of one, the coupling between the two being this gas piston mentioned earlier. The same way that fluid leaving the regenerator traverses about a third of the transfer line, fluid leaving the warm heat exchanger moves only about a third of the way towards the regenerator. The computer simulation shows that roughly a third of the way down the transfer line, fluid trajectories lag the pressure wave by 90 degrees. The fluid in this region is being compressed at the optimum phasing to produce some regeneration, a result noted in the previous section and clearly visible in the temperature drop at the outlet of the warm heat exchanger as shown in Figure 4. However, since the transfer line is not a very effective regenerator, there is only a very small refrigeration effect.

ATTENDANCE LIST

International Cryocooler Conference

August 18 & 19, 1988

Naval Postgraduate School
Monterey, CA

MR JOHN AHERN
EXTECH
738 PARKBROOK LN
GLENDORA CA 91740-0001
(818)963-8064

MR CHARLES J ARDUINI
MAGNAVOX GOVT & IND ELECTRONICS CO
46 INDUSTRIAL AVE
MAHWAH NJ 07430-0001
(201)529-1700

MR PAUL ASHLEY
HONEYWELL SATELLITE SYSTEMS DIV
19019 NORTH 59TH AVE
GLENDALE AZ 85308-0001
(602)561-3258

MR ZDENEK BACKOVSKY
ROCKWELL INTERNATIONAL
M/C SK21
2600 WESTMINSTER BLVD
PO BOX 3644
SEAL BEACH CA 90740-7644
(213)594-3759

MR GLENN H BALSCHUNAT
GENERAL ELECTRIC
M/S 350
FRENCH RD
UTICA NY 13503-0001
(315)793-6285

SANDRO BARBANERA
NATIONAL RESEARCH COUNCIL
VIA CINETO ROMANO 42
ROME ITALY -- 00156
(316)412-4851

MR JOHN BARCLAY
ASTRONAUTICS
MADISON WI

MR STEVEN BARD
JPL
4800 OAK GROVE DR
PASADENA CA 91109-0001
(818)354-4487

MR MARTIN BAREISS
AEG AKTIENGESELLSCHAFT
THERESIENSTR 2
7100 HEILBRONN FRG
-
07131-6212/81

MR FERNAND D BEDARD
DEPT OF DEFENSE
FT GEORGE G MEADE MD 20755-6000
(301)859-6555

MR W REED BEINAR
CARELTON TECHNOLOGIES INC
SEN SALES ENGR
STE 900
300 ESPLANADE DR
OXNARD CA 93030-0001
(805) 988-2947

BECKY BENEDICT
BALL AEROSPACE SYSTEMS GROUP
PO BOX 1062
BOULDER CO 80306-0001
(303)939-4794

MR BASCOM W BIRMINGHAM
BIRMINGHAM ASSOCIATES
5440 WHITE PLACE
BOULDER CO 80303-0001
(303)442-1248

MR LEON BLEDJIAN
AEROSPACE CORP
M4-916
2350 EAST EL SEGUNDO BLVD
EL SEGUNDO CA 90245-4691
(213)336-6895

MR EARL BRALEY
LEYBOLD INC
1860 HARTAG DR
SAN JOSE CA 95131-0001
(408) 436-2828

MR R WARREN BRECKENRIDGE
ARTHUR D LITTLE INC
ACORN PARK
CAMBRIDGE MA 02140-0001
(617)864-5770

MR JEFFREY A BRUNING
AIR FORCE TECHNOLOGY CENTER
HQ AFSTC/SWS
KIRTLAND AFB NM 87117-6008
(505)846-5790

MR D SCOTT BUCHANAN
BROMAGNETIC TECHNOLOGIES INC
4174 SORRENTO VALLEY BLVD
SAN DIEGO CA 92121-0001
(619)453-6300

MR DAN J BUCKLEY
NAVAL WEAPONS CENTER
CODE 3621
MISSILE SYSTEMS BRANCH
CHINA LAKE CA 93555-0001
(619)939-1686

MR WILLIAM W BURT
TRW INC
M/S 01-2060
1 SPACE PARK
REDONDO BEACH CA 90278-0001
(213)535-1859

MR ROD BYRNS
LAWRENCE BERKELEY LAB
2457 MARIN AVE
BERKELEY CA 94708-0001
(415)486-5109

MS CHRISTINA L CAIN
US AIR FORCE
AFWAL/FIEE
WRIGHT PATTERSON AFB OH 45433-65
(513)255-6078

MR DENIS CARRIER
NPS STUDENT
21 GLEN LAKE DR
PACIFIC GROVE
MONTEREY CA 93950-0001

MR STEPHEN H CASTLES
NASA/GSFC
GODDARD SPACE FLIGHT CTR
CODE 713
GREENBELT MD 20771-0001
(301)286-8986

MR CHUNG K CHAN
JPL
4800 OAK GROVE DR
M/S 183-901
PASADENA CA 91109-0001
(818)354-2777

MR FANG C CHEN
MARTIN MARIETTA ENERGY SYS
GROUP LEADER
PO BOX X
OAK RIDGE TN 37831-6070
(615) 574-0712

MR WILLIAM E CHEN
GE MAGNET SYTEMS
3001 W RADIO DR
FLORENCE SC 29501-0001
(803)664-1660

MR CHUCK CHRISTENSEN
CARLETON TECHNOLOGY INC
PO BOX 28
E AURORA NY 14052-0001
(716)687-4610

MR ALAN F CLARK
OFFICE OFNAVAL RESEARCH
LONDON
PO BOX 39
FPO,NY
UNITED KINGDOM -- 09510
44-1-409-4413

MR JOHN L CLARK
CRYO-TEK CORPORATION
8527 PHOENIX DR
MANASSAS VA 22110-0001
(703) 836-1717

MR CHARLIE R CLASS
MARTIN MARITTA DENVER ASTRONAUTICS
M/S DC4460
PO BOX 179
DENVER CO 80201-0001
(303) 971-9281

MR FREDERICK J COGSWELL
MASSACHUSETTS INST OF TECH
BLDG# NW17-281
CAMBRIDGE MA 02139-0001
(617) 253-7627

LESLIE COHEN
INSTITUTE FOR DEFENSE ANALYSES
1801 N BEAUREGARD ST
ALEXANDRIA VA 22311-0001
(703) 578-2994

MR RICHARD M COLGATE
COLGATE THERMODYNAMICS CO
14 NASSAU ST
PRINCETON NJ 08542-0001
(609) 921-8770

MR EUGENE C CRITTENDEN
NAVAL POSTGRADUATE SCHOOL
CODE 61 CT
MONTEREY CA 93943-0001
(408) 646-2855

DR J ALAN CRUNKLETON
MASSACHUSETTS INST OF TECH
OFFICE 41-208
CAMBRIDGE MA 02139-0001
(617) 253-2273

MR PETER W CURWEN
MECHANICAL TECH INC
968 ALBANY-SHAKER RD
LATHAM NY 12110-0001
(518) 785-2285

MR JEFFREY D DALTON
NAVAL WEAPONS CTR
MISSILE SYS BRANCH CODE 3621
CHINA LAKE CA 93555-0001
(619) 939-1694

MR RONALD J DE PUTTER
PHILIPS USFA BV
MEERENAKKERWEG 1
EINDHOVEN
NETHERLANDS - 5600 MD
(0) 40-722951

MR ANTHONY DEGREGORIA
ASTRONAUTICS TECH CTR
5800 COLLEGE GROVE ST
MADISON WI 53716-0001
(608) 221-9001

MR PETER F DOHERTY
GENERAL PNEUMATICS CORP
STE 349
8351 ROSSWELL RD
ATLANTA GA 30350-0001
(404) 396-4423

MR ANTON R DORR
DEPT OF DEFENSE
UNIT 2A
2032 ROYAL FERN CT
RESTON VA 22091-0001
(703) 733-5170

MR EDGAR A EDELSACK
GEORGETOWN CRYOGENIC INFO CTR
3530 W PLACE NW
WASHINGTON DC 20007-0001
(202) 337-5076

MR WOODY R ELLISON
GENERAL PNEUMATICS CORP
STE 107
7662 E GRAY RD
SCOTTSDALE AZ 85260-0001

MR MICHAEL FENNELL
ENERGY SCIENCE LABS
PO BOX 85608
SAN DIEGO CA 92138-0001
(619) 455-4688

MR PETER J FRASSO
VARIAN ASSOCIATES
VACUUM PRODUCTS DIV
3560 BASSETT ST
SANTA CLARA CA 95054-2704
(408) 496-2269

T H K FREDERKING
UNIVERSITY OF CALIFORNIA LA
BH 5405 CH E SEAS UCLA LA
LOS ANGELES CA 90024-0001
(213) 825-2491

MR VENKATARAO GANNI
KOCH PROCESS SYSTEMS INC
20 WALKUP DR
WESTBOROUGH MA 01581-0001
(508) 898-0380

MR STEVEN L GARRETT
NAVAL POSTGRADUATE SCHOOL
PHYSICS DEPT
CODE GIGX
MONTEREY CA 93943-0001
(408) 646-2540

MR CHARLES D GLENN
GLENN CO
1610 MANTON CT
CAMPBELL CA 95008-0001
(408) 378-0570

MR DAVID R GEDEON
GEDEON ASSOCIATES
16922 SOUTH CANAAN RD
ATHENS OH 45701-0001
(614) 592-5166

MR CRAIG S GOLART
US AIR FORCE
AFWAL/FIEC
WRIGHT-PATTERSON AFB OH 45433-0001
(513) 255-4853

MR PETER E GIFFORD
CRYOMECH INC
1630 ERIE BLVD EAST
SYRACUSE NY 13120-0001
(315) 475-9692

MR DAN GOLDBLATT
UCSB ENGRG
278 ELLWOOD BEACH DR #3
SANTA BARBARA CA 93117-0001
(805) 968-4068

MR GEORGE F GIGGEY
RAYTHEON CO
55 BEARFOOT DR
NORTHBORO MA 01532-0001
(617) 393-7300

MR GEOFFREY F GREEN
DAVID TAYLOR RESEARCH CTR
CODE 2712
ANNAPOLIS MD 21402-5067
(301) 267-2149

MR ADRIAN GLASS
THORN EMI ELECTRONICS LTD
ELECTRO OPTICS DIV
1 FOREST RD
FELTHAM MIDDX UK TW13 7HE
(01) 751-6464

MR WILFRED J GULLY
GM HUGHES ELECTRONICS
2999 LOMITA BLVD
TORRANCE CA 90505-0001
(213) 517-5664

MR ALEXANDER P GLASSFORD
LOCKHEED CORP
B556 0/59-40
1111 LOCKHEED WAY
SUNNYVALE CA 94089-0001
(408) 756-7119

PROF D HANS-DIETER HAHLBOHM
PHYSIKALISCH-TECHNISCHE
BUNDESANSTALT INST BERLIN
ABBESTRASSE 2-12
D 1000 BERLIN 10 (WEST) GERMANY
(030)3481-276

MR MARK HANES
HUGHES AIRCRAFT CO
3100 LOMITA BLVD
TORRANCE CA 90505-0001
(213)517-6771

MR JOHN H HESS
HEBREW UNIVERSITY OF JERUSALEM
GIVAT RAM CAMPUS-PHYSICS DEPT
JERUSALEM ISRAEL 91905
-
972-2-584744

KELLY W HEDEGARD
GENERAL PNEUMATICS CORP
STE 107
7662 GRAY RD
SCOTTSDALE AZ 85260-0001
(602) 998-1856

MR THOMAS J HOFLER
NAVAL POSTGRADUATE SCHOOL
MONTEREY CA

MR BEN PM HELVENSTEIJN
NASA ARC
M/S 244-10
MOFFETT FIELD CA 94035-0001
(415)694-3182

DR RONALD E HOLMES
TEXAS A & M UNIVERSITY
MECHANICAL ENGRG DEPT
COLLEGE STATION TX 77843-0001
(409) 845-4701

MR JOHN B HENDRICKS
ALABAMA CRYOGENIC ENGRG INC
PO BOX 2451
HUNTSVILLE AL 35804-0001
(205) 536-8629

MR DAVID HUSTVEDT
UCLA DEPT OF CHEMICAL ENGRG
5405 BOELTER HALL
LOS ANGELES CA 90024-1592
(213) 206-3384

MR LEROY M HEROLD
TRW SPACE & TECHNOLOGY GROUP
1 SPACE PARK
REDONDO BEACH CA 90278-0001
(213) 536-8438

YOSHIHIRO ISHIZAKI
ECTI
YAMANOUCHI 253-5
KAMAKURA KANAGAWA
JAPAN - 247
(0467) 25 38 25

MR DEVIN W HERSEY
BOEING AEROSPACE
M/S 82-23
PO BOX 3999
SEATTLE WA 98124-2499
(206) 773-2665

DR ULF ISRAELSSON
JET PROPULSION LAB
4800 OAK GROVE DR
PASADENA CA 91109-0001
(818) 354-9255

DR ALFRED JOHNSON
AEROSPACE CORP
M4/929
PO BOX 92957
LOS ANGELES CA 90009-0001

MR DEAN L JOHNSON
JET PROPULSION LABORATORY
M/S 238-528
4800 OAK GROVE DR
PASADENA CA 91109-0001
(818) 354-4942

MR JOHN W JOHNSON
SYSTRON DONNER CORP
SEATON-WILSON DIV
PO BOX 6939
BURBANK CA 91501-0001
(213) 849-3131

MR JACK A JONES
JET PROPULSION LAB/CALTECH
4800 OAK GROVE AVE
PRASADENA CA 91109-0001
(818) 354-4717

MR FRANK J KADI
LEYBOLD VACCUM PROD INC
5700 MELLON RD
EXPORT PA 15632-0001

MITUSHIRO KANEKO
ATOMIC ENERGY RESEARCH INST
NIHON UNIVERSITY
7-24-1 NARASHIHODAI FUNABASHI-SHI
CHIBA-KEN JAPAN - 274

MR KURT KARPEROS
LOCKHEED MISSILES & SPACE CO INC
M/S 0/59-40 B/589
1111 LOCKHEED WAY
SUNNYVALE CA 94089-3504
(408)742-3340

MR ALI KASHANI
STERLING FEDERAL SYS
1121 SAN ANTONIO RD
PALO ALTO CA
(415) 694-9600

DR RAINER KAUFMANN
DORNIER SYSTEM GMBH
7990 FRIEDICHSHAFEN
PO BOX 1360
F R GERMANY -

MR THOMAS G KAWECKI
NAVAL RESEARCH LAB
CODE 8222
4555 OVERLOOK AVE
WASHINGTON DC 20375-5000
(202) 767-6997

MR PETER J KERNEY
CTI-CRYOGENICS
266 SECOND AVE
WALTHAM MA 02254-9171
(617) 622-5391

MR PETER KITTEL
AMES RESEARCH CTR
MOFFETT FIELD CA 94035-0001
(415) 694-4297

MR TIMOTHY RAY KNOWLES
ENERGY SCIENCE LABS INC
10955 JOHN HOPKINS DR
SAN DIEGO CA 92121-0001
(619) 455-4688

YOEL KORNBLUM
CONTROL DATA CORP
2800 E OLD SHAKOPEE RD
MINNEAPOLIS MN 55440-0001
(612) 853-8925

MR STEPHEN KRAY
ASTRONAUTICS TECH CTR
5800 COLLEGE GROVE RD
MADISON WI 53716-0001
(608) 221-9001

MR OTTO C LEDFORD
ADVANCED TECHNOLOGY
DIR OF SPACE TECH
222 N SUPULVEDA BLVD
STE 1310
EL SEGUNDO CA 90245-0001
(213) 640-1050

MR JEFFREY M LEE
NASA AMES RESEARCH CTR
M/S 244-10
MOFFET FIELD CA 94035-0001
(415) 694-6525

MR JAMES M LESTER
BALL AEROSPACE SYSTEMS CORP
PO BOX 10102
BOULDER CA 80306-0001

MR JAMES R LHOTA
THE AEROSPACE CORP
MZ 250
PO BOX 92957
LOS ANGELES CA 90009-0001
(213) 336-5298

MR JOHN R LIGDA
THE AEROSPACE CORP
PO BOX 9045
ALBUQUERQUE NM 87119-9045
(505) 844-9969

MR PAUL D LINDQUIST
US AIR FORCE
AFWAL/FIEEA
WRIGHT-PATTERSON AFB OH 45433-0001
(513) 255-6078

MR WILLIAM A LITTLE
STANFORD UNIVERSITY
PHYSICS DEPT
STANFORD CA 94305-0001
(415) 723-4233

MR CHANG K LIU
LOCKHEED RES LAB
M/S 92-40 BLDG 205
3251 HANOVER ST
PALO ALTO CA 94304-0001

MR JAMES H LONG JR
SUPERCONDUCTOR TECHNOLOGIES INC
STE F
460 WARD DR
SANTA BARBARA CA 93111-0001
(805) 683-7646

MR RALPH C LONGSWORTH
APD CRYOGENICS INC
1919 VULTEE ST
ALLENTOWN PA 18103-0001
(215) 791-6708

MR XAVIER K MARUYAMA
NAVAL POSTGRADUATE SCHOOL
PHYSICS DEPT
MONTEREY CA 93943-0001
(408) 646-2431

MS JILL L LUDWIGSEN
NICHOLS RESEARCH CORP
STE 105
2340 ALAMO SE
ALBUQUERQUE NM 87106-0001
(505) 843-7364

FRITHJOF N MASTRUP
HUGHES AIRCRAFT CO
M/S F205 BLDG E54
PO BOX 902
EL SEGUNDO CA 90245-0001
(213) 616-9647

MR JOSEPH N MANFREDO
AIRESEARCH LOS ANGELES
ALLIED-SIGNAL AEROSPACE CO
2525 W 190TH ST
TORRANCE CA 90509-0001
(213) 512-1803

YOICHI MATSUBARA
ATOMIC ENERGY RESEARCH
NIHON UNIVERSITY
7-24-1 NARASHINODAI FUNABASHI-SHI
CHIBA-KEN JAPAN - 274
0474-66-1111

MR ENZO MARMENTINI
SYSTRON DONNER CORP
SEATON-WILSON DIV
PO BOX 6939
BURBANK CA 91510-6939
(213) 849-3131

MR FRANK E MCCREA
VARIAN ASSOCIATES
VACCUM PROD DIV
3560 BASSETT ST
SANTA CLARA CA 95054-2704
(408) 986-9888

MR GREGORY N MARTIN
EG&G ORTEC
100 MIDLAND RD
OAK RIDGE TN 37830-0001
(615)482-4411

MR JOHN E MCCULLOUGH
ARTHUR D LITTLE INC
20-549 ACORN PARK
CAMBRIDGE MA 02140-2390
(617) 864-5770

DR RICHARD A MARTIN
LOS ALAMOS NATIONAL LAB
M\S J765
PO BOX 1663
LOS ALAMOS NM 87544-0001

MOSES MINTA
VARIAN ASSOCIATES
VACCUM PROD DIV
3560 BASSETT ST
SANTA CLARA CA 95054-2704
(408) 496-2825

DR ARCHER S MITCHELL
WESTINGHOUSE ELECTRIC
10706 EASTWOOD AVE
SILVER SPRING MD 20901-0001
(301) 765-7228

MR MATTHEW P MITCHELL
MITCHELL STIRLING MACHINES SYS
PRES
STE 207 B
2550 NINTH ST
BERKELEY CA 94710-0001
(415) 845-2528

MR DARYL L MOSSMAN
AEROJET ELECTROSYSTEMS CO
100 W HOLLYVALE ST
AZUSA CA 91702-0001
(818)812-1767

MR RICHARD P MOYER
APD CRYOGENICS
1919 VULTEE ST
ALLENTOWN PA 18103-0001
(215) 791-6768

DR WILLIAM C MULRONEY
INSTITUTE FOR DEFENSE ANALYSES
1801 N BEAUREGARD ST
ALEXANDRIA VA 22311-0001
(703) 578-2746

MR ROGER D MURRY
AIRESEARCH
2525 W 190TH ST
TORRANCE CA 90509-0001
(213) 512-4588

MR HIROSHI NAGANO
PROFESSOR AT TOYAMA UNIVERSITY
SAN-EI BLDG 8 SAN-EI-CHO
SHINJUKU-KU TOYOKO 160 JAPAN
-
03-359-5231

MR CHARLES S NAIMAN
ICE INC
15 ORMOND PARK RD
BROOKVILLE NY 11545-0001
(516) 349-1080

DR CHARLES S NAIMAN
CHARLES S NAIMAN INC
PRES
160 LANCASTER TER
BROOKLINE MA 02146-0001
(617) 277-4184

ISSHIKI NAOTSUGU
NIHON UNIVERSITY
2-29-6 KYODO SETAGAYAKU
TOKYO JAPAN - 156
0249 44 1300

DR RAM NARAYAN
MAGNAVOX GOV & IND ELECTRONICS
46 INDUSTRIAL AVE
MAHWAH NJ 07430-0001
(201) 529-1700

MR TED C NAST
LOCKHEED CORP
508 NINO AVE
LOS GATOS CA 95032-0001
(408) 356-8239

MR RONALD NEIKIRK
LEBOLD CRYOGENICS
STE 4000
1815 NW 169TH PLACE
BEAVERTON OR 97006-0001
(503) 645-5921

BAO KHAC NGUYEN
AIR FORCE ASTRONAUTICS LAB
AFAL/RKLB
EDWARDS AFB CA 93523-0001
(805) 275-5541

MR MARTIN NISENOFF
NAVAL RESEARCH LAB
CODE 6854
WASHINGTON DC 20375-5000
(202) 767-3099

SHLOMO NOVOTNY
DIGITAL EQUIPMENT CORP
77 REED RD HL02-3/J3
HUDSON MA 01749-0001
(508) 568-5395

MR JAMES F PARADISE
WESTINGHOUSE ELECTRIC CORP
M/S 3F03
PO BOX 1521
BALTIMORE MD 21203-0001
(301) 765-4322

MR KEITH M PARKER
GE MAGNET SYSTEMS
3001 W RADIO DR
FLORENCE SC 29501-0001
(803) 664-1650

MR GEORGE PATTON
DAVID TAYLOR RESEARCH CTR
CODE 2712
ANNAPOLIS MD 21402-5067
(201) 267-3632

MR WILLIAM G PATTON
DAVID TAYLOR RESEARCH CTR
CODE 2712
ANNAPOLIS MD 21402-5067
(201) 267-2149

MR ROBERT L PAUGH
MMR TECHNOLOGIES INC
STE A-5
1400 NORTH SHORELINE BLVD
MTN VIEW CA 94043-1312
(415) 962-9620

HSIEN SHENG PEI
DIGITAL EQUIPMENT CORP
63 WOODRIDGE RD
WAYLAND MA 01778-0001
(617) 351-4913

MR STANLEY Z PEPLINSKY
AAI CORPORATION
SEN DESIGN ENGR
PO BOX 126
HUNT VALLEY MD 21030-0216
(301) 628-8514

MR WALTER PESCHKA
DFVLR GERMAN AEROSPACE
PFAFFENWALDRING 38-40
7 STUTTGART 80
WEST GERMANY - 7000
(0711) 6862-430

MR KENNETH R PINCKNEY
US AIR FORCE
PO BOX 5126
SD/CNWK
SANTA BARBARA CA 93108-0001
(213) 643-2059

DR WENDELL H POTTER
UNIV OF CALIFORNIA DAVIS
DEPT OF PHYSICS
DAVIS CA 95616-0001
(916) 752-3305

MR WILLEM G PULLEN
PHILIPS USFA BV
MEERENKKERWEG 1
EINDHOVEN
NETHERLANDS - 5600MD
(0) 40-723130

MR RAY RADEBAUGH
NATIONAL BUREAU OF STANDARDS
M/S 773.30
325 BROADWAY
BOULDER CO 80303-0001
(303)497-3710

MR RICHARD W RALSTON
MASSACHUSETTS INST OF TECH
LINCOLN LAB
PO BOX 73
LEXINGTON MA 02173-0001
(617) 981-7866

MR RONALD REUSS
ALLIED SIGNAL AEROSPACE CO
MGR ADV TECH PROG
M/S S-4
PO BOX 92248
LOS ANGELES CA 90006-0001
(213)417-6824

PAT R ROACH
NASA AMES RESEARCH CTR
M/S 244-10
MOFFETT FIELD CA 94035-0001
(415) 694-3191

MR GEORGE Y ROBINSON
NICHOLS RESEARCH CORP
19 HEMLOCK LN
ACTON MA 01720-0001
(508) 263-4643

MR RONALD G ROSS JR
JET PROPULSION LAB
M/S 157-102
4800 OAK GROVE DR
PASADENA CA 91109-0001
(818) 354-9349

MR SAMUEL C RUSSO
HUGHES AIRCRAFT CO
BLDG E55 M/S G232
PO BOX 902
EL SEGUNDO CA 90245-0001
(213) 619-9651

MR ROBERT E SARWINSKI
CRYOGENIC DESIGNS INC
2655 SODERBLOM AVE
SAN DIEGO CA 92122-0001
(619) 546-1870

MR ERWIN SCHROEDER
DAVID TAYLOR RESEARCH CTR
CODE 1844
BETHESDA MD 20084-0001
(301) 227-1660

MR JAMES K SHAFFER
CTR FOR NIGHT VISION & ELECTRO OPTICS
AMSEL-RD-NV-TS
FT BELVOIR VA 22060-0001
(703) 664-1345

MR ALI SHAIK
PHILIPS LABORATORIES
210/3RT SAIDABAD COLONY
HYDERABAD INDIA - 500659

MR WILLIAM R SHIELDS
JANIS RESEARCH CO INC
2 JEWEL DR
WILMINGTON MA 01887-0001
(617) 657-8750

MR MATTHEW M SKERTIC
HUGHES AIRCRAFT CO
BLDG 270 M/S 071
8433 FALLBROOK AVE
CANOGA PARK CA 91304-0001
(818) 702-1566

MR JOSEPH L SMITH JR
MIT
RM 41-204
CAMBRIDGE MA 02139-0001
(617) 253-2296

MR LARRY SMITH
MCC
12100 TECHNOLOGY BLVD
AUSTIN TX 78727-0001
(512) 250-2734

MR LAWRENCE D SOBEL
HUGHES AIRCRAFT
3100 W LOMITA BLVD
TORRANCE CA 90505-0001
(213) 517-5703

MR WALTER F STEWART
LOS ALAMOS NATIONAL LAB
M/S F611
PO BOX 1663
LOS ALAMOS NM 87545-0001
(505)665-1416

MR GRANT G STOCKWELL
ALLIED SIGNAL AEROSPACE CO
AIRESEARCH LOS ANGELES DIV
2525 W 190TH ST
TORRANCE CA 90509-0001
(213) 512-3391

MR JIM STOLZ
VARIAN VACUUM PROD DIV
SEN ELECTRONICS ENGR
3560 BASSETT ST
SANTA CLARA CA 95054-2704
(408) 986-988

MR WILHELM T STRASSER
LEYBOLD AG WG
BONNER STRASSE 458
COLOGNE (KOLN) NRW
WEST GERMANY - 5000

MR MICHAEL J SUPERCZYNSKI
DAVID TAYLOR RESEARCH CTR
CODE 2717
ANNAPOLIS MD 21402-0001
(301) 267-2149

MR ANDRZEJ SWIECICKI
QUANTUM TECHNOLOGY CORP
6237 148TH ST
SURREY BC CANADA -- V3S 3C3
(604)594-6170

MR GREGORY W SWIFT
LOS ALAMOS NATIONAL LAB
M/S K764
LOS ALAMOS NM 87545-0001
(505) 665-0640

MR WALTER L SWIFT
CREARE
PO BOX 71
HANOVER NH 03755-0001
(603) 643-3800

MR WILLIAM THOMPSON
AEROJET ELECTROSYSTEMS CO
1100 W HOLLYVALE ST
PO BOX 296
AZUSA CA 91702-0001
(818) 812-2267

MR RUSSELL TIPTON
FORMA SCIENTIFIC
MILCREEK RD
PO BOX 649
MARIETTA OH 45750-0649
(614) 373-4763

JEFFREY A TRIPP
US DEPT OF COMMERCE
RM 4113 14TH & CONSTITUTION AVE NW
WASHINGTON DC 20230-0001
(202) 377-3765

MR JEFFREY A TRIPP
US DEPT OF COMMERCE
14TH & CONSTITUTION AVE NW
H C HOOVER BLDG RM 4058
WASHINGTON DC
(202) 377-1309

MR EMANUEL TWARD
TRW SPACE & TECHNOLOGY GROUP
0111/2050
ONE SPACE PARK
REDONDO BEACH CA 90278-0001

COSTAS TZEMOS
CVI INCORPORATED
4200 LYMAN CT
HILLARD OH 43216-0001
(614) 876-7381

MR KENNETH L UHERKA
ARGONNE NATIONAL LAB
BLDG 331
9700 S CASS AVE
ARGONNE IL 60439-0001
(312) 972-7814

C LYN VOGT
SYSTRON DONNER CORP
SEATON-WILSON DIV
PO BOX 6939
BURBANK CA 91505-0001
(213) 849-3131

MANOS VOURGOURAKIS
HUGHES-EDSG
BLDG E-54 M/S F-204
PO BOX 902
EL SEGUNDO CA 90245-0902
(213) 616-9646

MARIJA VUKOVOJAC
BUTTERWORTHS
PO BOX 63
GUILFORD SURREY
ENGLAND - GU2 SBH
0483 300966

MR BUFORD T WALTERS
CRYO-TEK CORPORATION
8527 PHOENIX DR
MANASSAS VA 22110-0001
(703) 836-1717

MS NANCY K WELKER
DEPT OF DEFENSE
9800 SAVAGE RD
FT MEADE MD 20755-6000
(301) 859-6555

MR ALBERT W WELZ JR
ARTHUR D LITTLE INC
20 ACORN PARK
CAMBRIDGE MA 02140-0001
(617) 864-5770

MR RICHARD WENKER
AIRESEARCH MANUFACTURING CO
GARRETT CORP
2525 W 190TH ST
TORRANCE CA 90509-0001

MR RONALD WHITE
US AIR FORCE
AFWAL/FIEEA
WRIGHT-PATTERSON AFB OH 45433-0001
(513) 255-6078

MR RICHARD J WILLIAMS
AEROJET ELECTRO-SYSTEMS CO
BLDG 160 DEPT 4323
PO BOX 296
AZUSA CA 91702-0001
(818) 812-1864

MR RICHARD C WOLGAST
LAWRENCE BERKELEY LAB
1 CYCLOTRON RD
BLDG 90-2148
BERKELEY CA 94720-0001
(415) 486-5786

MR SCOTT WOOLAWAY
BALL AEROSPACE
1600 COMMERCE ST
BOULDER CO 80302-0001
(303) 939-6220

MR SHIGERU YOSHIDA
TOYO OXYGEN CO LTD
3-3 MIZUE-CHO
KAWASAKI-KU
KANAGAWA JAPAN -- Z10
044-266-2652

AVIHU ZE-EVI
ELSCINT
R & D MGR
PO BOX 550
HAIFA ISRAEL -

MR YUAN ZHOU
CRYOGENIC LAB
CHINESE ACADEMY OF SCIENCES
PO BOX 2711
BEIJING CHINA - 10080
28.9491 BEIJING

MR STEVEN G ZYLSTRA
GENERAL PNEUMATICS CORP
STE 107
7662 E GRAY RD
SCOTTSDALE AZ 85260-0001
(602) 998-1856